Investigation of the formation mechanisms of the High Burnup Structure in the spent nuclear fuel - Experimental simulation with ions beams

Yara Haddad

NNT : 2017SACLS519

THÉSE DE DOCTORAT
DE
L'UNIVERSITÉ PARIS-SACLAY
Préparée à l'Université Paris-sud

ÉCOLE DOCTORALE N°576 PHENIICS: Particules hadrons énergie et noyau : instrumentation, imagerie, cosmos et simulation
Spécialité de doctorat : énergie nucléaire

INVESTIGATION OF THE FORMATION MECHANISMS OF THE HIGH BURNUP STRUCTURE IN THE SPENT NUCLEAR FUEL – EXPERIMENTAL SIMULATION WITH IONS BEAMS

Par

Mme Yara Haddad

Thèse présentée et soutenue à Orsay, le 07 Décembre 2017

Composition du jury :

M. Bertrand Reynier	Professeur, ENSTA ParisTech	Président du Jury
Mme Nathalie Moncoffre	Directrice de recherche CNRS, IPN de Lyon	Rapporteur
M. Alberto Quaranta	Professeur, Université de Trento (Italie)	Rapporteur
M. Jean-Luc Béchade	Chercheur-ingénieur, SRMP, CEA Saclay	Examinateur
M. Patrick Simon	Directeur de Recherche CNRS, CEMTI Orléans	Examinateur
M. Thierry Wiss	Commission européenne, JRC, Allemagne	Examinateur
Mme Aurelie Gentils	Chargée de recherche CNRS, CSNSM Orsay	Examinatrice
M. Frédérico Garrido	Professeur, Université Paris-Sud	Directeur de thèse

THESIS

INVESTIGATION OF THE FORMATION MECHANISMS OF THE HIGH BURNUP STRUCTURE IN THE SPENT NUCLEAR FUEL – EXPERIMENTAL SIMULATION WITH IONS BEAMS

Submitted by

Yara Haddad

To fulfill the requirements for the degree of doctor of nuclear energy

at the

UNIVERSITY PARIS-SACLAY
(UNIVERSITY PARIS-SUD)

In front of the jury comprising

Bertrand Reynier	Professor, ENSTA ParisTech	President of jury
Nathalie Moncoffre	Research Director CNRS, IPN of Lyon	Referee
Alberto Quaranta	Professor, University of Trento (Italy)	Referee
Jean-Luc Béchade	Research engineer, SRMP, CEA Saclay	Examiner
Patrick Simon	Research Director CNRS, CEMTI Orléans	Examiner
Thierry Wiss	European Commission, JRC, Germany	Examiner
Aurelie Gentils	Researcher CNRS, CSNSM Orsay	Examiner
Frédérico Garrido	Professor, University Paris-Sud	Supervisor

December 07, 2017

Acknowledgments

I would like to acknowledge and extend my heartfelt gratitude to the following persons who have made the completion of this PhD thesis.

A special gratitude I give to my advisor, Dr. Frédérico Garrido whose contribution in stimulating suggestions and encouragement, helped me to pass and write this thesis by contributing and forcing me to learn more and more by his vital suggestions and instructions. I would like to thank him for encouraging my research and for allowing me to grow as a research scientist, his advice on my research has been priceless. I have been extremely lucky to have a supervisor who cared so much about my work, and who responded to my questions all the time starting from the Master up to this moment.

Besides my advisor, I would like to thank Dr. Aurélie Gentils for her help in performing the TEM experiments, teaching me how to use TEM techniques, answering my questions and helping me a lots in analyzing the images. Thank you for your support, help and for giving me the opportunity to work with you.

I would also like to thank all members of my group: professors and friends, Dr. Lionel Thomé, Dr. Gaël Sattonnay, Dr. Aurélien Debelle, Najah Mejai, Diana Bachiller Perea, Suheyla Bilgen, for their help, advice and their elegant deal.

Many thanks to the SCALP facility staff for their kind assistance during my experiments. Special thanks to Cyril Bachelet and Cédric Baumier, they have always managed to give us beam time and helped me to finish my experiments. I would also like to thank Lucie Delauche for her kind help and nice period we spent together in preparing samples, thanks for her help.

My sincere thanks to the direction of the CSNSM laboratory for welcoming me in this laboratory, for helping me with the administrations during my thesis and for giving me the opportunity to attend several conferences. I would also like to thank the École Doctorale “PHENIICS” for the financial support for my thesis.

A special thanks to my family. Words can not express how grateful I am to my adorable parents and to my brothers and sisters who helped me a lot in finishing this PhD thesis by their encouragement and supporting words all the time specially the moments I felt a little bit down when I miss them. My deepest gratitude also to my beloved friend Walaa Ayasrah for supporting me in everything at every moment.

I would also like to thank all of my friends here in France and in Jordan, who supported me in writing, and incented me to strive towards my goal.

Thanks again to all who helped me and to whom I forgot to mention!

Abstract

The aim of this thesis is to investigate and reproduce the specific features of the microstructure of the high burnup structure of the irradiated nuclear fuel and to explore the various relevant parameters involved in the formation of such a structure, in evaluating their importance, and in clarifying the synergies between them. This goal has been reached by using a very simplified model system - namely uranium dioxide single crystals - irradiated with low energy La or Xe ions at 773 K, corresponding to the temperature at the periphery of the genuine fuel.

The energies and masses of bombarding ions were chosen to investigate the destabilization of the solid due to: (i) the elastic nuclear collisions and by (ii) the chemical contribution of impurities at high concentrations by implanting different ions in UO_2, namely Xe and La, having very distinct solubility: La species are soluble in UO_2 while Xe ions are insoluble.

In situ Rutherford Backscattering Spectrometry in the channeling mode (RBS/C) and *in situ* Transmission electron Microscopy (TEM), both techniques coupled to ion irradiation, were performed to visualize, quantify and provide information with respect to the fraction of radiation-induced defects and the formation of bubbles, cavities, or precipitates. The channeling data were analyzed afterwards by Monte Carlo simulations assuming two class of defects comprising (i) randomly displaced atoms (RDA) and (ii) bent channels (BC) defects. Regarding the RDA evolution, a sharp step increase appears from 0.4 to 4.0 *dpa* (corresponding to a low concentration of implanted ions), regardless of nature of ions, followed by a saturation of the fraction of RDA for both ions over a wide range of irradiation. A sharp increase of RDA fraction is observed specifically for crystals implanted with Xe ions at a high concentration exceeding 1.5 % (corresponding to the dose of more than 125 *dpa*). Regarding the BC evolution, for both ions, the evolution shows an increase in the fraction of BC up to 4.0 *dpa*, then the fraction of BC almost saturates for Xe and La ions.

In situ TEM results show that a similar radiation-induced defects appear for both ions and the same evolution of defects formation as a function of the fluence is observed. The various defects evolved as a function of the fluence: black dot defects were observed as a first type of defects created, then dislocation lines and loops appeared and evolved until they started to be become less distinguishable, the restructuring process continued by forming a tangled dislocation network. A high density of nanometer-sized gas bubbles with a mean diameter 2 nm was observed at room temperature for the Xe-implanted crystal at a threshold dose of 4 *dpa*.

The coupling between both techniques (*in situ* RBS/C and TEM) demonstrates that the difference between the two plateaus of saturation for the two ions and the dramatic increase of RDA at high concentration of implanted Xe ions can be ascribed to: (i) the solubility of La compared to Xe ions leading to the formation of nanometer-sized gas bubbles and (ii) the size of implanted species in UO_2 matrix where insoluble Xe atoms have an atomic radius much larger than the cationic radius of U^{4+} atoms, (La^{3+} atoms have a similar atomic radius as U^{4+} atoms) responsible for an increase of the stress in UO_2 crystal.

Contents

Introduction

Nuclear energy is used to generate heat and electricity from the early 1950's. It provides about 4.8% of the world's energy and 10.6% of the world's electricity in 2014 [1]. Nuclear energy includes nuclear fission, nuclear decay, and nuclear fusion. To produce electricity from the fission process, nuclear reactors are used to initiate and control a sustained nuclear chain reaction, where the heat that is generated is transferred to a working fluid (gas or liquid) which runs through turbines used to rotate generators and then getting the electricity.
There are currently 447 operable nuclear power reactors around the world, with a further 61 under construction [2] with several different types:

1- Light water reactors: with two categories Pressurized Water Reactor (PWR) and Boiling Water Reactor (BWR)
2- Pressurized Heavy Water Reactor 'CANDU'
3- Gas-cooled Reactor
4- Light Water Graphite Reactor
5- Fast Neutron Reactor (FBR)

The most common reactors used in the world nowadays are light-water reactors (LWRs), which use ordinary water both as a moderator, to slow down the neutrons associated with the nuclear chain reaction in the reactor core, and as a coolant to carry away the produced heat. LWRs come in two main varieties, Pressurized Water Reactors (PWRs), where the water is maintained at high pressure so as to prevent its boiling into steam, and Boiling Water Reactors (BWRs), where the water is allowed to boil.
Pressurized Water Reactors (PWR) is the most common type reactor used nowadays; this reactor uses ordinary water as both coolant and moderator, where the water in the primary circuit (coolant) is pumped under high pressure through the reactor core to extract the heat which is generated by the fission process of the fuel (see figure I). This heated water flows through steam generator to transfer the heat to the second circuit where the steam is generated to run through the turbines used to drive generators and then to produce the electricity.

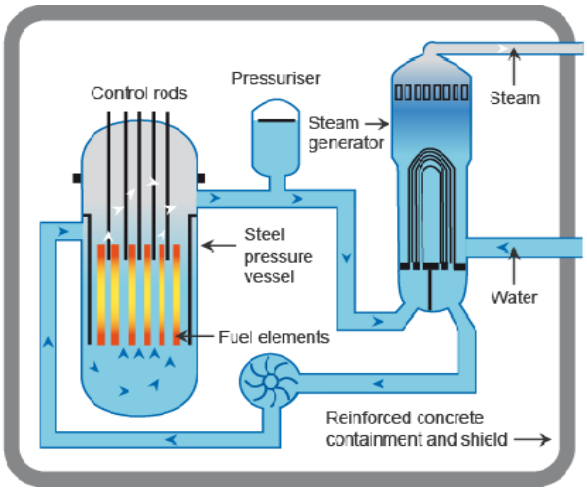

Figure I: A typical Pressurized Water Reactor (PWR) [3]

The reactor core of PWR has many fuel assemblies (about 150-250 fuel assemblies) with 80-100 tons of uranium, and with 200-300 rods per each assembly [3] composed of uranium dioxide UO_2 (see figure II), that is the fuel for electricity producing in nuclear power stations.

[1] Key World Energy Statistics. International Energy Agency, 2016
[2] The Nuclear fuel cycle overview, World nuclear association, 2016
[3] Nuclear Power reactors, World nuclear association, 2017

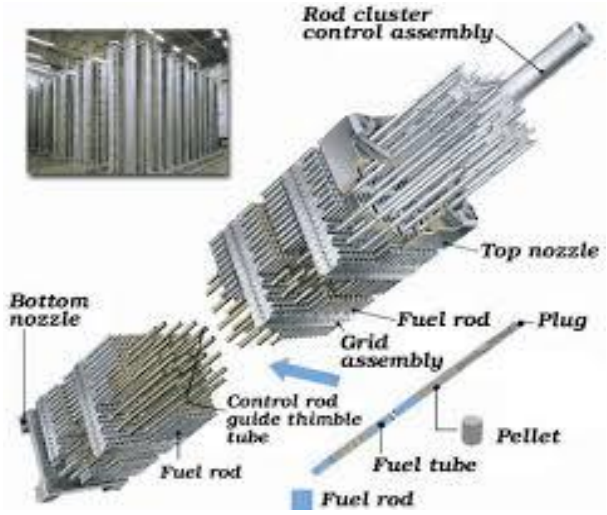

Figure II: Schematic view of PWR fuel assembly [4]

UO_2 is a fluorite-type ceramic oxide (cubic structure) with a melting temperature of 3140 K. During the reactors operation, ^{235}U included in the fuel will be submitted to fission and a large amount of energy is deposited by both electronic and nuclear stopping of the two fission fragments produced by the fission process with kinetic energies in the MeV range. As a consequence, radiation damage is created by the radiation, and a high concentration of impurities fission products is generated, all are finally trapped in the fuel.

To study the radiation performance of UO_2 during operating the reactor, it is important to understand the behavior of the fission products, which are more than 30 elements, classified in three groups [5]:

- Soluble elements in the lattice, like lanthanides, and this affect the oxygen to metal ratio.
- Gaseous and volatile elements like (Xe, Kr, Cs, I), that precipitate and form bubbles when their concentration is high enough.
- Elements forming solid precipitates, such a metals (such as Mo, Cd, In).
- Elements found in ceramics inclusions like (Ba, Zr, Nb).

All these incorporated elements are responsible for thousands of displacements for the UO_2 atoms because each individual fission process changes the structure of the material. Therefore it is important to study these effects created by the fission process on the stability of the fuel.

Although it is well established that uranium dioxide does not become amorphous under irradiation, UO_2 exhibits a defective structure, whose specific microstructure depends on several parameters (e.g. local burnup, local temperature, irradiation conditions, nuclear and electronic stopping and incorporated impurities). In particular, a zone located at the peripheral region of the nuclear fuel pellet (100-200 µm extension) submitted to extreme irradiation conditions, leading to grain subdivision and pore formation - referred to as the High Burnup Structure (HBS) - focuses attention on the role played by the various parameters either in a separate or in a combined way on the solid destabilization [6-7].

[4] Nuclear Fuel Fabrication, World nuclear association, 2017.
[5] Donald R.Olander. Fundemantal aspects of nuclear reactor fuel elements, Technical information center, 1976.
[6] Hj.Matzke, M. Kinoshita. Polygonization and high burnup structure in nuclear fuels, Journal of Nuclear Materials, 247(1997)108-115.
[7] K. Nogita , K. Une , M. Hirai , K. Ito , K. Ito , y. Shirai. Effect of grain size on recrystallization in high burnup fuel pellets. Journal of Nuclear Materials, 248 (1997) 196-203.

A full understanding of the formation of this structure during irradiation became an object to study worldwide for both scientific interest and for safety and commercial reasons. Therefore, several studies of the specific microstructure HBS were performed to understand the polygonization process that appears in the HBS and to identify the mechanisms and the conditions (burnup, temperature, the high concentration of fission product and fission gases, pressure, grain size, etc.) of the formation of this specific structure in the nuclear fuel. Investigating such a structure requires an investigation of a genuine nuclear spent fuel that is considered as a big challenge to scientists since it is highly radioactive material, it requires a lot of special safety procedures as well as special equipment. The aim of this work is to perform modeled experiments in a much simplified fuel: uranium dioxide single crystal. In this work, the specific microstructure of the nuclear spent fuel was experimentally simulated by using ion beams provided by accelerator facilities, to both damage the solid and incorporate foreign elements in the lattice. *In situ* implantation and characterization experiments were performed by using a simplified model system – namely uranium dioxide single crystals – irradiated with low-energy ions at 773 K in order to examine the respective contributions of (i) radiation-defects production and (ii) implanted species, to the formation of a specific microstructure. Moreover, by using a specified ion, the chemical contribution of these implanted impurities including their modifications on the chemical and physical properties of nuclear fuel can also be investigated. It is important to mention, the results that obtained from this work are not intended to provide a complete knowledge about this specific microstructure but they will be useful to explore the apparition of such a structure and to explain the structural modifications of nuclear spent fuel.

Thesis outlines

This thesis is organized in five chapters as the following:

The first chapter introduces the uranium dioxide as nuclear fuel in light water reactors describing its properties, processes and the changes which occur during its operating life in the reactor core. The effect of radiation in the nuclear fuel including the theory of the interaction between charged particles with the material and the appearance of a specific effects occurring at very high burnup structure will be discussed in this chapter.
The second chapter presents in details the simulation experiments that were performed to reproduce and investigate the conditions leading to the formation of the high burn up structure and the different characterization techniques that were applied, including Rutherford Backscattering Spectrometry in Channelling mode (RBS/C) and Transmission electron Microscopy (TEM). A general introduction about the Monte-Carlo simulation code which was used to quantify that damage is also presented.
The third chapter presents in details the Rutherford Backscattering spectrometry experiments in Channelling geometry (RBS/C) that were performed during this thesis and shows the analysis of RBS/C spectra for crystals implanted with both ions, using a Monte Carlo simulation code and assuming a two-defect model. The description of the model and the effect of each class of defects on the simulation spectra is presented. The damage evolution extracted from the simulations is also discussed.
The fourth chapter presents the Transmission Electron Microscopy (TEM) experimental results. The damage evolution of implanting different ions (La or Xe) ions will be shown.
The fifth chapter discusses the role of implanting foreign elements and the effect of temperature on the damage evolution in irradiated UO_2. In this chapter, the damage evolution that was obtained by both RBS/C and TEM and the coupling between the results provided by the techniques is discussed.
Conclusions and Perspectives presents conclusions from the work, and recommendations are made for the future work.

Chapter 1

Irradiation effects in the spent nuclear fuel

The first section of this chapter gives an introduction about the uranium dioxide, as it is the nuclear material used as nuclear fuel in Light water reactors, describing its properties, processes and the changes that occur during its operating life in the reactor core.
The last two sections present the spent fuel and the radiation damage induced in irradiated uranium dioxide. The specific effects occurring at very high burnup structure finally discussed.

1.1 Uranium dioxide (UO_2): the nuclear fuel in LWRs

Ceramics are widely accepted as nuclear reactor fuel materials (e.g. UO_2, (U, Pu) O_2, UC, U-Si) and the most popular for nuclear energy production is the uranium dioxide which is the much used fuel over the world especially in light water reactors LWRs.
Uranium dioxide has a fluorite-type crystalline structure in which uranium atoms form a faced centered cubic (*fcc*) sublattice [Willis 1964] and oxygen atoms locate at all available tetrahedral positions, as shown in the figure 1-1:

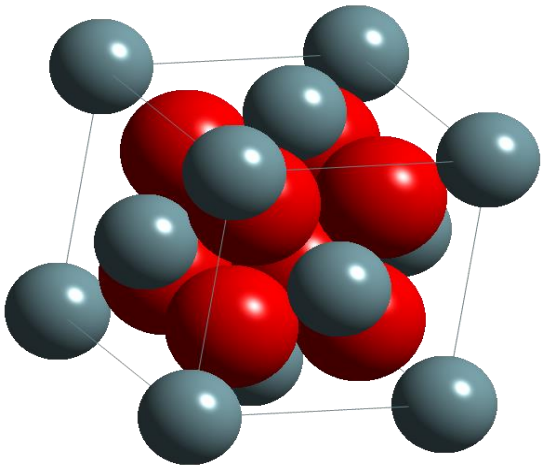

Figure 1-1: Drawing of uranium dioxide crystal in which uranium atoms locate at *fcc* position (Grey) and oxygen atoms locate all available tetrahedral positions (red).

Uranium dioxide (also known as urania or uranous oxide), that is mainly used as nuclear fuel in nuclear reactors since early days, can be also used as a mixture of UO_2 and PuO_2 (plutonium dioxide). (U, Pu)O_2 is called a mixed oxide (MOX fuel) and exhibits the same fluorite-type structure as UO_2 and PuO_2.

Uranium dioxide has several properties [Stehle *et al.* 1975] which give it advantages to be used as fuel, such as a high melting temperature (~3140K) [Olander 1976] and tolerance towards irradiation. Furthermore, UO_2 is a good trap for the fission products and the actinides which are produced during operation. These elements are highly radioactive and chemically toxic so they must be confined inside the structure of the fuel and not to be released.

Nevertheless, it has also disadvantages such as a low thermal conductivity, brittleness and a strong temperature gradients (~ $1.7x10^3$ $K.cm^{-1}$) [Olander 1976] since the temperature of the center of the fuel is always higher than the surface of the fuel rod and this lead to phenomena such as close pores migration from the low temperature region toward the center of the fuel pin; important constituents of the fuel, such as the fission products, oxygen, plutonium are redistributed from their initial concentration profile; thermal stress causes the fuel to either deform plastically in the high temperature region or to crack in the low temperature zones [Olander 1976].

Moreover UO_2 is not stable in an oxygen-rich environment where UO_2 can quickly interact with oxygen and forms oxygen-rich uranium oxides, such as U_4O_9, U_3O_7 or U_3O_8. This will reorganize the crystallographic structure of UO_2. Therefore, the interaction between the UO_2 and the oxygen in the reactor core is avoided by filling the gap full with helium under high pressure of 0.1 to 0.3 MPa. Table 1-1 presents selected important properties for UO_2:

Table 1-1: Some selected important properties for UO_2 [FINK *et al.* 1981], [Yamada *et al.* 2000], [Hausner 1965], [Soullard *et al.* 1985], [Meis & Chartier 2005]

Molecular formula	**UO_2**
Molar mass ($g.mol^{-1}$)	270.03
Density ($g.cm^{-3}$) **solid state** **liquid state**	 10.96 9.573
Melting Temperature (K)	~ 3140
Thermal conductivity (W/m.K) **solid state (298 K)** **Liquid state**	 8.89 2.5
Heat capacity C_p (J/Kg.K)	
298 (K)	235
1500 (K)	330
2000 (K)	376
2500 (K)	510
Latent heat of fusion (kJ/kg)	289
Displacement threshold energy (eV)	$E_d(U) = 40$ $E_d(O) = 20$
Crystal structure	Cubic $Fm\bar{3}m$
Cell parameter at 293 K (pm)	547.0

1.1.1 Uranium dioxide during in reactor operation and High Burnup Structure (HBS) formation (RIM effect) in the nuclear fuel

During the operating life of UO_2 in the reactor core, a large amount of heat is generated inside the fuel fission chain reaction process. In this process neutrons emitted by a fissioning nucleus induced fission in other fissionable nuclei; and then the neutrons from these fissions induce fissions in other fissile or fissionable nuclei, and so on. Each fission process produce ~200 MeV as it is shown in the table 1-2:

Table 1-2: Emitted energies for fission of ^{235}U [Lamarsh & Baratta 2001]

Energy From	Emitted energy(MeV)
Fission fragments	168
Fission product decay	27
Prompt gamma-rays	7
Fission neutrons (kinetic energy)	5

From the table, it is clear that most (~ 85%) of the energy released in the fission appears as a kinetic energy of the fission fragments, and this large amount of energy deposited by the fission products in the fuel pellet affects its structure by creating radiation defects. In addition to this, the progressive incorporation of the fission fragments inside the fuel changes the composition and the properties of uranium dioxide.

The fission process is almost always asymmetric [Lamarsh & Baratta 2001], so that the masses of the two fission fragments are substantially different, and this is indicated in figure 1-2, where the fission products yield, that is the percent of fission fragments produced with a given mass number A for fission induced by thermal neutrons in ^{235}U, is presented.

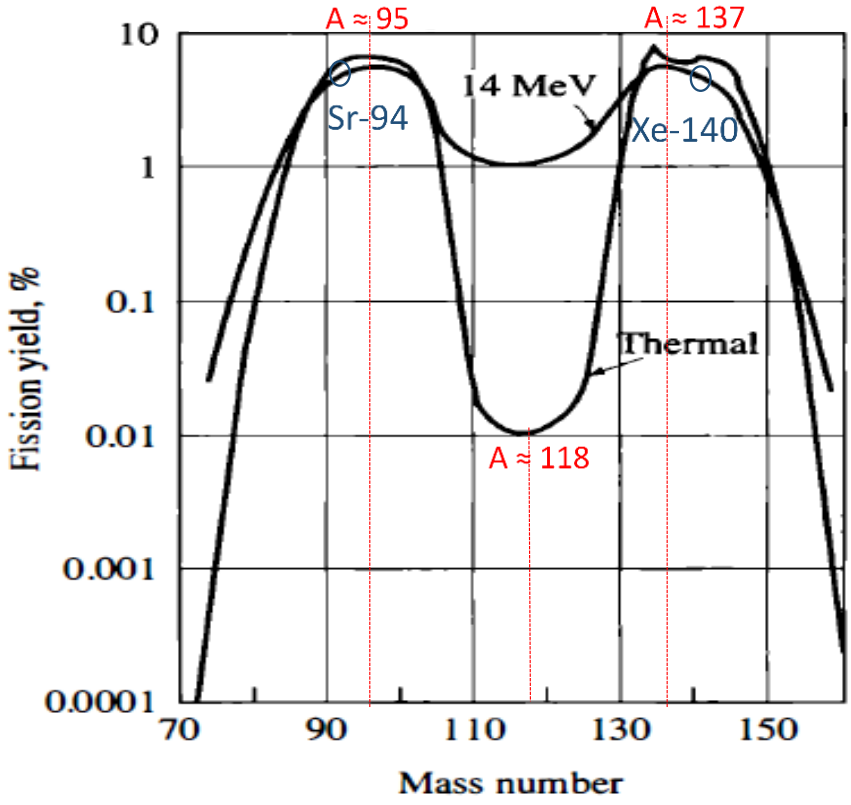

Figure 1-2: Fission-product yields for thermal and 14-MeV fission neutrons in ^{235}U [Lamarsh & Baratta 2001]

There are three classes for these fission products [Matzke *et al.* 1994]:

- Soluble elements in the solid UO_2, like the rare earths, these elements affects the oxygen to metal ratio and the oxygen potential.

- Gaseous and volatile elements (Kr, Xe, Rb, Cs, I) where Cs can react with the fuel to form Cs-uranates, while Kr and Xe precipitate in bubbles.

- Elements forming solid precipitates (so-called five-metal particles, consisting of Pd, Ru, Rh, Tc and Mo, or oxide precipitates)

During the operating life of the nuclear fuel in the reactor core, and with time, the concentration of these fission products and heavy elements such as plutonium and other heavier actinides (Am, Cm) will increase up to the point where it is no longer practical to continue to use the fuel. It is then called "spent" nuclear fuel where about one-fourth to one-third of the total fuel load is spent and removed from the reactor every 12 to 18 months and replaced with fresh fuel.

The composition, heat output and radioactivity per ton of heavy metal of the spent fuel depend upon the burn-up and the initial amount of fissile material. For LWR spent fuel with a burnup of 50 GWd/tHM, the spent fuel consists in concentration of about 93.4% uranium (~ 0.8% U-235), 5.2% fission products, 1.2% plutonium (12 kg or 1.5 weapon equivalents per ton of fuel), and 0.2% minor transuranic elements (neptunium, americium, and curium).

As an example to present this composition [Billard], a conventional PWR reactor of 1 GWe with uranium enriched to 3.5% studied where a ton of fresh fuel contains 967 kg of uranium-238 and 33 kg of fissile isotope 235 as the following:

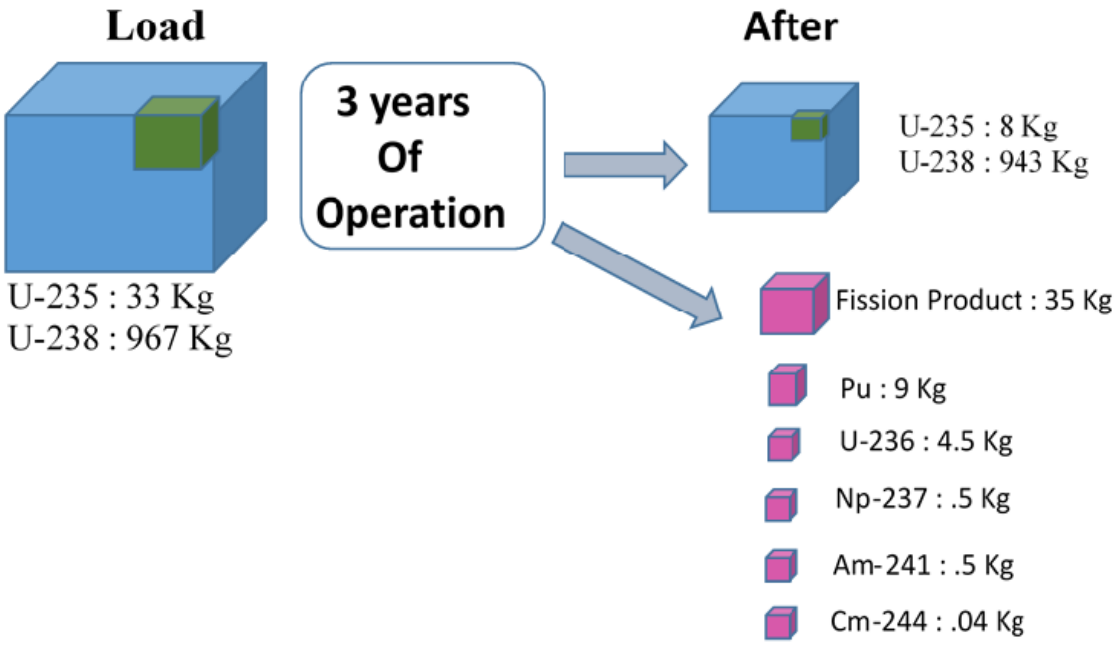

Figure 1-3: Standard nuclear spent fuel composition, distribution (in kg per ton of fuel), and produced masses of major radioactive elements found after the discharge of the spent fuel of a PWR operated in standard conditions [Billard].

Irradiation of fuel has also generated three different categories of elements [overview of the spent fuel 2011]:

1) Fission products at a rate of approximately 35 kg per ton of fuel. They come from the fission of uranium-235 and the fission of the plutonium formed during irradiation. Part of the fission products has reached stability when the reactor is discharged, but the major part is still very radioactive.

2) Actinides, nuclei obtained when uranium captures one or several neutrons without fission. Figure 1-4 presents how these actinides form. Thus, one finds almost 10 kg of plutonium, which represents about 1% in mass, the fissile isotope 239 being the most abundant (5.7 kg). Actinides involve major actinides (plutonium and uranium) and minor actinides like (neptunium, americium, curium, berkelium, californium, einsteinium, and fermium) which are less abundant, at the rate of approximately 0.8 kg per ton of fuel. The most abundant minor actinide is neptunium-237.

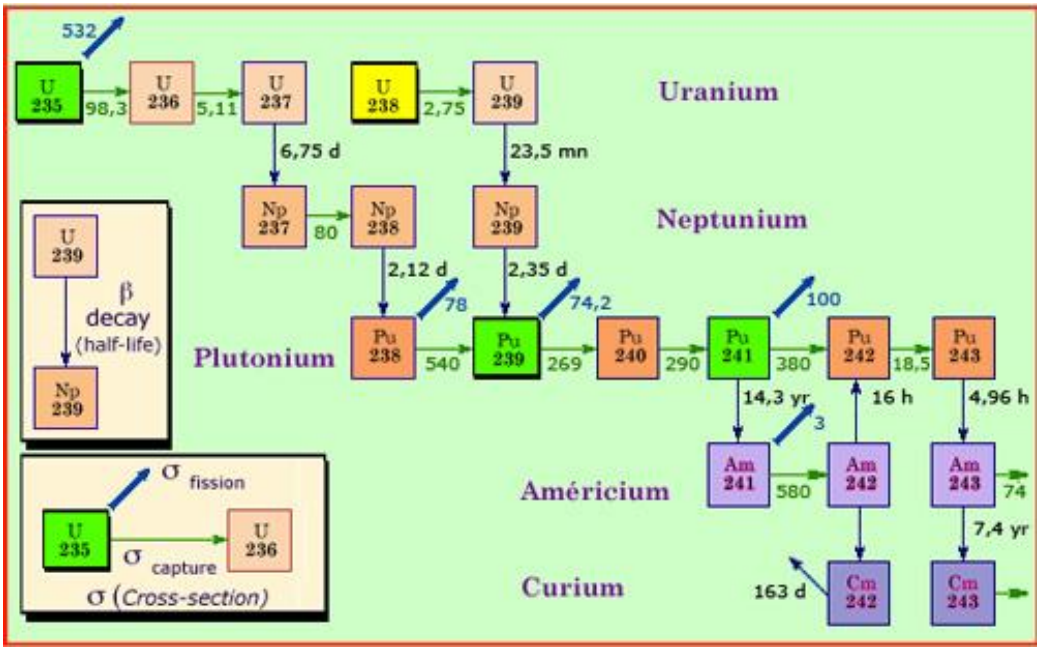

Figure 1-4: Actinides formation after uranium captures one or several neutrons without fission [Radioactivity and its applications]

Most of the fission products have a short radioactive period and undergoes a series of beta decays to form stable end products after a few years. Two medium-life fission products, strontium-90 and cesium-137, have a radioactive period of thirty years. Finally a small part of the fission products that have very long periods like (^{107}Pd, ^{129}I) disappear very slowly by beta decay but, as a result, are not very active. Most actinides are also disappearing slowly by multiple alpha decays [overview of the spent fuel 2011].
Since LWR fuels began to be tested, a typical observation in the post-irradiation examinations of these fuels (spent fuel) had a porous and fine grained microstructure at the peripheral region, and it is subjected to many restructuring processes related directly to the irradiation of the fuel with neutrons through the nuclear reactions and indirectly through the thermo-mechanical conditions existing. The consequences of such reactions is shown in figure 1-5, where a cross section of UO_2 fuel rod and scanning electron micrographs at different radial positions is presented:

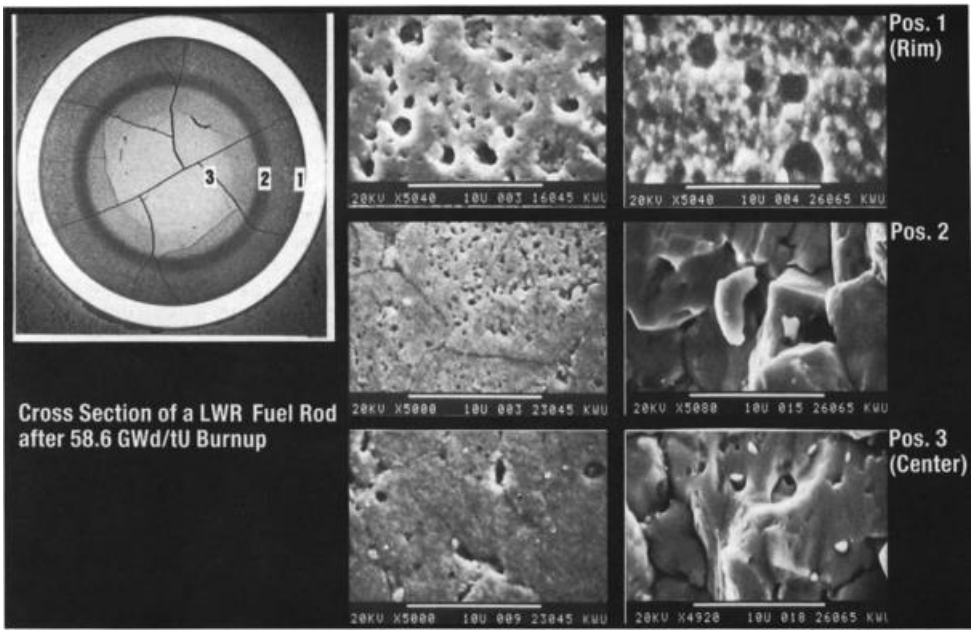

Figure 1-5: Cross section and fuel structure (scanning electron micrographs) of a LWR fuel rod after high burnup [STEHLE 1988].

During the operating life of the reactor core, the cylindrical UO_2 fuel pellet undergoes a transformation that affects its peripheral region (the rim) [Rondinella & Wiss 2010]. Especially in recent years, the burnup of light water reactor, LWR, UO_2 fuel has frequently been increased to more than 45 GWd/tM where above this burnup, a porous outer ring is formed with a typical thickness of 100-200 µm [Matzke 1992]. The observation of a newly formed structure is not new, as early as 1958 Barney reported that fully enriched UO_2 becomes porous at 10% burnup even at a low temperature of 773K. Then Bleiberg, Berman and Lustman reported in 1962 that at low temperature « grain subdivision » occurred in UO_2 fuel pellets after 2 x 10^{21} fission/cm^3 (where 2.5 x 10^{21} fission/cm^3 corresponds to about 10 GWd/tM) [Walker *et al.* 1992].

In the recent years it has become evident that the surface of UO_2 fuel pellet becomes increasingly porous with increasing burnup and many studies were carried out to investigate this structure. Matzke and Lassmann performed many studies to observe the rim structure and to identify the mechanisms that are responsible to the appearance of such structure [Matzke *et al.* 1989], [Matzke 1992], and [Lassmann *et al.* 1995]. In the rim region [OSAISAI *et al.* 1990], [PEARCE *et al.* 1983], [Lamarsh *et al.* 2001], [Spino *et al.* 1996] the local burnup is largely increased by up to a factor of 2.5 as compared to the average burnup due to Pu-formation by resonance absorption of neutrons, where the capture cross section of ^{238}U for epithermal neutrons (in the eV range) is very high as shown in figure 1-6 [Matzke *et al.* 1994]. This process leads to the production of fissile ^{239}Pu *via* beta decay of ^{239}Np, and this results in a gradient in Pu-concentration that falls off into the fuel volume.

$$ {}^{1}_{0}n + U^{238} \rightarrow U^{239} \rightarrow Np^{239} + \beta^{-} \rightarrow Pu^{239} + \beta^{-} $$

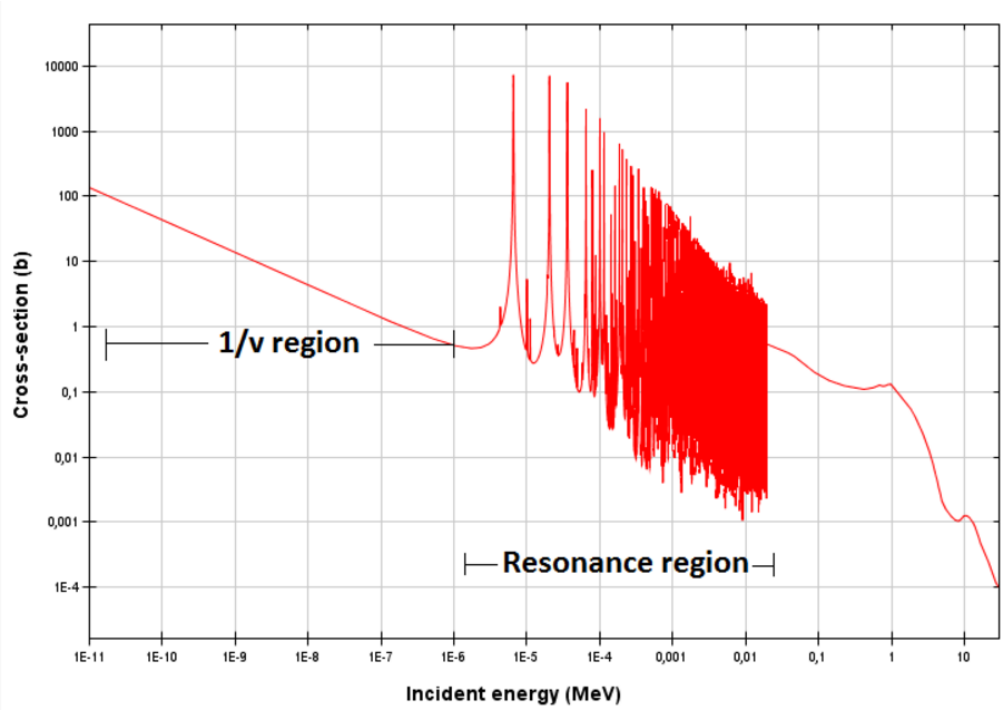

Figure 1-6: Capture cross section for ^{238}U versus incident neutron energy [JANIS].

It was then realized that this zone appears to be thin with thickness of 100-200 µm that corresponds to 4-8% of the fuel volume.
The term « rim effect » or High Burnup Structure (HBS) describes the following observations and characterizations [Rondinella & Wiss 2010], [Matzke 1992], [Lassmann *et al.* 1995], [Une *et al.* 1992], [Nogita *et al.* 1997], [Ray *et al.* 1997], [Matzke *et al.* 1994], [Rest & Hofman 1994], [Matzke & Kinoshita 1997]:
1- Pu- and burnup increase.
2- Development of fission gas pores (porous region) with a typical diameter 1-2 µm and the maximum porosity between 10% and 22%. The fission gas pore density increases with increasing the local burnup.
3- A large reduction in crystallite size, where the original grain, with a typical size of around 10 µm, subdivide by factor of 10^4 to 10^5 into sub-micron grains with a size of about 0.2 to 0.3 µm. In these fine grains, a lower overall dislocation density and a much lower density of intergranular fission gas bubbles and precipitates are found.
4- A decrease in the content of fission xenon within the UO_2 grains (athermal release of Xe from the UO_2 grains), this had been confirmed by the electron probe microanalysis (EPMA) measurements.

Figure 1-7 shows a typical scanning electron microscope SEM image obtained for the rim structure, where a fraction of porous zone is clearly shown.

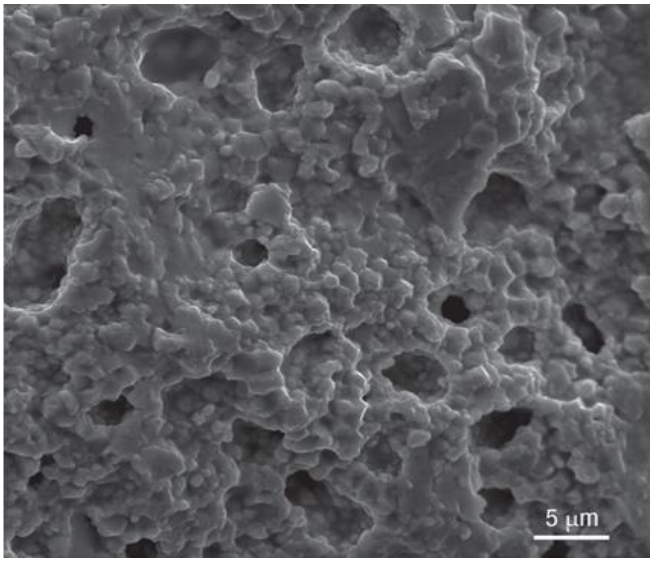

Figure 1-7: SEM showing the high-burn-up structure developed at the pellet rim in the fuel of a commercial nuclear reactor of rod average burn-up of 97.8 MWd/kgM.

The formation of this new structure during irradiation became an object to study worldwide and the process of polygonization has a large scientific interest and considerable technological importance specifically when industrials decided to increase the commercial burnup above 50 MWd/KgM (average) of the LWR fuels. Extending the operational life of the nuclear fuel to improve the efficiency of the materials flow process has a consequence in a reduction of the cost of the fuel cycle, these importance related to safety point of view where by appearing of rim structure many things have to take into account such :
1- The high fission rate and thus the high heat production in the rim zone flattens the temperature profile in the UO_2 fuel rod, while the increased burnup and the high porosity in the rim region reduce its thermal conductivity, this creates a heat barrier increasing the central fuel temperature.
2- An increased gas released can be expected as a consequence.
3- The high concentration of fission products and of Pu together with small grain size near the surface are of concern for spent fuel storage and disposal since in the case of water access, they correspond to the highest radioactive zone.

Therefore, it is necessary to model the high burnup structure and investigate its properties in order to assess the impact of such a structure appearance on high burnup fuel performance, and at the same time to find and identify the scientific explanation of what are the mechanisms which are responsible and governing the formation of rim structure. Consequently, a number of studies and experiments carried out to understand the polygonization process that occurred at the rim structure.

In this framework, this thesis aims to investigate the formation of the HBS and to identify the mechanisms and the conditions (burnup, temperature, the high concentration of fission product and fission gases, pressure, grain size, etc.) for the formation of the rim structure in the nuclear fuel, because it is still the exact mechanism is not fully understood. The next sections present in general the theory of ion-solid interactions. Since the highly charged fission fragments will interact with atoms of the uranium dioxide target we are talking about ion-material interaction, the processes of creation the defects in materials under irradiation, specifically the fate of these ions, they will deposit their energies to the target and the fate of the target linked with the amount of energy deposited by the projectile. These processes create defects inside the target affecting the structure of the material and have some potential implications on its mechanical and chemical properties.

1.1.2 Radiation effect on the nuclear fuel

Charged particles can be ions, or may be electrons, positrons and protons, and any other particles that have an electric charge. All of these particles cause effects inside the materials while there is interaction between the particle and the atom target. This section presents the interaction of ions with materials as they are the most important charged particles related to the damage production and effects created by them.

When we discuss about ion-solid interactions, we are taking about projectile (ions) and the target (material), mainly the fate of the ions will deposit their energies to the target and the fate of the target linked with the amount of energy deposited by the projectile leading to the creation of defects. In physics, ions interact with materials by two type of interaction: elastic (interaction ion-atom) the so-called nuclear energy loss, corresponding to the interaction of the particle with the atom as a whole, and inelastic (electronic) the so-called electronic energy loss. The trajectory of these ions inside the materials during their travel appears as random trajectories as shown in figure 1-8 which shows the SRIM simulation for Xe ions with energy 500 KeV inside uranium dioxide, as a typical example:

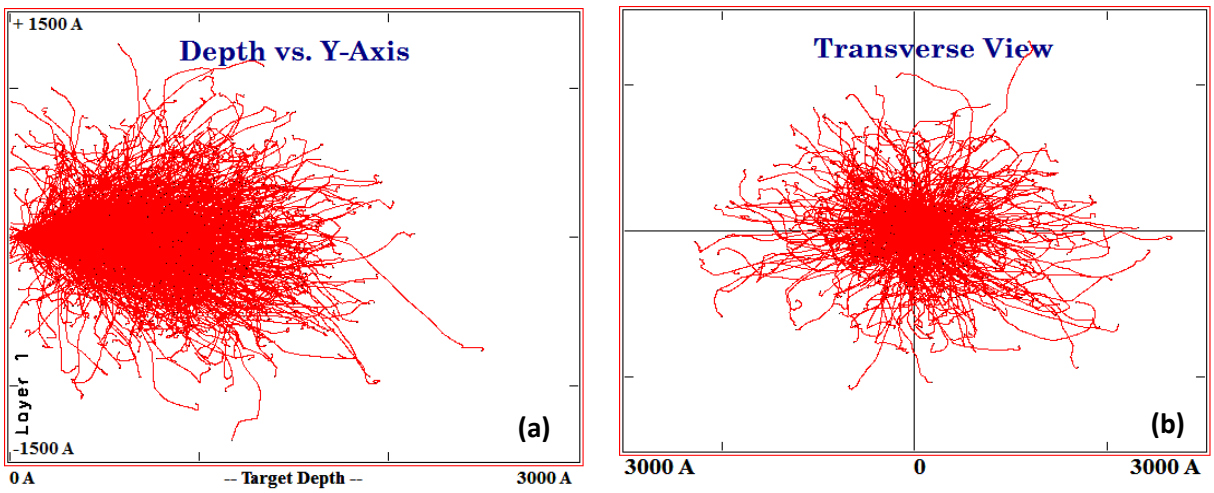

Figure 1-8: Typical trajectories of 500-KeV Xe ions crossing a target of UO_2 (a) and its transverse view (b) calculated by the SRIM Monte Carlo code.

Since the ions [Knoll 2000] penetrate into the target, they immediately interacts simultaneously with many electrons (inelastic interactions related to this coulomb interaction between the ions and the orbital electrons surrounding the nucleus) and the result of this interaction is excitation or ionization of the collided atoms; moreover elastic interactions related to the ballistic collisions between the ions and the atomic nucleus of the target also take place. The kind and the intensity of the interaction mainly depends on the ion energy: if it has a high energy the dominant interaction is the inelastic interaction and it is continues during traveling the ion inside the matter, while if it had low energy as in the present case, the elastic interaction is the dominant one. Due to these kinds of interactions the ions start to lose its energy from the moment it enters the matter and continue losing energy and slowing down until it stop inside the material.

1.1.2.1 Inelastic collisions

The inelastic collisions [Dunlop *et al.* 1992] are related to the coulomb interactions between the ions and the orbital electrons of the matter atoms. During the travel of the ions inside the solid there is attraction force between the ions and the electrons and there is a repulsion force related to electrons of the ions and the electrons of the matter so it complex interaction in fact. In this collision the internal energy of the colliding bodies may change and the kinetic energy does not conserve as it is in the elastic collision. When the ion enters into the matter [Knoll 2000], it starts to interact with the electrons of the matter's atoms and there is an attractive coulomb force between them, and this depend how much the ion is far away from the electron, this attractive force will may be sufficient to raise the electron to a higher electronic shell (excitation) or to let the electron to leave the atom (ionization), and because this portion of energy given to the electron is small, the ion can interact with many electron. This process is a continuous process and the ion will lose its energy during all the path. During this path, the ion charge will change (the number of the electrons of the ion will change) depending on the velocity of the ion. The process of slowing down the ions can be divided into three velocity domains with respect to the mean quadratic velocity of orbital electrons ($v_e = \langle v_e \rangle^{1/2}$): the high, intermediate, slow velocity domains.

If the velocity of the ion is high ($v_{ion} \gg v_e$), the ion will be fully stripped and no electron will stay around. The charge of the ion will be equal to the atomic number $\left(Z_{eff} = Z \right)$.
In the case of intermediate velocity, the velocity of the ion is similar to the velocity of the electrons ($v_{ion} \sim v_e$) the ion captures electrons continuously and partially stripped [14]. The effective charge of ion as Bohr suggested ($Z_{eff} = Z - n_e$) in this domain is proportional to the velocity of the ion for ($v \leq v_{Bohr} Z^{2/3}$):

$$Z_{eff} = Z^{1/3} \frac{v}{v_{Bohr}} \qquad (1-1)$$

Where: $v_{Bohr} = \frac{e^2}{4\pi\varepsilon_0 \hbar} = \alpha c = 2.2 \text{ x } 10^6 \text{ m.s}^{-1}$

Experimentally, it has been found the effective charge follows more closely to the following formula [Nastasi *et al.* 2014]:

$$Z_{eff} \sim Z \left[1 - exp\left(- \frac{v}{v_{Bohr} Z^{2/3}} \right) \right] \qquad (1-2)$$

In the last case, if the velocity of the ion is much less than the velocity of the electrons in their orbits ($v_{ion} \ll v_e$), the probability of capture electrons is far higher, and then the charge of the ion decreases and the ion slows down until it stops while the nuclear interaction starts to be more important at low velocity.

1.1.2.2 Elastic collisions

The elastic collision [Dunlop *et al.* 1992] is related to the interaction between the incident ion and an atom in the matter. This interaction assumes the kinetic energy and momentum conservation principles. To introduce these principles and its relation with the irradiated matter, we assume here two particles, first one with mass m_1 and velocity v_1 which is the ion in our case, and the second one with mass m_2, initially at rest, which present the atom in the matter bombarded with the ion. The first particle move in the direction of particle two. After collision, the first particle moves at a different velocity and with Θ_1 angle related to the incident direction, while particle two moves with velocity v_2' and with angle Θ_2

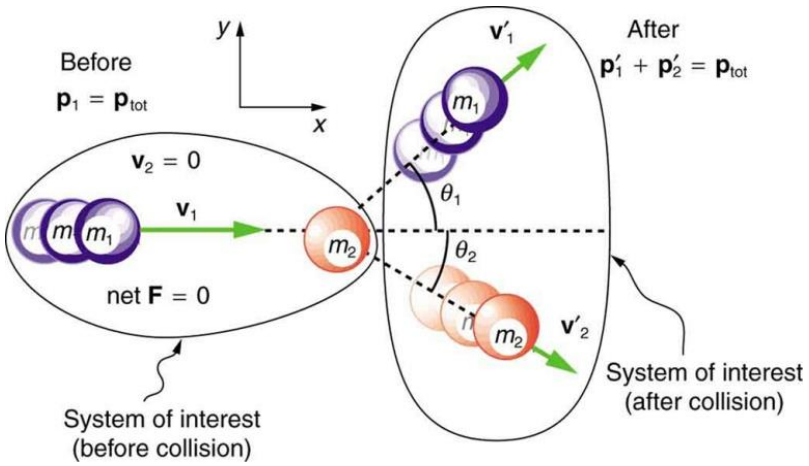

Figure 1-9: Schematic of a two-body elastic collision, assuming that the target atom (index 2) is at rest before the collision, and the ion (index 1) has a velocity v_1.

The conservation of the kinetic energy applied to the system of two interaction particles:

$$E_c\,(\text{before}) = E_c\,(\text{after})$$

$$\frac{m_1 {v_1}^2}{2} + 0 = \frac{m_1 {v_1'}^2}{2} + \frac{m_2 {v_2'}^2}{2} \qquad (1-3)$$

The conservation of momentum principle:

$$\vec{P}_{\text{before}} = \vec{P}_{\text{after}}$$

$$m_1\vec{v}_1 + 0 = m_1\vec{v}_1' + m_2\vec{v}_2' \qquad (1-4)$$

$$m_1 v_1 = m_1 v_1' \cos\theta_1 + m_2 v_2' \cos\theta_2 \qquad (1-5)$$

And to find the energy transferred from projectile to the target, we have to solve the two equations conservation of energy and momentum, this gives the following formula [Dunlop *et al.* 1992]:

$$E_T = \frac{4m_1m_2}{(m_1+m_2)^2}\frac{m_1 {v_1}^2}{2}\cos^2\theta_2 \qquad (1-6)$$

And the maximum energy transferred to the target is:

$$E_{Tmax} = \frac{4m_1m_2}{(m_1+m_2)^2}\frac{{m_1v_1}^2}{2} = \frac{4m_1m_2}{(m_1+m_2)^2}E_{c_1} \qquad (1-7)$$

The energy left to the ion is given by:

$$E'_{c_1} = E_{c_1} - E_{Tmax} = K.E_{c1} \qquad (1-8)$$

Where K is the kinematic factor, defined as:

$$K = [\frac{\sqrt{m_2^2 - m_1^2 sin^2\theta_1} + m_1\cos\theta_1}{m_1+m_2}]^2 \qquad (1-9)$$

So it clear that the energy transferred to the target depend on the mass of the ion and the mass of the target. Also, if certain cases when ($\theta_2 = 0$) and $m_1 = m_2$ the transfer energy is the maximum, if $m_1 < m_2$ the projectile may be backscattered, while if $m_1 > m_2$ the projectile will scatter at an angle which is less than or equal 90°.

Figure 1-10 shows the ratio of the maximum energy transferred to the target atom from the projectile as a function of the ratio between the masses of the colliding bodies.

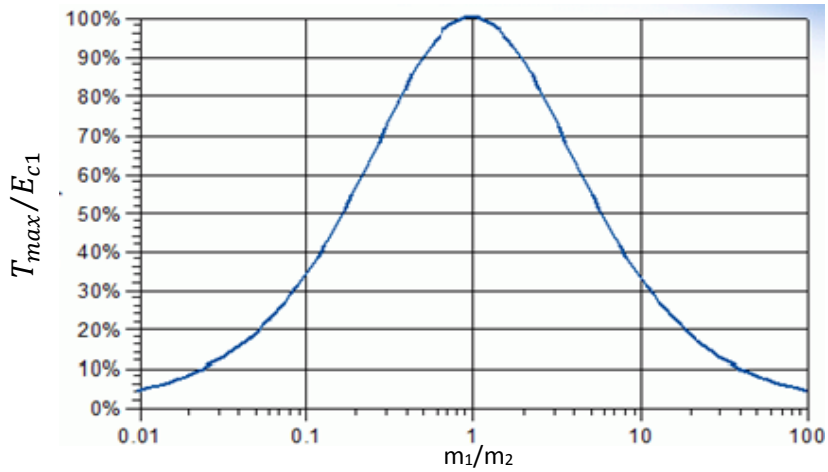

Figure 1-10: Maximum energy transfer versus the ratio of masses of projectile and target atom (m_1/m_2)

It is clear from the figure that the maximum energy transferred T_{max} becomes higher if the mass of the projectile is closer to the mass of the target atom, where the energy transfer will be 100% if the mass of the projectile equals the mass of the target atom for a head-on collision (θ = 0°).

1.1.2.3 Stopping power (or stopping force)

The rate at which charged particles lose energy during they travel inside the material is called the stopping power or stopping force [Dunlop *et al.* 1992]. It is usually measured in KeV.nm^{-1}, MeV.µm^{-1} or eV. Å^{-1}.

The stopping power is made up from two parts corresponding to the two interaction mechanisms between the ion and the matter: the electronic stopping power due to the interaction with the orbitals electrons of the material and the nuclear stopping power with the material's atoms.

The stopping power is given in the following mathematical formula:

$$-\left(\frac{dE}{dx}(E)\right)_{overall} = -\left(\frac{dE}{dx}(E)\right)_{electronic} - \left(\frac{dE}{dx}(E)\right)_{nuclear} \qquad (1-10)$$

Where:

$-\left(\frac{dE}{dx}(E)\right)_{electronic}$: Due to electronic collision

$-\left(\frac{dE}{dx}(E)\right)_{nuclear}$: Due to nuclear collision

$-\left(\frac{dE}{dx}(E)\right)_{overall}$: The overall stopping power which is the sum of the two stopping power

The minus sign on the rate of losing energy to indicate that the ions are losing energy during their travel inside the matter.

Numerical values of the stopping power depends on several parameters such as the characteristics of the ion (mass, charge and velocity of the ions) and the composition of the material which the ion passes through (the atomic number and density of the matter). Table 1-3 figure out this dependence by examples of the stopping power calculated for different ions with different energies in uranium dioxide.

Table 1-3: The overall stopping power calculated for different ions in UO_2 by the SRIM code

Ion's energy (MeV)	Xe (KeV/nm)	La (KeV/nm)	Ce (KeV/nm)	He (KeV/nm)
100	25.5	21.2	21.2	.045
10	6.3	5.7	5.7	.210
1	4.2	4.3	4.4	.621
.1	3.75	3.81	3.86	.2

Figure 1-11 which represents the stopping power as a universal case irrespective of ion or target; basically it has the same behavior but not same values for different kinds of ion and targets:

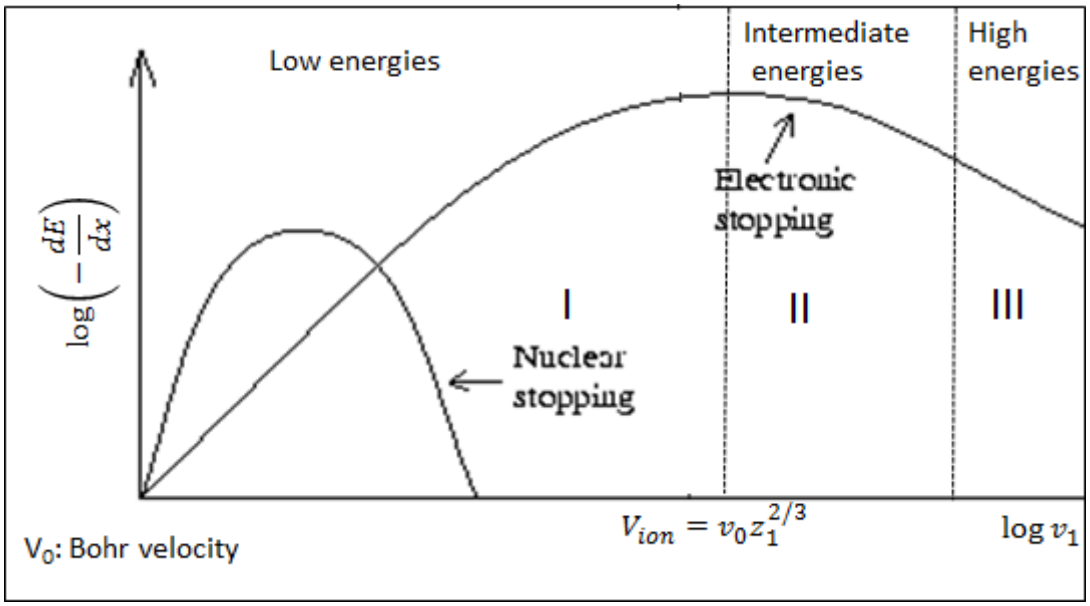

Figure 1-11: The stopping power of an ion versus its velocity

It is clear from the figure that the stopping power can divided into three domains with the energy of the ion: (I) low energy ($v_{ion} \ll v_e$) (II) medium energy ($v_{ion} \leq v_e$) (III) high energy ($v_{ion} \gg v_e$)

(I) For swift ions (few MeV for light ions) [Dunlop *et al.* 1992], [Bethe 1930], [Bloch 1933], and [Echenique *et al.* 1990]: the ion is totally stripped and ($v_{ion} \gg v_e$ ($electron\ speed\ in\ its\ orbital$ "$Bohr\ velocity$")), the electronic stopping power in this domain can be estimated by Bethe and Block theory for ions with small velocities of the particle compared to the velocity of light:

$$-\frac{dE_1}{dx} = \frac{4\pi N Z_1^2}{m_e v_1^2} * \left(\frac{e^2}{4\pi\varepsilon_0}\right)^2 * \left[ln\left(\frac{2m_e v_1^2}{I}\right)\right] \qquad (1-11)$$

Where:

v_1: the velocity of the particle

$E_1\ and\ Z_1$: the energy and charge of the particle

e and m_e : the charge and the mass of the electron

N: the electron density of the target

I: mean excitation potential of the target

ε: Vacuum permittivity

According to this formula, it is clear that the electronic stopping power is essentially proportional to the reciprocal of the square of the ion velocity, which gives the explanation for why we observed the increase of electronic stopping power while ions slowdown in matter over this energy range.

(II) In the medium range (MeV range): The ion can no longer be assumed to be fully stripped off, where the charge of the ion decreases with decreasing velocity where the velocity of ion becomes comparable to the velocity of orbital electrons. In this domain, the Bethe and Block theory is no longer valid, and the electronic stopping power goes through a maximum when $v_{ion} \approx v_e$ and tends to fall down after. The theoretical estimation of the electronic stopping power in this domain is difficult because the process of capture and loss electrons is tricky to compute numerically.

To calculate the electronic stopping power in a practical way, the validity of the Bethe and Block theory to this domain is extended by introducing the concept of effective charge [Yarlagadda *et al.* 1978]. This approach was introduced first by Bohr [[Bohr 1940], [Bohr 1941] and [Lamb 1940]], where the effective charge is directly proportional to the speed of ion as mentioned before in formula (1-2).

When the ion's velocity decreases more and more until it is ($v_{ion} \ll v_e$) where the speed of orbital electrons is higher than the speed of incident ion as shown in figure 1-11 in region I, many electrons are captured and the charge of the ion decreases. The electronic stopping power is supposed to be proportional to the speed of the projectile ion. In this region the theory was proposed by Lindhard & Scharff [Lindhard & Scharff 1961] and Fisov [Firsov *et al.* 1957], [Firsov *et al.* 1957], [Firsov *et al.* 1958], and [Firsov *et al.* 1957] with the following formula:

$$-\left(\frac{dE}{dx}\right)_e = 8\pi N \left(\frac{e^2}{4\pi\varepsilon_0}\right) a_0 \frac{Z_1^{7/6} Z_2}{\left(Z_1^{2/3} + Z_2^{2/3}\right)^{\frac{3}{2}}} \frac{v}{v_{Bohr}} \qquad (1-12)$$

Where: $a_0 = \frac{4\pi\varepsilon_0 h^2}{me^2} = 5.29 * 10^{-11}\ m\ is\ the\ Bohr's\ radius$

At the end of the path inside the matter, ions slow down to low energy domain below a few MeV where the nuclear stopping power is the dominant corresponds to nuclear interaction.

From figure 1-11, it is clear at high and medium energies the stopping power is dominated by the electronic stopping power because the nuclear stopping power is very small. We can neglect it, but it is also not zero, it takes place even it is rare, but it is very small compared to the electronic. Conversely in low energy domain ($v_{ion} \ll v_e$), the electronic stopping power is less important and the nuclear stopping power is the dominant process.

The nuclear stopping power described by Thomas-Fermi model which take into account the screening due to electrons and the repulsion between nuclei of both the ions and a target atom [Dunlop *et al.* 1992]:

$$E_p = \frac{Z_1 Z_2 e^2}{4\pi\varepsilon_0 r}\ \Phi\left(\frac{r}{a}\right) \qquad (1-13)$$

Where:

a: Typical dimension of the atom (screening radius)

$\Phi\left(\frac{r}{a}\right)$: screening function

Such a potential is included into simulation softwares, such as the SRIM code. Figure 1-12 shows the evolution of stopping power of xenon ion in UO_2 as a function of its energy calculated by SRIM code (see Appendix B). The figure shows that the total kinetic energy of the fission fragments (~ 168 MeV) is in the range where the fissions fragments will do electronic collision with the UO_2 atoms once they are created in the fuel pellet and when the energy of the fission fragments decreases due to the interaction with atoms during its path, the ballistic collisions will take place.

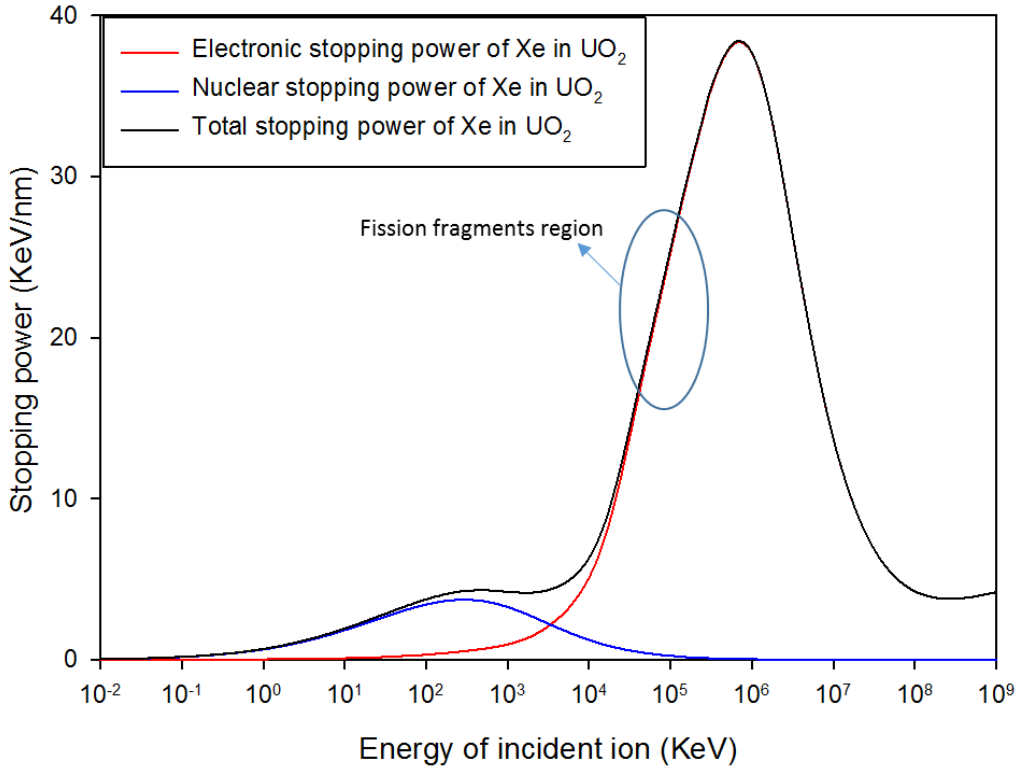

Figure 1-12: Stopping power of xenon ions in UO_2 calculated according to the SRIM code.

1.2 Radiation induced defects

When ions penetrate into the material, they do electronic and nuclear collision depending on their energies, and during these collisions, the ions give part of their energies to the material atoms, and this process creates defects inside matter depending on the type of interaction and on the amount of energy transferred to the atoms as mentioned before. Therefore, it is important to study the role played by these defects, and the fate of material after irradiation. For that reason the next section describes these defects and how the UO_2 behave under irradiation.

1.2.1 Defects created by inelastic collision (electronic)

As mentioned before, since the ion penetrates the matter, the interactions with atoms and electrons take place. This transformation of energy generally consists into two parts: (i) continuous energy loss between the ion and the cloud of orbital electrons leading to excitation or ionization of the matter's atoms with no direct displacement of these atoms, (ii) discrete energy loss to certain atom due to binary collision between them leading to the creation of Frenkel pair and collision cascades. The importance of both processes depends on the ion's energy.

When the ion enters into matter with a high energy, the dominant interaction is the electronic interaction. The coulomb interaction between the ion and the electrons of the matter's atoms will let a part of the ions energy transferred to the electrons and do excitation or ionization depending in its energy, leading to heat the matter and to an increase of its temperature. If the energy transferred is high enough, defects can be created corresponding to a high increase in matter's temperature, while in the case of transferring small amount of energy, no defect is created just small increase in the temperature could be observed.

In the case of ionization, when the electrons removed completely from their shells, this creates electron-hole pairs. In a metallic materials no defects are created since the electron-hole pairs will annihilate due to the big number of mobile electrons. Conversely in non-metallic materials e-hole pairs can be stabilized. If the energy which is transferred to the electron is higher than the energy needed to remove it from its shell, and the energy which the electron have after the leaving the atom give the ability to do another interactions and lose its energy inside the matter in different ways, an electromagnetic cascade is created.

The initial energy which is transferred from the ion to the electron is distributed radially and this distribution will be inverse with the radius square ($1/R^2$) [Toulemonde *et al.* 1992]. The excess of positive charges makes that area not stable because of the repulsive force between these positive charges, so this will may lead to explosion and damage related to displacement atoms if they receive an energy more than the binding energy required to keep atoms in their positions (range of eV) [Hayashi *et al.* 1997] .The model which was developed to explain this mechanisms of formation an amorphous latent track in solid is the "Ion explosion model" developed since 1965 by Fleischer, Price and Walker [Fleischer *et al.* 1965].

Another theory was also proposed in 1960 called the "thermal spike" model [Fleischer *et al.* 1965], [Lifshits *et al.* 1960], which supposes that the target is consider to be made of two continuous physical systems: the electron gas and the atomic lattice. Under an intense electronic excitation, the space and the temperature of the electron gas and the atomic lattice is governed by the following differential equations corresponding to the equation of heat (Fourier's law) in a cylindrical geometry:

$$\begin{cases} C_e \frac{\partial T_e}{\partial t} = \frac{1}{r}\frac{\partial}{\partial r}\left[rK_e(T_e)\frac{\partial T_e}{\partial r}\right] - g(T_e - T_l) + A(r,t) \\ C_l \frac{\partial T_l}{\partial t} = \frac{1}{r}\frac{\partial}{\partial r}\left[rK_l(T_l)\frac{\partial T_l}{\partial r}\right] - g(T_e - T_l) \end{cases} \quad (1-14)$$

Where:

T_e,T_l: The temperature of the electron gas and the atomic lattice, respectively

C_e, C_l, K_e, K_l: Specific heats and the thermal conductivities of electrons and lattice atoms, respectively.

$A(r,t)$: The energy obtained through the electron cascade after the passage of an ion

g: Electron-lattice coupling constant

This coupled system has no analytical solution but can be solved numerically. The solution shows that the ion can deposit a high density of energy in a short time that leads to a high temperature of the target within the cylindrical zone. As a consequence, the inter-atomic links between atoms in this area can be broken, then atoms become highly disordered and fusion of solid can occur there. This cylindrical region, called an amorphous latent ion track, which exists during a very short time but the trace of ion track often referred to as " latent track" can be found under the form of point defect or molten to frozen zone in some cases.

1.2.2 Defects created by elastic collisions (Nuclear energy loss)

The defects are created by elastic collisions when the ions have a low energy, mainly at the end of the ion path inside of the matter. These collisions lead to energy transfer to the atom; if this energy is higher than the displacement threshold energy (E_d), then the atom will leave its position inside the lattice. When the atom leaves its lattice position, it leaves an empty position called a vacancy, these point defects and the vacancies are called "Frenkel pair" defect as shown in figure 1-13:

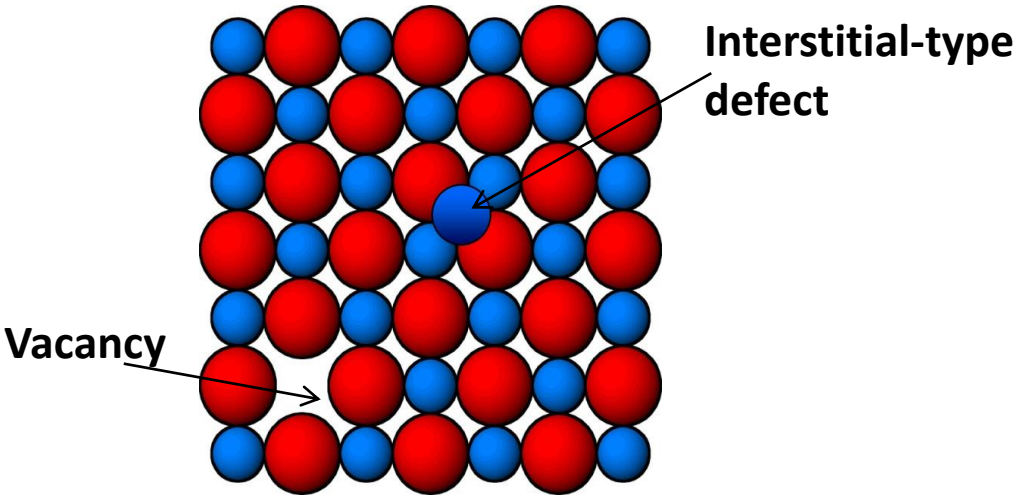

Figure 1-13: Schematic of a Frenkel pair: an atom leaves its regular position, creates a vacancy and stays in an interstitial-type position.

A displaced atom from the ion is called a Primary knock-on atom (PKA). It has often a kinetic energy high enough to do collisions with other atoms leading to a second displacement, and this can do the same with other atoms and so on. These points defects create a displacement cascade, and the ion along its path initiates several collision cascade because it displaces numerous PKA along its path.

To estimate the number of displaced atoms by PKA, which is very important quantity in the field of studying the radiation damage, Kinchin and Peace theoretical model uses the following estimation [Dunlop *et al.* 1992], [Almeida & Raisanen 2005]:

$$\begin{cases} \mathrm{N}(E_T) = 0 & \text{if the } E_T < E_d \quad (1-15) \\ \mathrm{N}(E_T) = 1 & \text{if the } E_d < E_T < 2E_d \quad (1-16) \\ \mathrm{N}(E_T) = E_T/2E_d & \text{if the } E_T > 2\,E_d \quad (1-17) \end{cases}$$

Where: $\mathrm{E_T}$: kinetic energy of the PKA

$\mathrm{E_d}$: Displacement threshold energy

And to improve this model, the electronic stopping force can be also included in:

$$\mathrm{N}(E_T) = \mathrm{C}\frac{E_T - E_\varepsilon}{2E_d} \quad (1-18)$$

Where C ≈ 0.8, E_ε:inelastic energy loss inside the cascade

The total number of displaced atoms along the entire ion range is:

$$N_{total} = \frac{E_{cl}}{2E_d} \quad (1-19)$$

Where: $\mathrm{E_{cl}}$: kinetic energy of the projectile ion

$\mathrm{E_d}$: Displacement threshold energy

The concept of displacements per atom (*dpa*) is one of the most important concepts in the field of radiation damage and the irradiation experiments. The more convenient quantity in irradiation experiments is *dpa*, rather than the fluence (in particles per unit surface) or flux (mostly in particles per unit of surface and time), which related to the average number of times a given atom is displaced from its regular lattice sites as a results of ion bombardment. The displacements per atom (*dpa*) is essentially proportional to the radiation energy deposited per volume and it can be calculated by formula (1-20):

$$dpa = \frac{Number\ of\ displaced\ atoms\ in\ a\ given\ volume}{Number\ of\ material\ atoms\ in\ same\ volume} \quad (1-20)$$

This simplified model gives the defect concentration of primary damage vacancies and interstitials in the material. Assuming no point defects are lost to a surface or other defect sink, naturally the concentrations for vacancies, interstitials and Frenkel pairs are equal. During the collision cascade, vacancies and interstitial can be produced close together which let them to recombine and this recombination process can reduce the number of created defect. Only a few percent of the initially created point defects can survive and are capable of successfully produced a radiation inducing defect. Therefore, many investigations and studies regarding the radiation effect on uranium dioxide have been conducted to understand the behavior of this material under irradiation, its interactions with ions and to study the stability of such a nuclear fuel in nuclear reactors where various classes of defects can be produced as interaction between the fission fragments (ions) with the matrix itself depending on their energy: low-energy ions are used to study the effects of nuclear collision (point defects, dislocations, amorphization, etc.), whilst swift ions are used to study the effects of electronic slowing down (defects cluster, latent tracks, etc.)

The next section presents some of the investigations which were carried out mainly by using single crystals of uranium dioxide as the simplest model to obtain a good knowledge of radiation defects and the behavior of uranium dioxide under irradiation. Several techniques including Rutherford backscattering spectrometry in Channelling condition (RBS/C), X-Ray diffraction analysis (XRD) and transmission Electron Microscopy (TEM), were applied to do the investigation. The next section shows the most important of these studies.

1.3 Uranium dioxide behavior under irradiation.

Many studies and experiments were performed to investigate the radiation damage in uranium dioxide in different experimental conditions. The first part of this section presents the studies that were done to investigate the effect of the electronic and nuclear stopping power in irradiated UO_2 and to identify the effects of impurities on irradiated UO_2 structure. The second part of the section presents the studies that were performed to better understand the HBS structure and the radiation defects in uranium dioxide at high temperature in both commercial LWR fuels and conducted on single crystals of UO_2 to better understand the parameters involved In the formation of the HBS structure.

1.3.1 Radiation damage in uranium dioxide

1.3.1.1 Radiation damage in uranium dioxide related to electronic stopping power

Matzke *et al.* [Matzke *et al.* 2000] studied the radiation effects on UO_2 with different swift heavy ions using a wide range of energies 72 MeV to 2.7 GeV, and fluence from 5 x 10^9 to 10^{17} ions/cm^2. They observed that the threshold stopping power of fission fragments for formation of visible tracks in UO_2 is in the range 22-29 KeV/nm. While Fission fragments of fission energy (18-22 KeV/nm) are below this threshold energy but nevertheless form thermal spike in UO_2 observable tracks can be found at the surface.
By using 72 MeV ^{127}I ions the following consequence of fission fragments impact, i.e., lattice parameter increase, fission gas bubble formation, resolution of fission gas from bubbles and fission-enhanced diffusion were observed. The swelling of UO_2 was confirmed to be small and the technology important process of polygonization (grain subdivision" Rim effects" in operating UO_2-fuel) could be observed.

Nogita *et al.* [Nogita *et al.* 1999] studied the irradiation effects in polycrystalline UO_2 by irradiating the samples with 100 MeV iodine ions at temperature below 470 K over a fluence range from 1x10^{14} to 2x10^{15} ions.cm^{-2}. The surface of the specimens was analyzed by scanning electron microscopy (SEM) and X-ray diffractometry (XRD). The depth profiles of incident iodine ions and defect clusters were measured by secondary ion mass spectrometry (SIMS) and transmission electron microscopy (TEM), respectively. The lattice parameter change, which is associated with point defect accumulation, increased with ion fluence. Defect clusters of dislocations and dislocation loops were identified, and their depth profiles were in good agreement with the calculated damage profile.

Sonoda *et al.* [Sonoda *et al.* 2010] studied the properties of ion tracks and the microstructural evolution under accumulation of ion tracks in UO_2 irradiated with 100 MeV Zr^{10+} and 210 MeV Xe^{14+} ions. By the cross-sectional observation of UO_2 under irradiation with 210 MeV Xe^{14+} ions at 570 K, elliptical changes of fabricated pores that exist till 6 µm depth and the formation of dislocations have been observed when the ion fluence exceeds 5x10^{14} ions/cm^2 .The drastic changes of surface morphology and inner structure in UO_2 indicate that the overlapping of ion tracks will cause point defects, enhance the diffusion of point defects and dislocations, and form sub-grains at relatively low temperature.

In another work, Garrido *et al.* [Garrido *et al.* 1997] studied UO_2 single crystals irradiated with 340-MeV Xe ions. RBS-channelling techniques was applied to study the structural modifications induced by irradiation. This work reported the good stability of the crystalline structure under irradiation.

Resonant scattering $^{16}O(^{4}He,^{4}He)^{16}O$ occurring at 3.045 MeV was applied to the study of oxygen sublattice modifications. A strong disordering of both U and O sublattices was observed, even at very low ion irradiation fluence (~10^{13} cm^{-2}).

In 2009, Garrido *et al.* [Garrido *et al.* 2009] studied the radiation stability of Urania and yttria-stabilised cubic zirconia single crystals submitted to intense electronic excitations induced by 944-MeV Pb^{53+} ions. Various analytical techniques (TEM, AFM, RBS/C, XRD) were employed to examine the modifications induced at the surface and in the crystal bulk. At low fluence irradiation leads to the formation of localized ion tracks whose center is hollowed in the surface region over a depth of 100 nm and to the formation of nanometer-sized hillocks. Both features are interpreted as resulting from an ejection of matter in the wake of the projectile. Track overlapping at high fluence results in the formation of micrometer-sized domains (50 nm) in the crystal bulk characterized by a slight disorientation (~ 0.2º) with respect to the main crystallographic orientation of the crystal.

K.Hayashi *et al.* [Hayashi *et al.* 1997] studied on the radiation damage of UO_2 irradiated with high energy heavy ions in the order of 100 MeV. Sliced UO_2 pellets for LWR were irradiated at temperatures below 470 K, with 100-300 MeV iodine and 100 MeV nickel ions over a fluence range from $2x10^{13}$ to $1.8x10^{16}$ atom.cm^{-2}. The results show that the lattice parameter changes ($\Delta a/a_0$) at the surface, induced by 100 MeV iodine and nickel irradiations were reasonably scaled by the displacement per atom (*dpa*) scaling parameter as in figure 1-14, and that the changes, however, could not be scaled by the electronic energy deposition at the surface. In the 100-300 MeV iodine irradiation, the lattice parameter slightly increased with increasing incident ion energy. The above results suggest that the defect formation corresponding to the lattice parameter change was mainly due to the nuclear energy deposition under the present experimental conditions, with an additional contribution of the electronic energy deposition.

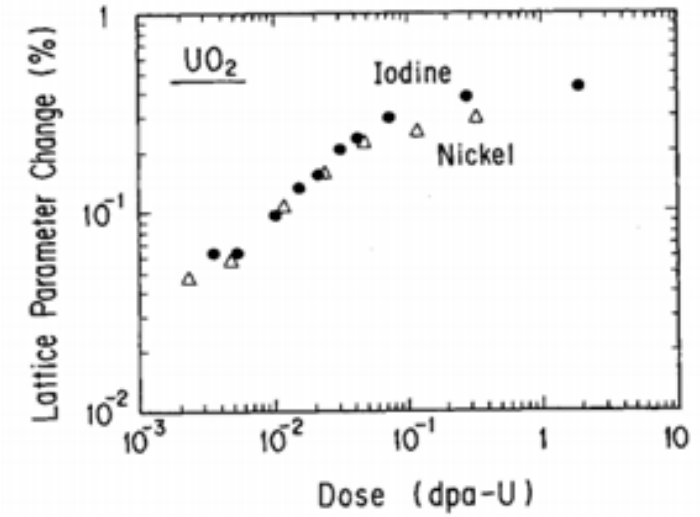

Figure 1-14: (a) Lattice parameter changes of UO_2 irradiated with 100 MeV ^{58}Ni and ^{127}I ions as a function of displacement per uranium atom at the surface.

1.3.1.2 Radiation damage in uranium dioxide related to nuclear stopping power

In this section, both radiation damage and the effect of incorporated impurities have been considered since they have thier effect on the structure especially at high concentration.

In 2008, Garrido *et al.* [Garrido *et al.* 2008] studied urania single crystals implanted with low-energy inert gases (He or Xe). They observed the damage in-growth, due to both ballistic and chemical contributions, was investigated by *in situ* RBS/C experiments in the channelling mode and TEM. They reported that two main steps in the disordering kinetics were observed for both inert gases. Relevant key parameters were found to be: the number of displaced lattice atoms created by the slowing-down of energetic ions during the implantation process; the concentration of noble gas atoms in the solid which cause the formation of large stress fields surrounding gas aggregates. A first step in the accumulated damage was reported to be due to the radiation effect scaled with the number of displacement per atoms, while the second step due to the formation of inert gas bubbles at high implanted concentration.

The primary radiation damage state induced by 10 KeV energetic recoils in UO_2 was also investigated by molecular dynamics simulations [Tian *et al.* 2011]. The simulations show that the direction of the primary Knock-on atom (PKA) has no effect on the final primary damage state. It is found that most of the displaced atoms do not result in defects. 77% and 96.3% of displaced uranium and oxygen atoms located at crystalline positions, creating replacements. The number of oxygen Frenkel pairs is about 2.5 times higher than the uranium Frenkel pairs. 89.5% of the total interstitial clusters are composed of the cluster involves 2–3 point defects. The fractions of vacancies and interstitials in clusters are 65.6% and 44.5%, respectively.

In 2012, P. Garcia *et al.* [Garcia *et al.* 2012] studied the effect of the rare gases which are produced in important quantities as a result of the fission events and α-decay of actinides on the oxide fuels. Many studies were performed on the same topic due to the potential impact of the rare gases on the integrity of fuel rods. This study shows that rare gases which constitute an abundant class of fission products are particularly insoluble and therefore tend either to be released from the fuel or form small nano-metre sized clusters. Bubbles are liable to grow and become trapping sites for migrating defects or other insoluble atoms. Interactions between migrating atoms, defects and existing clusters will determine the rate and extent to which clusters grow. Because the transfer of gas from within the grain to the grain boundaries is thought of as being the rate limiting process for fission gas release, a review of phenomena occurring on the sub-grain scale is carried out.

A. Michel *et al.* [Michel *et al.* 2012] studied the evolution of the xenon aggregation in UO_2 with increasing implantation fluence by using the Transmission Electron Microscopy (TEM) technique. A UO_2 thin foil was implanted at fluences ranging from $3x10^{12}$ to $7x10^{14}$ at cm^{-2} with 390 keV Xe^{3+} ions at an irradiation temperature of 873 K. The TEM results shows the presence of nanometer-sized bubbles above a fluence of $6x10^{12}$ Xe cm^{-2} as shown in figure 1-15 and an increase in the bubble density was observed between $6x10^{12}$ Xe cm^{-2} and $2x10^{14}$ Xe cm^{-2}.

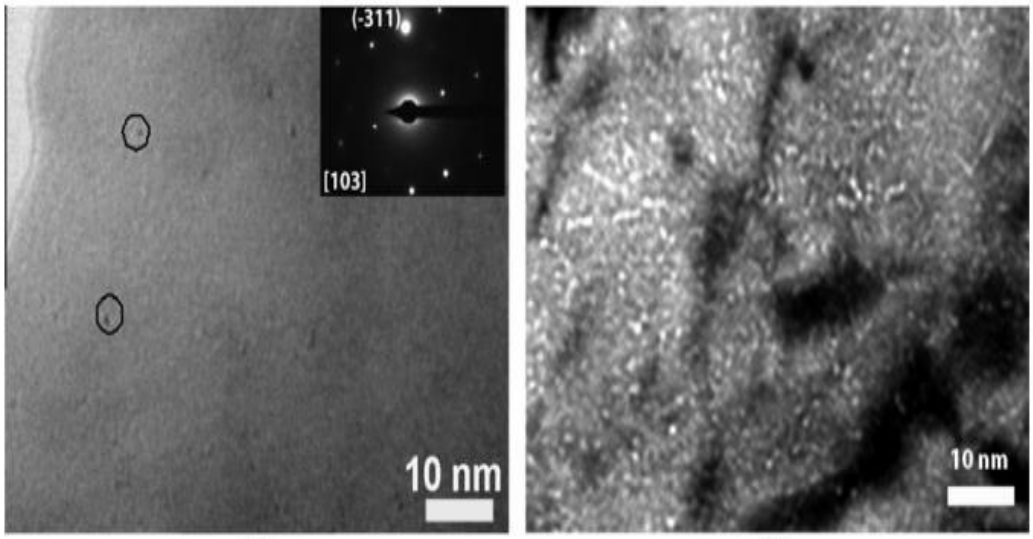

Figure 1-15: TEM images of UO_2 thin foils implanted with 390 keV Xe ions at 873 K and at a fluence of (a) 6 x 10^{12} Xe cm^{-2} in overfocused beam conditions: dark spots and (b) 7 x 10^{14} Xe cm^{-2} in underfocused beam conditions: bright spots [Michel *et al*. 2012].

Another TEM work was carried out by C. Sabathier *et al.* [Sabathier *et al.* 2008] on a set of UO_2 thin foils following the implantation of 390 keV Xe^{3+} and 300 keV Cs^{2+} ions, respectively. The TEM results reveal the nature and quantity of defects formed as a function of Xe and Cs ion fluences but do not appear to be dependent upon the nature of the implanted ions. In addition to dislocation and dislocation loop formation, Xe and Cs aggregates were observed. When the samples reached Xe and Cs fluences of $2x10^{15}cm^{-2}$ and 10^{16} cm^{-2}, they were annealed for 20 min in 370 K steps from 570 to 970 K. After each annealing stage, the images were acquired at room temperature. The technique of underfocused and overfocused objective lens was also used to check whether nanobubbles were formed.

At several Xe and Cs concentrations, the threshold temperatures for aggregate formation were determined which is reached at concentrations of 0.4 at. %. Xe precipitation occurred above 870 K. The threshold temperature for Xe precipitation decreased to 670 K for the higher concentration samples (2 at.%) and to 770 K for Cs implanted samples at this concentration. No significant differences in the bubble size and densities were observed between the high concentration Xe or Cs samples where the size and the density of bubbles for these two cases were identical within the error of the measurements (~2 nm in size and ~10^{23}–10^{24} m^{-3} density).

G. Sattonnay *et al.* [Sattonnay *et al.* 2006] studied the behavior of He and Xe implanted into UO_2 single crystals is studied by *in situ* TEM experiments before and after annealing up to 973 K. The TEM micrographs showed that annealing induces the formation of noble-gas bubbles in both cases. However, the size (25 nm for He and 3–5 nm for Xe) and the nucleation temperature (873 K for He and 673 K for Xe) of bubbles depend on implanted species. These results are explained by the radiation damage produced by ion implantation and the diffusion mechanisms involved in each case.

Another *in situ* Transmission Electron Microscopy (TEM) was conducted in 2014 [He *et al.* 2014] to understand the microstructure evolution of UO_2 irradiated with Xe ions. Therefore single crystal UO_2 were irradiated with 300 keV Xe irradiation at room temperature. The results show that the microstructure evolution occur as nucleation and growth of dislocation loops at low irradiation doses, followed by a transformation to extended dislocation segments and tangles at higher doses as shown

in figure 1-16. Xe bubbles with dimensions of 1-2 nm were observed after irradiation at room-temperature irradiation at a fluence 5 x 10^{14} ions.cm^{-2}. Electron Energy Loss Spectroscopy indicated that UO_2 remained stoichiometric under room temperature Xe irradiation.

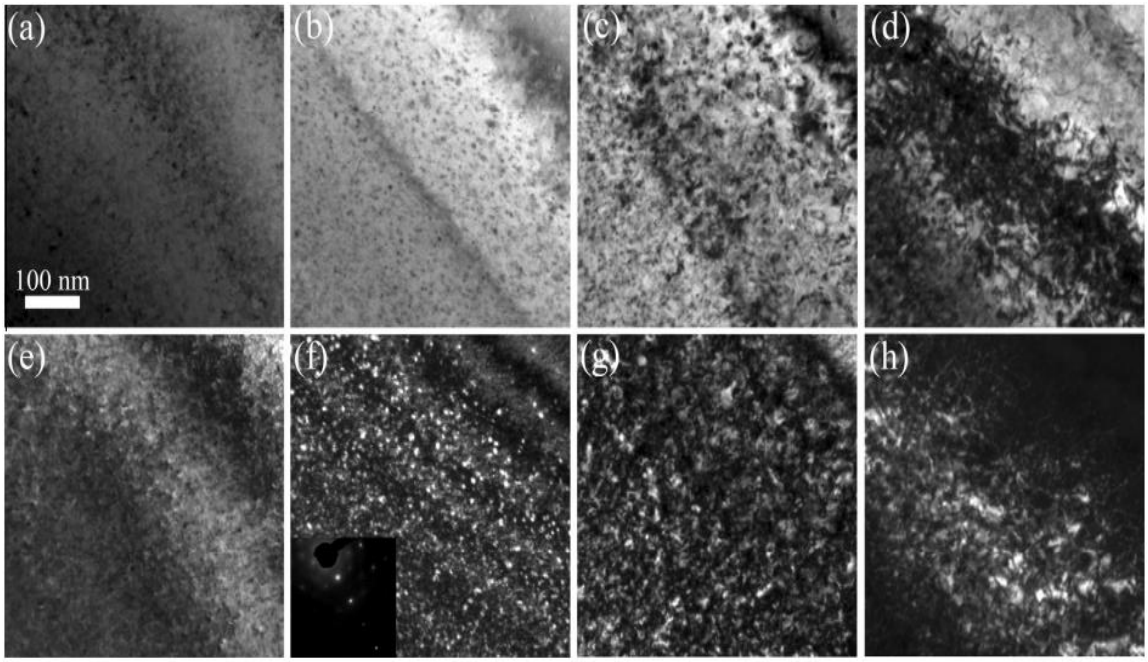

Figure 1-16: Sequential bright field (BF) and dark field (DF) TEM images showing the nucleation and growth of defects in UO_2 single crystal irradiated with 300 keV Xe at room temperature at various fluences: (a) and (e) not irradiated; (b) and (f) 5x10^{14} ions/cm^2 ; (c) and (g) 1x10^{15} ions/cm^2 ; (d) and (h) 1x10^{16} ions/cm^2 . (a)–(d) are bright field images and (e)–(f) are dark field images [He *et al.* 2014].

As many studies performed to investigate the xenon distribution in UO_2, various authers were also interest to study the He distribution and its migration in implanted UO_2 sintered disks as it is one of the most important gases in irradiated UO_2 .This is has a special importance in related to the direct storage of the spent nuclear fuel. Therefore, in 2004, S. Guilbert *et al.* [Guilbert *et al.* 2004] studied the behavior of helium implanted in sintered UO_2 as a function of annealing temperature. UO_2 disks have been implanted with 1 MeV ^{3}He ions at a fluence of 1x10^{16} cm^{-2}. These implantation conditions lead to a local helium concentration of 0.2 at. % at a depth of 1.9 µm in UO_2. The ^{3}He (d,α)^{1}H Nuclear Reaction Analysis method was used to determine the helium depth profile after various annealing stages. The experimental results measured after 1473 K anneal were analyzed using a simple model which satisfactorily reproduces the observed helium depth profile changes. The intragranular helium diffusion coefficient was estimated (~ 6 x 10^{-17} m^2.s^{-1} at 1373 K).

Belhabib *et al.* [Belhabib *et al.* 2015] studied the helium location in implanted UO_2 single crystals and the effects of temperature and annealing on the behavior of helium in uranium dioxide. The coupling of Nuclear Reaction Analysis based on the reaction of ^{3}He with deuterons (^{3}He (d,p) ^{4}He) (NRA/C) and Rutherford backscattering spectrometry in channelling mode (RBS/C) techniques provides information about the location of helium atoms. After implantation, the technique reveals that a large fraction of helium atoms occupy octahedral interstitial sites of the UO_2 matrix. This result was confirmed by Monte Carlo simulations, which show that 97% of helium atoms are located at the center of these sites. For an annealing temperature of 870 K, helium remains stable in such sites. After annealing at 1073 K for 30 min, the majority of helium atoms that were trapped in the UO_2 single crystal, evaluated to 95% become randomly distributed in the matrix. This characteristic may be associated with the precipitation of the helium atoms in the form of bubbles.

A micro-focused X-ray fluorescence (µ-XRF) and X-ray diffraction (µ-XRD) study was performed by Mieszczynski *et al.* [Mieszczynski *et al.* 2014] to investigate the microstructural changes in a set of commercial grade UO_2 fuel samples. The results are associated with conventional UO_2 materials and relatively larger grain chromia-doped UO_2 fuels, irradiated in a commercial light water reactor plant (average burn-up: 40 MWd. kg^{-1}). The lattice parameters of UO_2 in fresh and irradiated specimens have been measured and compared with theoretical predictions. The doped fuel has a smaller lattice parameter than the standard UO_2 as a result of chromia doping. Increase in micro-strain and lattice parameter in irradiated materials is highlighted. All irradiated samples behave in a similar manner with UO_2 lattice expansion occurring upon irradiation, where any Cr induced effect seems insignificant and accumulated lattice defects prevail. Elastic strain energy densities in the irradiated fuels are also evaluated based on the UO_2 crystal lattice strain and non-uniform strain. The µ-XRD patterns further allow the evaluation of the crystalline domain size and sub-grain formation at different locations of the irradiated UO_2 pellets.

As shown from the previous studies and from the results of the different experiments and investigations that uranium dioxide has high resistance to irradiation and no amorphisation was reported. Nevertheless, the authors demonstrate during their studies that in the peripheral region of the nuclear fuel pellet and in some uranium dioxide samples, which they irradiated to high ion fluences at high temperature a new porous structure with small grain size, so they have started to study this structure to understand what is the reasons for appearing such a structure and if this structure will affect the stability of the uranium dioxide sample during in-core operating and storing it in the spent fuel storage. Therefore, the next section will present the spent fuel properties, composition, high burnup structure and its characterization.

1.3.2 Radiation damage in uranium dioxide at moderate temperature (~ 773 K - 873 K): formation of the High Burnup Structure (HBS)

The investigations of radiation damage in uranium dioxide at moderate temperature (~ 773 K - 873 K) were performed in both commercial LWR spent fuels and conducted on simulation experiments performed on UO_2 single crystals.

1.3.2.1 Studies performed on spent nuclear fuel

M.E. Cunningham *et al.* [Cunningham *et al.* 1992] performed a study to define the behavior of light water reactor fuel which is irradiated to high burnup levels, in particular the effect of extended burnup on fission gas release and on the fuel rod performance. For that activities include acquiring, irradiating, examining 82 well characterized LWR fuel rods of different designs and irradiation conditions that had been irradiated to extended burnup levels, where rod average burnup levels range from 22 to 69 MWd/KgM with peak pellet-average burnup levels of 25-83 Mwd/KgM. In addition to general post-irradiation examination, fuel pellets from 43 of the fuel rods were also subjected to one or more additional examinations that included optical and scanning electron microscopy, electron probe microanalysis (EPMA), X-ray fluorescence (XRF), UO_2 density, ^{148}Nd based burnup analysis, where whole pellet retained fission gases analysis carried out by using both methods EPMA and XRF to evaluate and detect the radial distribution of xenon in the fuel. It is observed a microstructure change related to irradiation to high burnup levels (up to 83 MWd/KgM pellet average).
The development of a well-defined, unique microstructure region at the fuel pellet edge (rim) is evidenced; this region is characterized by the loss of optically-definable grain structure, an increase in porosity, and depletion of matrix fission gas that begins to develop at a pellet-edge burnup of about

65 MWd/KgM for LWR UO_2 fuel. The width of this rim region was estimated by using a combination of optical ceramograghy and EPMA data by comparing data for xenon (matrix xenon retention) to data for neodymium and defining the fuel radius where the relative neodymium and xenon concentrations diverge as illustrated in figure 1-17. It was observed that this region increases with increasing the burnup and its width of about 250 µm at a pellet-edge burnup of 120 MWd/KgM.

They observed also that the rim region holds the potential for significant localized increase in the athermal release of fission gases at high burnup levels, but the concentration of the rim released to the fractional release of the total fission gas produced in the rod is small.

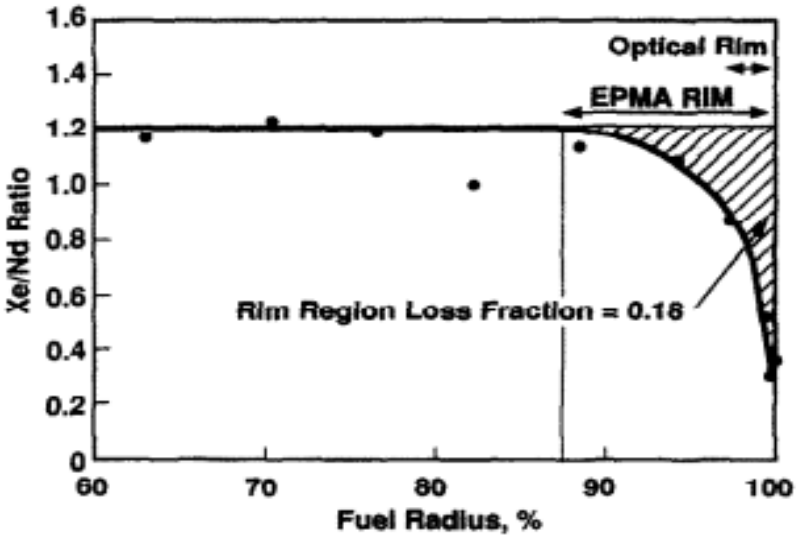

Figure 1-17: Example of analyzing EPMA data for rim width and rim region xenon depletion [Matzke *et al.* 1989].

Another study performed in USA by L.E. Thomas *et al.* [Thomas *et al.* 1992] to investigate the microstructure changes in commercial light water reactor (LWR) fuel irradiated to average burnup near 50 MWd/KgM was performed by analysis transmission electron microscopy and Auger electron spectrometry.

During this study, several aspects of the fuel behavior were examined:
1- Precipitation of the fission gases in dense, highly pressurized inclusions.
2- Apparent solution of Cs, Ba, Zr, Te in the UO_2 matrix.
3- The "rim effect" involving restructuring of the enhanced burnup region at the fuel outer edge. The Figure 1-18 shows this characteristic structure which are observed on the surface of small fragment from the rim of fuel by SEM photos.

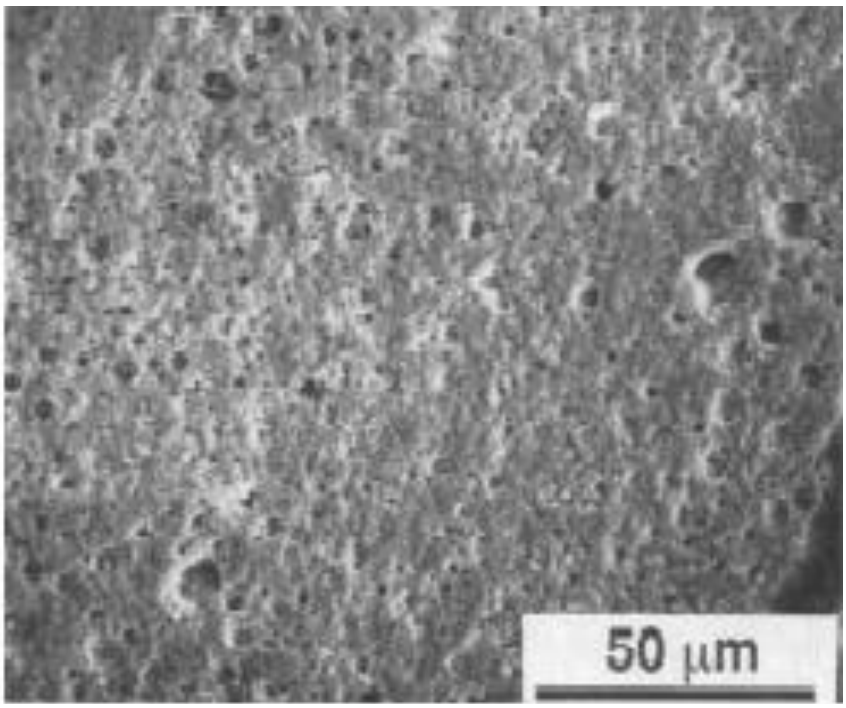

Figure 1-18: SEM photo showing characteristics rim structure in fuel pellet [Thomas *et al.* 1992]

The authors observed that the high burnup rim region showed an extremely fine-grained structure formed by recrystallization of the original UO_2, and that this restructuring is possibly driven by the stored energy of fission products in solution or confined to small bubbles. This phenomenon is expected to extend across LWR fuel pellets irradiated to higher burnups.

It was initially though that the enhancement of the plutonium concentration in the rim zone was the cause of the microstructural change. This statement has been shown to be incorrect after many investigations were performed by Walker *et al.* [Walker *et al.* 1992] using electron probe microanalysis (EPMA) and scanning electron microscopy (SEM). They found that the formation of plutonium does not appear to play a direct role in the microstructure changes, while the restructuring that is a function of the local burnup and the porosity containing part of the fission gas lost from the UO_2 matrix is playing the role. The experiment carried out for different fuels with average burnups extending from 31.5 to 75 MWd/KgM and with ^{235}U enrichments ranging from 1.5 to 7%. The average threshold burnup for the microstructure changes and the temperature limit the distance over which these changes in LWR fuel occur were calculated by using the burnup analysis code VIMBURN and the fuel performance code EIMUS which are 40-45 MWd/KgM and 1373 to 1473 K, respectively. It is shown that in addition to the precipitation of small gas filled pores (bubbles), there is a reduction in the grain size at the rim structure. The SEM technique shows that many of the grains are smaller than 0.5 µm and level of porosity varies between 10-30% with 2 µm in size as shown in figure 1-19 below.

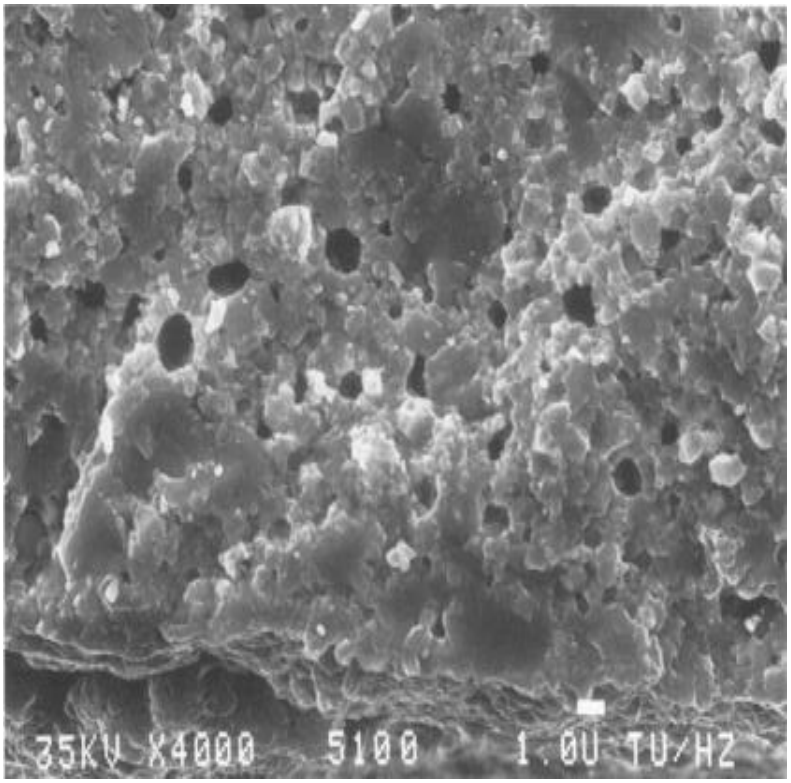

Figure 1-19: Scanning electron micrograph showing the microstructure of the porous rim of specimen at a local burnup 82 MWd/kgM PWR fuel.

Hj. Matzke and J.Spino studied [Matzke & Spino 1997] the process of grain subdivision in UO_2 depending on previous results for ion irradiation technique and by a new investigation to the rim structure in high burnup UO_2 fuel pellet. They observed by using high resolution transmission electron microscopy (HRTEM) that ion irradiation with fission fragment ions caused first the formation of subgrain boundaries, and at higher doses, polygonization was completed at a well-defined threshold. The rim structure was investigated by optical, scanning, transmission electron microscopy, EPMA and oxygen potential measurements. The oxygen potential, the hardness H and the fracture toughness KIC of rim structure were measured, and they found that hardness remained relatively constant along most of the pellet radius, with the exception of a periphery region that shows a reduction of up to 30% of average occurred toward the pellet edge due to increase the porosity there. The KIC changes at smaller radial positions than other properties, indicating a nucleation of subgrains process not affecting all properties to the same content and the improvement of its values in rim structure can be twice as larger than unirradiated UO_2 probably due to the small grain size.

Figure 1-20 shows a typical example of the relative hardness for the fuel with 66.6 MWd/KgM, where the ratio between the local hardness and the average hardness for the plateau is plotted for the same fuel.

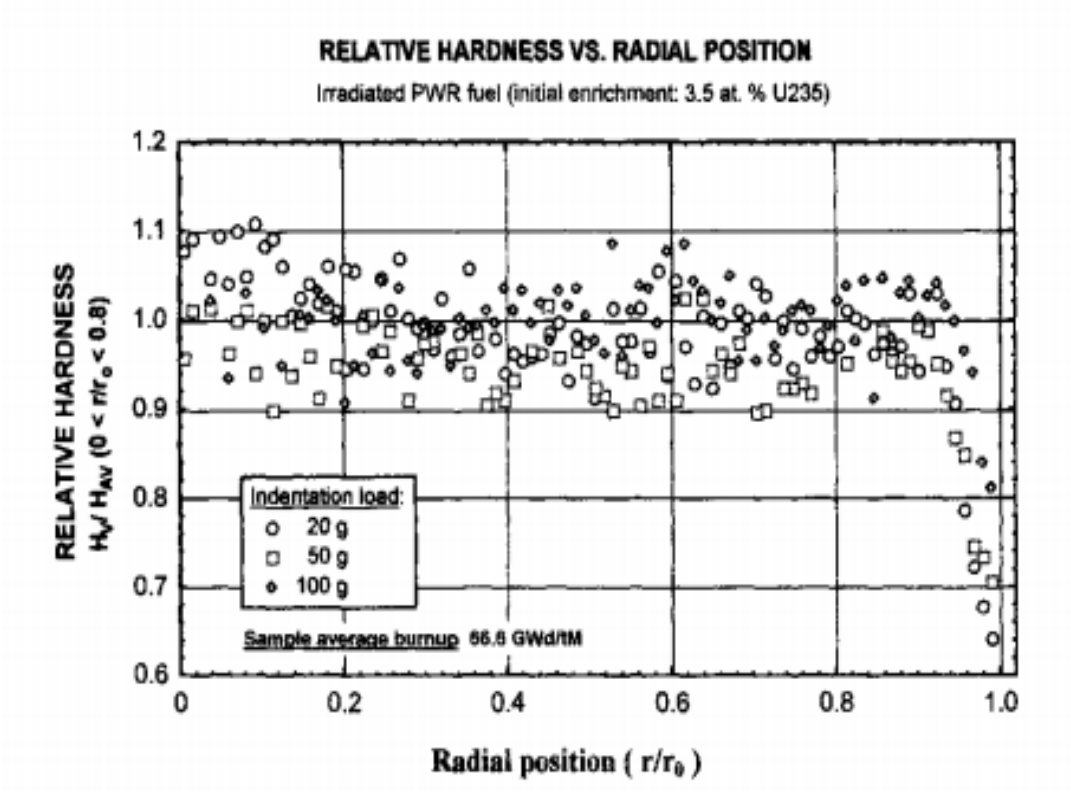

Figure 1-20: Relative hardness for a fuel irradiated at 66.6 MWd/KgM [Matzke & Spino 1997]

The authors of the experiments also observed a reduction in the thermal conductivity of UO_2 in the rim region due to increase the porosity that is responsible for an increase the fuel temperature.

Another study was carried out by Sonoda *et al.* [Sonoda *et al.* 2002] in 2002 in order to identify the conditions of the rim structure formation as a function of burnup and temperature, and to clarify the formation mechanics of HBS. UO_2 fuel disks were irradiated at four thermal conditions, between 673 and 1573 K, and at four different burnups between 36 and 96 MWd/KgM. Scanning electron microscopy (SEM) and transmission electron microanalysis (TEM) were used to observe the microstructural evolution as a function of the irradiation parameters. The SEM observation show the transition from the original to subdivided grains in the rim part, the threshold burnup determined between 55 and 82 MWd/KgM and the temperature threshold of rim structure formation could be (1273±100) K. Figure 1-21 shows, and TEM observation of restructured samples show that most of subgrain boundaries are low angle and are heavily decorated by fission gas bubbles in range 3.5 – 8 nm.

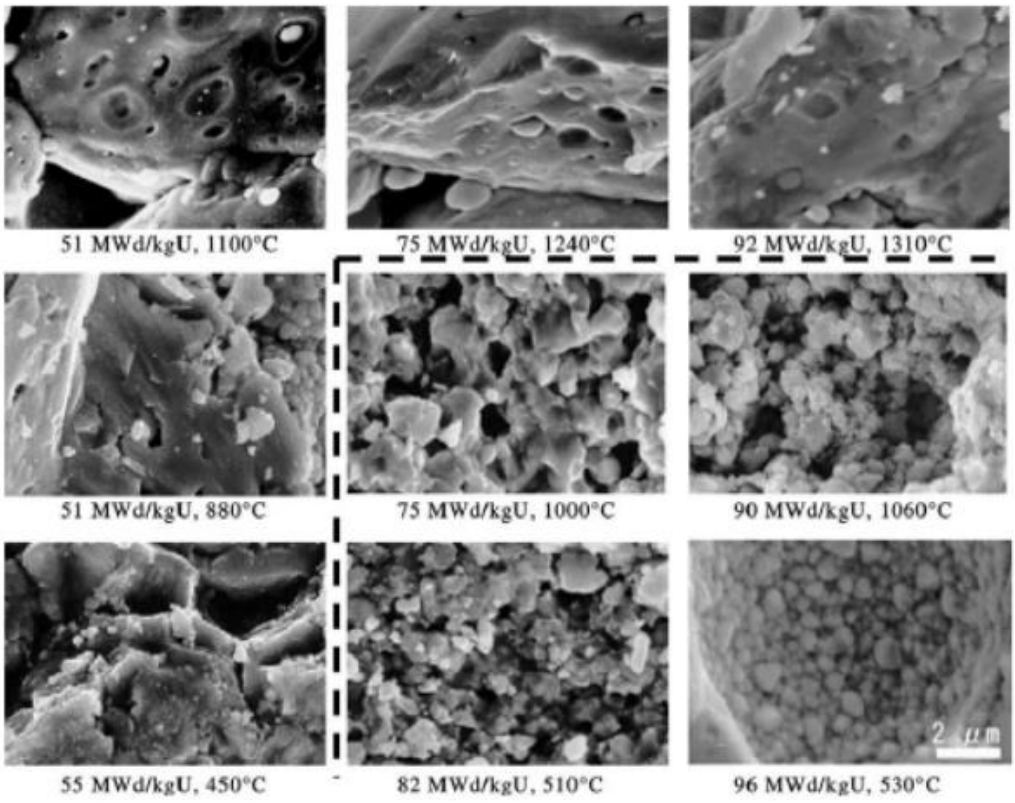

Figure 1-21: SEM of the fuel microstructure as a function of both burnup and irradiation temperature [Sonoda *et al.* 2002]

Lassmann *et al.* [Lassmann *et al.* 1995] performed a study to identify and determine the concept of a burnup threshold for the formation of the rim structure by analyzing the experimental data from different sources that indicate the existence of a transition zone between the normal UO_2 structure and the fully developed HBS.
A simple model developed to describe the formation of HBS and the Xe-depletion and the consequence of the results with the experimental data (Figure 1-22) shows the Xe concentration as a function of local burnup. They classified the pattern into three groups:

- At burnup below ~ 60-75 MWd/KgU the xenon concentration varies linearly with burnup reaching ~ 1wt % at 60 MWd/KgU

- For burnup between ~ 60-120 MWd/KgU the xenon concentration sharply decreases down to 0.25 wt% at 120 MWd/KgU.

- Above 120 MWd/KgU the xenon concentration is constant and about 0.25 wt% and it is clear that the Xe generated is at equilibrium with the Xe lost to the fission pores.

The three groups are attributed by many authors to the three zones in the fuel: un-restructred, transition zone and HBS zone. By analysis the measurements of EPMA for the radial Xe-profile, a threshold burnup is obtained in the range 60-75 MWd/KgU, where the lower value maybe attributed to the beginning of the transition from the normal UO_2 structure towards the formation of the HBS, wherever the higher value is the threshold for the homogenous and fully developed HBS zone.

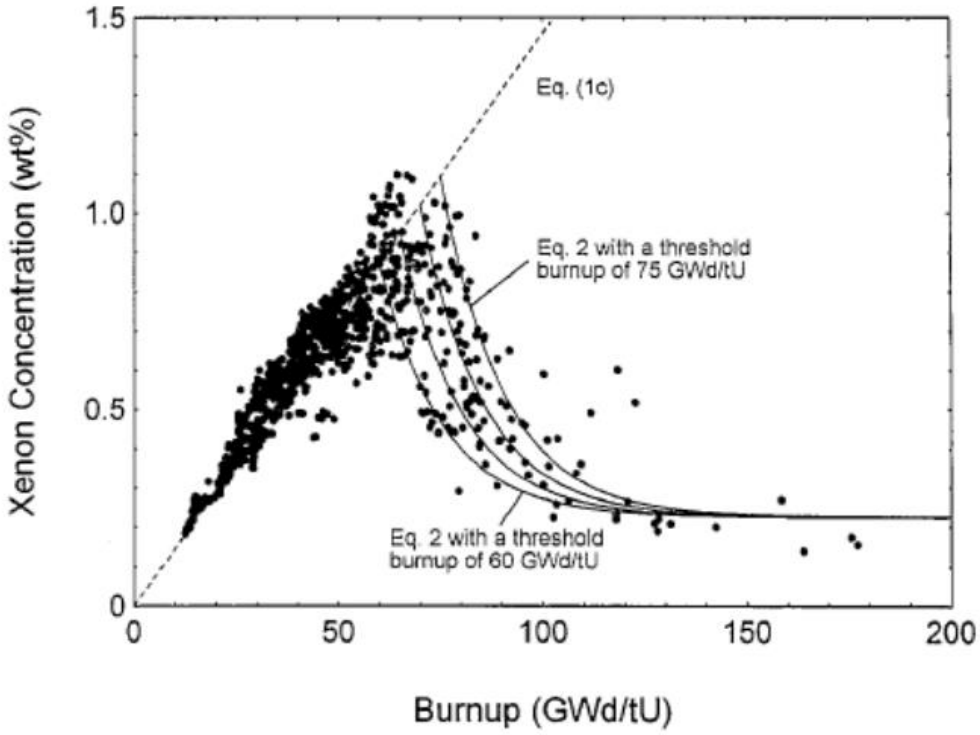

Figure 1-22: Xe-concentration as a function of local burnup, the threshold burnup was varied between 60-75 Wd/KgU [Lassmann *et al.* 1995].

Another Experimental results for the Xe depletion in the matrix of high burn-up fuel are presented from the High Burnup Rim Project (HBRP) in 2014 by L. Holt *et al.* [Holt *et al.* 2014]. In this project a number of UO_2 fuel discs with ^{235}U enrichment of 25.8 wt. % were irradiated. The Xe content of the fuel discs was analyzed by means of electron probe microanalysis (EPMA). The influence of the burn-up and irradiation temperature on the Xe concentration was investigated using a multi-physical approach involving various simulation tools. The temperature influence was modelled by means of the temperature dependent effective burn-up. Good agreement was found between the modelled temperature threshold of the effective burn-up and the experimental temperature threshold between un- and restructured fuel in the HBRP.

Mogensen *et al.* [Mogensen *et al.* 1999] used XRF and EPMA results for retained xenon from Battelle's high burn-up effects program [Knudsen *et al.* 1988], [Knudsen *et al.* 1992] are re-evaluated to study the behavior of fission gas in the rim region of high burn-up UO_2 fuel pellets. The data reviewed are from commercial low-enriched BWR fuel with burnups in the range 44.8-54.9 GWd/tU and high enriched PWR fuel with burn-ups from 62.5 to 83.1 GWd/tU. It is found that the highly burn-up structure penetrated much deeper than initially reported. The local burn-up threshold for the formation of the high burn-up structure in those fuels with grain sizes in the normal range lay between 60 and 75 GWd/tU. The high burn-up structure was not detected by EPMA in a fuel that had a grain size of 78 µm although the local burn-up at the pellet rim had exceeded 80 GWd/tU. It is concluded that fission gases had been released from the high burn-up structure in three PWR fuel sections with burn-ups of 70.4, 72.2 and 83.1 GWd/tU. In the rim region of the last two sections, at the locations where XRF indicated gas release, the local burn-up was higher than 75 GWd/tU.

1.3.2.2 Studies performed on UO_2 single crystals

A number of studies were performed in the European Institute for transmission Elements, and most of them were carried out by Hj. Matzke *et al.* [Matzke *et al.* 1994]. UO_2 single crystals of <100>, <111>, <110> orientations were implanted at Karlsruhe with Xe ions of 300 KeV energy, at ranging of 1 x 10^{16} to 1 x 10^{17} ion.cm^{-2} and analyzed with He ions with 2 MeV for RBS to deduce the damage. Most implantations were done at room temperature, but some crystals were implanted at 77K or 773 K.

During one of the study, they observed at a given critical dose ~ 5x10^{16} ion.cm^{-2} (impurities concentration ~ 5-7%) dramatic changes of the damage peak in the channelling spectra. These peaks eventually reached the random yield. The analysis of these peaks by X-ray diffraction measurements and electron microscope analysis showed that polygonization (rather than amorphization) had occurred in the samples of UO_2 causing a fine-grained polygonization structure with a misalignment between grains of a few degrees only. According to what they obtained, this phenomena was related to polygonization in terms of overpressurized gas bubbles causing cleave and microfracture. They indicated that the process is rather independent of temperature in the range 77 to 773 K and the presence of a critical concentration of insoluble fission products is decisive in the polygonization process.

In summary, as this section presents and shows many studies and experiments have been intensively investigated to understand the HBS and to study the radiation effects in uranium dioxide in both genuine irradiated fuel (spent fuel) or on irradiated single crystals (uranium dioxide samples), by applying different experimental conditions and different characterization techniques including Rutherford Backscattering Spectrometry in channelling geometry (RBS/C), and X-ray diffraction analysis (XRD), and Transmission electron Microscopy (TEM). It is clear that these studies show similar characterization for the HBS that characterized by the formation of pore structure, formation of subgrains, Xe depletion of the original grains. However the mechanics of the formation of HBS remain eventually not well understood.

Due to the complexity of the system and to the number of the parameters and conditions involved in the nuclear fuel irradiation, a fully scientific description of HBS formation mechanisms is still missing, despite several models and experiments performed in the past. Therefore, the main goal of this thesis is to reproduce some of the specific microstructure of the high burnup structure of the irradiated nuclear fuel by using a very simplified model system - namely uranium dioxide single crystals - and the use of energetic ion beams for generating the radiation damage and doping of the solid, in order to examine and to check the various relevant parameters involved in the formation of high burnup structure, in evaluating their importance, and in clarifying the synergies between them. In this thesis, the main parameters that have been studied include: (i) radiation defects induced by collision cascades at low energy; (ii) soluble and insoluble impurities located in the crystal structure (iii) temperature of the fuel. The following chapters will present the methods used to simulate the microstructure of spent nuclear fuel the experimental simulation of the irradiation effects in nuclear fuel, how it was performed, the results of these experiments and the analysis of the data.

References

[Almeida & Raisanen 2005]

Pde Almeida and J. Raisanen. Atomic displacement in solids, analysis of the primary event and the collision cascade. Eur. J. Phys. 26:371-389, 2005.

[Belhabib et al. 2015]

T. Belhabib, P. Desgardin, T. Sauvage, H. Erramli, M.F. Barthe, F. Garrido, G. Carlot, L. Nowicki, P. Garcia. Lttice location and annealing behaviour of helium atoms implanted in uranium dioxide single crystals. Journal of Nuclear Materials, 467:1-8, 2015.

[Bethe 1930]

H. A. Bethe. Ann. Phys. (Leipz.), 5, page 325, 1930.

[Billard]

Isabelle Billard, quels traitements pour les déchets nucléaires presentation, Ires/In2p3 université du strasbourg.

[Bloch 1933]

F. Bloch. Ann. Phys. (Leipz.), 16, page 285, 1933.

[Bohr 1940]

N. Bohr. Scattering and stopping of fission fragments. Phys. Rev., 58:654-655, Oct 1940.

[Bohr 1941]

N. Bohr. Velocity-range relation for fission fragments. Phys. Rev., 59:270-275, Feb 1941.

[Cunningham *et al.* 1992]

M.E. Cunningham, M.D. Freshley and D.D. Lanning. Development and characteristics of the rim region in high burnup UO_2 fuel pellets. Journal of Nuclear Materials, 188:19, 1992.

[Dunlop *et al.* 1992]

Duniop, F. Rullier-Albenque, C. Jaouen, C. Temolier and J. Davenas. Materials under irradiation, 1992.

[Echenique *et al.* 1990]

P. M. Echenique, F. Flores, R. H. Ritchie. Dynamic screening of Ions in condensed Matter. solid state physics, volume 43, 1990.

[Fink *et al.* 1981]

J.K. FINK, M.G. CHASANOV and L.LEIBOWITZ. Thermophysical properties of Uranium doixede. Journal of Nuclear Materials, 102:17-25, 1981.

[Firsov *et al.* 1957]

O. B. Firsov. Zh.Eksp. Teor. Fiz. [Engl. Transl. Sov. Phys. JETP 5, p1192-1196(1957)], 32:1464, 1957.

[Firsov *et al.* 1957]

O. B. Firsov. Zh.Eksp. Teor. Fiz. [Engl. Transl. Sov. Phys. JETP 6, p5340-537(1958)], 33:696, 1957.

[Firsov *et al.* 1958]

O. B. Firsov. Zh.Eksp. Teor. Fiz. [Engl. Transl. Sov. Phys. JETP 7, p308-311(1958)], 34:447, 1958.

[Firsov *et al.* 1957]

O. B. Firsov. Zh.Eksp. Teor. Fiz. [Engl. Transl. Sov. Phys. JETP 5, p1192-1196(1957)], 32:1464, 1957.

[Fleischer *et al.* 1965]

R. L. Fleischer, P. B. Price and R. M. Walker. Ion explosion spick mechanism for formation of charged-particle tracks in solid. J. Appl. Phys. 36:3649, 1965.

[Garcia *et al.* 2012]

P. Garcia, G. Martin, C. Sabathier, G. Carlot, A. Michel, P. Martin, B. Dorado, M. Freyss, M. Bertolus, R. Skorek, J. Noirot, L. Noirot, O. Kaitasov, S. Maillard. Nucleation and growth of intragranular defect and insoluble atom clusters in nuclear oxide fuels. Nuclear Instruments and Methods in Physics Research B, 277:98–108, 2012.

[Garrido *et al.* 1997]

F. Garrido, C. Choffel , J.-C. Dran, L. Thomé, L. Nowicki , A. Turos. Structural modifications in uranium dioxide irradiated with swift heavy ions. Nuclear Instruments and Methods in Physics Research B, 127-128: 634-638, 1997.

[Garrido *et al.* 2008]

F. Garrido, L. Vincent, L. Nowicki, G. Sattonnay, L. Thomé. Radiation stability of fluorite-type nuclear oxides. Nuclear Instruments and Methods in Physics Research B, 266: 2842–2847, 2008.

[Garrido *et al.* 2009]

F. Garrido, S. Moll, G. Sattonnay, L. Thomé, L. Vincent. Radiation tolerance of fluorite-structured oxides subjected to swift heavy ion irradiation. Nuclear Instruments and Methods in Physics Research B, 267:1451–1455, 2009.

[Grimes *et al.* 2008]

R. W. Grimes, R. J. M. Konings & L. Edwards. Greater tolerance for nuclear materials, Nature Materials, 7:683 – 685, 2008.

[Guilbert *et al.* 2004]

S. Guilbert, T. Sauvage, P. Garcia, G. Carlot, M.-F. Barthe, P. Desgardin, G. Blondiaux, C. Corbel, J.P. Piron, J.-M. Gras. He migration in implanted UO_2 sintered disks. Journal of Nuclear Materials, 327:88–96, 2004.

[Hayashi *et al.* 1997]

K. Hayashi, H. Kikuchi, K. Fukuda. Radiation damage of UO_2 by high-energy heavy ions. Journal of Nuclear Materials, 248:191-195, 1997.

[Hausner 1965]

H. Hausner. Determination of the melting point of Uranium dioxide. Journal of Nuclear Materials, 15(3):179-183, 1965.

[He *et al.* 2014]

L.F. He, J. Pakarinen, M.A. Kirk, J. Gan, A.T. Nelson, X.-M. Bai, A. El-Azab, T.R. Allen. Microstructure evolution in Xe-irradiated UO_2 at room temperature. Nuclear Instruments and Methods in Physics Research B, 330:55–60, 2014.

[Holt *et al.* 2014]

L. Holt, A. Schubert, P. Van Uffelen , C.T. Walker, E. Fridman, T. Sonoda. Sensitivity study on Xe depletion in the high burn-up structure of UO_2. Journal of Nuclear Materials, 452:166–172, 2014.

[JANIS]

Java-based Nuclear Data Information Software; The JEFF-3.1.1 Nuclear Data Library.

[Knoll 2000]

Glenn F. Knoll, Radiation Detection and Measurement. John Wiley & Sons, Inc., USA, 3rd Edition, 2000.

[Knudsen *et al.* 1992]

P. Knudsen, C. Bagger, M. Mogensen, H. Toftegaard, Proceedings of the Technical Committee on Fission Gas Release and Fuel Rod Chemistry Related to Extended Burnup, Pembroke, May 1992, IAEA-TECDOC-697, 1993, p. 193.

[Knudsen *et al.* 1988]

P. Knudsen, C. Bagger, H. Carlsen, B.S. Johansen, M. Mogensen, I. Misfeldt, Proceedings of the ANS Topical Mtg. on LWR Fuel Performance, Williamsburg, USA, 1988, p. 189.

[Lamarsh *&* Baratta 2001]

John R. Lamarsh, Anthony J. Baratta. Introduction to nuclear engineering,by Prentice-Hall, Upper Saddle River, New Jersey 07458, 2001.

[Lamb 1940]

W. E. Lamb. Passage of uranium fission fragments through matter. Phys. Rev., 58: 696-702, Oct 1940.

[Lassmann *et al.* 1995]

K. Lassmann, C.T. Walker, J. van de Laar, F. Lindstrom. Modelling the high burnup UO_2 structure in LWR fuel. Journal of nuclear materials, 226:1-8, 1995.

[Lifshits *et al.* 1960]

I. M. Lifshits, M. I. Kaganov, and L. V. Tanatarov. On the theory of irradiation-induced changes in metals. Journal of nuclear energy. Part A. Reactor science, 12(1-2): 69-78, 1960.

[Lindhard & Scharff 1961]

J. Lindhard and M. Scharff. Energy dissipation by ions in the KeV region. Phys. Rev., 124:128-130, Oct 1961.

[Matzke *et al.* 1989]

Hj. Matzke, H. Blank, M. Coquerelle, K. Lassmann, I.L.F. Ray, C. Ronchi and C.T. Walker. Oxide fuel transients, 166:165-178, 1989.

[Matzke 1992]

Hj.Matzke. On the rim effect in high burnup UO_2 LWR fuels. Journal of nuclear materials, 189:141-148, 1992.

[Matzke *et al.* 1994]

Hj. Matzke, A. Turos, G. Linker. Polygonization of single crystals of the fluorite-type oxide UO_2 due to high dose ion implantation. Nuclear Instruments and Methods in Physics Research B 91 (1994) 294-300.

[Matzke & Kinoshita 1997]

Hj.Matzke, M. Kinoshita. Polygonization and high burnup structure in nuclear fuels, Journal of Nuclear Materials, 247:108-115, 1997.

[Matzke & Spino 1997]

Hj.Matzke and J.Spino. Formation of the rim structure in high burnup fuel. Journal of nuclear materials, 248:170-179, 1997.

[Matzke *et al.* 2000]

Hj. Matzke, P.G. Lucuta, T. Wiss. Swift heavy ion and fission damage effects in UO_2. Nuclear Instruments and Methods in Physics Research B, 166-167:20-926, 2000.

[Meis & Chartier 2005]

C.Meis, A. Chartier. Calculation of the threshold displacement energies in UO_2 using ionic potentials. Journal of Nuclear Materials, 341:25-30, 2005.

[Michel *et al.* 2012]

A. Michel, C. Sabathier, G. Carlot, O. Kaïtasov, S. Bouffard, P. Garcia, C. Valot. An in situ TEM study of the evolution of Xe bubble populations in UO_2. Nuclear Instruments and Methods in Physics Research B, 272: 218–221, 2012.

[Mieszczynski *et al.* 2014]

C. Mieszczynski, G. Kuri, C. Degueldre, M. Martin, J. Bertsch, C.N. Borca, D. Grolimund, Ch. Delafoy, E. Simoni. Irradiation effects and micro-structural changes in large grain uranium dioxide fuel investigated by micro-beam X-ray diffraction. Journal of Nuclear Materials, 444: 274–282, 2014.

[Mogensen *et al.* 1999]

M. Mogensen, J.H. Pearce, C.T. Walker. Behavior of fission gas in the rim region of high burn-up UO_2 fuel pellets with particular reference to results from an XRF investigation. Journal of Nuclear Materials, 264:99-112, 1999.

[Nastasi *et al.* 2014]

M. Nastasi, J. W. Mayer, O. Wang. Ion Beam Analysis: Fundamentals and Applications. Taylor & francis group, 2014.

[Nogita *et al.* 1997]

K. Nogita , K. Une , M. Hirai , K. Ito , K. Ito , y. Shirai. Effect of grain size on recrystallization in high burnup fuel pellets. Journal of Nuclear Materials, 248:196-203, 1997.

[Nogita *et al.* 1999]

K. Nogita , K. Hayashi , K. Une , K. Fukuda. Depth profiles of damage accumulation in UO_2 and $(U,Gd)O_2$ pellets irradiated with 100 MeV iodine ions. Journal of Nuclear Materials, 273:302-309, 1999.

[Nuclear Power reactors overview 2017]

Nuclear Power reactors, World nuclear association, 2017, **[website]. Available here:** http://www.world-nuclear.org/information-library/nuclear-fuel-cycle/nuclear-power-reactors/nuclear-power-reactors.aspx.

[Nuclear Fuel Fabrication overview 2017]

Nuclear Fuel Fabrication, World nuclear association, 2017,**[website]. Available here:** http://www.world-nuclear.org/information-library/nuclear-fuel-cycle/conversion-enrichment-and-fabrication/fuel-fabrication.aspx.

[Olander 1976]

Donald R. Olander. Fundamental aspects of nuclear reactor fuel elements. Technical information center, 1976.

[OSAISAI *et al.* 1990]

F.E. OSAISAI, S.G. PRUSSIN and D.R. OLANDER, Concentration profiles of neutron-induced radioactivites in UO_2 fuel specimens. Journal of Nuclear Materials, 173:149-158, 1990.

[Overview of the spent fuel 2011]

Spent fuel from nuclear power reactors, an overview of a new study by the international panel on fissile materials, 2011.

[PEARCE *et al.* 1983]

J.H. PEARCE, R. SUMERLING and R. HARGREAVES. Studies of the radial distribution of Pu, Xe and Cs in irradiated thermal-reactor UO_2 fuel, using an electron probe microanalyser. Journal of Nuclear Materials, 116:1-9, 1983.

[Radioactivity and its applications]

Radioactivity and its applications to the general public, World nuclear association, EDP Sciences and Institut National de Physique Nucléaire et Physique des Particules (IN2P3), **[website]. Available here:** http://www.radioactivity.eu.com/site/pages/Minor_Actinides.htm.

[Ray *et al.* 1997]

I.L.F. Ray, Hi. Matzke, H.A. Thiele, M. Kinoshita. An electron microscopy study of the RIM structure of a UO_2 fuel with a high burnup of 7.9% FIMA .Journal of Nuclear Materials, 245:115-123, 1997.

[Rest & Hofman 1994]

J. Rest, G.L. Hofman. Dynamics of irradiation-induced grain subdivision and swelling in U,Si, and UO, fuels. Journal of Nuclear Materials, 210:187-202, 1994 .

[Rondinella & Wiss 2010]

V. V. Rondinella and T. Wiss. The high burnup structure in nuclear fuel. Materialstoday, 13:12, 2010.

[Sabathier *et al.* 2008]

C. Sabathier, L. Vincent, P. Garcia, F. Garrido, G. Carlot, L. Thomé, P. Martin, C. Valot. In situ TEM study of temperature-induced fission product precipitation in UO_2. Nuclear Instruments and Methods in Physics Research B, 266:3027–3032, 2008.

[Sattonnay *et al.* 2006]

G. Sattonnay, L. Vincent, F. Garrido, L. Thomé. Xenon versus helium behavior in UO_2 single crystals: A TEM investigation. Journal of Nuclear Materials, 355:131–135, 2006.

[Sonoda *et al.* 2010]

T. Sonoda, M. Kinoshita, N. Ishikawa, M. Sataka, A. Iwase, K. Yasunaga. Clarification of high density electronic excitation effects on the microstructural evolution in UO_2. Nuclear Instruments and Methods in Physics Research B, 268:3277–3281, 2010.

[Sonoda *et al.* 2002]

T. Sonoda, M. Kinoshita, I. L. F. Ray, T. Wiss, H. Thiele, D. Pellottiero, V. V. Rondinella , Hj. Matzke. Transmission electron microscopy observation on irradiation-induced microstructural evolution in high burn-up UO_2 disk fuel. Nuclear instruments and methods in physics research B, 191:622-628, 2002.

[Soullard *et al.* 1985]

J. Soullard. High voltage electron microscope observations of UO2. Journal of Nuclear Materials, 135(2 - 3):190 – 196, 1985.

[Spino *et al.* 1996]

J. Spino , K. Vennix, M. Coquerelle .Detailed characterization of the rim microstructure in PWR fuels in the burn-up range 40-67 GWd/tM. Journal of Nuclear Materials, 231:179-190, 1996.

[Stehle *et al.* 1975]

H. Stehle, H. assmann and F. Wunderlich. Uranium dioxide properties for LWR fuel rods. Journal nuclear engineering and design 33: 230-260, 1975.

[STEHLE 1988]

H. Stehle. Performance of oxide nuclear fuel in water-cooled power reactors. Journal of Nuclear Materials, 153:3- 15, 1988.

[Thomas *et al.* 1992]

L.E.Thomas, C.E.Beyer and L.A.Charlot. Microstructural analysis of LWR spent fuels at high burnup. Journal of nuclear materials, 188:80-89, 1992.

[Tian *et al.* 2011]

X.F. Tian, T. Gao, Chongsheng Long, JiuKai Li, Gang Jiang, Hongxing Xiao. Dynamical simulations of radiation damage induced by 10 keV energetic recoils in UO_2. Nuclear Instruments and Methods in Physics Research B, 269:1771–1776, 2011.

[Toulemonde *et al.* 1992]

M. Toulemonde, C. Dufour, and E. Paumier. Transient thermal process after a high-energy heavy-ion irradiation of amorphous metals and semiconductors. Phy. Rev. B, 46:14362-14369, Dec 1992.

[Une *et al.* 1992]

K. Une, K. Nogita, S. Kashibe and M. Imamura. Microstructural change and its influence on fission gas release in high burnup UO, fuel. Journal of Nuclear Materials, 188:65-72, 1992.

[Walker *et al.* 1992]

C.T. Walker, T. Kameyama, S. Kitajima and M. Kinoshita. Concerning the microstructure changes that occur at the surface of UO, pellets on irradiation to high burnup. Journal of Nuclear Materials, 188:73-79, 1992.

[Willis 1964]

B.T.M. Willis. Structures of UO_2, UO_{2+x} and U4O9 by neutron diffraction. Journal de Physique, 25(5):431, 1964.

[Yamada *et al.* 2000]

Kazuhiro Yamada, Ken Kurosaki, Masyoshi Uno, Shinsuke Yamanaka. Evolution of thermal properties of uranium dioxide by molecular dynamics. Journal of Nuclear Materials, 377: 10-16, 2000.

[Yarlagadda *et al.* 1978]

B. S. Yarlagadda, J. E. Robinson, and W. Brandt. Effective-charge theory and the electronic stopping power of solids. Phys. Rev. B, 17:3473-3483, May 1978.

Chapter 2

Methodology

This chapter presents the simulation experiments that were performed to investigate the formation mechanisms of the High Burnup structure, the different characterization techniques that were applied including Rutherford Backscattering Spectrometry in the channelling mode (RBS/C) and Transmission electron Microscopy (TEM). The Monte-Carlo simulation code that was used to quantify that damage is also discussed.

2.1 Experimental simulation for the investigation of High Burnup Structure (HBS) in spent fuel

The investigation of the high burnup structure in uranium dioxide fuel pellet after its operating life in the reactor core requires the study of the nuclear spent fuel or alternatively put a uranium dioxide samples in the reactor core where it is bombarded by neutrons at high flux and high temperature. Such an experiment is not easy to perform because the spent fuel contains fission fragments, actinides, nuclei that decay by β- or α emission, that are unstable leading to a high level of radioactivity. Those drawbacks seriously hamper much a type of investigation, on the genuine fuels.

These problems can also be tackled by using accelerators which are used to implant a highly simplified fuel - uranium dioxide single crystal - with foreign elements that simulate the presence of fission products to induce both radiation damage and the presence of fission products. The main idea is to reproduce a structure with a similar composition as the spent fuel irradiated in nuclear reactor with no danger or hazard. Therefore, simulation experiments were performed during this thesis at "Centre de Sciences Nucléaire et de Sciences de la Matière" (CSNSM) lab by using the accelerated ion beam – SCALP/JANNuS facility - to irradiate uranium dioxide with different ions at 773 K to study the effects of different parameters such as the fluence and the role played by the chemical nature of the ion (soluble and insoluble species) on the nuclear fuel under specific conditions of irradiation.

In this work, experimental simulations have been performed to better understand the parameters responsible for creation of a highly defective structure in the nuclear fuel due to (i) the effect of radiation damage produced by low energy (ii) the role of the temperature (773 K) or (iii) the influence of doping foreign elements, especially at high concentration.
The samples that simulate the nuclear fuel were depleted UO_2 (0.3% ^{235}U) single crystals irradiated with external accelerated ions at 773 K. Irradiated samples are characterized by various techniques including *in situ* Rutherford Backscattering Spectrometry in channelling mode (RBS/C) and *in situ* Transmission electron Microscopy (TEM), both techniques coupled to ion irradiation.

2.2 Experiments

The <100>-orientated uranium dioxide single crystals were implanted in well-defined ions beam conditions (nature, energy and fluence of ion) at 773 K at the SCALP/JANNuS facility at CSNSM laboratory at university Paris-Sud at Orsay, France by using the 190 kV IRMA ion implanter as shown in the figure 2-1:

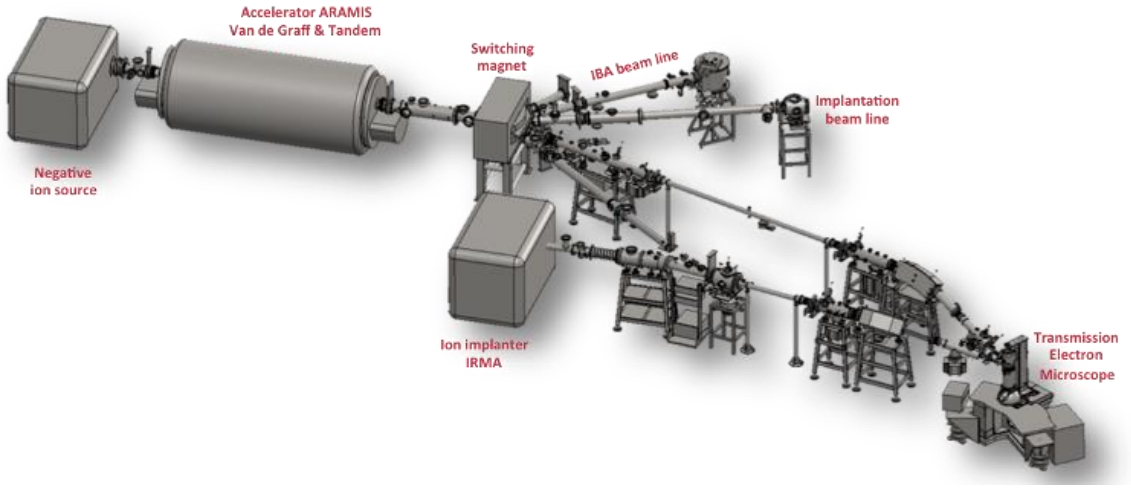

Figure 2-1: Schematic view of the SCALP facility located at CSNSM laboratory; this facility is composed of a 2-MV tandem accelerator (ARAMIS) and a 190 KV ion implanter (IRMA) that can be coupled with a 200 KV Transmission electron microscope [JANNuS-Orsay/SCALP].

The SCALP/JANNuS facility is composed of an ion accelerator and an ion implanter that are linked by an ion beam line to perform, without changing experimental conditions, *in situ* implantations and ion beam characterization. Table 2-1 shows the main characterizations of each electrostatic machine [JANNuS-Orsay/SCALP].

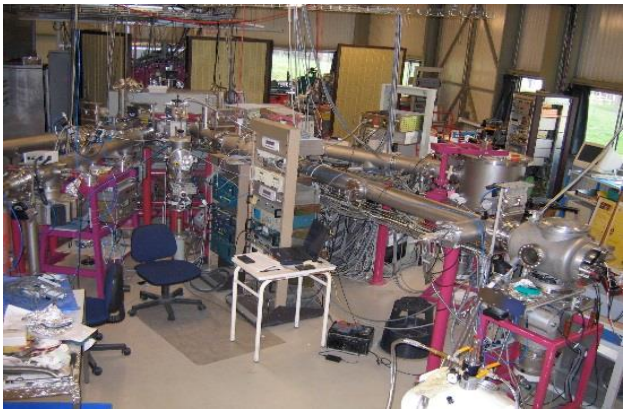

Figure 2-2: The accelerators and the ion implanter IRMA at SCALP facility

Table 2-1: The main characterizations of SCALP/JANNuS accelerators

Accelerator name	**Type of source**	**Ions range**	**Energy range**	**Irradiation equipments**	**On line characterization**
ARAMIS	- Negative ion source - Penning ion source placed at the terminal producing gaseous elements like He and hydrogen	Almost every ions except noble gases between H —> Bi	0.5 to 15 MeV	Scanning device, under vacuum irradiation between 100K and 1200K	Channelling RBS, PIXE, TEM, ERDA
IRMA	Positive ion source	Almost every ions between H —>Bi	10 to 570 keV	Scanning device, under vacuum irradiation between 100K and 1200K	Channelling RBS, TEM

The JANNuS – Orsay platform is comprising a 200 kV TEM connected at the two accelerators. It allows the observation in real time the structural evolution of materials under irradiation conditions between 77 K and 1300 K.

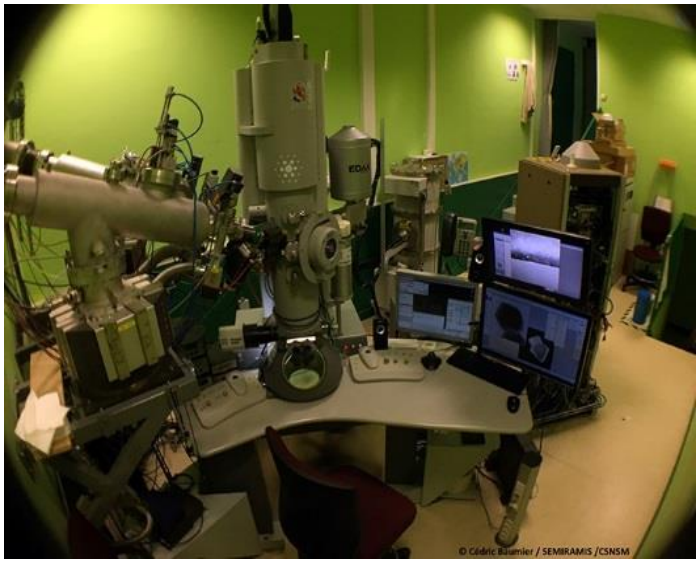

Figure 2-3: The Electron Transmission Microscopy at the JANNuS-Orsay facility.

2.2.1 *In situ* Channeling coupled to ion irradiation

Crystals were implanted with different ions (namely Xe and La) at 773 K for accumulated fluence ranging from $5x10^{13}$ cm^{-2} to a few 10^{16} cm^{-2} (corresponding to a concentration of incorporated impurities ranging from 0.01 to ~ 5 at. %). After each step of implantation, the crystal was characterized by *in situ* RBS/C technique. The crystals were irradiated on a special specimen holder making 7° tilting angle with respect to the main crystallographic orientation of the crystals to prevent any channelling of bombarding ions.

The chosen experimental conditions simulate the damage induced by fission fragments close to the end of their range, where the process of defect creation corresponds essentially to the elastic slowing-down. The range, range straggling, the number of displacements per atom (*dpa*) induced by irradiation and the concentration of incorporated ions at the maximum of the distribution were calculated by the SRIM code. Table 2-2 presents the irradiation conditions used during the experiments and the SRIM calculations assuming that the displacement thresholds for uranium and oxygen sub-lattice are $E_d(U)$ = 40 eV and $E_d(O)$ = 20 eV, respectively [Soullard *et al.* 1985].

Table 2-2: Conditions of ion implantations performed in uranium dioxide single crystals at 773 K for *in situ* RBS/C

Ion	Z	Mass(u)	Energy (KeV)	Range R_p (*nm*)	Range straggling ΔRp (*nm*)	Nuclear stopping *Sn* (*KeV/nm*)	Electronic stopping *Se* (*KeV/nm*)	Fluence (cm^{-2})	*dpa* max	Fraction of implanted ions at max (at. %)
$^{131}Xe^{3+}$	54	130.905	470	83	39	3.33	0.61	5 x 10^{13} - 4 x 10^{16}	327	~ 5%
$^{139}La^{3+}$	57	138.906	500	86	41	3.60	0.42	5 x 10^{13} - 3 x 10^{16}	245	~ 4%

2.2.2 *In situ* TEM coupled to ion irradiation

Regarding *in situ* TEM experiments, UO_2 thin foils were implanted with 260 KeV Xe^{2+} ion or 265 KeV La^{2+}at 773 K using the JANNuS-Orsay facility (with IRMA ion implantor and TEM connected together). These energies were chosen to allow the implanted ions to stay inside the thin foil that has a thickness of 40 to 60 nm. The thickness of the thin foil is measured by EELS. The range of the ions according to SRIM code calculations is Rp ~ 40 nm assuming the implantation incident angle between the ion beam and the normal to the surface is 42° as shown in figure 2-4. This implantation angle was chosen to move the sample towards the fixed incident ion beam direction and to get better contrast on the images.

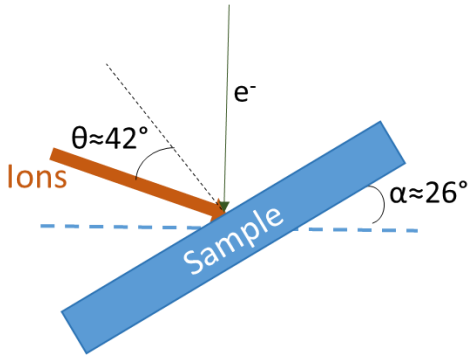

Figure 2-4: Schematic view of the implantation and characterization conditions

Fluences ranged from 10^{13} up to $4x10^{15}cm^{-2}$, mean flux for Xe and La ions is $1.2x10^{11}$ and 1.2×10^{12} $cm^{-2}.s^{-1}$, respectively. Table 2-3 presents the irradiation conditions used during the TEM experiments

Table 2-3: Conditions of ion implantations performed in uranium dioxide single crystals at 773 K for *in situ* TEM

Ion	Z	Mass(u)	Energy (KeV)	Range R_p (*nm*)	Range straggling ΔRp (*nm*)	Nuclear stopping *Sn* (*KeV/nm*)	Electronic stopping *Se* (*KeV/nm*)	Fluence (cm^{-2})	*dpa* max	Fraction of implanted ions at max (at. %)
$^{131}Xe^{2+}$	54	130.905	260	39	22	3.7	0.51	1×10^{13} - 4×10^{15}	44	~ 0.9 %
$^{139}La^{2+}$	57	138.906	265	39	22	3.9	0.3	5×10^{13} - 7×10^{14}	7.6	~ 0.17 %

Figure 2-5 shows a schematic presents the simulation experiments that have been done during this thesis to reproduce the HBS and to characterize the damage created in single crystals UO_2. The characterization techniques is discussed in details in this chapter.

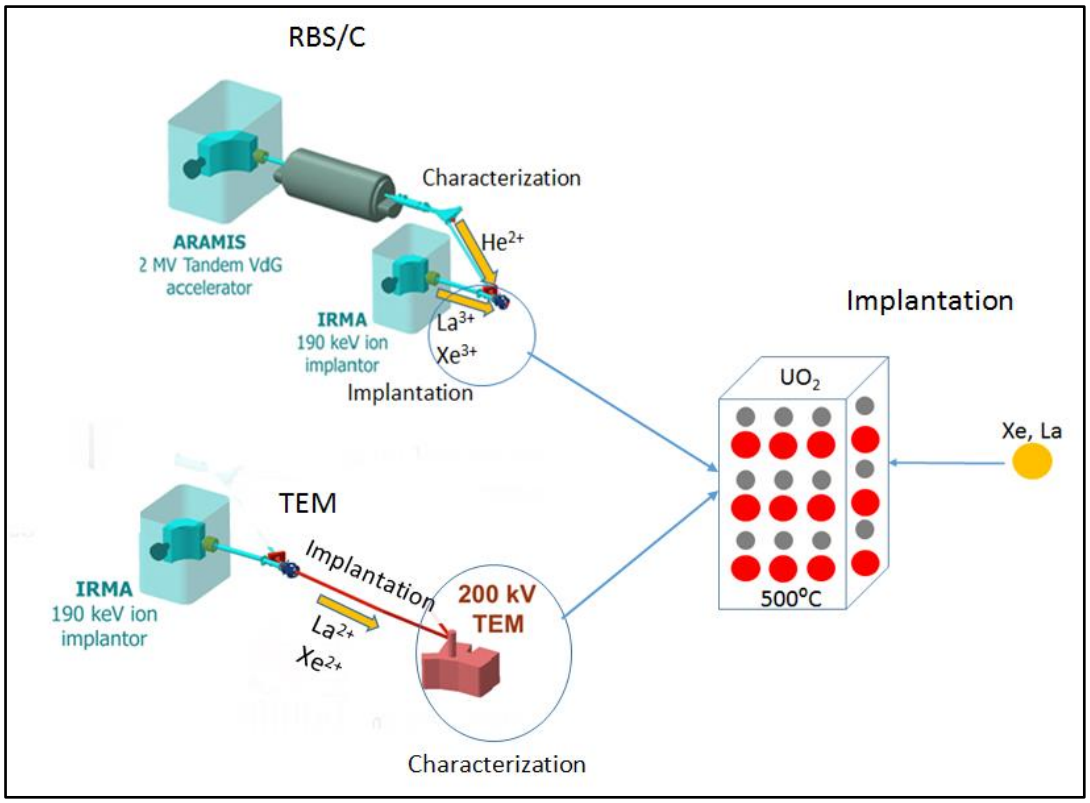

Figure 2-5: Schematic of the simulation experiments were performed to reproduce nuclear spent fuel and the characterization techniques that were used to characterize the damage.

2.3 Samples preparation

The <100>- orientated uranium dioxide (0.3 % ^{235}U) single crystals were prepared and have been used as simple model to modelize the nuclear fuel. This section describes the crystals prepared for the RBS/C and TEM experiments.

2.3.1 RBS/C crystal preparation

The preparation of crystals prepared for RBS/C experiment starts by cutting off the samples from a block with a specific crystallographic orientation by using the Laue X-Ray diffraction method. Then the samples were mechanically polished until mirror-liked finish in slices of 1 mm thickness (see figure 2-6) using diamond glued on plastic discs down to 0.5 µm. They were annealed at 1670 K under a mixture of Ar/H_2 gases of 10% of H_2 in order to remove any defects created during the cutting or polishing processes and to keep the ratio of O/U to 2.00.

$$UO_{2+x} + xH_2 \xrightarrow{Ar/H_2 enviroment} UO_2 + xH_2O$$

The quality of the samples were checked by Rutherford Backscattering Spectrometry technique in the channelling mode by measuring the ratio between the yields in a random and in an aligned direction. The measured minimum axial yield $\chi_{min} \simeq 1\ or\ 2\%$.

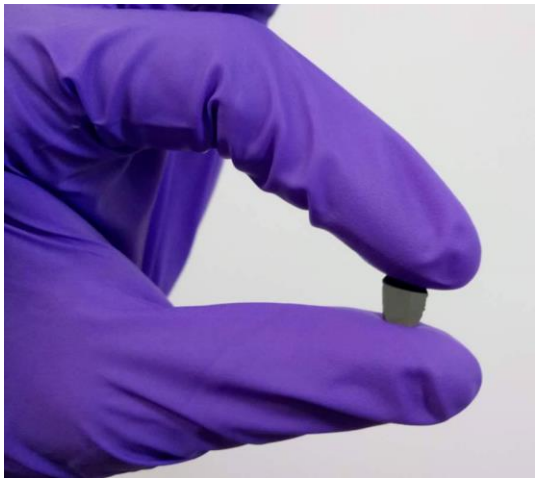

Figure 2-6: Bulk UO_2 single crystal sample polished until mirror-liked finish

2.3.2 TEM crystal preparation

The crystals were first polished until mirror-liked finish and annealed as the same steps as the one prepared for the RBS/C investigation. They were then mechanically thinned from ~1 mm to 1-5µm of thickness with the tripod technique. Afterwards, the electron transparent thin foils were obtained by two different methods: (i) some thin foils were thinned down to electron transparency using the ion milling technique before the beginning of this thesis. We used these thin foils for our first scheduled *in situ* TEM experiment as they were already prepared, and (ii) the other thin foils were prepared during this thesis by using the chemical etching technique as shown in figure 2-7 [Manley 1968] in order to avoid mechanical damage as they were prepared free of deformation or strain hardening compared to ion milling thinning that may cause radiation and thermal damages inside the thin foils. In fact, we observed some black dots and defects inside the thin foils that were prepared by using ion milling technique as it will be discussed in the section 4.1.3.

The thickness of the thin foils were measured by Electron Energy Loss Spectroscopy (EELS). This method uses the energy distribution of electrons that pass through a thin sample to analyze the content of the sample, measure the thickness of the sample by recording Zero-loss peak (ZLP), the total spectrum intensity and create images with unique contrast effects .

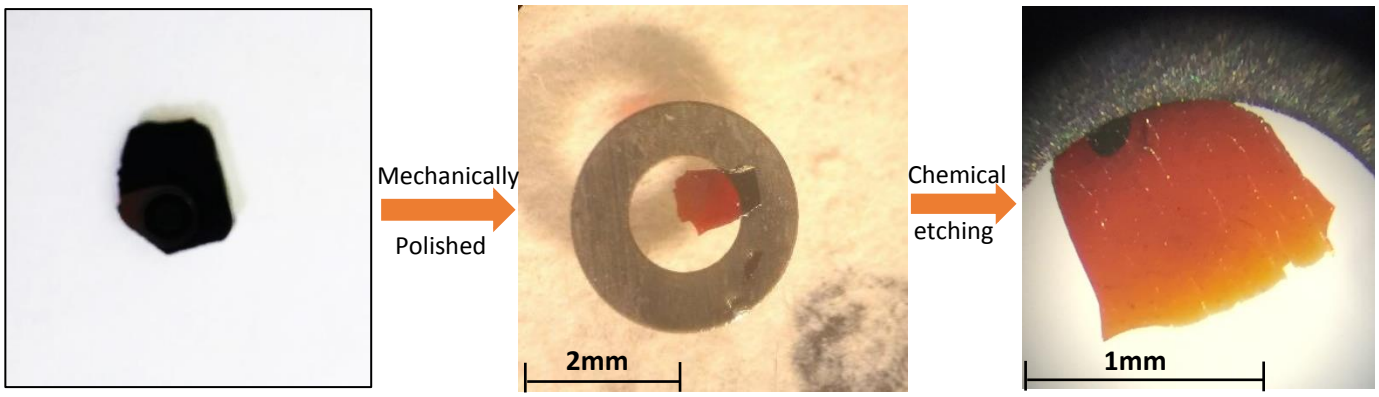

Sample polished until mirror-liked finish of 1 mm thickness

Sample mechanically thinned from ~ 1 mm to 1-5µm of thickness

Electron transparent sample after chemical etching

Figure 2-7: various steps of the TEM sample preparation using the chemical etching technique

2.4 Technique used to analyze the damage evolution

There are many existing techniques to characterize the defects created in irradiated materials. Among them are Rutherford Backscattering Spectrometry/Channelling mode (RBS/C) technique and Transmission Electron Microscopy (TEM). This chapter presents this two technique and how they can be used to evaluate the damage and defects produced in irradiated materials and to investigate the defective structure for the specific case of irradiated uranium dioxide samples. While Rutherford backscattering spectrometry in the Channelling mode can be used to identifying and quantifying the depth distribution of defects in materials, Transmission Electron Microscopy can visualize the defects and bubbles inside the irradiated materials and this provides the evolution of the radiation damage.

2.4.1 Rutherford Backscattering Spectrometry (RBS)

This technique is one of the standard ion beam analysis techniques. It provides a fully quantitative depth profile of the elemental composition of a sample surface (typically the first few micrometers) and provides a quantitative analysis of the damage versus depth inside irradiated material in the channelling mode [Thomé *et al.* 2012], [Garrido *et al.* 2005], [Thomé & Garrido 2001], [Garrido *et al.* 2008], [Thomé *et al.* 2005. It is based on the elastic collisions between the probing ions used as projectiles and the atoms of the material. These projectiles are commonly light elements, like helium or hydrogen, with energies ranging from a few hundreds of kilo electron volts to few mega electron volts. Then conditions provides almost pure Rutherford cross sections of interaction, that are eventually non defective for the probed material.
Figure 2-8 sketches the principle of the technique: an incident ion beam with certain energy E_1 is directed toward the material, and after the interaction with the atoms nuclei in case of small value of the input parameter *p* to an atom of the target, a small part of these ions are backscattered towards the detector at fixed angle θ with respect to the incident beam. Different detected energies correspond to different depth of interactions and different types of atoms of the target, allowing the identify depth and the nature of the atoms of the target at any depth X.

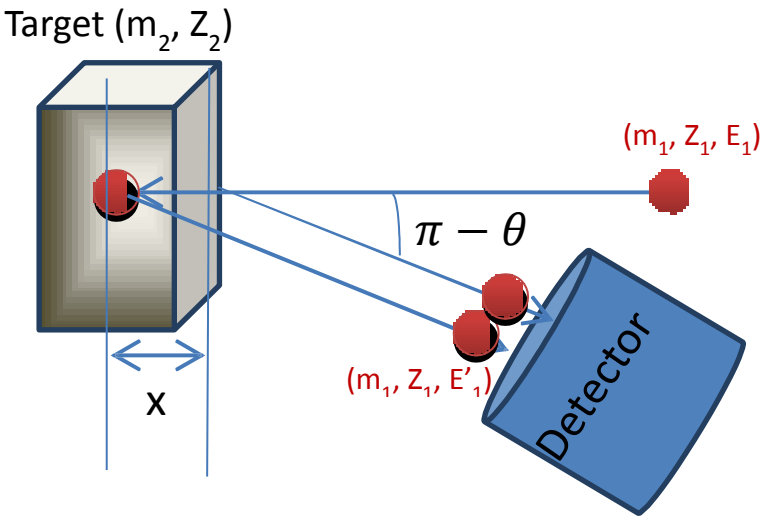

Figure 2-8: Schematic view of an RBS experiment showing the geometry of the experiment, the detector, and the sample

2.4.1.1 Scattering cross section

This technique is based on the probability of scattering. Such a probability is defined by the scattering cross section in the solid angle direction of angle θ in the laboratory frame of reference given by the following formula:

$$\frac{d\sigma}{d\Omega} = \frac{1}{16} \times \left(\frac{Z_1 Z_2 e^2}{4\pi\varepsilon_0 E_{c1}}\right)^2 \times \frac{1}{\sin^4(\theta/2)} \qquad (2-1)$$

Where: Z_1: $atomic\ number\ of\ the\ projectile$

Z_2: $atomic\ number\ of\ the\ target$

ε_0: $vacuum\ permittivity$

θ: $scattering\ angle$

E_{c1}: $kinetic\ energy\ of\ the\ projectile$

It is clear from the formula that the scattering cross section is inversely proportional to the squared energy of the projectile, and has proportional relation to the squared atomic number of the target. In the case of the light ions as projectiles, this technique is more efficient if the target atoms are heavy.

During this thesis, in RBS/C experiments, the samples were uranium dioxide single crystals, for which U is heavy atom and the helium ions were used to study the damage profile. The ions have energy 3.085 MeV during the experiment. Such a specific energy was chosen to take advantage of the elastic resonant nuclear reaction of ^{16}O ($He + O^{16} \rightarrow Ne^{20^*} \rightarrow O^{16} + He$) , which was used to enhance the yield of ^{16}O by a factor ~15, therefore the U and O signals can be obtained on the same spectrum [Thomé *et al.* 2004].

The compositional depth profile can be determined by using RBS by knowing the energy of the backscattered ions and the depth in the sample where the backscattering takes place. The energy of backscattered ion can be determine by applying the following formula, assuming the atom is located at the sample surface:

$$E_{c1}^{/} = KE_{c1} \qquad (2-2)$$

Where $E_{c1}^{/}$: the detected energy of ion that backscattered
K: Kinematic factor
E_{c1}: The initial energy of the incident ion

$$K = \frac{{M_1}^2}{(M_1 + M_2)^2} \left\{\cos\theta \pm \left[\left(\frac{M_2}{M_1}\right)^2 - \sin^2\theta\right]^{\frac{1}{2}}\right\}^2 \qquad (2-3)$$

The depth at which the backscattering takes place is determined by applying the following formula, corresponding to the well-known surface approximation:

$$E_{c1}^{/}(x) = KE_{c1} - xS \qquad (2-4)$$

$$x = \frac{KE_{c1} - E_{c1}^{/}(x)}{S} \qquad (2-5)$$

$$S = K \left(\frac{dE}{dx}\right)_{in} \frac{1}{\cos\theta_{in}} + \left(\frac{dE}{dx}\right)_{out} \frac{1}{\cos\theta_{out}} \qquad (2-6)$$

Where $E_{c1}^{/}(x)$: the detected energy of ion that backscattered at depth x
K: kinematic factor
E_{c1}: the initial energy of the incident ion
x: the depth where the backscattering takes place
S: stopping factor
$\theta_{in} = 0$
$\theta_{out} = \pi - \theta$
$\cos\theta_{in} = 1$
$\cos\theta_{out} = \cos(\pi - \theta) = -\cos\theta$

2.4.1.2 Ion Channelling

The Channelling effect (or phenomenon) applies when the incoming ions beam is aligned with a main crystallographic direction or plane of a single crystal. In this specific case a strong decrease of the interaction between the projectile and the atomic nuclei leads to a decrease of the backscattering yield, because the incoming ions are guided into channels or along planes, which decreases the probability of direct collisions - this phenomenon called ion channelling.

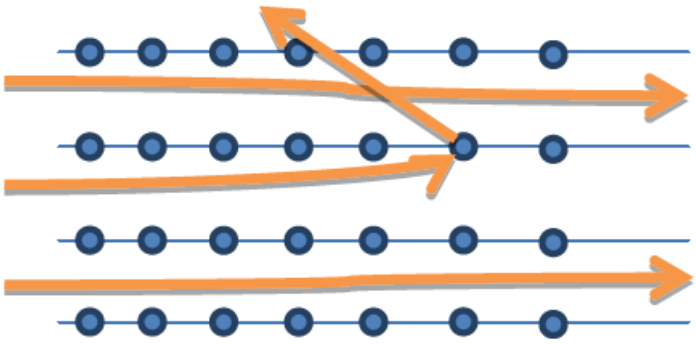

Figure 2-9: Schematic drawing of the ion channelling phenomenon

From channelling measurements, information can be obtained regarding the presence of crystalline defects inside the target since the presence of defects increases the probability of the probing ions to be backscattered. By comparing the backscattering yield in the channelling condition with in a random orientation, only a small percentage of these ions are backscattered (about a few % compared with the random spectrum). This feature is well presented in the figure 2-10, where the typical spectra recorded along a main axis and off any major crystallographic directions are presented. The figure, shows the spectra recorded in three different conditions: The blue spectrum is recorded on a virgin crystal (which was not irradiated before), the red spectrum represents the random oriented crystal, which is obtained by rotation of the single crystal with an angle of 4° with respect to the main crystallographic direction to avoid channelling effects; the black spectrum shows the aligned case recorded in a defective crystal, where a strong decrease in the yield and the presence of a the peaks of damage is clear and easy to see.

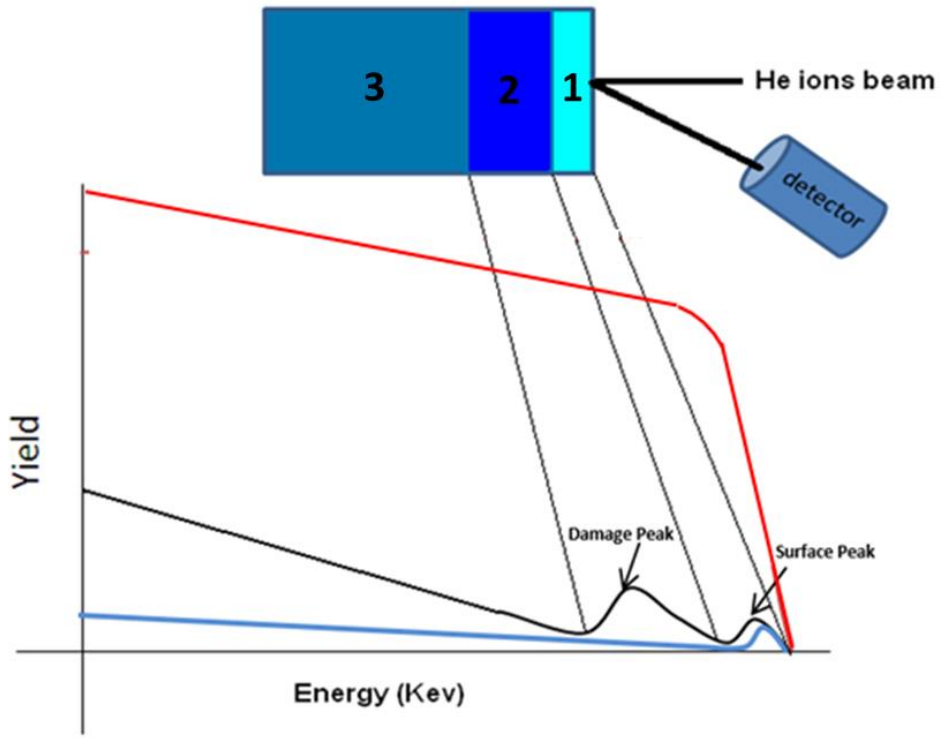

Figure 2-10: Typical RBS/channelling technique spectra recoded on a single crystal containing defects solely in region number 2 in the target. The red spectrum represents the random spectrum, the black spectrum represents the aligned recorded on a defective crystal, and the blue represents a non-defective crystal.

The Random Spectrum is obtained by rotating the sample around the incident beam by a certain angle (a few degrees). The backscattering signal is quite high as the probability for backscattering of incidents ions is high. This spectrum is equivalent to the one that would be obtained in a fully amorphized sample or a polycrystalline sample with small crystallite size. The random recorded spectra consists of: (i) a front due to the ions that are backscattered from the atoms located at the surface; and (ii) a signal at lower energy that presents the ions with a lower energy that are backscattered from the atoms at deeper depths in the crystal.

The spectra recorded on the virgin crystal when the beam is oriented along a main crystallographic orientation shows a dramatic decrease of the backscattering yield as most of the incident ions will continue their path in their channels and small fraction of ions only will backscattered. The ratio of the backscattering yield of the aligned spectra for virgin crystal over the yield of the random spectrum integrated at a given energy windows is called minimum axial yield (χ_{min}) and it is typically between 1 and 2 %.

For a defective crystal, the aligned spectrum is composed mainly from three different parts: first one is the surface peak due to the ions that are backscattered from the atoms located at the surface of the crystal over a depth of a few atomic layers; the second part is the damage peak which corresponds to the backscattered ions by the displaced atoms from their regular locations within the structure due to radiation damage; and the last part present the de-channelling contribution, which is induced by the progressive dechannelling of probing ions by the defects, electrons of the target and the thermal vibration.

2.4.2 Transmission Electron Microscopy

2.4.2.1 The principles of the Transmission Electron Microscopy

The Transmission Electron Microscopy (TEM) is a non-destructive microscopy technique where a beam of highly accelerated electrons is transmitted through a very thin sample (< 0.1 μm thick) that is hold on a goniometer, which can tilt the sample along two different orthogonal axes to investigate different planes in the sample and to obtain the diffraction pattern for the appropriate set of crystallographic planes, interacting with the sample as it passes through to form an image onto an imaging device.

This technique uses high energy electrons because they have a small wavelength (e.g. wavelength of 200 keV electron is almost 2.5 pm that is much smaller than the diameter of an atom) which let them are capable of much higher magnifications and they provide images with higher resolution than a light microscope, allowing to see much smaller objects in detail.
Louis de Broglie's equation shows that the wavelength of electrons is related to their energy, E_c , and, if we ignore relativistic effects, we can show approximately that (ignoring the inconsistency in units)

$$\lambda = \frac{h}{p} = \frac{h}{\sqrt{2mE_c}} \qquad (2-7)$$

Where h = Plank's constant (6.62607 x 10^{-34} J.s),
m: mass of an electron is 9.1×10^{-31} kg.
E_c: kinetic energy of the electron.

TEMs provide many information about the topographical, morphological, compositional crystalline, and crystallographic defects in crystalline structure.

The electron transmission microscopy consists of several instruments (see figure 2-11):

1- Illumination system:
   a- An electron gun which is the source of the electrons, the cathode, may be a heated tungsten filament or a lanthanum hexaboride (LaB_6) source.
   b- Condenser system which focuses the electron beam or board it onto the specimen.
2- Image-producing system: it consists of the objective lens, movable specimen stage, and intermediate and projector lenses, to focus the electron beam passing through the specimen to form a real, highly magnified image.
3- Imaging-recording system: it consists of a fluorescent screen for viewing and focusing the image and a digital camera for permanent records to converts the electrons image into some form of image perceptible to the human eye.

These instruments work under low pressure, typically on the order of 10^{-4} Pa to allow voltage difference between the electron gun and the ground which allow beam of the electron passing straight without an arc and to increase the mean free path of the electrons (decrease of the interactions between the electrons and gases).

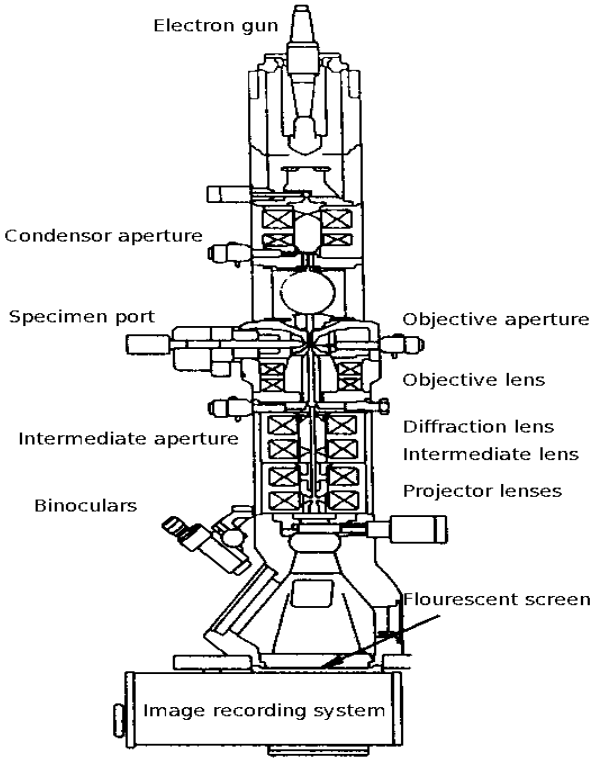

Figure 2-11: Main components of a transmission electron microscopy

The electron transmission microscopy can be operated into two different modes: imaging or diffraction. Operating into the two different modes can be performed by using the objective lens which takes the electrons emerging from the exit surface of the specimen, disperses them to create a diffraction pattern (DP) in the back-focal plane (BFP), and recombines them to form an image in the image plane as shown in figure 2-12 [Williams & Carter 2009].

In imaging mode, the image is obtained from the information that contained in the electron wave exiting from the sample. Figure 2-12 shows that all rays emerging from a point in the object (distance d_o from the lens) that are gathering by the lens converge to a point to form the image (distance d_i from the lens), while in diffraction mode, all parallel rays coming from the object are focused in the focal plane (distance from the lens) to from the diffraction pattern.

It it important to mentioned that to obtain high resolution images, this requires thinner samples and higher energies of incident electrons.

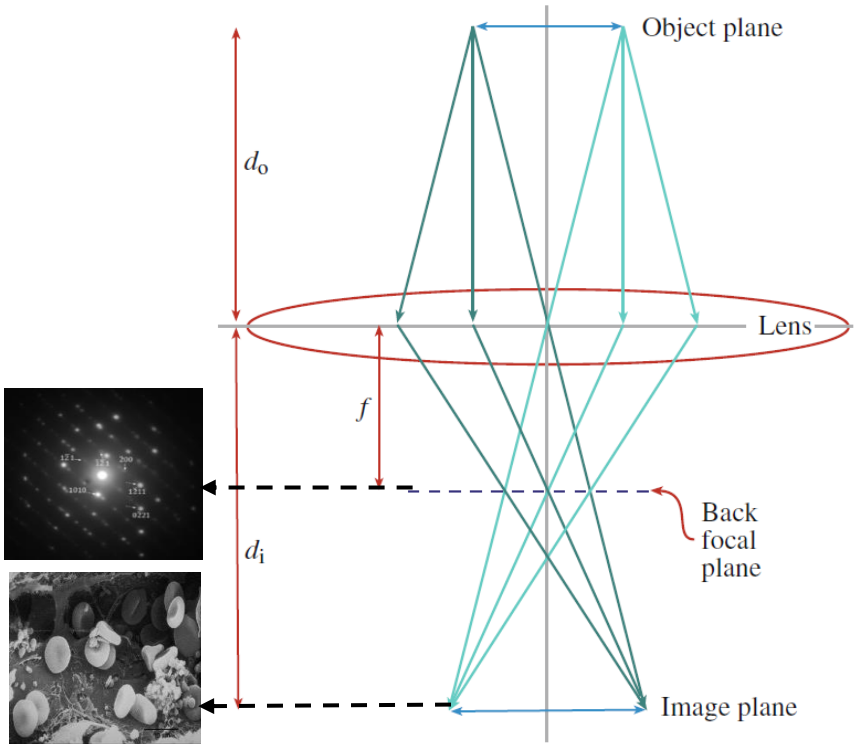

Figure 2-12: A complete ray diagram for a finite object, symmetrically positioned around the optic axis showing the two different mode of operation: imaging or diffraction.

Figure 2-13 presents a schematic that shows the two different mode of operation in details. Figure 2-13.a shows how to see the diffraction pattern: the user has to adjust the imaging-system lenses so that the back-focal plane of the objective lens acts as the object plane for the intermediate lens. Then the diffraction pattern is projected onto the viewing screen/CCD. Conversely, figure 2-13.b if someone wants to look at an image instead, you re-adjust the intermediate lens so that its object plane is the image plane of the objective lens. Then an image is projected onto the viewing screen/CCD.

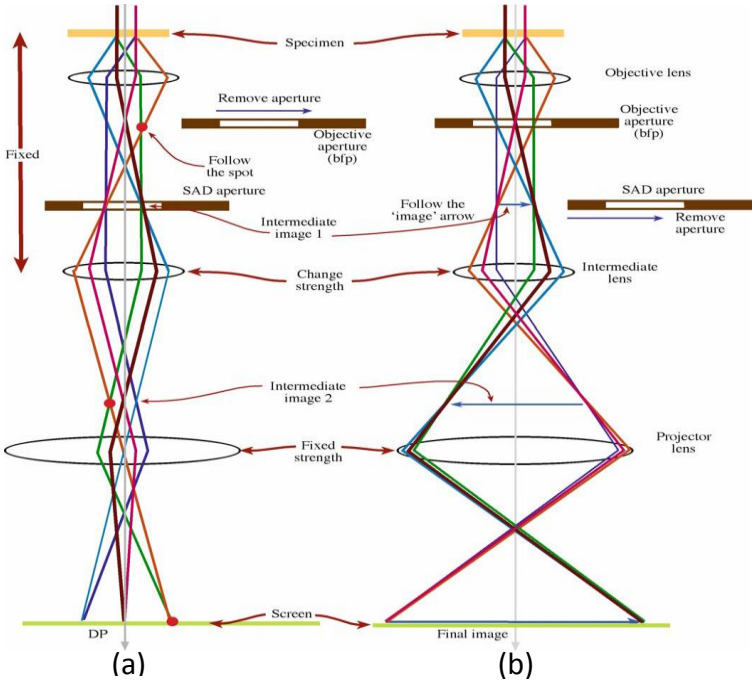

Figure 2-13: Schematic presents the two different mode of operating in TEM, where (a) in diffraction mode and (b) in imaging mode [Williams & Carter 2009].

TEM has several applications and comprises a variety of methods and fields in material science [Electron Microscopy Unit/Weizmann Institute of Science]:

- Bright Field (BF)/Dark Field (DF) image methods can provide information about size and morphology of particles, can detect crystalline areas, defects, grain boundaries and phases. Figure 2-14 shows the BF and DF images can be obtained by using the direct beam A to form a BF image while using only the electrons B that are not in the direct beam to form a DF image.

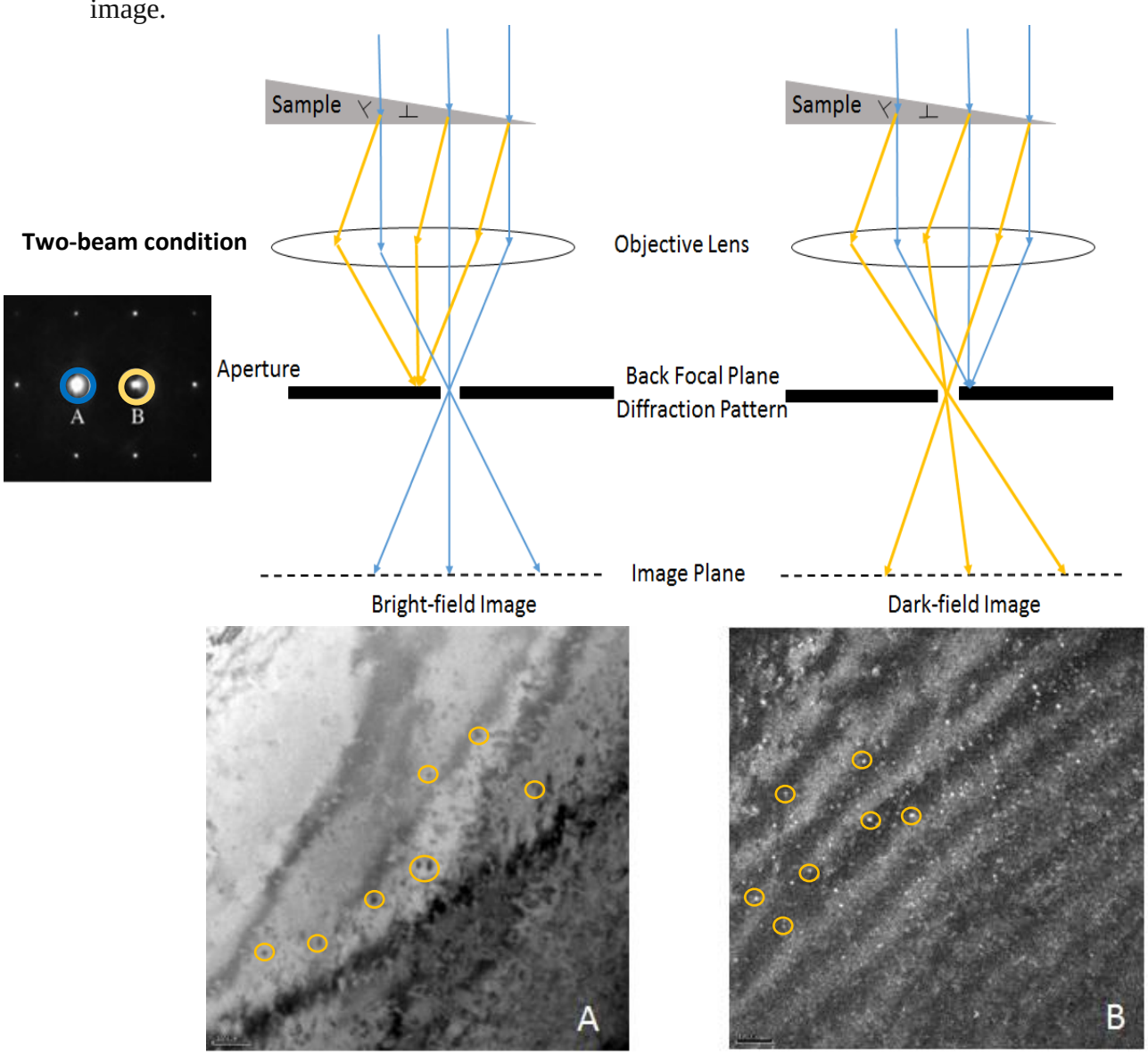

Figure 2-14: Bright-field (A) and dark-field images (B) recorded on defected UO_2 thin foil. These images allow the user to observe different types of defects created in irradiated materials. Defects are indicated by circles.

- Electron Diffraction (ED) is applied to obtain crystallographic information such as lattice parameters, crystal symmetry and orientation.

- High Resolution Transmission Electron Microscopy (HRTEM) allows lattice fringe imaging that can be directly related to the structure and visualization of defects and interfaces at atomic scale resolution. It allows one to obtain image of crystallographic structure at an atomic scale. In imaging mode, the contrast arises by modifying the phase of the incoming electron wave, and not the amplitude as in the conventional microscopy mode.

TEM can be used with *in situ* ion irradiation that allows a direct observation of the radiation damage and changes that occur in the microstructure of materials on the nanoscale while they are under irradiation. The insights which can be obtained by direction observations of *in-situ* TEM experiments are: defects/bubbles formation, motion, growth, coalescences, recovery and destruction, diffusion, effects induced by ionization or collision cascades, grain size changes, grain growth and shrinkage, compositional changes, mechanical and structural changes, and phase changes.

2.4.2.2 Plane-view and cross section TEM observation

The observations can be obtained by using two different geometries to analyze irradiated samples:

- Plan view: it provides images of the surface or at a certain depth that is not always straightforward to obtain.

- Cross section: to observe the effects of radiation in depth by observing the location of defects inside the irradiated material.

Regarding TEM sample preparation, figure 2-15 shows the two different methods of sample perpetration corresponds to the two different modes of observation. For the plan view samples is requires mechanical polishing back-thinning by using tripod until the edge of the sample is electron transparent; the last step of transparency can be completed if required by chemical etching or ion thinning at low incident angle which gives a thin high quality zone over a large width. While the preparation for the cross section samples is more complicated in cutting the sample into small slices and gluing them together surface against surface to form a block of material, where the interface of interest lies in the middle of the piece, then the steps are the same as for the sample for plane view with more difficulties to keep the area of interest while doing polishing.

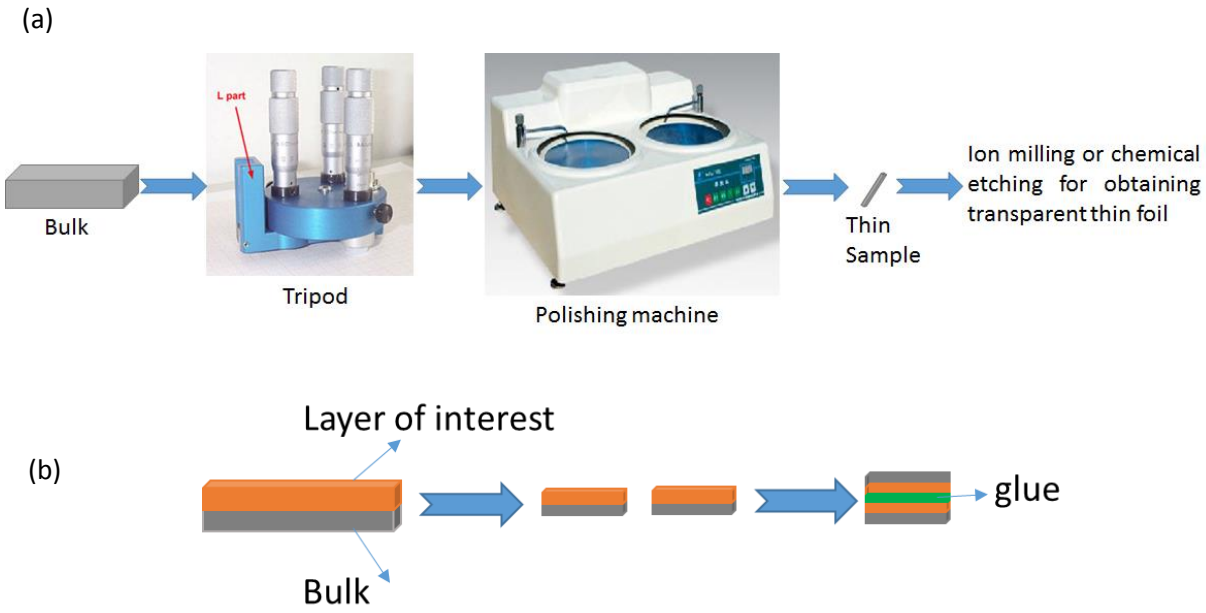

Figure 2-15: Sample preparation for plane-view TEM observation (a) and cross section (b)

2.5 Computer tool simulations

Computer simulation program has been used to interpret the experimental results of ion channelling technique which used to quantify the structural defects located on the surface layer of a crystalline material over a typical depth of a few μm. The experimental results of ion channelling technique are usually represent the backscattering spectra measured across a major axis or along planes or the recoding of angular scans. Interpretation of these data is not straightforward. There are many analytical methods to analyze the spectra and simplified the channelling data analysis but the accuracy is not perfect.
A two-beam approximation can be performed to analyze the channelling data and the results provide a quantitative measurement of defects versus depth, assuming there are randomly displaced atoms. This approach was proposed by Bøgh in 1968 [Bøgh 1968]. Therefore, Suitable monte-Carlo simulations performed on a computer provides a convenient way to analyze the data in more accurate way and considering various type of defects [Barrett 1990], [Turos *et al.* 2014], [Turos *et al.* 2010], [Jagielski et *al.* 2012], [Smulders & Boerma 1987], [Garrido *et al.* 2006]. In this work, Monte-Carlo simulation method performed that called McChasy developed by Lech Nowicki at the Andrzej Soltan Institute for Nuclear Studies in Warsaw, Poland, as a tool to analyze the channelling data.

2.5.1 Principles of Monte-Carlo channelling simulations

Monte-Carlo simulation method is a computational technique of calculating integrals by sampling probability distributions. In case of ion-crystal interaction the sampling is made at atomic plane by the calculation of the probability of close encounter.
In the code, the calculation takes into account the distance between the ion and the atom (the impact parameter) and when this distance becomes small enough the nuclear reaction (scattering with the nucleus) around its site occurs and the ion is backscattered [Nowicki *et al.* 2005].

The distribution probability of a given atom has Gaussian-like distribution around the atomic location (atom from the lattice or interstitial) due to the atomic thermal vibrations [Willis & Prior 1975].
In Cartesian coordinates (x, y, z) where the z axis coincides with the channelling axis, the probability P_i^j of close encounter at an atomic plane j is given by [Barrett 1971]:

$$P_i^j = \frac{\cos\psi_i^j}{2\pi N u_A^2} \exp\left[- \frac{\left(x_i^j - x_A^j\right)^2 + \left(y_i^j - y_A^j\right)^2}{2u_A^2} \right] \qquad (2-8)$$

Where:
i: Number acts of sampling.
x_i^j ,y_i^j: the projectile impact point at the plane j during the sampling i.
x_A^j ,y_A^j: equilibrium location of target atom A at the plane.
u_A: dimensional root-mean-square amplitude of the thermal vibration for the A atom.
ψ_i^j: angle between projectile velocity vector and the channelling axis.
N: number of samplings.

A statistical estimation of number of backscattering events corresponding to the [z; z + dz] depth interval can be found by the following formula:

$$K^A(z) = \sigma^A N_{tot} \Omega \sum_j \sum_{i=1}^{N} P_i^j \qquad (2-9)$$

Where:
σ^A: Rutherford backscattering cross section.
N_{tot}: total number of projectiles.
Ω: solid angle of detection.
N: number of samplings

The summation is made for all the acts of sampling and all atomic planes in the indicated depth interval. The "depth-spectrum" $K^A(z)$ that is the chain of K^A values calculated for subsequent depth intervals can be transformed to the energy spectrum by taking into account the energy loss of projectiles on the entrance and exist paths. Such spectra, obtained for each element in the crystal, are finally added together to the final backscattering spectrum. If the sampling is done uniformly at each atomic plane in the crystal the random spectrum is produced. The relative accuracy of the results in this code is proportional to the $1/\sqrt{N}$ and this can be reduced by increasing N.

2.5.2 McChasy simulation code

McChasy (Monte-Carlo Channelling SYmulation) is a Monte-Carlo simulation code used to calculate the ion-crystal interaction in the channelling mode to evaluate quantitatively the amount of defects present in different crystal structure including the fluorite-type structure such UO_2.

The analysis in this code is performed in several steps: The first step is to: (i) define the crystal which is going to investigate (structure, chemical composition, thermal vibration of each component and different parameters related to the atoms of the crystal), (ii) identify the ion beam parameters (nature of the ions, energy, and beam divergence), (iii) the geometry for RBS/C measurement (scattering geometry, solid angle of the detector), and (iv) the parameters of the electronics of the experiment (preamplifier, amplifier, detector and the energy/channel converting factors). In a second step, the sample divided into thin layers of a given thickness and we can introduce inside each layer a certain fraction of defects. An example of a McChasy input file that has been used for this thesis is shown in Appendix C. After running the code a simulated spectra is obtained for the RBS spectra for the backscatting ions and their yield correspond to certain energy. The final step is to normalize the obtained spectra for comparison with the experimental data. Typically, one simulation with good statistics (N_{tot}. 50000) takes 90 mins.

In this code, the ZLB potential [ZIEGLER *et al.* 1985], [Nowicki *et al.* 2005] is used to include the electron screening of the ion-atom interaction. The importance of this code that it enables the user to define substitutions of atoms in the structure. This option becomes very important when the crystal is heavily irradiated since or a high concentration of ions that modify the composition of the structure and eventually the trajectories of probing ions.
By applying such a code, information about the distribution of the defects inside the matter is obtained and the amount of damage can be evaluated at any depth. The code can take into account various classes of defects such point defects, defects clusters, dislocations and polygonisation of the crystal.

References

[Barrett 1971]
John H. Barrett, Monte Carlo Channelling Calculations. Phys. Rev. B, 3:1527-1547 Mar 1971.

[Barrett 1990]
John H. Barrett, Methods of channelling simulation. Phys. Rev. B44 :367-372, 1990.

[Bøgh 1968]
E. Bøgh. Defect studies in crystals by means of channelling. Canadian Journal of Physics, 46(6):653–662, 1968.

[Electron Microscopy Unit/Weizmann Institute of Science]
https://www.weizmann.ac.il/Chemical_Research_Support/EM_Unit/Home

[Garrido *et al.* 2005]
F. Garrido, Application of ion beams in materials science of radioactive waste forms: focus on the performance of spent nuclear fuel. Nuclear instruments and methods in Physics Resreach B 240:250-257, 2005.

[Garrido *et al.* 2006]
F. Garrido, L. Nowicki and L. Thomé. Channelling investigation of the crystalline structure of U_4O_{9-y}. PHYSICAL REVIEW B 74:184114, 2006.

[Jagielski *et al.* 2012]
J. Jagielski, A. Turos, L. Nowicki, P. Jozwik, S. Shutthanandan, Y. Zhang , N. Sathish, L. Thomé, A. Stonert, I. Jozwik-Biala. Monte Carlo simulations of channelling spectra recorded for samples containing complex defects. Phys. Rev. B273:91-94, 2012.

[JANNuS-Orsay/SCALP]
The JANNuS-Orsay/SCALP facility consists of a Transmission Electron Microscope coupled to two ion accelerators, IRMA and ARAMIS, **[website].** Available here: http://www-csnsm.in2p3.fr/SCALP

[Manley 1968]
A.J. Manley. The Thinning of Sintered Uranium Dioxide to Electron Transparency by Chemical-polishing. Journal of Nuclear Materials, 15(1):143-145, 1965.

[Nowicki *et al.* 2005]
Lech Nowicki, Andrzej Turos, Renata Ratajczak, Anna Stonert, Frederico Garrido. Modern analysis of ion channelling data by Monte Carlo simulations. Nuclear Instruments and Methods in Physics Research B 240:277–282, 2005.

[Smulders & Boerma 1987]
P. Smulders and D. Boerma. Computer simulation of channelling in single crystals. Phys. Rev. B29:471-489, 1987.

[Soullard *et al.* 1985]
J. Soullard. High voltage electron microscope observations of UO2. Journal of Nuclear Materials, 135(2 - 3):190 – 196, 1985.

[Thomé & Garrido 2001]
L. Thomé, F. Garrido, Application of ion beams to nuclear waste issues: evolution of nuclear ceramics. Vacuum 63:619-626, 2001.

[Thomé *et al.* 2004]
L. Thomé *et al.*, On the use of the ^{16}O (^{4}He, ^{4}He)^{16}O resonanace for the evolution of radiation damage in oxides. Nuclear instruments and methods in Physics Resreach B 219-220:99-104, 2004.

[Thomé *et al.* 2005]
L. Thomé *et al.*, Use of ion channelling for the study of the damage induced in ceramics by ion irradiation. Vacuum 78:401-408, 2005.

[Thomé *et al.* 2012]
L. Thomé et al., Use of channelling for the study of radiation effects in nuclear materials. Nuclear instruments and methods in Physics Resreach B 290:6-12, 2012.

[Turos *et al.* 2010]
A. Turos, L. Nowicki, A. Stonert, K. Pagowska, J. Jagielski, A. Muecklich. Monte Carlo simulations of ion channelling in crystals containing extended defects. Phys. Rev. B268:1718-1722, 2010.

[Turos *et al.* 2014]
A. Turos, P. Jozwik, L. Nowicki, N. Sathish. Ion channelling study of defects in compound crystals using Monte Carlo simulations. Phys. Rev. B332:50-55, 2014.

[Williams & Carter 2009]
Transmission Electron Microscopy, A Textbook for Materials Science. David B. Williams, C. Barry Carter. Springer Science & Business Media, Aug 5, 2009.

[Willis & Prior 1975]
B. T. M. Willis, A. W. Prior, Thermal vibrations in crystallography, Cambridge University Press, Cambridge, 1975.

[ZIEGLER *et al.* 1985]
J.F. ZIEGLER, J.P. Biersack, U. Littmark. The Stopping and Range of Ions in Soilds, Pergamon, New York, 1985.

Chapter 3

Damage evolution in urania by using *in situ* ion channelling coupled to ion irradiation

This chapter presents the Rutherford Backscattering in Channelling geometry (RBS/C) experiments that were performed during this thesis. The first section shows the channelling spectra of *in situ* RBS/C experiments recorded on UO_2 single crystals implanted at 773 K with either the noble gas xenon (Xe) or with lanthanum (La) ions. Implantation with La is selected here as an illustrative example to explain the methodology that was used.

lanthanum ions were used to study the effect of soluble ions into the uranium dioxide fluorite-type structure and to compare it with implanting uranium dioxide with a noble gas Xe, which is insoluble [Brillant *et al*. 2011], [IMOTO 1986]. The main idea aims to study the effect of different impurities with different chemical contribution on UO_2, while the masses and atomic numbers of both ions are very close.

The second section shows the analysis of RBS/C spectra for crystals implanted with both ions by using the two-defect model. The description of the model and the effect of each class of defects on the simulated spectra is presented. The damage evolution extracted from the simulation is finally discussed.

3.1 *In situ* Rutherford Backscattering in channelling geometry (RBS/C) experiments coupled to ion irradiation

Investigation for reproducing and studying the various stages of the formation of the high burnup structure have been performed by using 500 keV La ions or 470 keV Xe ions accelerated to bombard uranium dioxide single crystals at 773 K. *In situ* RBS/C were performed using the IRMA/ARAMIS connection for the ion implantation and ion beam analysis, respectively. The energy for both ions Xe and La were chosen to provide almost the same values of projectile range and range straggling. Crystals were alternatively implanted at 773 K and characterized by RBS/C at almost room temperature (the crystal alignment procedure was started while the temperature was lower than ~ 320 K).

Table 3-1: Experimental conditions used for RBS/C experiments. Range and range straggling were calculated by using the SRIM code.

Ions implanted	Z	Mass(u)	Energy (KeV)	Range R_p(*nm*)	Range straggling ΔRp (*nm*)	Fluence range (cm^{-2})	Mean flux ($cm^{-2}.s^{-1}$)	Fraction of implanted ions at max (at. %)
$^{131}Xe^{3+}$	54	130.905	470	83	39	From $5x10^{13}$ up to $4x10^{16}$	$1.2x10^{11}$	~ 5%
$^{139}La^{3+}$	57	138.906	500	86	41	From $5x10^{13}$ up to $3x10^{16}$	1.2×10^{12}	~ 4%

3.1.1 Irradiation with lanthanum ions

Typical RBS/C random and axial spectra obtained by using a 3085 keV ^{4}He probing ion beam on a high quality virgin UO_2 single crystal are presented in figure 3-1. The random recorded spectra consists of: (i) an uranium front at 2887 keV due to the He ions that are backscattered from the U atoms at the surface of the crystal; (ii) an uranium signal at lower energy that presents the He ions with a lower energy that are backscattered from the U atoms at deeper depths in the crystal (depth up to 2 µm from the surface); (iii) a resonant peak (at about 1045 keV) that is the consequence of the elastic resonant scattering $^{16}O(^{4}He,^{4}He)^{16}O$ at 3038 keV of the He ions with the oxygen, which enhance the backscatting yield on oxygen sub-lattice at a typical depth ranging from between 50 to 200 nm [Thomé *et al*. 2004].

Regarding the axial recorded spectra, it consists of: (i) a surface peak (at about 2887 keV) due to the He ions that are backscattered from the U atoms at the surface of the crystal; (ii) a dechannelling part (the signal at an energy below 2887 keV); (iii) a resonant peak (at about 1045 keV).

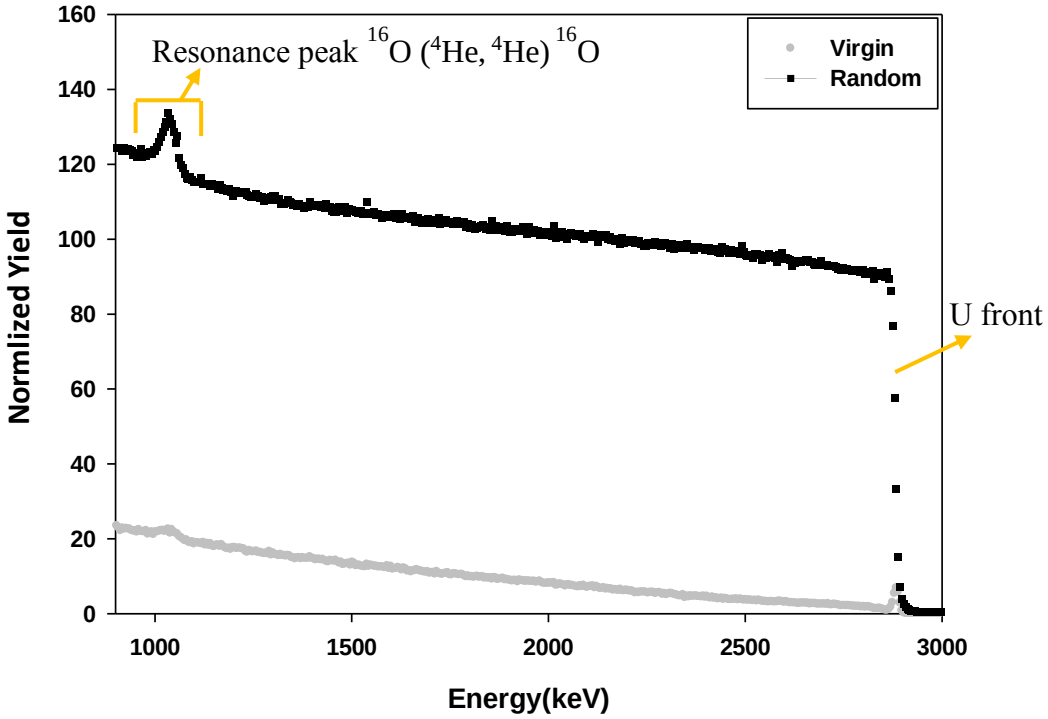

Figure 3-1: RBS spectra recorded on a defect-free <100> - oriented UO_2 single crystal in random (squares black symbols) and aligned directions (grey circles). The ^{4}He beam energy is 3085 keV. The backscattering angle is 165°.

The RBS/C spectrum recorded in the axial direction reveal a low backscattering yield due to the channelling effect and demonstrate the good crystallinity of the single crystal (χ_{min} < 2%, in good agreement with the theoretical value derived from Monte Carlo simulation 1.5%).

Figures 3-2 and 3-3 present the random and axial channelling spectra recorded on crystals implanted with 500 keV La ions at 773 K at increasing ion fluence. Spectra strongly differ from the spectra recorded on the virgin crystal: they show a higher axial yield compared to the virgin level and the existence of a new peak at an energy ranging from ~ 2600 to 2887 keV (known as the "damage peak"), due to the direct backscattering of He ions on U atoms displaced from their regular lattice sites in the channels, superimposed on a dechannelling component. Figures 3-2 and 3-3 part (a) and (b) display the axial channelling spectra recorded in the low fluence range ($\Phi \leq 1.3 \times 10^{15} cm^{-2}$) and in the high fluence range ($\Phi \geq 1.3 \times 10^{15} cm^{-2}$), respectively. The RBS spectra were recorded after

each implantation step after cooling the sample below 300 K (the crystal alignment was started while the temperature was lower than ~ 320 K).

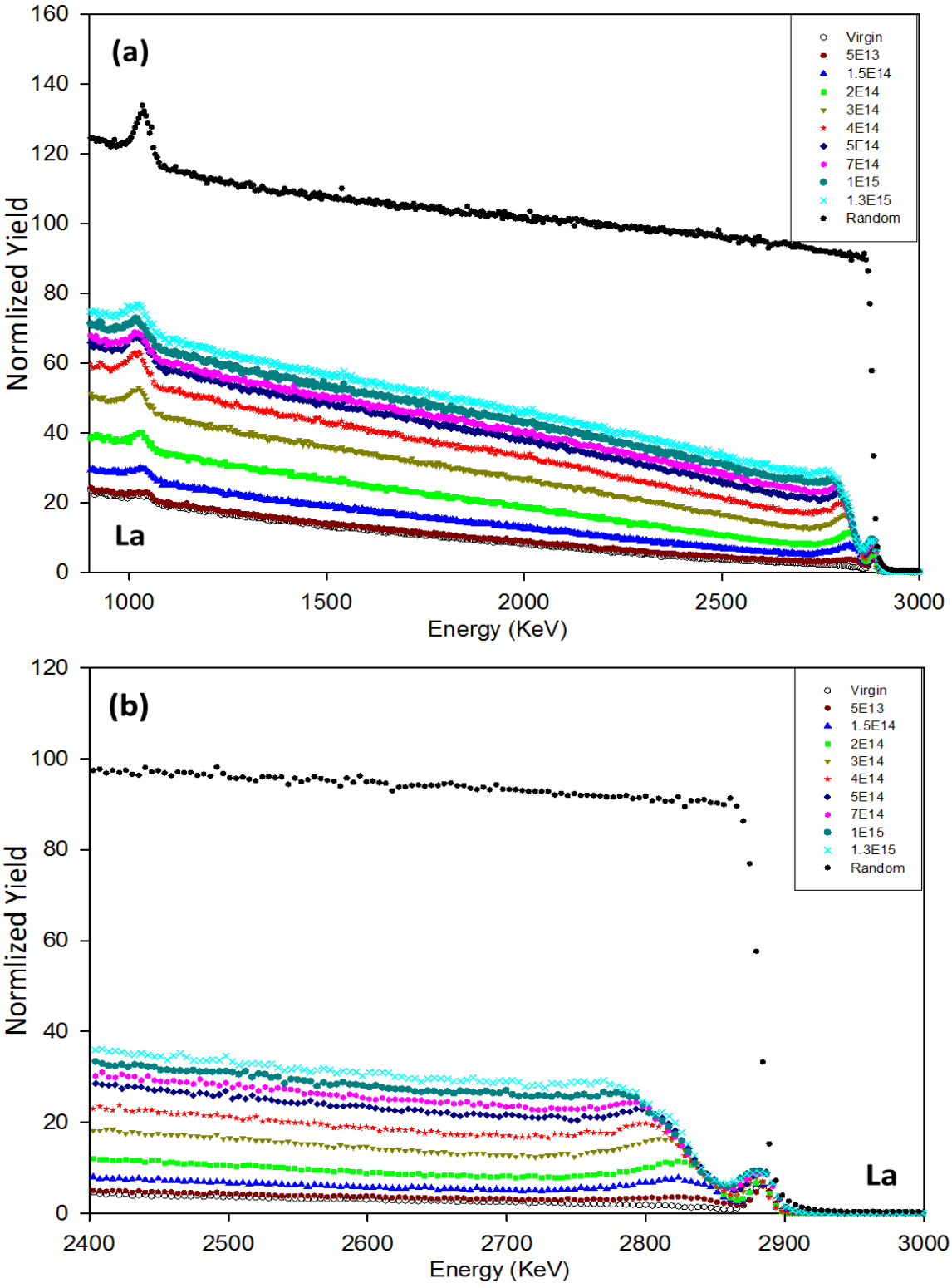

Figure 3-2: Random and aligned RBS channelling spectra (a) and high energy part of channelling spectra (b) recorded on a UO_2 crystal implanted sequentially with La ions at low fluence**.** Fluences are measured in unit of cm^{-2}. Implantation temperature is 773 K. The random spectrum was recorded at a fluence $\Phi = 3x10^{14}$ cm^{-2} (black circles). Experimental channelling spectra are plotted in symbols for fluences of $\Phi = 5x10^{13}$ cm^{-2} (dark red circles), $1.5x10^{14}$ cm^{-2} (blue triangles up), $2x10^{14}$ cm^{-2} (green squares), $3x10^{14}$ cm^{-2} (dark yellow triangles down), $4x10^{14}$ cm^{-2} (red stars), $5x10^{14}$ cm^{-2} (dark blue diamonds), $7x10^{14}$ cm^{-2} (pink circles),$1x10^{15}$ cm^{-2} (dark cyan circles), $1.3x10^{15}$ cm^{-2} (cyan crosses).

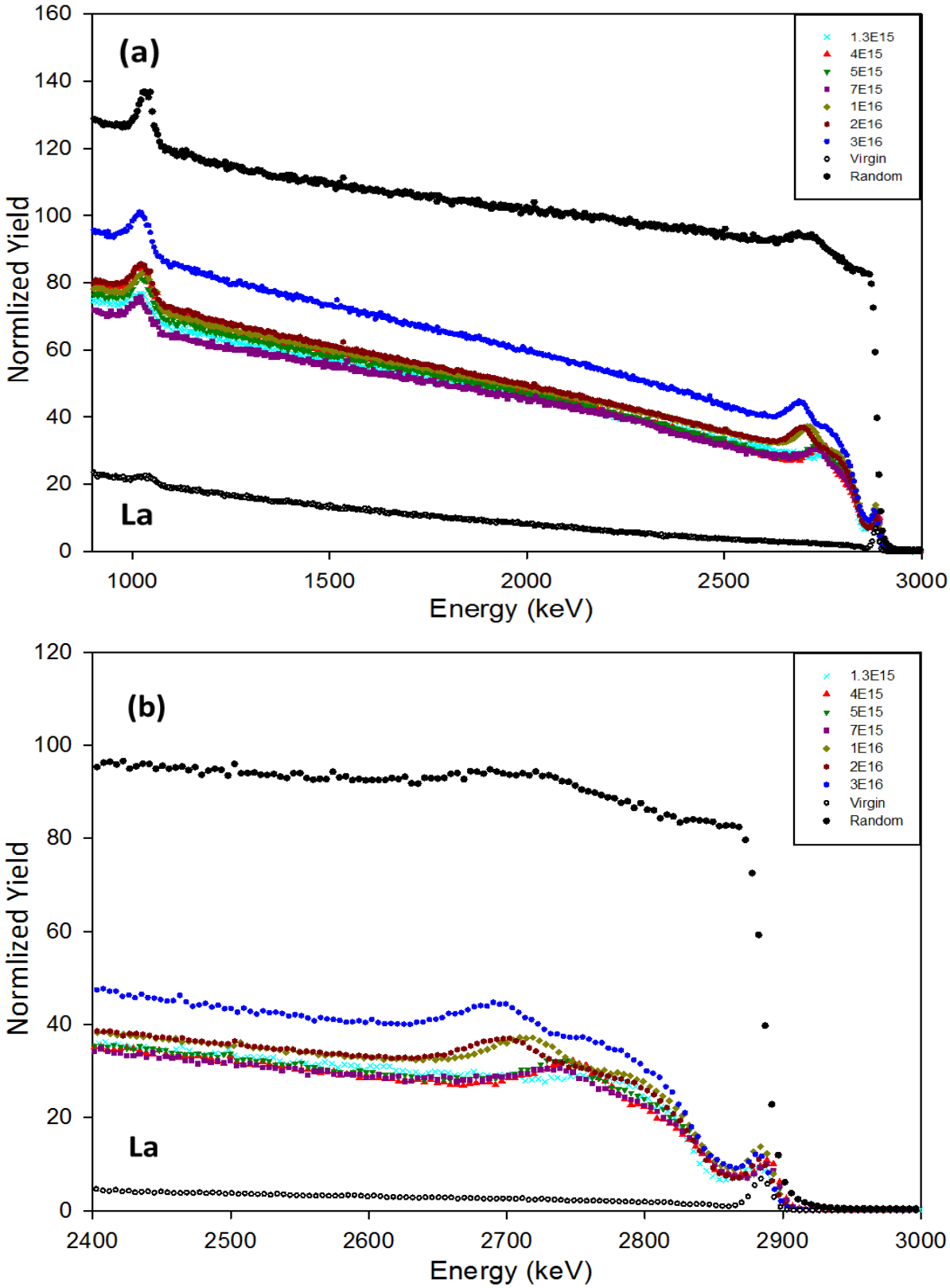

Figure 3-3: Random and aligned RBS channelling spectra (a) and high energy part of channelling spectra (b) recorded on a UO_2 crystal implanted sequentially with La ions at high fluence. Fluences are measured in unit of cm^{-2}. Implantation temperature is 773 K. The random spectrum was recorded at a fluence $\Phi = 2x10^{16}$ cm^{-2} (black circles). Experimental channelling spectra are plotted in symbols for fluences of $\Phi = 1.3x10^{15}$ cm^{-2} (cyan "x"), $4x10^{15}$ cm^{-2} (red triangles up), $5x10^{15}$ cm^{-2} (green triangles down), $7x10^{15}$ cm^{-2} (dark pink squares), $1x10^{16}$ cm^{-2} (dark yellow diamonds), $2x10^{16}$ cm^{-2} (dark red circles), $3x10^{16}$ cm^{-2} (blue circles).

The random spectrum was recorded at high fluence, figure 3-3 shows a different shape with respect to the one registered on a crystal implanted at low fluence, as a consequence of the high concentration of the impurities implanted in the solid. Two different features can be observed by comparing the random spectrum at low and high fluence. The first one is located near the surface and it shows a lower backscattering yield on U at high fluence compared to the low fluence. The second feature is the appearance of an extra peak, whose front locates at about ~ 2755 keV. Such a peak corresponds to the backscattering of He ions on La atoms incorporated by the implantation process. This feature does not appear for the low fluence because the backscattering yield on La is small compared to that of U since $\sigma_U/\sigma_{La} = (Z_U/Z_{La})^2 = (92/57)^2$= 2.6, and the La concentration is small.

Regarding the axial spectra, the damage peak increases in both width and amplitude with increasing the fluence; due to the increase of the fraction of defects and the extension towards deeper depth as a function of the fluence of the defective zone, the dechannelling contribution, as measured in the undamaged zone, increases as well, as a consequence of the defects created in the irradiated zone.

Some differences between the RBS/C spectra recorded at low and high fluence ranges are clearly seen. At low fluence, the high-energy side of the damage peak, close to the surface located at about 2860 keV, remains almost constant and it progressively extends at larger depth when fluence increases. Conversely, at high fluence, a different shape is evidenced that is characterized by an increase of damage peak in the surface region and the presence of a new peak at ~ 2700 keV. It is also observed that at low fluence range shows a rapid increase of the dechannelling yield with increasing the fluence, while at high fluence the level of the signal remains essentially constant within this range of fluence as shown in figure 3-3, except for the highest irradiated fluence $\Phi = 3x10^{16}$ cm^{-2}.

3.1.2 Irradiation with xenon ions

A similar *in situ* RBS/C experiments were performed on the IRMA/ARAMIS facility by using a 3085 keV ^{4}He beam on high quality UO_2 single crystal implanted with 470 keV Xe ions at 773 K. Figures 3-4 and 3-5 show the random and the axial channelling spectra that were recorded for implanted UO_2 single crystal with Xe ions at different fluences. The same division between low fluence and high fluence range as for La implantations is used here. In a similar way to what was observed for La implanted crystals, the random spectrum recorded at high fluence, figures 3-4 and 3-5 show a different shape, as a consequence of high concentration of Xe ions implanted in the structure. The peak that corresponds to backscattering of He ions on Xe atoms is visible for high implantation fluence and the front of this peak locates at about ~ 2737 keV. Both ions, regardless the nature of the ion, show a similar effect on the random spectrum when the crystals are implanted at high fluence. Such a feature is not surprising since the characteristic of the two implanted ions are very similar.

Regarding the axial spectrum, in the low fluence range, the damage peak created due to the implantation of Xe ions increases in both width and amplitude with increasing the fluence, as what was obtained for La ions. However a new feature close to the surface for the high fluence spectra is seen: the backscattering yield of the He ions increases dramatically compared to the low fluence range and the yield is far higher for Xe implanted crystal compared to the La implanted crystal. The signal of the axial spectra increases with increasing the fluence and the dechannelling signal recorded from 1000 to 2600 keV for both low and high fluence ranges shows a similar continuous increase in yield, while decreasing the energy of backscattering He ions for all the fluences, as shown in figures 3-4 and 3-5.

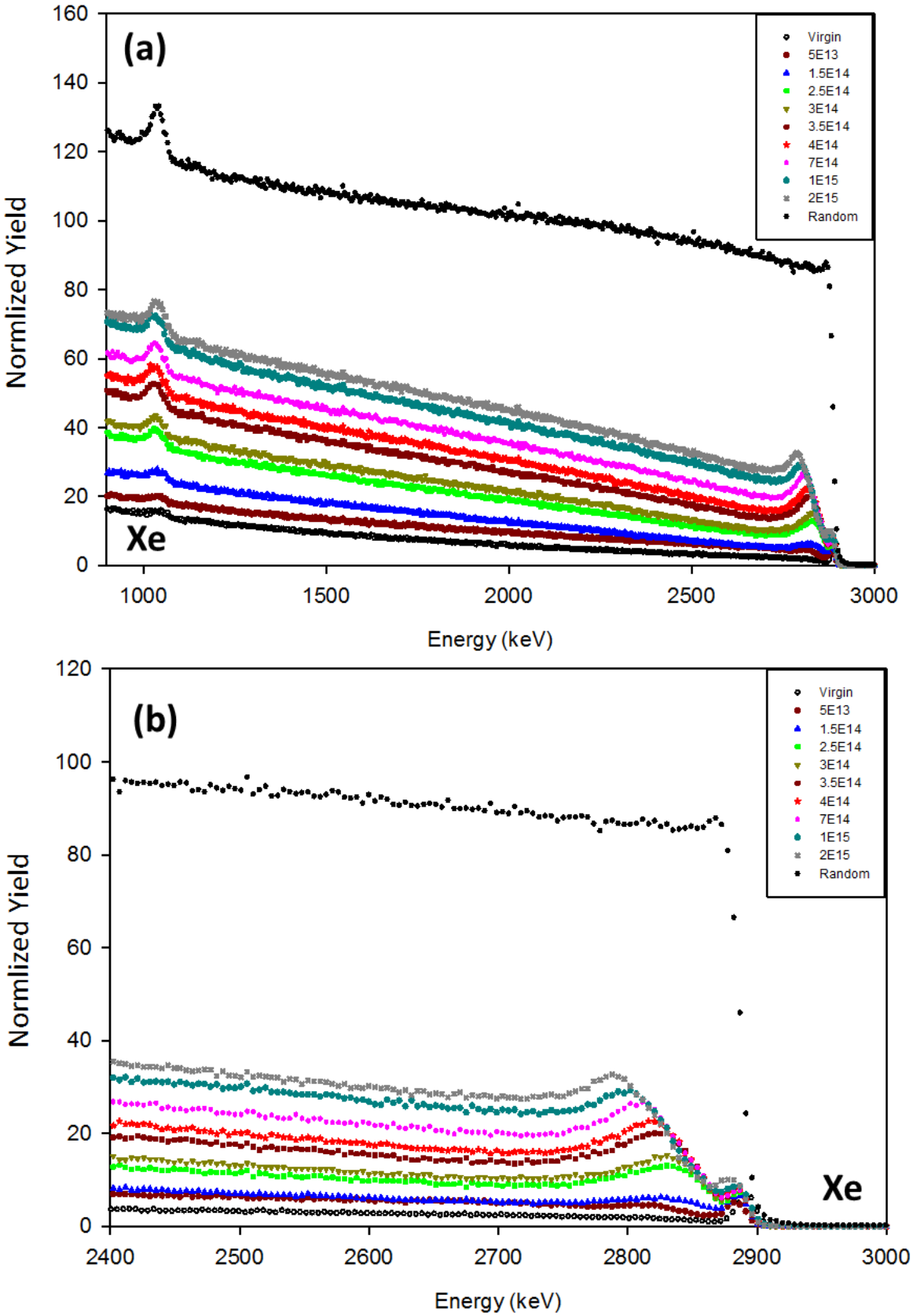

Figure 3-4: Random and aligned RBS channelling spectra (a) and high energy part of channelling spectra (b) recorded on a UO_2 crystal implanted sequentially with Xe ions at low fluence. Fluences are measured in unit of cm^{-2}. Implantation temperature is 773 K. The random spectrum was recorded at a fluence $\Phi = 2.5x10^{14}cm^{-2}$ (black circles). Experimental channelling spectra are plotted in symbols for fluences of $\Phi = 5x10^{13}$ cm^{-2} (dark red circles), $1.5x10^{14}$ cm^{-2} (blue triangles up), $2.5x10^{14}$ cm^{-2} (green squares), $3x10^{14}$ cm^{-2} (dark yellow triangles down), $4x10^{14}$ cm^{-2} (red stars), $7x10^{14}$ cm^{-2} (pink circles), $1x10^{15}$ cm^{-2} (dark cyan circles), $2x10^{15}$ cm^{-2} (dark grey crosses).

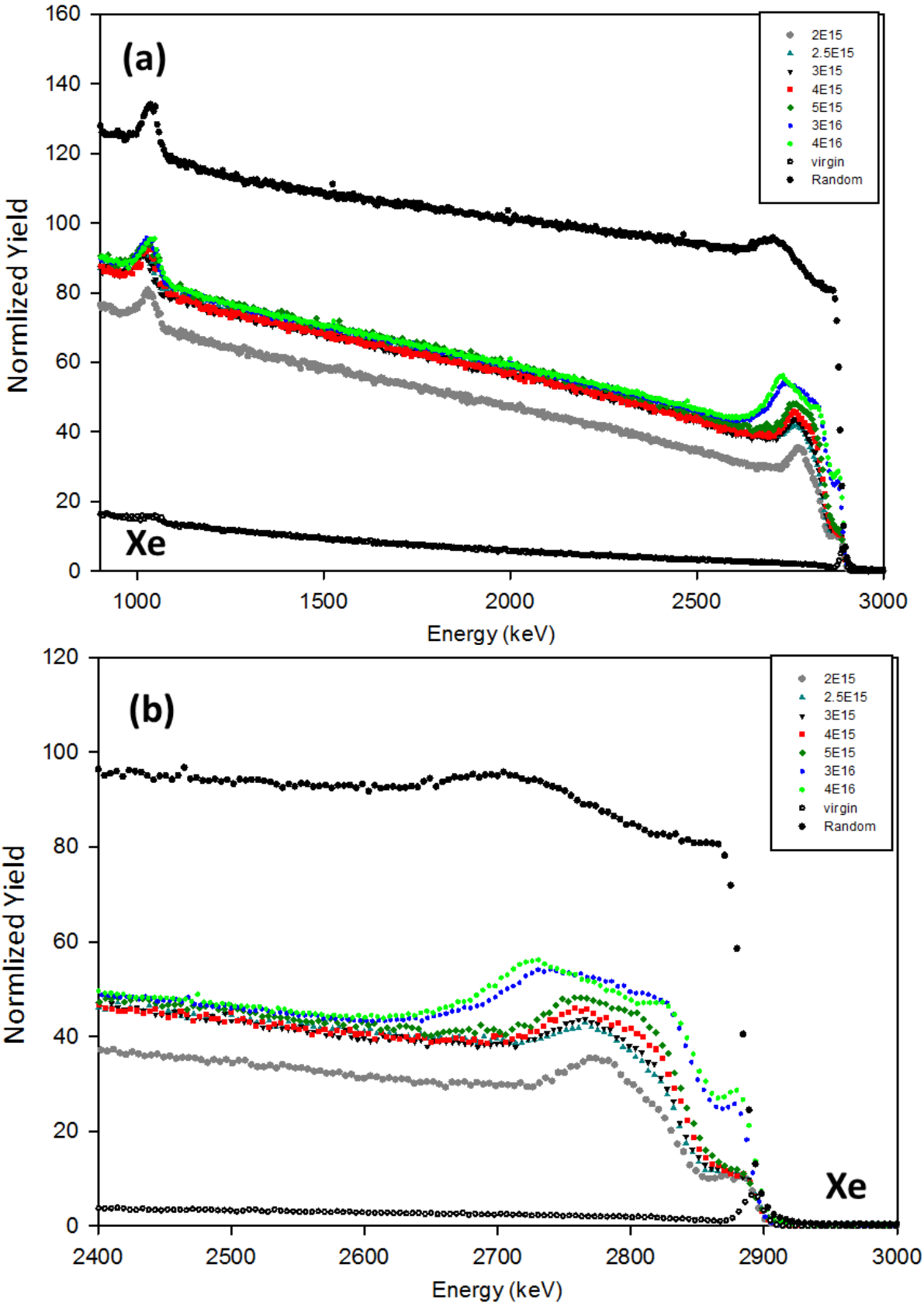

Figure 3-5: Random and aligned RBS channelling spectra (a) and high energy part of channelling spectra (b) recorded on a UO_2 crystal implanted sequentially with Xe ions at low fluence. Fluences are measured in unit of cm^{-2}. Implantation temperature is 773 K. The random spectrum was recorded at a fluence $\Phi = 3x10^{16}$ cm^{-2} (black circles). Experimental channelling spectra are plotted in symbols for fluences of $\Phi = 2x10^{15}$ cm^{-2} (dark grey circles), $2.5x10^{15}$ cm^{-2} (dark cyan triangles up), $3x10^{15}$ cm^{-2} (black triangles down), $4x10^{15}$ cm^{-2} (red squares), $5x10^{15}$ cm^{-2} (green diamonds), $3x10^{16}$ cm^{-2} (blue circles), $4x10^{16}$ cm^{-2} (green circles).

To summarize the RBS/C results, the implantation of single crystal UO_2 with low energy insoluble noble gas Xe and the soluble La ions led to defect creation in UO_2. The radiation damage depends mainly on the ion fluence and also depends on the nature of the ions. The damage created by implanting insoluble ions differs from the one created by implanting soluble ions.

Monte Carlo simulation code was used to fit the experimental data and to provide a quantitative amount of defects present in the crystal structure by calculating the ion-crystal interaction at any depth. In the next section, the two-defect model that is used for simulation will be discussed.

3.2 Simulation of the radiation damage by using the two-defect class model

To quantify the damage created in single crystals bombarded with low-energy ions and to investigate the depth profile of displaced atoms from their regular positions in the crystal, Rutherford backscattering spectrometry data in the Channelling geometry were analyzed by a Monte-Carlo simulation code (see the chapter 2). From a theoretical point of view, the existence of two channelling processes explain the shape of RBS/C spectrum: (i) direct backscattering of probing ions on atoms displaced within the channels of the structure and (ii) scattering of ions that interact continuously with the matrix atoms until they leave the channel at a certain depth in the crystal, where this process occurs as a consequence of continuous deflection of their path in the channel due to small-angle collision (mostly with electrons) leading to dechannelling of the ions and then to backscattering. The RBS/C spectrum as mentioned in the previous section consists of two main signals, where the first one is coming from the direct backscattering ions superimposed over the dechannelling signal. Different types of defects located in the irradiated structure are responsible for the different contributions of the spectra that are obtained from RBS/Channelling technique, especially in the case of a highly defective material. Although the channelling technique is limited when it is applied for highly defective materials, where many defects are existing in the channels or the channels themselves are distorted under irradiation, it is still useful to classify and defects responsible of dechannelling as: (i) obstruction-type (e.g. atoms off its regular position in the matrix, a stacking fault) responsible for mostly direct scattering and (ii) distortion- type dechannelling (e.g. lattice distortion, dislocation), mostly responsible for dechannelling with a negligible contribution for direct scattering.

In this work, the two-defect model was used to analyze the RBS/C spectra assuming two type of defects: (i) randomly displaced atoms (RDA) to reproduce the defects responsible for the creation of the damage peak in RBS/C spectra and (ii) bent channels (BC) responsible for an increase of the dechannelling signal. By using this two-defect model, it is possible to determine the damage evolution (the damage profile) in urania as well as to explore the difference between implanting soluble ions (La) versus insoluble ions (Xe).

3.2.1 Description of the two-defect model

Many defects could be created as a result of materials irradiation, and the processes of creation and organization of these defects are complex. The implantation with low-energy ions creates defects near the surface and the different types of defects present in the irradiated layers of the material are responsible for the different contributions of the spectrum that are obtained from RBS/Channelling technique. The atoms randomly displaced from their regular positions (such as interstitial type, cluster of atoms) are mostly responsible for the creation of a damage peak; the second type of defects which has a main influence on the dechannelling part of the spectrum correspond to atoms only slightly displaced from their regular position and line defects such a dislocations, where the positions of atoms are correlated.

The model that was used to simulate RBS/C spectra in this work assumes a simplified model of defects. The two dominant types of defects taken into account are: (i) randomly displaced atoms (RDA), which assumes that a given fraction of both U and O atoms are randomly displaced into the lattice (similar to the effect of the presence of like Frenkel pair defects) that are mostly responsible for the creation the damage peak; and (ii) bent channels (BC) defects which assumes a distorted atomic rows (similar to the effect of dislocations), which contributes to the formation of the dechannelling part of the spectra.

Although a the main contribution of the dechannelling appears at a larger depth in the low energy region as shown in RBS/C spectra, i.e. at a lower energy with respect to the damage peak, this does not mean that these defects are located in deeper depth. In fact, the two kinds of defects are created in the same damaged region but their effects appear also at low energy when ions cross the underling virgin part of the crystal, because the angle distribution of the probing ions was strongly modified while crossing the defective region in the crystal.

For the sake of simplicity, the model assumes that both the RDA and BC are created on the same defective zone in the near- surface region, in agreement with the creation of radiation-induced defects by low-energy ions. It is assumed that the bent channel defect has a constant concentration over the whole damage region as shown in figure 3-6, whilst a given arbitrary distribution of RDA is allowed over the same region. This approach limits the number of fitting parameter that can be varied independently and allows us to study the effect of fluence over a very large range and to compare different type of bombarding ions.

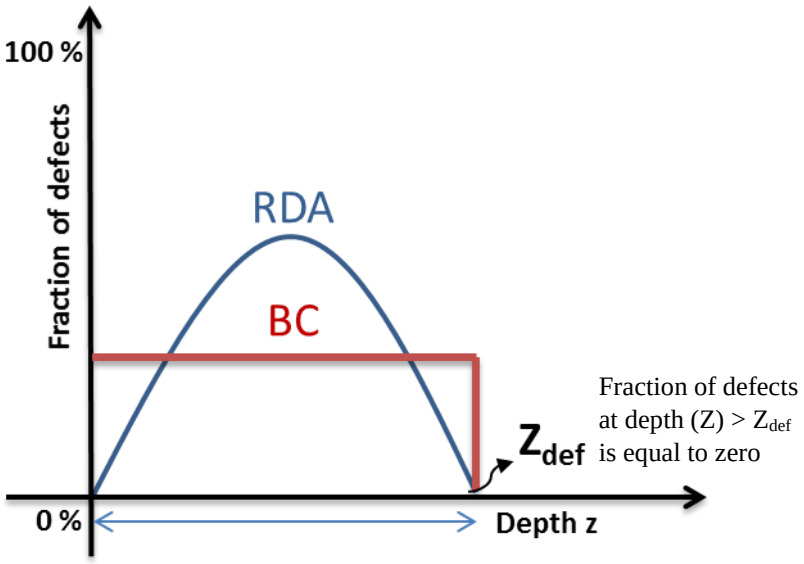

Figure 3-6: A schematic drawing of a model of the depth distribution of the defects up to the thickness Z_{def}. A profile of RDA defects (blue) and a constant fraction of BC defects (red) are incorporated on the damaged layer from the surface z = 0 up to the depth Z_{def}.

The model assumes a volume fraction of randomly displaced atoms and bent channels in the range of 0 to 1. When the fraction of RDA reaches 1 ($f_{RDA} = 1$), an amorphous structure is created. Regarding the bent channels, they are modeled as Arctangent function [Turos *et al.* 2014]**:**

$$f(z) = d\ Arctan(gz)$$

Where d is related to the Burgers vector that measures the lattice distortion caused by the presence of the bent channel and g depends on physical properties of a crystal and dislocation.

The bent channels are characterized by the length L of the curved region and by the angle η with respect to the undistorted channels as shown in figure 3-7. The total length L of the curved region is given by the following formula [Turos *et al.* 2010]:

$$L = 2rsin\eta$$

Where L: is the length, η: is the inclination angle, and r: is the curvature radius

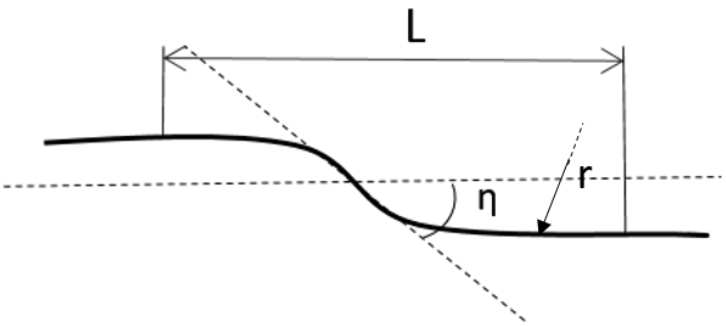

Figure 3-7: A schematic representation of a bent channel characterized by its length (L) and angle (η) of the distortion with respect to the undistorted channels.

3.2.2 Monte-Carlo simulation of RBS/C spectra

In this section, the random and the aligned RBS/C spectra were simulated by using the Monte-Carlo simulation code McChasy assuming a two-defect model. This sections discusses in details the model that was used, and the MC simulations that were obtained.

3.2.2.1 Determination of the simulation parameters

In uranium dioxide (space group $Fm\bar{3}m$), uranium atoms are sited at the (0,0,0)… positions of the cubic cell and the oxygen atoms at $\left(\frac{1}{4},\frac{1}{4},\frac{1}{4}\right) and \left(\frac{1}{4},\frac{1}{4},\frac{3}{4}\right)$ ... [Willis 1964]. The cell parameter is a = 547.0 pm. The simulations were performed assuming that implanted impurities are located in the octahedral positions in the fluorite-type structure. The influence of these incorporated atoms in the crystal structure on the behavior of probing ions is essentially negligible at low implantation fluence, but their role become significant at a fluence larger than ~ a few 10^{15} cm^{-2}.

The root-mean-square amplitudes of U and O atoms used in the simulations were fixed by comparing the axial spectra and angular scans recorded on the virgin crystal (before implantation) with the Monte-Carlo simulations for different values of thermal vibrations. All values were in a good agreement with the ones previously recorded on virgin UO_2 crystals [Garrido *et al.* 2006]. Typical root-mean-square amplitudes of thermal vibration vary from $\sqrt{\langle u_U^2 \rangle} = 6.0\ pm\ to\ 8.5\ pm$ and $\sqrt{\langle u_O^2 \rangle} = 9.0\ pm\ to\ 12\ pm$, depending on the intrinsic quality of the single crystals.

3.2.2.2 Simulation of the random spectra

The random spectra are analyzed by using Monte-Carlo simulation code assuming the two-defect model. Figures 3-8 show that two-defect model fits successfully the random spectra even with that different shapes at high fluence (figure 3-8.b) compared to the low fluence (figure 3-8.a). The spectra show: (i) a peak located in between 2600 and 2750 keV recorded from the backscattering of He ions on La atoms located in the matrix (the front of backscattering signal due to La atoms located near the surface at 2737 keV) and (ii) a lower backscattering yield at the surface compared to one that is un-irradiated due to the modification of the stopping power on the implanted layer. This MC model assumes that all Xe and La atoms are located at the octahedral positions in the lattice.

The depth distribution of these impurities was calculated by analyzing the random RBS spectra recorded for the crystal implanted at high fluence. The peak corresponding to the incorporation of La or Xe and the deficiency in the U yield close to the surface (see figure 3-3.b, 3-5.b), allow the determination of the parameters of the implantation profile (range Rp and range straggling ΔRp, assuming Gaussian shaped distribution). These parameters (Rp ~ 65 nm and ΔRp ~ 40 nm) that were determined experimentally for both ions are not totally in agreement with the values calculated by SRIM simulation code (Rp = 83 nm and ΔRp = 39 nm). The shift in Rp corresponds mostly to the modifications of the crystal's surface (sputtering effects) which is not considered in SRIM calculations. Figure 3-9 shows an example of peak fitting in random RBS spectrum to determine the depth distribution of incorporated La atoms implanted at a fluence $2x10^{16}cm^{-2}$.

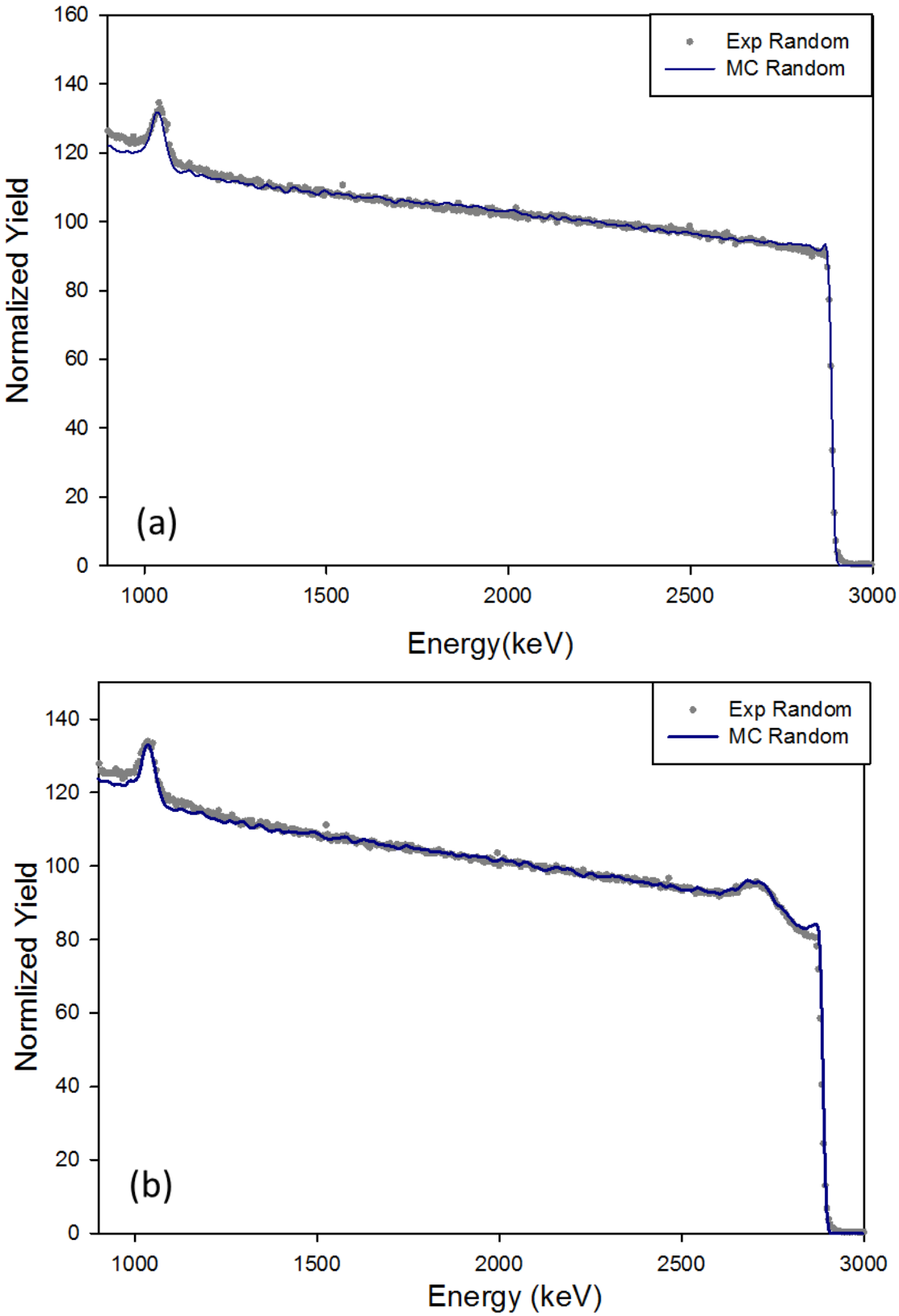

Figure 3-8: Random RBS spectra recorded on a UO_2 crystal implanted with 500 KeV La ions at 773 K at low fluence in (a) and high fluence in (b). Solid lines present the best MC fits for the random channelling spectra that recorded for each implanted fluence. The random spectrum was recorded at a fluence $\Phi = 3x10^{14}$ cm^{-2} (grey circles) in (a) and at a fluence $\Phi = 2x10^{16}$ cm^{-2} (grey circles) in (b).

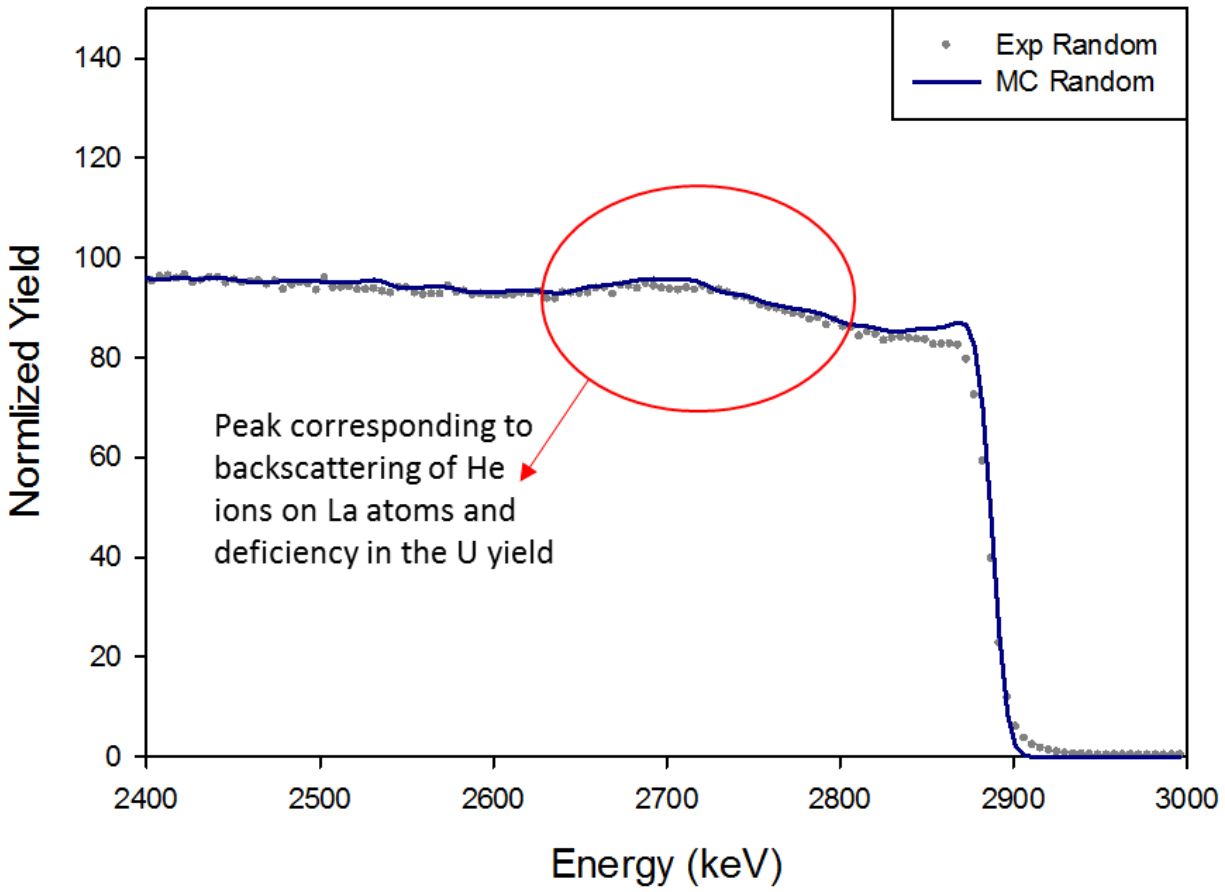

Figure 3-9: Experimental RBS spectrum at the high energy part of channelling spectra recorded in random (gray circles) direction for UO_2 implanted with 500 KeV La ions at 773 K and the corresponding MC simulation performed using a Gaussian shaped distribution (Rp = 65 *nm* and ΔRp = 40 *nm*).

3.2.2.3 Simulation of the axial channelling spectra

In this section, the RBS/C aligned spectra were simulated by using the Monte-Carlo simulation code McChasy assuming a two-defect model. The influence of both RDA and BC on the simulation channeling spectra are discussed in this section.

3.2.2.3.1 The influence of randomly displaced atoms on the channelling spectra

As mentioned in section 3.2.1, the two-defect model assumes a simple model composing of two type of defects: (i) randomly displaced atoms (RDA) and (ii) bent channels (BC). To understand the role of each type of defect on the channelling spectra, as first step, the randomly displaced atoms were incorporated as defects created in the uranium dioxide structure and no bent channel was considered. This can be done by assuming a fraction of RDA in each sub-lattice over the whole irradiated depth. Simulations of spectra obtained from the code are compared with the experimental spectra, and a new depth distribution of defects is defined, until the simulation spectra are considered to be compatible with the experimental one. The role of RDA on the axial channelling spectra obtained for UO_2 implanted with La ions at fluence $3x10^{14}$ cm^{-2}, as shown in figure 3-10, is presented here a typical example. The main influence of RDA can be shown on the damage peak, while its effect on the dechannelling signal appears essentially at depth larger than the damage zone. Regarding its effect on the dechannelling signal, it is observed that the presence of RDA leads to an increase of the dechannelling yield as a compared to the virgin spectrum, but far too low compared to the experimental spectrum. In order to fit the whole spectrum, the profile of RDA is defined in the code as a table of fraction of randomly displaced atoms on both U and O sub-lattice at every depth and the fractions in the table are modified until we obtained finally a good agreement between simulation and experimental data. Figure 3-10 shows that a good agreement in both the height and the width of the damage peak can be achieved but there is an underestimation of the dechannelling yield. The fitting of the whole spectrum can be performed by two way either (i) a broader defect distribution or (ii) assuming other class of defect to compensate the difference between the experimental and the simulated spectrum in the dechannelling contribution.

we test the first possibility by extending the RDA distribution: the profile of RDA is extended up to a larger depth (i.e. larger than the depth of the damage peak) to increase the dechannelling yield. Although the new profile of RDA allows us to fit the channelling spectra in an excellent way (see figure 3-10), the extension of the defects to depth far larger than the implanted profile calculated by SRIM code (the maximum implanted depth for La ions in UO_2 is 200 nm) is unrealistic (significant fraction of RDA is extended up to 1 μm). Such a result is physically unacceptable. Another classes of defect definitely needed to be taken into account to fit the experimental data.

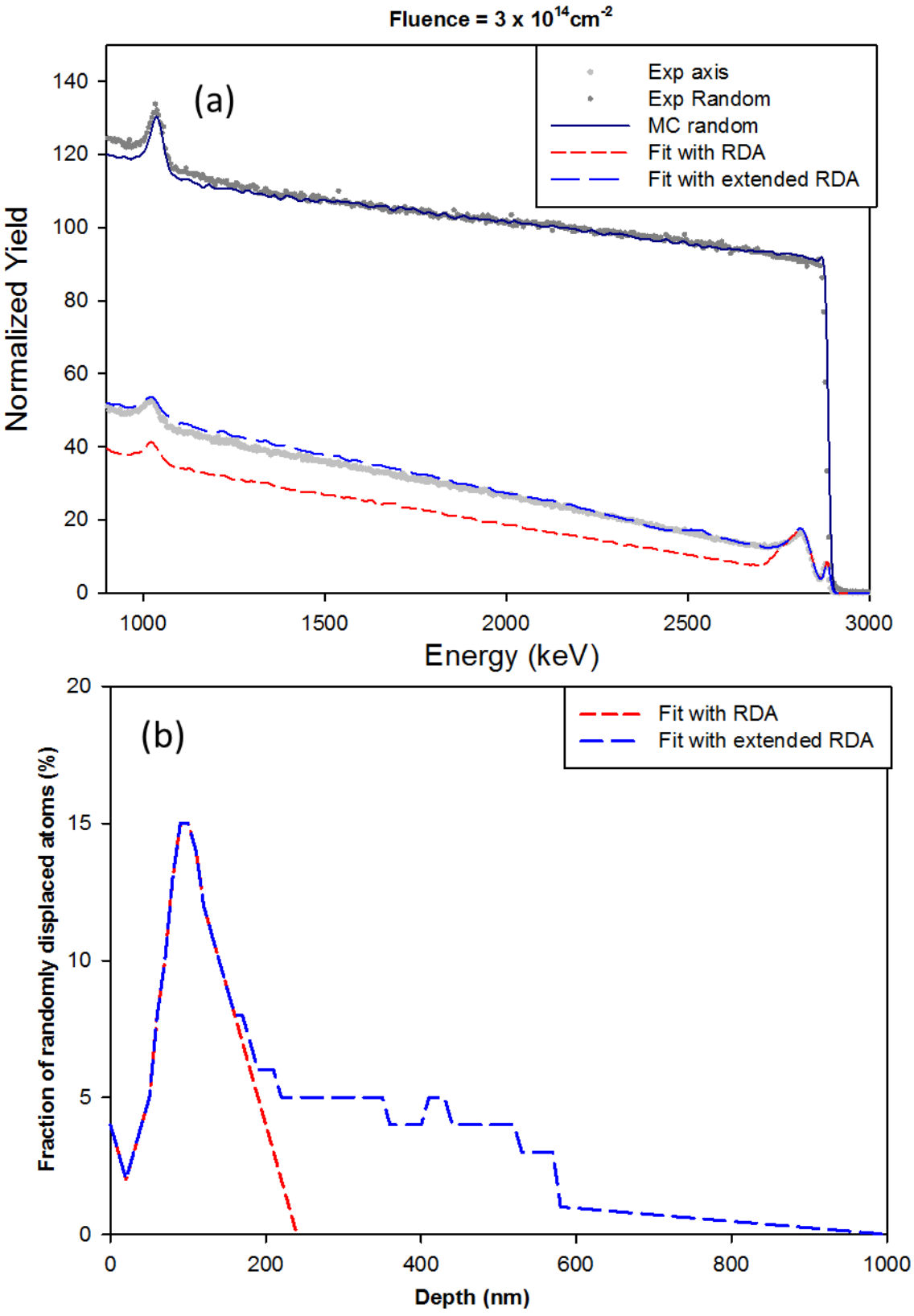

Figure 3-10: Random and aligned fits to RBS channelling spectra recorded on a UO_2 crystal implanted with La ions at a fluence $\Phi = 3x10^{14}cm^{-2}$ (a) and the corresponding depth distribution of defects (b). Short-dashed red lines represent distribution of RDA (b) that allows us to fit the damage peak (a). Medium-dashed blue lines represent the distribution of RDA (extended RDA) that allows to fit the whole spectrum for the whole the energy range.

3.2.2.3.2 The influence of bent channels on the channelling spectra

The previous section shows the need to include another type of defect with the randomly displaced atoms class to fit the experimental channelling spectra and to compensate the underestimated dechannelling signal. In this part, the bent channels are considered as the sole class of defect in irradiated crystals. In this kind of assumption, bent channels represent the distortion type defects, such as dislocations that could be created under irradiation.

A typical example of the analysis using BC as the sole class of defect is shown in the figure 3-11 where UO_2 implanted with La at fluence $3x10^{14}$ cm^{-2} (same fluence that has been analyzed by RDA for comparison). Different distribution of BC were considered to compare the best distribution able to fit successfully the experimental spectra: (i) a very sharp distribution of BC assuming a maximum fraction of defects is centered at the La implanted range, based on the actual implanted profile of La ions in the damage zone (at depth ~ 85 nm) and (ii) a constant value of the BC distribution is assumed for sake of simplicity up to the end of the defective thickness. Simulation spectra are shown in figure 3-11.

The results show that the spectrum obtained from simulation reveals that even though a very sharp distribution of BC is used, no damage peak can be evidenced. Conversely, the dechannelling yield shows a similar level and trend (slope) compared to the experimental data. As a conclusion, the dechannelling yield can be reproduced with a suitable distribution of BC.

Since the use of BC essentially affects the level of the dechannelling yield, a constant distribution of BC can also be tested. As seen on figure 3-11, a constant distribution of BC from 0 up to 220 nm corresponding to the extension profile seen by using the RDA profile in the previous section 3.2.2.3.1, with a fraction of 4.7 % is used as input. The result obtained is quite interesting since the spectrum obtained is very similar to the one calculated assuming a sharp distribution of BC. On the defective zone, no damage peak is observed: the signal increases rapidly with increasing depth. Beyond this zone, the dechannelling signal reveals a similar behavior compared to the dechannelling yield obtained using the sharp profile of BC. The result discussed here lead to a very important conclusion: since the calculated dechannelling yield reveals to be eventually insensitive of the exact details of the depth distribution of BC, a constant profile of BC is then assumed for the sake of simplicity in the following Monte-Carlo simulations to account for the radiation damage created by ion irradiation. Such a results is in fact not surprising: the dechanneling signal measures at a given depth the integral number of distortion-type defects that are crossed by the probing ions. Therefore, such a yield is essentially independent of the details of the integrated region.

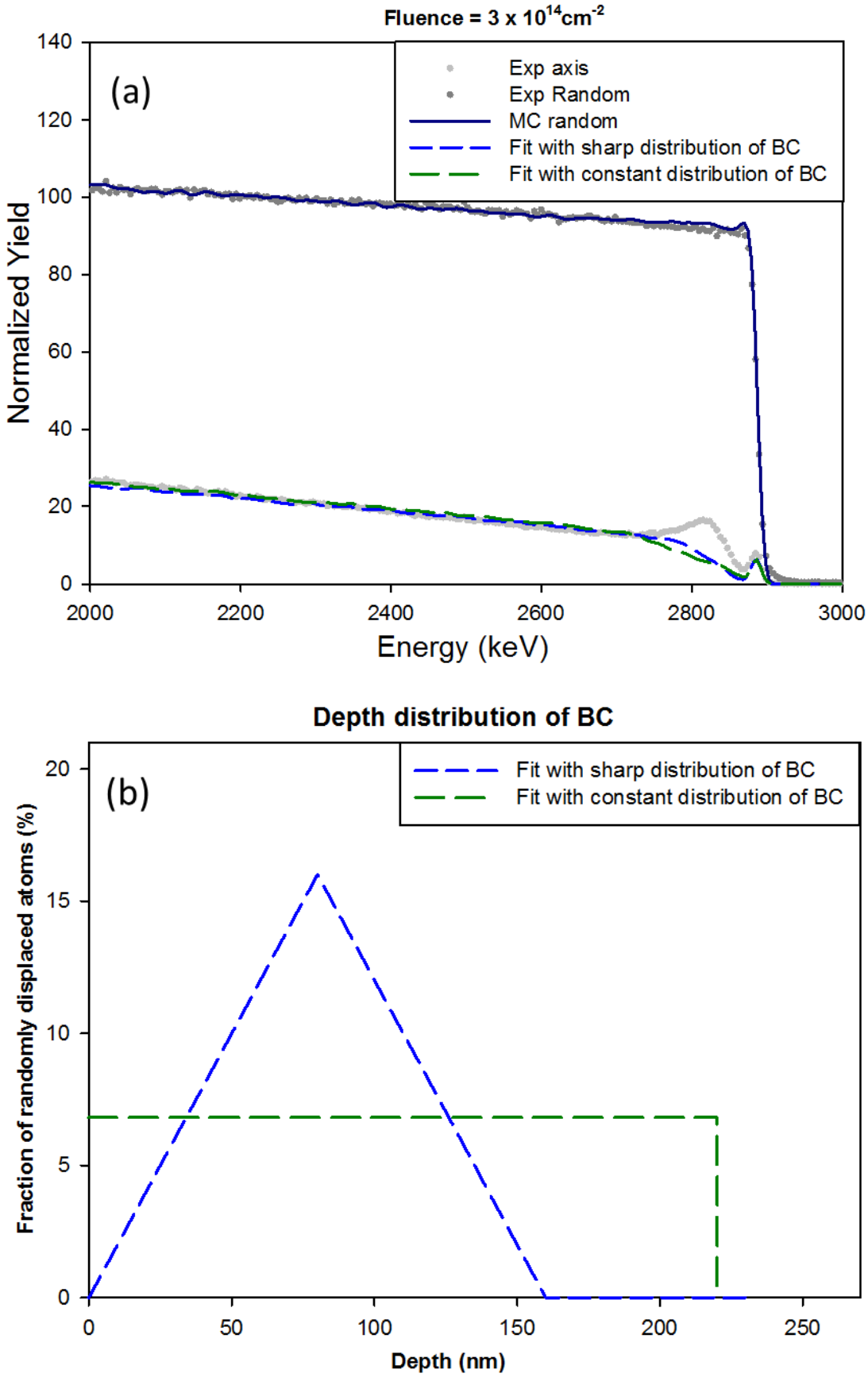

Figure 3-11: Random and aligned fits to RBS channelling spectra recorded on a UO_2 crystal implanted with La ions at a fluence $\Phi = 3x10^{14}cm^{-2}$ (a) and the corresponding depth distribution of BC (b). Medium-dashed blue lines represent a sharp distribution of BC assuming the maximum fraction of BC is centered at the ion's implanted range. Large-dashed green lines represent a constant distribution of BC from the surface up to a given depth. Fits were performed assuming L = 50 nm and η= 25°.

3.2.2.3.3 Monte Carlo simulation with the two-defect model: RDA and BC type

As shown in section 3.2.2.3.1 and 3.2.2.3.2, fitting RBS/C with one type of defects RDA or the BC type is not satisfactory and the performed Monte Carlo simulation fail to fully reproduce the experiment channelling spectra. In fact, the RDA-type of defects is able to reproduce the damage peak, while it underestimates the dechannelling signal at depth deeper than the implanted zone. Conversely, the BC-type of defect is able to fit the dechannelling signal without the damage peak. Therefore, it is needed to use the two type of defects: the RDA-type in combination with BC-type to be able to fit well the entire RBS/C experimental spectra including the damage peak and the dechannelling signal: the RDA-type fits mainly the damage peak, whilst BC-type is used as a complementary defect to fit the dechannelling signal.

In this section, Monte Carlo simulation with two types of defects are shown and the steps to fit are described. In a first step, RDA distribution is defined as input data to fit the damage peak. Once the damage peak is well fitted, the BC defect is defined to fit the dechannelling signal as it is improving the underestimation of the dechannelling signal that is obtained by assuming one type of defect (RDA-type). As shown in the previous section, a constant fraction of BC defined in the damage zone starting from 0 and then increased step by step up to the value that gives the best fitting of RBS/C spectra. After including BC in the input data, the damage peak is modified so a modification of the RDA distribution is needed at every step of changing BC to maintain the best fit of damage peak, keeping in mind that both RDA and BC have their own contribution to the dechannelling signal and that BC gives an extra contribution in the damage peak zone even it is mainly fit the dechannelling signal at larger depth.

A continuous change in RDA and BC fraction has to be done until the MC simulation shows the best agreement with the experimental spectra. This final step allows to extract the depth distribution of both RDA and BC fractions to give a quantitative estimation of defect distribution. A typical example of the analysis by assuming two-defect model shows in the figure 3-12 corresponding to the UO_2 crystal implanted with La at fluence 3 $x10^{14}$ cm^{-2}, as previously discussed.

The two parameters of the BC - length (L) and the angle (η) - affect the contribution of BC to the channelling spectra, keeping in mind that choosing these values has to fulfil the following conditions: (i) the combination of these parameters reasonably reflects the true created defects, i.e. good agreement with the defects that are observed by other alternative investigating technique e.g. TEM observation and (ii) the combination of BC + RDA allows the reproduction the channelling spectra.

The experimental value of the BC parameters were chosen in a reasonable range by using the values extracted from the TEM analysis (see chapter 4). L = 50 nm and η = 25° were taken as mean values. These values were also ensured after many test and simulations for all implanted crystals, over the entire fluence range to have the best values that are able to fit the channelling spectra, as shown in figure 3-12. It is important to mention that the parameters of BC (the length and the angle) are used for all the axial spectra for both ions (La and Xe) with same values in order to allow an easy comparison over the entire fluence range and for the two ions.

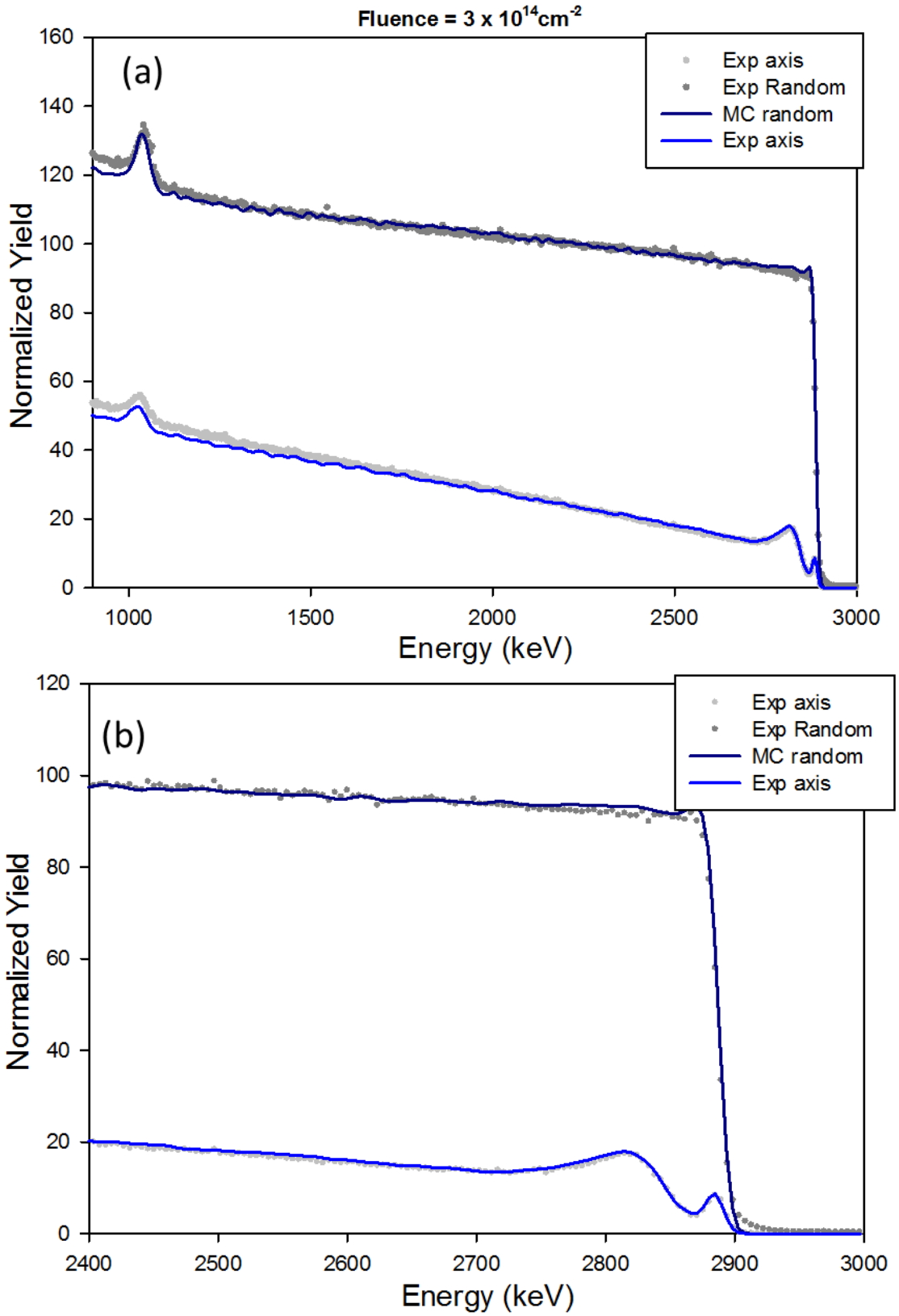

Figure 3-12: Random and aligned best fit to the RBS channelling spectra recorded on a UO_2 crystal implanted with La ions at 773 K at a fluence $\Phi = 3x10^{14}cm^{-2}$ assuming two-defect model (RDA and BC) (a) and high energy part of channelling spectra (b). This model allows one to fit the entire spectrum including the damage peak and the dechannelling signal up to a very large depth.

Figure 3-13 shows the influence of the length (a) and the angle of the BC (b) on the simulated channelling spectra. It is clear that the angle of the distorted part has a straight influence on the dechanneling part while the length of the BC has an inverse influence on the dechannelling yield. As it can be seen, the higher length of the BC leads to reduce the intensity of interaction with the channeled ions and as a consequence that will reduce the dechannelling yield. Conversely, the higher the angle of BC, the higher the probability to dechanneled the ions and the higher the dechannelling yield. The angle induces an extra transverse force acting on the channeled ion that will progressively deviate and eventually dechannels the probing ions. In summary, the two defect model provides a satisfactory description of the ion-irradiated solid that incorporates various type of defects. Therefore, the following simulations will focus on the use of the two-defect model (RDA + BC) to analyze the channelling spectrum in which the values of angle and the length of BC are fixed to be L = 50 nm and η = 25° for all crystals at all irradiation fluences.

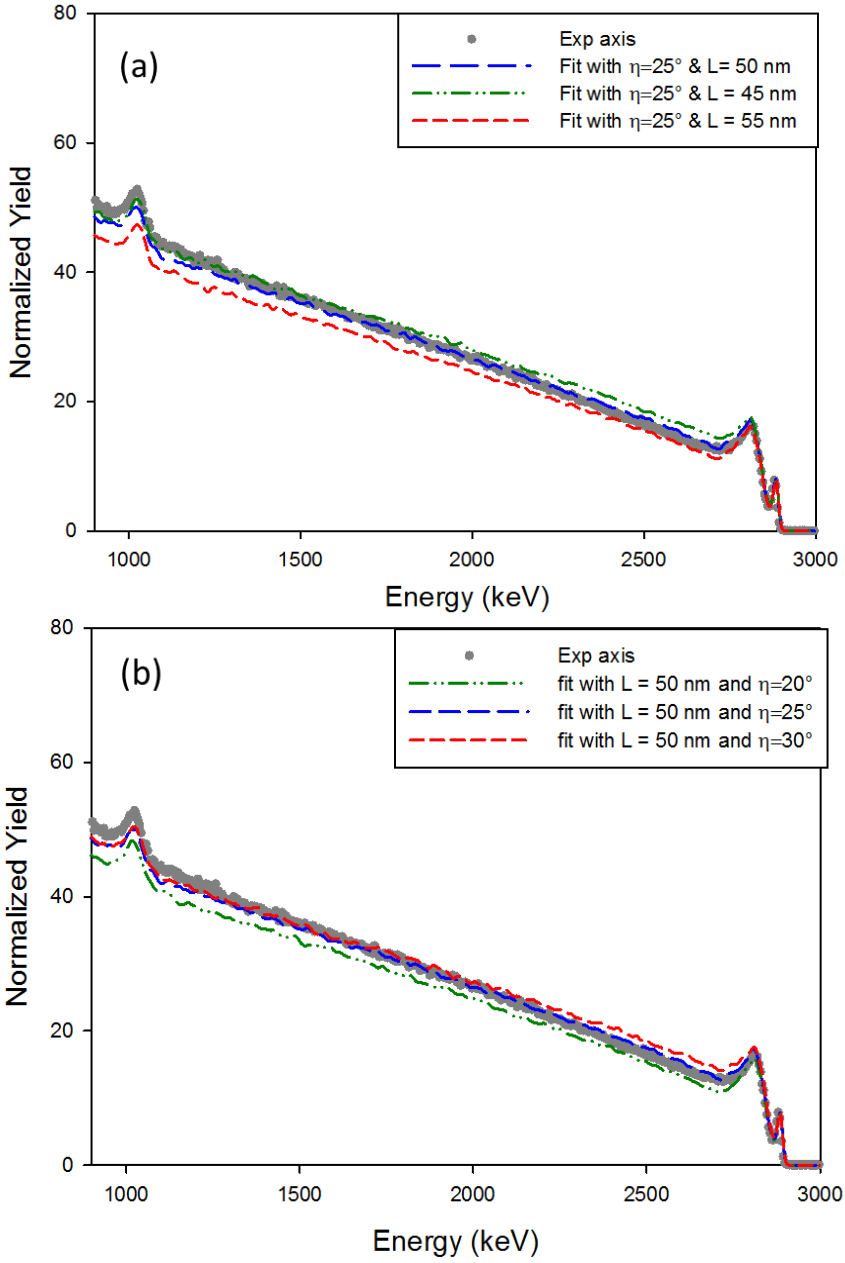

Figure 3-13: Aligned fits to the RBS channelling spectra recorded on a UO_2 crystal implanted with La ions at 773 K at a fluence $\Phi = 3x10^{14}cm^{-2}$ with different values of (a) the length L and (b) the angle η of BC. The best fits of the channelling spectrum is obtained by assuming constant fraction of BC with L = 50 nm and η = 25°as the medium-dashed blue lines shows.

3.3 Damage evolution

In this section, Monte-Carlo simulations of the channelling spectra are shown for both implanted Xe and La crystals at all the implanted fluences. The depth distributions of RDA and BC are presented. The last part of this section shows the damage evolution, as fraction of created defects versus accumulated fluence. The comparison between the defects creation due to irradiation with the two different ions having different chemical contribution is finally presented.

3.3.1 Analysis of axial channelling spectra

Channelling data corresponding to the 500-keV La implanted in UO_2 single crystal at 773 K are analyzed by using the Monte-Carlo simulation code assuming a two-defect model with the parameters L = 50 nm and η = 25° for the BC. Figures 3-14 and 3-15 display the MC simulations with two-defect model (combination of RDA and BC) that show the best fit to the experimental data. Figures 3-14 and 3-15 show a very good agreement between MC simulation spectra and the experimental data in the energy window from ~ 2000 keV to 2887 keV (corresponding to a depth from zero at the surface up to 1 μm). In particular, the damage peak is well fitted well by using the two-defect model. While the ion fluence increases, the intensity and the broadening of the damage peak are well reproduced by the fitting procedure. At high fluence (higher than $1x10^{16}$ cm^{-2}), where big changes in the shape and depth of damage peak are observed, the fits also successfully reproduce the spectra. Some discrepancies appear at depths that largely exceed the damage zone (z > 1 μm) likely due to: (i) the multiple scattering processes for the probing ions that is not taken into account in the simulation code and (ii) the uncertainties in the stopping power of probing channeled ions at large depth. This does not limit the accuracy of the two-defect model for investigating the depth distribution of damage over the first ~ 1 μm, i.e. at a depth far larger correspond to the implantation zone. Therefore, we can conclude that the two-defect model (RDA and BC) is able to fit and reproduce successfully all channelling spectra that were recorded in single crystals implanted with low energy La ions at 773 K over the whole fluence range.

Some discrepancies are evidenced at depths larger than the damage zone after the damage peak (i.e. corresponding to energy range from 2630 keV to 2750 keV) where there is some underestimation of the simulations in comparison to the experimental data. Therefore, an advanced model, including the incorporation of true dislocations and clusters defects will be useful. Such a code is currently being developed in Warsaw but it requires considerable efforts and it will be available within a few years.

The same analysis has been performed with same procedure for the channelling spectra that were obtained from a crystal implanted with 470 keV Xe ions. Figures 3-16 and 3-17 displays the best MC simulations to the experimental data recorded an Xe implanted single crystal UO_2 at 773 K. It is observed that two-defect model fits also successfully the entire spectrum including the damage peak and the dechannelling signal. The MC simulations spectra shows a good agreement with the experimental spectra over a large energy range of backscattering ions. Some discrepancies are observed at depths exceeding the damaged zone and near the damage peak (i.e. corresponding to energy range from 2630 keV to 2750 keV), as they were also seen for La ions implantation. However this discrepancy does not limit the two-defect model to use it in obtaining the damage profile in irradiated crystals.

To conclude this section, we have shown that MC two-defect model is able to fit the channelling spectra assuming a profile distribution of RDA defect and constant concentration of BC defect. The damage profile (defects versus depth) could be extracted from the MC simulation data as it is shown in the next section.

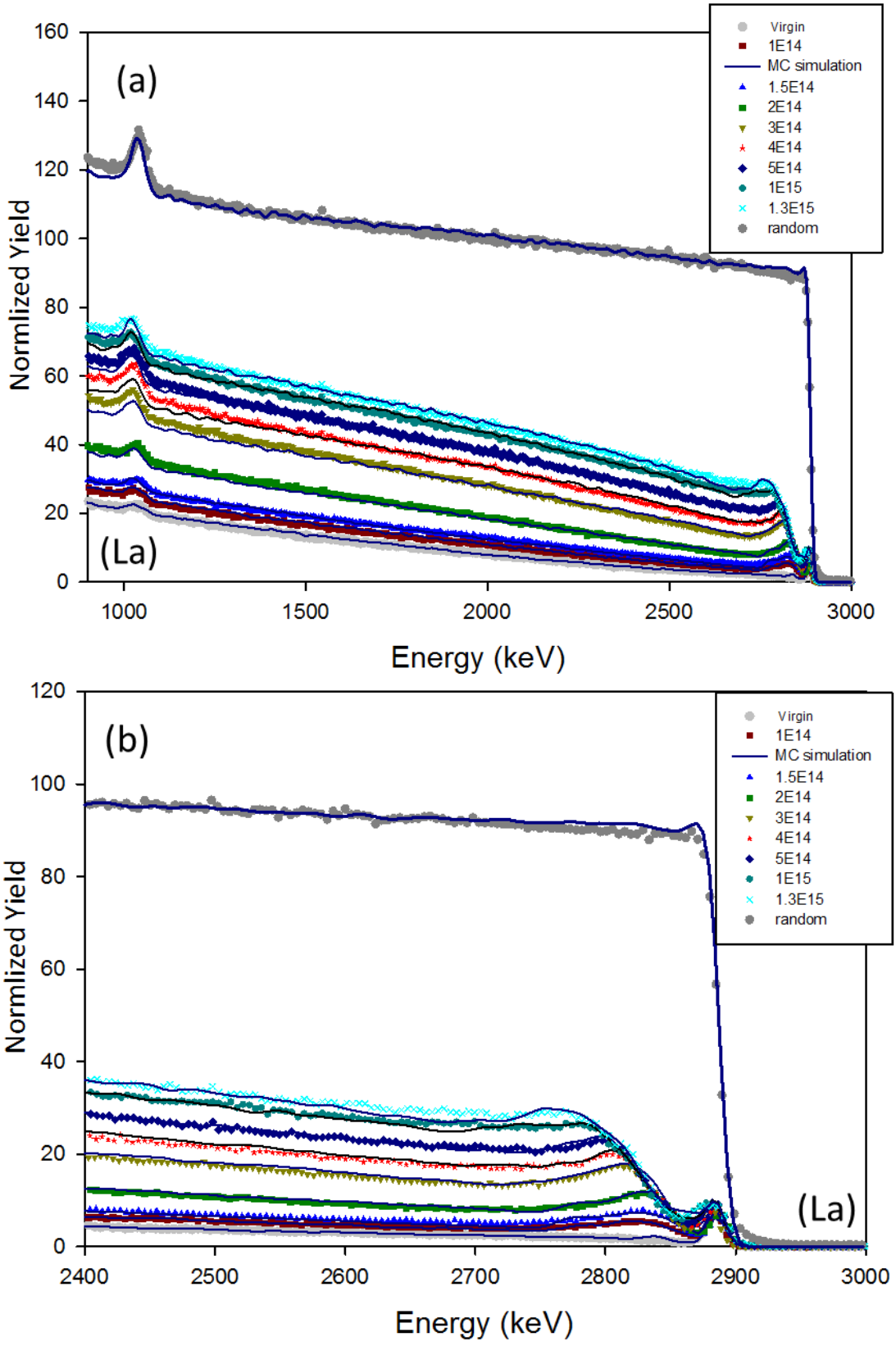

Figure 3-14: Random and aligned MC simulation to RBS channelling spectra (a) and high energy part of channelling spectra (b) recorded on a UO_2 crystal implanted sequentially with La ions at low fluence. Fluences are measured in unit of cm^{-2}. Implantation temperature is 773 K. The random spectrum was recorded at a fluence $\Phi = 3x10^{14}$ cm^{-2} (black circles). Experimental channelling spectra are plotted in symbols for fluences of $\Phi = 1x10^{14}$ cm^{-2} (dark red squares), $1.5x10^{14}$ cm^{-2} (blue triangles up), $2x10^{14}$ cm^{-2} (green squares), $3x10^{14}$ cm^{-2} (dark yellow triangles down), $4x10^{14}$ cm^{-2} (red stars), $5x10^{14}$ cm^{-2} (dark blue diamonds), $1x10^{15}$ cm^{-2} (dark cyan circles), $1.3x10^{15}$ cm^{-2} (cyan crosses). Fits were performed assuming L = 50 nm and $\eta = 25°$ (see text).

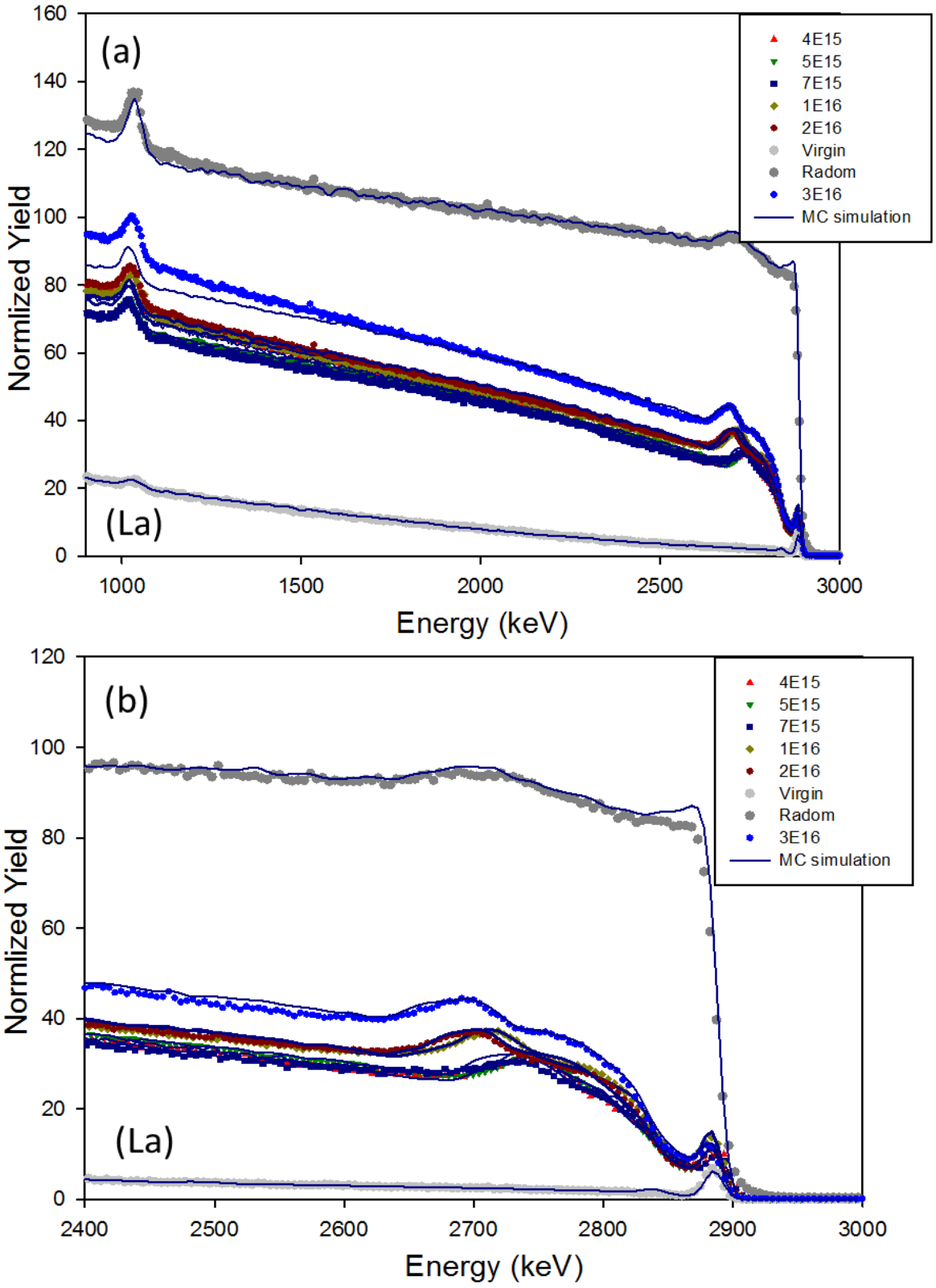

Figure 3-15: Random and aligned MC simulation to RBS channelling spectra (a) and high energy part of channelling spectra (b) recorded on a UO_2 crystal implanted sequentially with La ions at high fluence. Fluences are measured in unit of cm^{-2}. Implantation temperature is 773 K. The random spectrum was recorded at a fluence $\Phi = 2x10^{16}$ cm^{-2} (black circles). Experimental channelling spectra are plotted in symbols for fluences of $\Phi = 4x10^{15}$ cm^{-2} (red triangles up), $5x10^{15}$ cm^{-2} (green triangles down), $7x10^{15}$ cm^{-2} (dark blue squares), $1x10^{16}$ cm^{-2} (dark yellow diamonds), $2x10^{16}$ cm^{-2} (dark red circles), $3x10^{16}$ cm^{-2} (blue circles).Fits were performed assuming L = 50 nm and $\eta = 25°$ (see text).

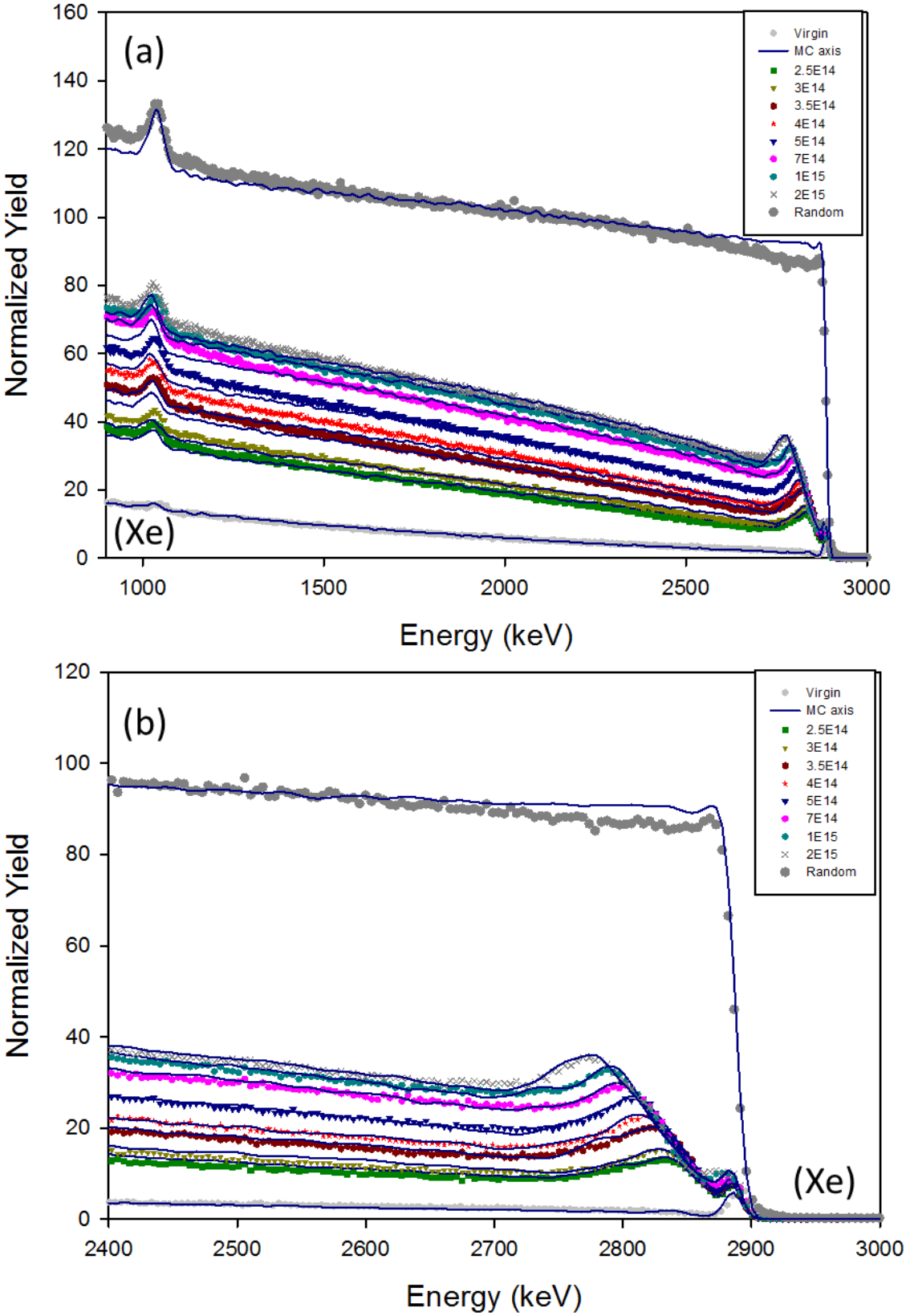

Figure 3-16: Random and aligned MC simulation to RBS channelling spectra (a) and high energy part of channelling spectra (b) recorded on a UO_2 crystal implanted sequentially with Xe ions at low fluence**.** Fluences are measured in unit of cm^{-2}. Implantation temperature is 773 K. The random spectrum was recorded at a fluence $\Phi = 2.5x10^{14} cm^{-2}$ (black circles). Experimental channelling spectra are plotted in symbols for fluences of $\Phi = 2.5x10^{14}$ cm^{-2} (green squares), $3x10^{14}$ cm^{-2} (dark yellow triangles down), $3.5x10^{14}$ cm^{-2} (dark red squares), $5x10^{14}$ cm^{-2} (dark blue triangles down), $4x10^{14}$ cm^{-2} (red stars), $7x10^{14}$ cm^{-2} (pink circles), $1x10^{15}$ cm^{-2} (dark cyan circles), $2x10^{15}$ cm^{-2} (dark grey crosses). Fits were performed assuming L = 50 nm and $\eta = 25°$ (see text).

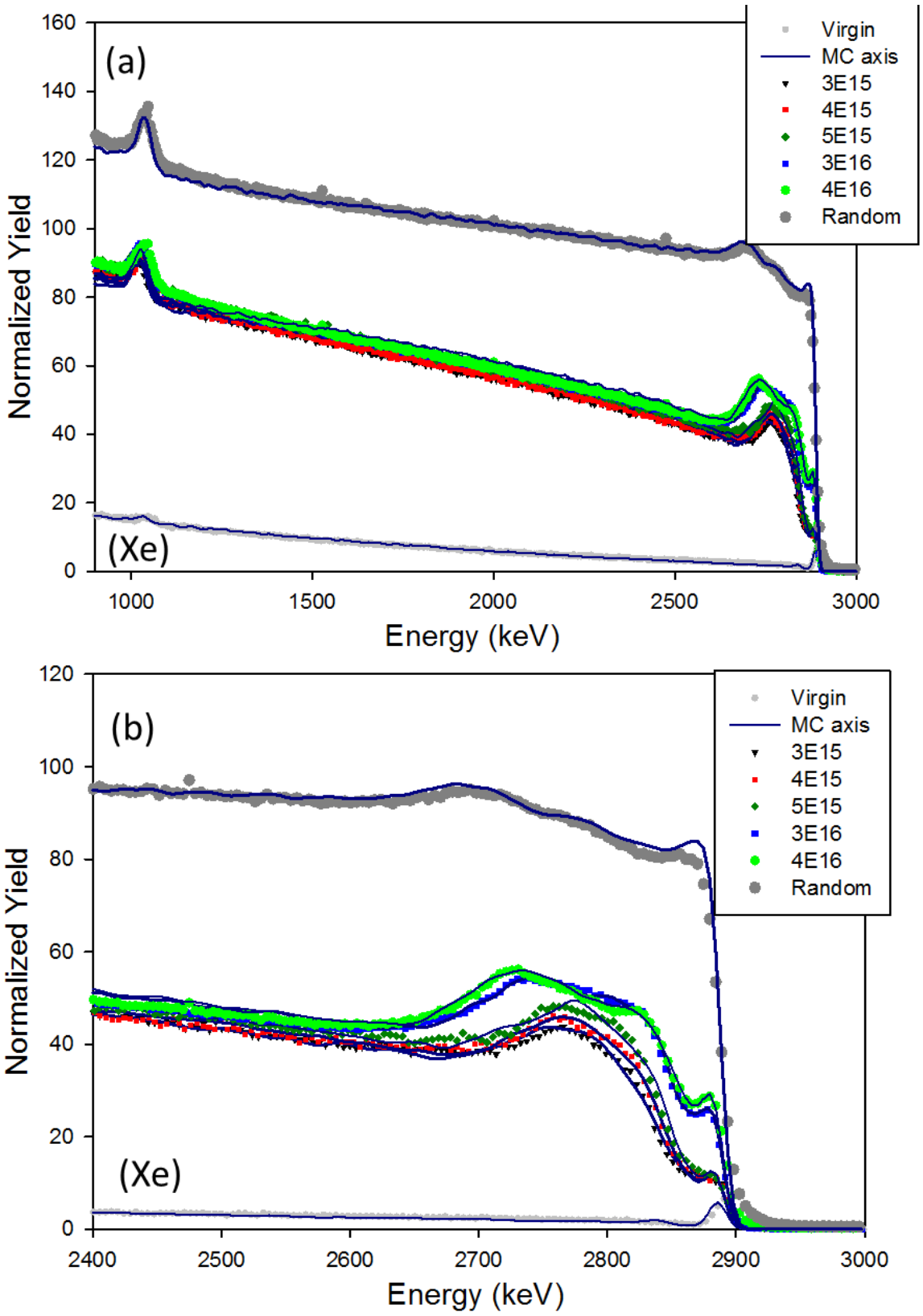

Figure 3-17: Random and aligned MC simulation to RBS channelling spectra (a) and high energy part of channelling spectra (b) recorded on a UO_2 crystal implanted sequentially with Xe ions at high fluence**.** Fluences are measured in unit of cm^{-2}. Implantation temperature is 773 K. The random spectrum was recorded at a fluence $\Phi = 4x10^{16} cm^{-2}$ (black circles). Experimental channelling spectra are plotted in symbols for fluences of $\Phi = 3x10^{15}$ cm^{-2} (black triangles down), $4x10^{15}$ cm^{-2} (red squares), $5x10^{15}$ cm^{-2} (green diamonds), $3x10^{16}$ cm^{-2} (blue circles), $4x10^{16}$ cm^{-2} (green circles). Fits were performed assuming L = 50 nm and $\eta = 25°$ (see text).

3.3.2 Evolution of depth distribution of defects (RDA & BC)

As mentioned before, UO_2 single crystals were implanted with La and Xe ions with fluence ranging from 0 to $4x10^{16}$ cm^{-2} at 773 K. Afterwards, all the spectra were analyzed by using Monte Carlo code assuming two-defect model. The code provides us with the damage profile and the fraction of RDA and BC at each damage layer for each implanted fluence for both La and Xe ions.

3.3.2.1 Evolution of the distribution of the randomly displaced atoms defects

In this section the evolution of RDA fraction is shown. For sake of simplicity and after careful study of the depth distributions, the results can be divided into three ranges according to the behavior of the RDA fraction evolution: (i) low implanted fluence range (0 to $\Phi \leq 5x10^{14}$ cm^{-2}), (ii) medium implanted fluence range ($5x10^{14}$ $cm^{-2} \leq \Phi \leq \sim 5x10^{15}$ cm^{-2}) and (iii) high implanted fluence range ($\Phi \geq \sim 5x10^{15}$ cm^{-2}) . It is important to mention that the fraction of RDA in the depth between 0-30 nm that corresponds to the surface peak is excluded from the distributions for all the fluence range. Such a peak increases due to the mostly modifications of the crystal's surface and we are interested in study the damage peak and damage profile at a deeper than the surface peak itself. We are mostly focusing on the evolution of the damage peak.

(i) *The low fluence range*: Figure 3-18 represents the distribution of RDA versus depth for low La and Xe implanted fluences. The distribution of RDA for both ions shows a similar behavior: the RDA defects are mainly centered between 80 to120 nm which is around the range of the implanted ions, taking an example for La ions, the maximum RDA for $2x10^{14}cm^{-2}$ is at 86 nm. The distribution of RDA for La and Xe ions shows that for both ions, the features are similar regardless the nature of ions and their different chemical contribution. The fraction of RDA increases and the profile broadens toword larger depth with increasing the fluence of implanted ions. It is important to mentioned, that the profile of displaced atoms strongly differs from the profile of displaced atoms calculated by the SRIM simulation.

(ii) *The medium fluence range:* The evolution of RDA defects follow a totally different behavior compared to the low fluence range for both ions. Figure 3-19 represents the distribution of RDA at the medium fluence range. A similar behavior of the RDA evolution for both ions is seen, where the width of the distribution of RDA is progressively increased toward larger depth as the fluence increases. It is observed that within this medium ion fluence range, the maximum fraction of RDA saturates for crystal implanted with La ions and Xe ions. Moreover, there is a clear difference in this fraction recorded at the maximum of the distribution between the two ions: the damage in crystal implanted with 470 keV Xe ions saturates at a much higher level (the average maximum fraction of RDA is 23%) in comparison to the crystal implanted with 500 keV La ions (the average maximum fraction of RDA is only 16%).

(iii) *The high fluence range:* The distribution of RDA for both ions La and Xe shows similarities in the maximum depth of created damage that does not exceed 300 nm. Conversely, differences between the two ions La and Xe are evidenced. Regarding La ions, as shown in figure 3-20, the maximum fraction of RDA does not increase dramatically with increasing the fluence even for the highest fluences, the maximum value is 20%. An increase in the width of the damage zone is clearly seen especially near the surface compared to the medium fluence range. So implanting more La ions creates more damage near the surface. With respect to the Xe implanted crystal, a very distinct distribution of RDA is obtained in case of high fluence of implantation $\Phi \geq 3 \times 10^{16}$ cm^{-2} (corresponding to concentration over 3 at. %): a huge damage is seen close to the surface as shown in figure 3-20. In fact, The distribution can be divided into two regions, the first one from the surface

up to the maximum range of implanted Xe ions (Rp + ΔRp ~125 nm) where the fraction of RDA is the highest, and a second region corresponding to z > Rp + ΔRp. This difference is likely to be due to the high concentration of implanted Xe ions that stop in the first region. In fact Xe ions are insoluble and forms bubbles at that region as it will be shown by TEM in the next chapter. The second region shows lower and almost constant fraction of RDA around 30% which is almost the same level that is observed for the medium fluences.

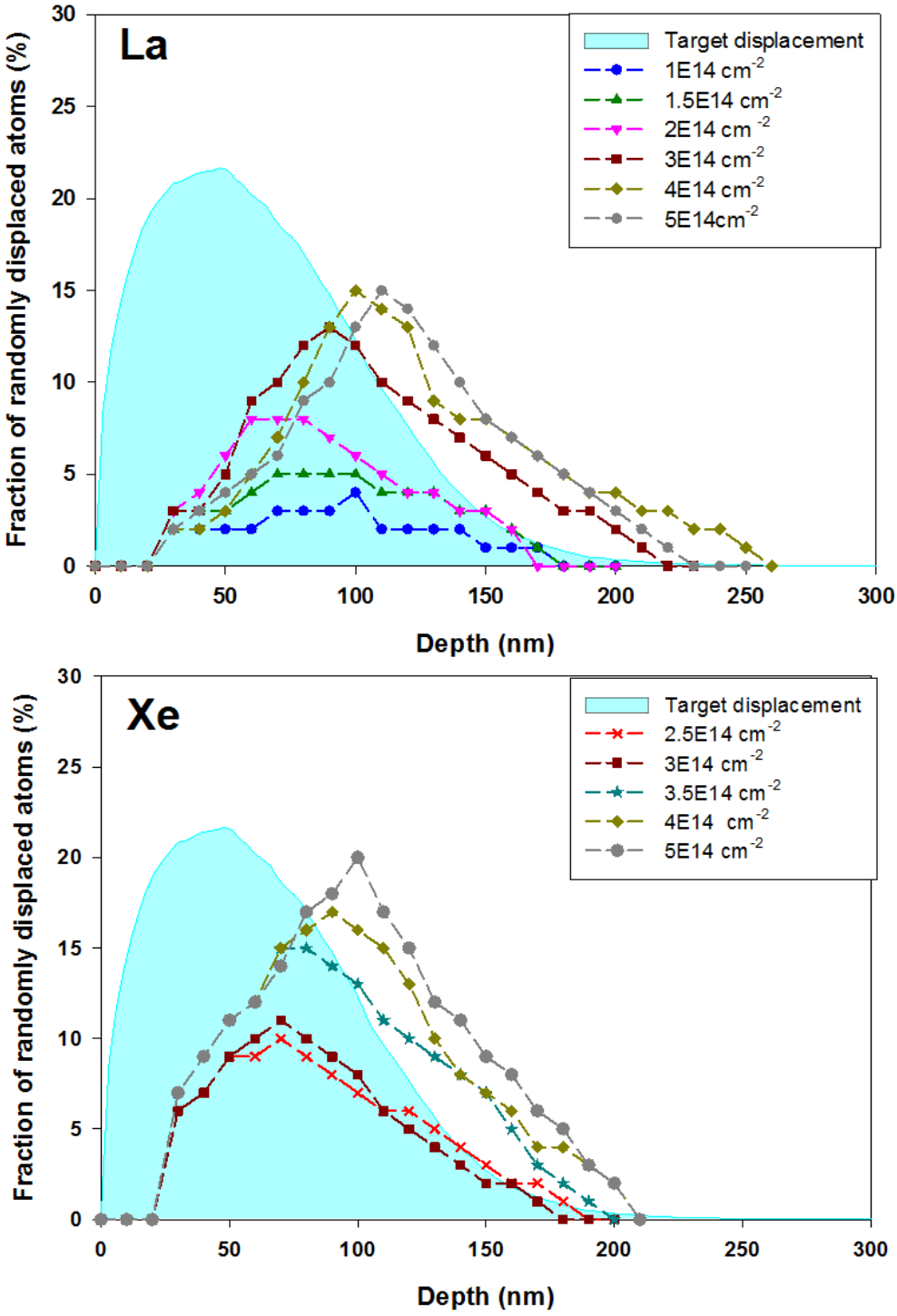

Figure 3-18: Fraction of RDA versus depth in UO_2 crystals implanted with La or Xe in the low fluence range ($\Phi \leq 5x10^{14}$ cm^{-2}) as extracted from MC simulations. The parameters for BC are L = 50 nm and η = 25°. Depth distribution of displaced matrix atoms according to SRIM (Cyan filled area) are plotted in an arbitrary unit.

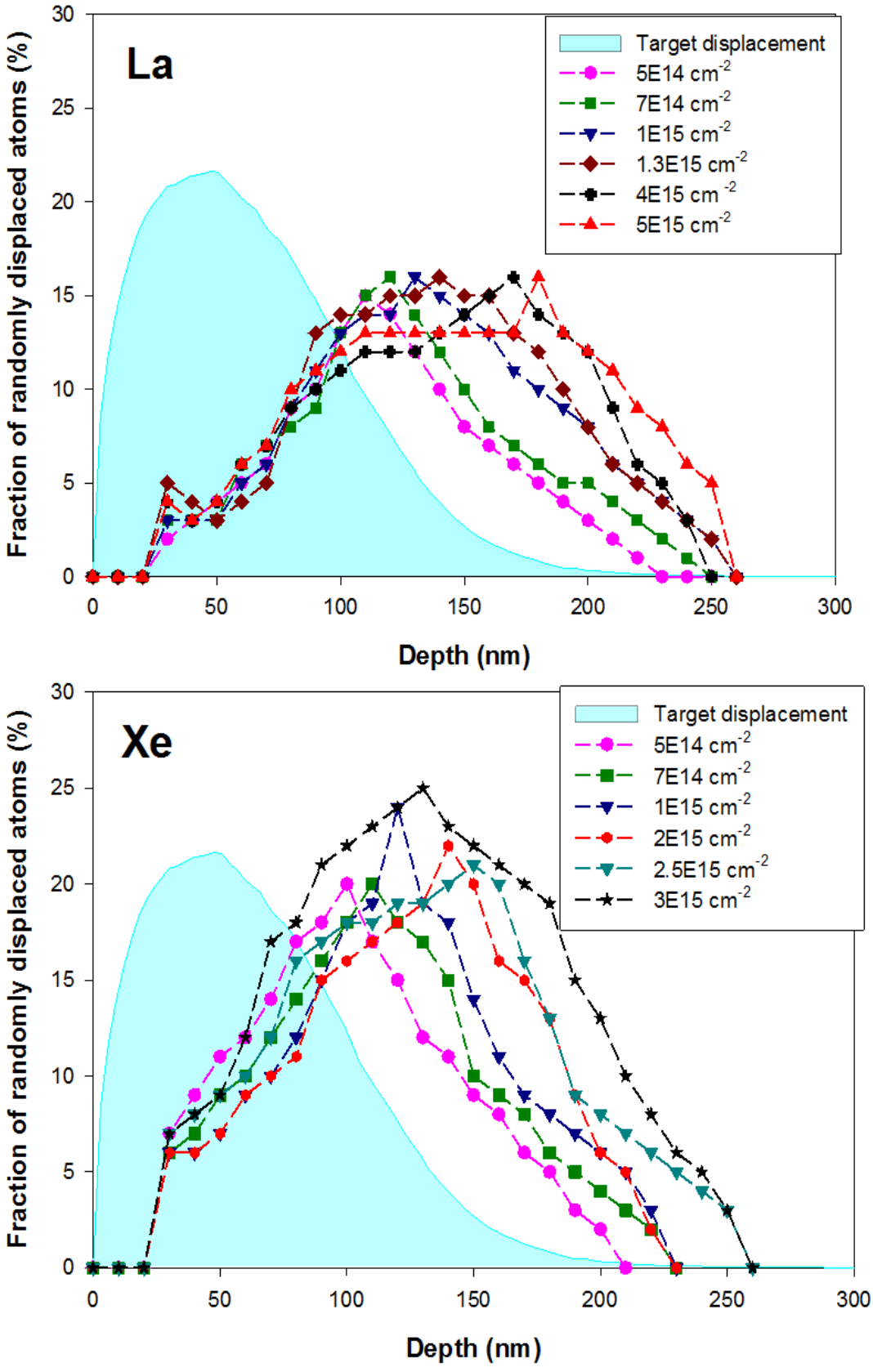

Figure 3-19: Fraction of RDA versus depth in UO_2 crystals implanted with La or Xe in the medium fluence range ($5x10^{14}$ $cm^{-2} \leq \Phi \leq \sim 5x10^{15}$ cm^{-2}) as extracted from MC simulations. The parameters for BC are L = 50 nm and η = 25°. Depth distribution of displaced matrix atoms according to SRIM (Cyan filled area) are plotted in an arbitrary unit.

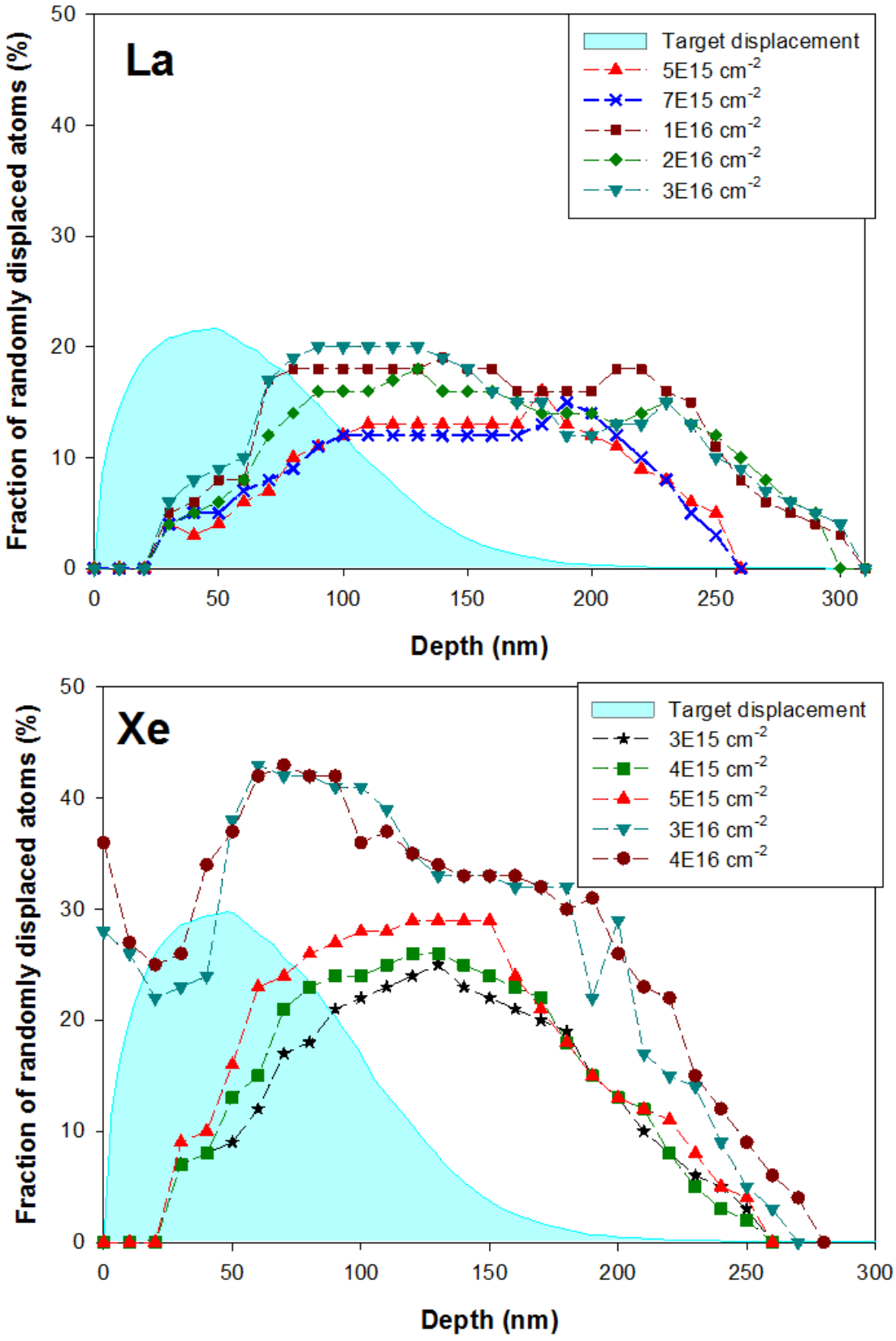

Figure 3-20: Fraction of RDA versus depth in UO_2 crystals implanted with La or Xe in the high fluence range ($\Phi \geq \sim 5x10^{15}$ cm^{-2}) as extracted from MC simulations. The parameters for BC are L = 50 nm and $\eta = 25°$. Depth distribution of displaced matrix atoms according to SRIM (Cyan filled area) are plotted in an arbitrary unit.

3.3.2.2 Evolution of the distribution of bent channels defects

The distributions of BC versus depth are shown in figures 3-21.b, 3-22.b and 3-23.b. These distributions have been extracted from the analysis of the channelling data using MC simulation code for both crystals implanted with Xe and La ions assuming the same value of parameters of BC (L = 50 nm and η = 25°) for both ions and at all fluences as mentioned before.

The figures display the distribution of BC at the three ranges of fluences as it is classified in in section 3.3.2.1 that are low, medium and high ion fluences for both ions, as well as the evolution of RDA for direct comparison.

(i) *The low fluence range*: In this fluence range both ions show the same evolution of the fraction of BC. The BC fraction increases with increasing the fluence but it shows a limited increase. The maximum fraction of BC for both ions in this range is 8%.

According to these results that obtained by MC simulations, we can conclude that in this fluence range, both class of defects (RDA and BC) that are essentially representing point defects, defect clusters and extended defects are created under irradiation.

(ii) *The medium fluence range*: Regarding the La-implanted crystal as shown in figure 3-22.b, the fraction of BC shows only a small evolution (increase of about 3%). It can be concluded that both class of defects (RDA and BC) stay almost with the same fraction but the damage extends toward deeper depth as more La ions are implanted. Regarding the Xe-implanted crystal, the BC fraction increases with increasing the fluence from 8% up to 14%, while the fraction of RDA at the maximum stays almost constant with the ion fluence. Both RDA and BC within this fluence range for both ions extend into deeper depth from 200 nm to 260 nm.

In conclusion, in this range of fluence larger difference between the two ions (Xe and La) are evidenced: for La- implanted case the fraction of RDA and BC are almost constant while for Xe-implanted crystal both fractions of RDA and BC are increasing.

(ii) *The high fluence range*: The fraction of BC for both ions in this fluence range almost saturate and the maximum thickness of damage is 300 nm. The BC fraction stays almost constant even if the crystal is implanted with a high concentration of impurities. Some increase with 3% regarding La ions at high concentration of implanted La about (4 at. %) is seen.

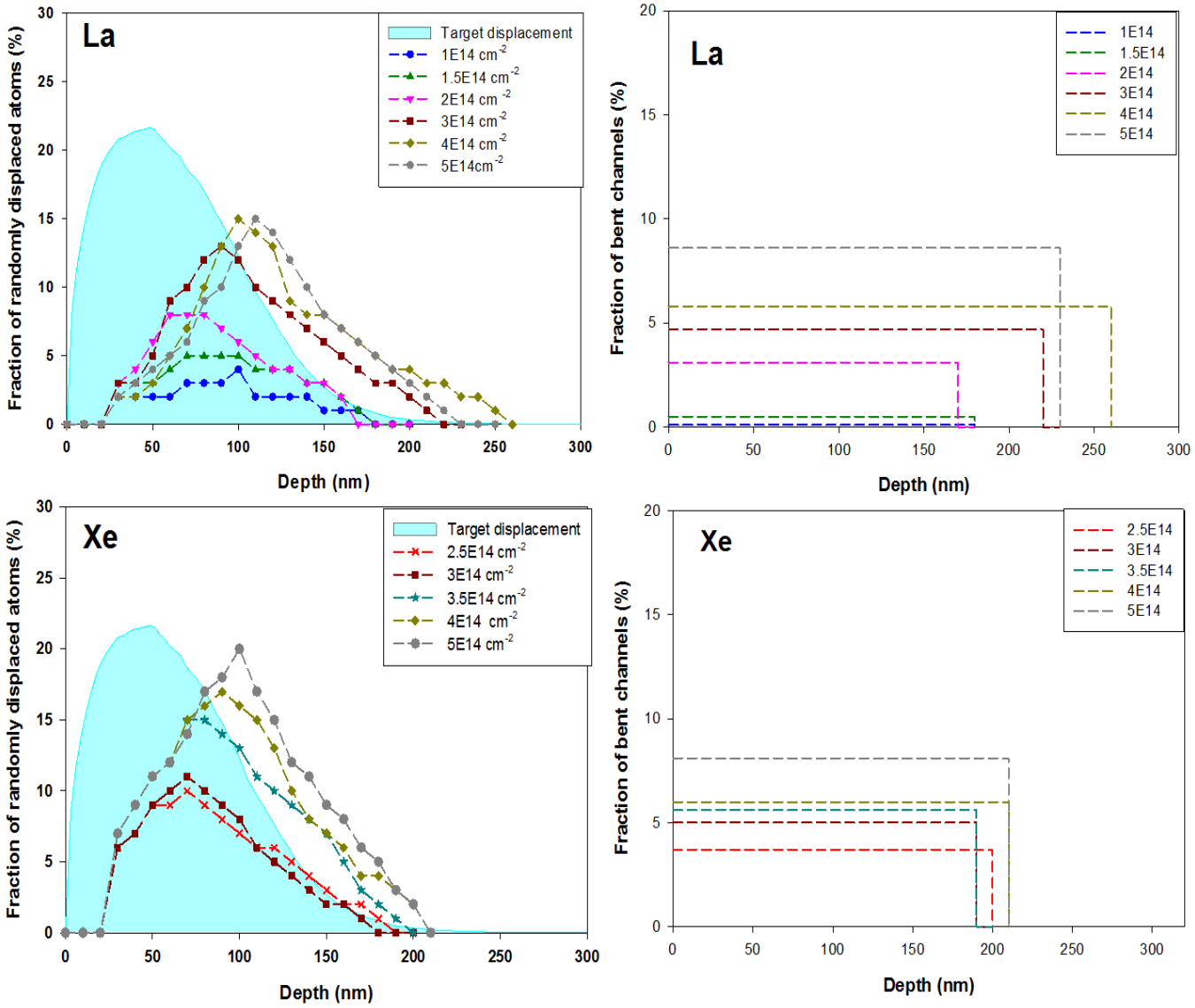

(a) (b)

Figure 3-21: Fraction of RDA (a) and BC (b) versus depth in UO_2 crystals implanted with La or Xe at low fluence ($\Phi \leq 5x10^{14}$ cm^{-2}) extracted from MC simulations. The fitting parameters for BC are L = 50 nm and $\eta = 25°$. Depth distribution of displaced matrix atoms according to SRIM (Cyan filled area) are plotted in an arbitrary unit.

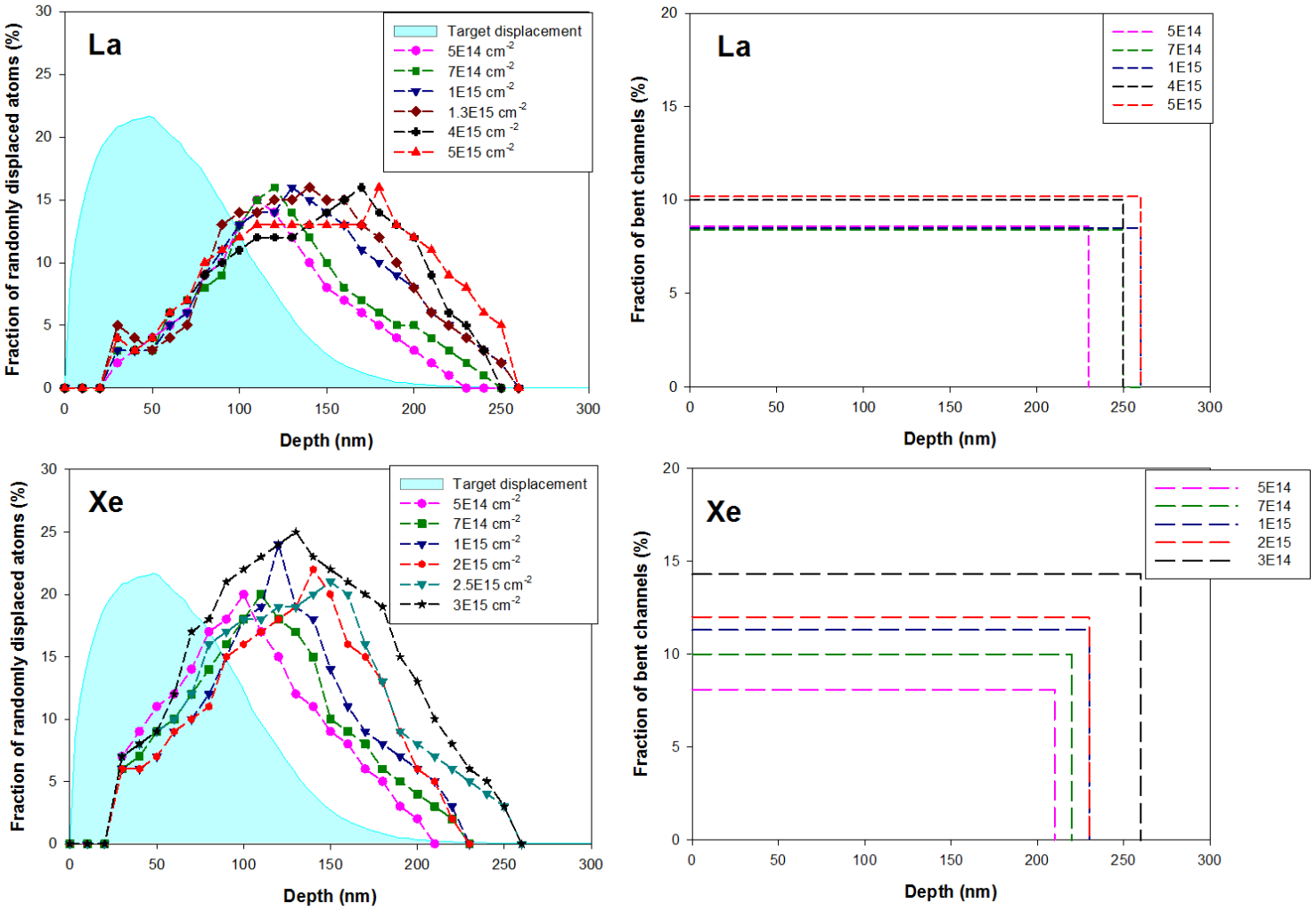

(a) (b)

Figure 3-22: Fraction of RDA (a) and BC (b) versus depth in UO_2 crystals implanted with La or Xe at medium fluence range ($5x10^{14}$ $cm^{-2} \leq \Phi \leq \sim 5x10^{15}$ cm^{-2}) extracted from MC simulations. The fitting parameters for BC are L = 50 nm and $\eta = 25°$. Depth distribution of displaced matrix atoms according to SRIM (Cyan filled area) are plotted in an arbitrary unit.

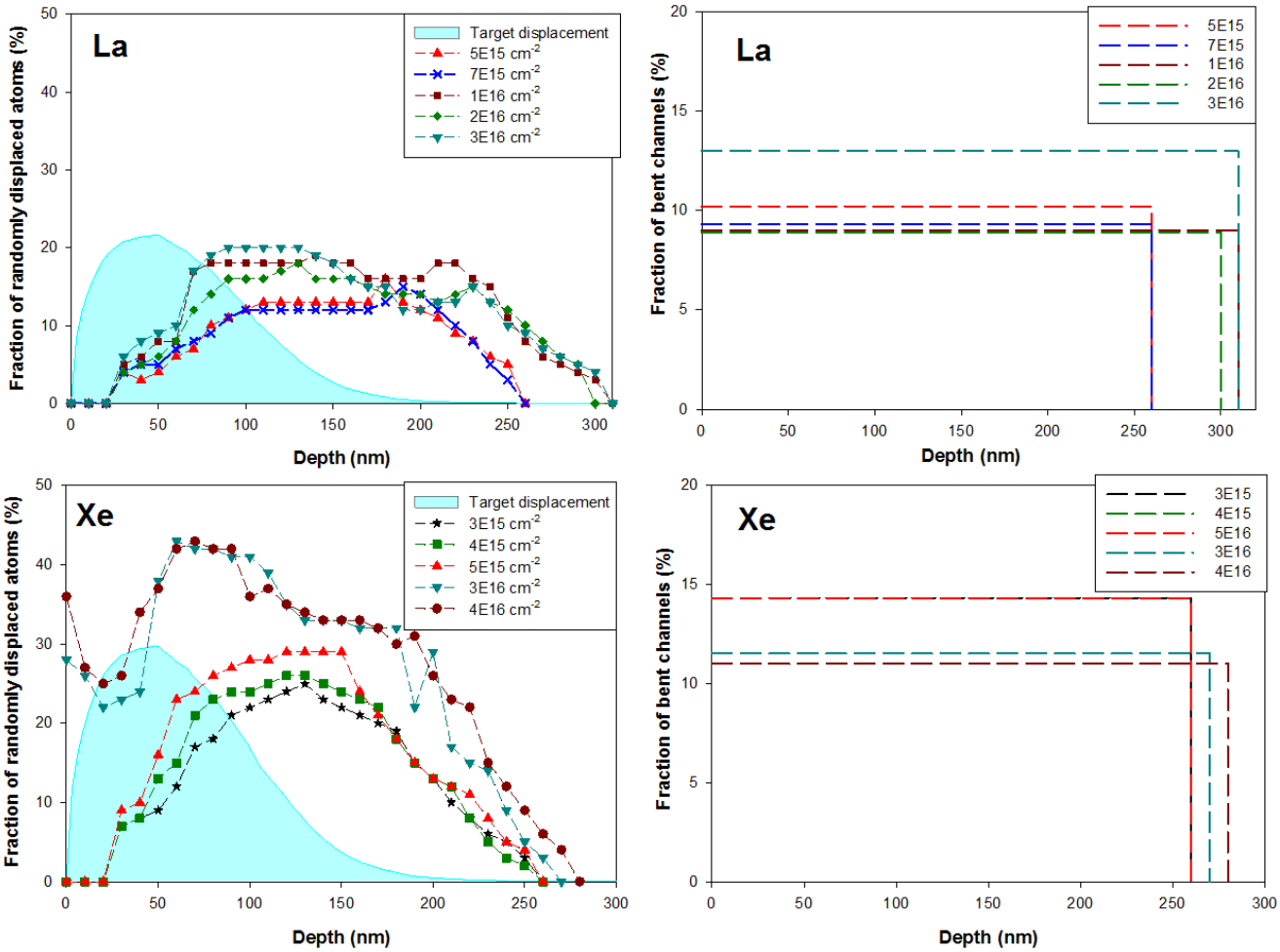

(a) (b)

Figure 3-23: Fraction of RDA (a) and BC (b) versus depth in UO_2 crystal implanted with La or Xe at high fluence range ($\Phi \geq \sim 5x10^{15}$ cm^{-2}) extracted from MC simulations. The fitting parameters for BC are L = 50 nm and η = 25°. Depth distribution of displaced matrix atoms according to SRIM (Cyan filled area) are plotted in an arbitrary unit.

3.4 Kinetic of damage accumulation

Figures 3-24 and 3-25 display the evolution of maximum fraction of RDA and BC created at all the implanted fluence and in the low fluence range, respectively. The evolution of RDA and BC are presented for both ions Xe and La on the same figure to compare the effects induced by the two ions of similar but different in nature since one is soluble (La) and the other is insoluble (Xe). The uncertinites in the fraction of RDA and BC are also defined (see Appendix D).

The evolutions of RDA show: (i) a sharp step increase appears from $5x10^{13}$ cm^{-2} to $4x10^{14}$ cm^{-2} (corresponding to a low concentration of implanted ions). This step is observed for both ions (La and Xe) regardless their nature. This sharp increase is a consequence of the radiation damage (defects created due to ballistic collision), which is independent of the nature of ions.

(ii) After this sharp increase, the fraction of RDA for both ions saturates over a wide range of irradiation, i.e. from ~ $4x10^{14}$ cm^{-2} to ~ $2x10^{16}$ cm^{-2}. A large difference between the two plateaus at saturation between the two ions is evidenced: the plateau at saturation present a higher level (~ 25%) for Xe ions than for the La ions (~16%).

(iii) A second sharp increase of RDA fraction is observed only for crystal implanted with Xe ions at high concentration exceeding $2x10^{16}cm^{-2}$ (corresponding to the concentration of implanted ions of more than 2 %). This second step increase is not observed for crystal implanted with La ions.

The evolutions of BC show similar evolution for both ions as shown in figure 3-24. For both ions, the evolution shows a strong increase in the fraction of BC up to $5x10^{14}cm^{-2}$. Then the fraction of BC almost saturates for Xe and La ions around 13% and 10%, respectively. It is observed that the difference between the two plateaus of saturation between the two ions is small about 3%. Even at high fluence where the crystal is heavily irradiated, the fraction of BC stays almost constant.

In conclusion, the comparison between RDA and BC for both ions shows that: the evolution of both RDA and BC occurs at almost the same range of fluence (between $5x10^{13}cm^{-2}$ to $4x10^{14}cm^{-2}$). Then the evolution for both type of defects saturates over a wide range of fluence except at high fluences, where for the specific case of Xe the RDA recorded at the maximum increases sharply again. An in-depth interpretation of the damage kinetics will be performed in the chapter 5.

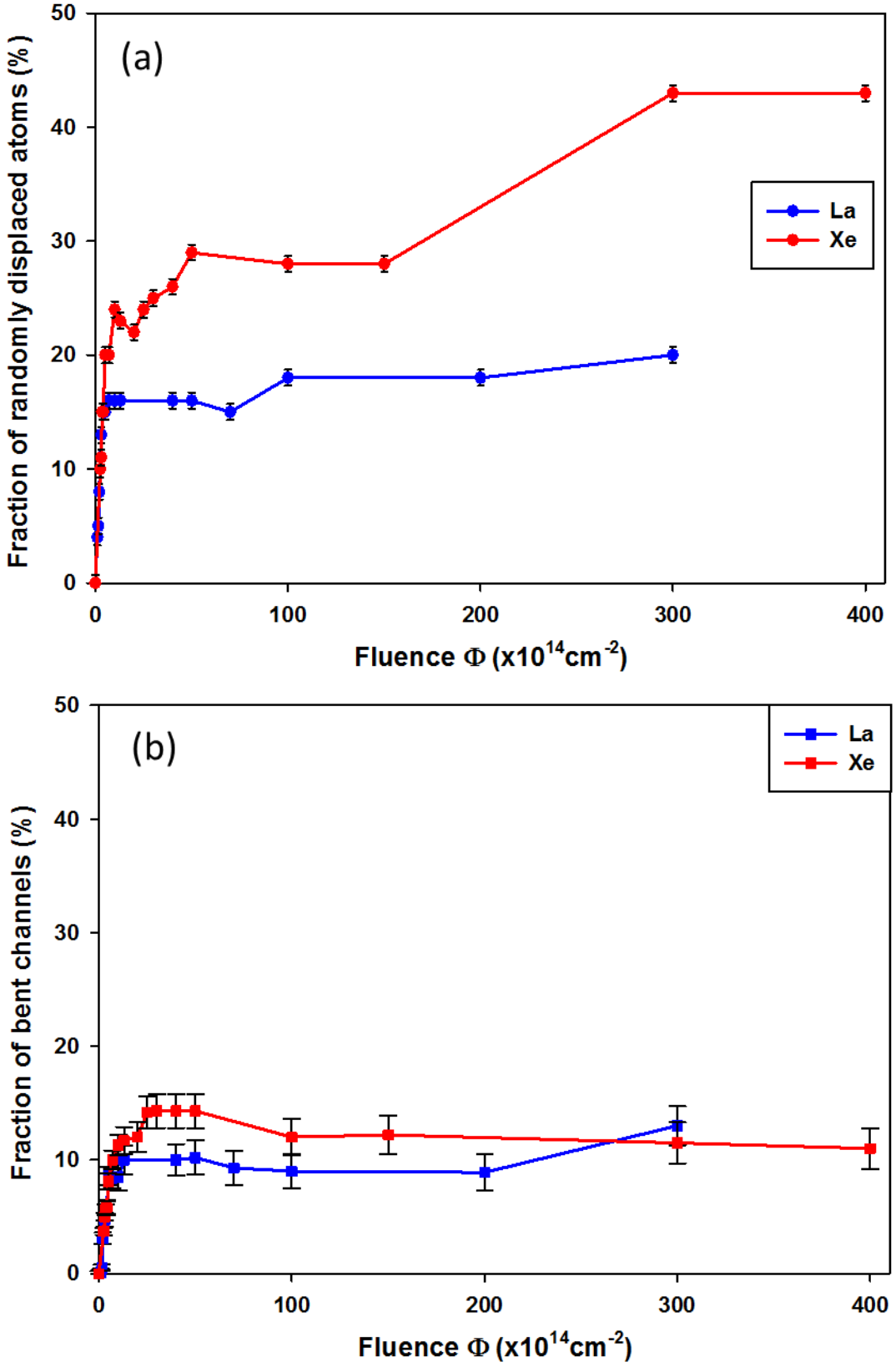

Figure 3-24: Evolution of the maximum fraction of RDA (a) and BC (b) extracted from the MC simulation versus ion fluence.

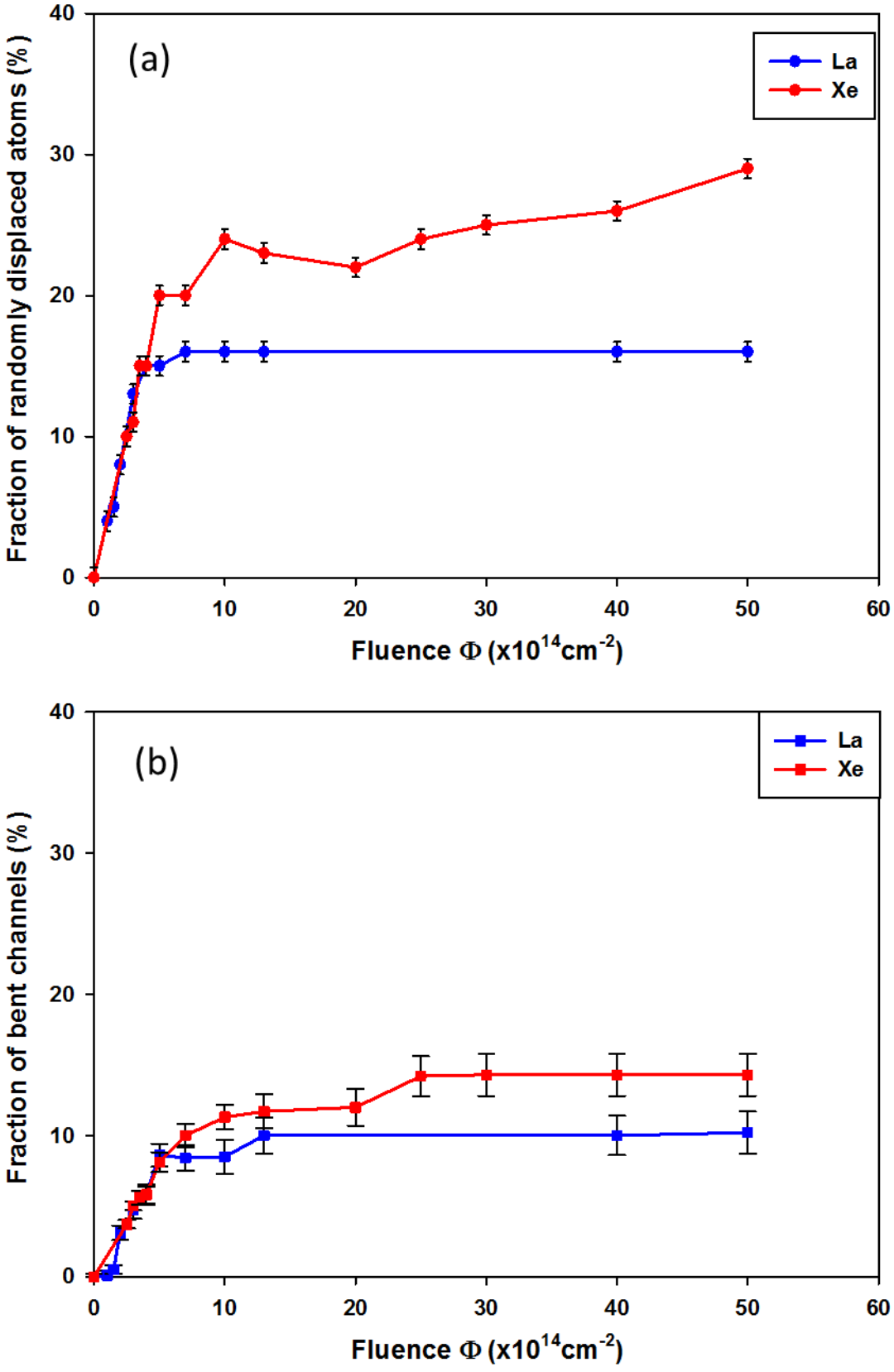

Figure 3-25: Evolution of the maximum fraction of RDA (a) and BC (b) extracted from the MC simulation in the low fluence range.

References

[Brillant et al. 2011]
G. Brillant, F. Gupta, A. Pasturel. Fission products stability in uranium dioxide. Journal of Nuclear Material 412:170–176, 2011.

[Garrido *et al.* 2006]
F. Garrido, L. Nowicki and L. Thomé. Channelling investigation of the crystalline structure of U_4O_{9-y}. PHYSICAL REVIEW B 74:184114, 2006.

[IMOTO 1986]
S. IMOTO. Chemical state of fission products in irradiated UO_2, Journal of Nuclear Material 140:19-27, 1986.

[Thomé *et al.* 2004]
L. Thomé *et al*., on the use of the ^{16}O (^4He, ^4He) ^{16}O resonance for the evolution of radiation damage in oxides. Nuclear instruments and methods in Physics Research B 219-220:99-104, 2004.

[Turos et *al.* 2010]
A. Turos, L. Nowicki, A. Stonert, K. Pagowska, J. Jagielski, A. Muecklich. Monte Carlo simulations of ion channelling in crystals containing extended defects. Nuclear Instruments and Methods in Physics Research B 268:1718–1722, 2010.

[Turos *et al.* 2014]
A. Turos, P. Jozwik, L. Nowicki, N. Sathish, Ion channeling study of defects in compound crystals using Monte Carlo simulations. Nuclear Instruments and Methods in Physics Research B 332:50–55, 2014.

[Willis 1964]
B.T.M. Willis, Structures of UO_2, UO_{2+x} andU_4O_9 by neutron diffraction. Journal de Physique, 25 (5), pp.431-439, 1964.

Chapter 4

Damage evolution in urania by using *in situ* Transmission Electron Microscopy coupled to ion irradiation

This chapter presents the Transmission Electron Microscopy (TEM) experiments that were performed to investigate the microstructural evolution in UO_2 crystals induced by the implantation of low energy ions. In this chapter the experimental conditions and the images that were obtained by *in situ* TEM experiments on single crystals UO_2 implanted with lanthanum (La) ions or noble gas xenon (Xe) at 773 K are presented and discussed. The analysis of TEM images and the damage evolution of implanting La or Xe ions are finally discussed.

4.1 *In situ* microstructure observation by Transmission Electron Microscopy

In situ TEM experiment with low energy La and Xe ions at 773 K were performed at the JANNuS-Orsay facility (with IRMA ion implantor and TEM connected together) to investigate at the atomic scale the formation and evolution of defects in irradiated UO_2 single crystals.

4.1.1 Experimental conditions

Thin <100> oriented UO_2 single crystals were implanted either with 265 KeV La ions (R_p ~ 39 nm) or with 260 KeV Xe ions (R_p ~ 40 nm) at 773 K. The implantation incident angle (the angle between the ion beam and the normal to the surface) is 42°. Bright field TEM images were recorded at different fluence steps up to $4x10^{15}cm^{-2}$, at 773 K and/or at room temperature (see the temperature details below). The experimental conditions were fully detailed in chapter 2.

Table 4-1: Experimental conditions used for TEM experiments. Range and range straggling were calculated by using the SRIM code.

Ions implanted	Z	Mass(u)	Energy (KeV)	Range R_p (*nm*)	Range straggling ΔR_p (*nm*)	Fluence range (cm^{-2})	Mean flux ($cm^{-2}.s^{-1}$)	Fraction of implanted ions at max (at. %)
$^{131}Xe^{2+}$	54	130.905	260	40	24	From 10^{13} up to $4x10^{15}$	$1x10^{11}$	~ 0.4%
$^{139}La^{2+}$	57	138.906	265	39	23	From 10^{13} up to $7x10^{14}$	$4x10^{11}$	~ 0.09%

4.1.2 Irradiation with lanthanum ions (La)

Before irradiation the virgin crystal was examined. We observed on the bright field (BF) image (see figure 4-1) a homogenous zone with almost no defect, except some holes created during the chemical etching induced by the acid (see the chapter 2 describing the experimental procedure). The thin foil has a thickness of 40 to 60 nm as measured by Electron Energy Loss Spectroscopy (EELS) [Egerton 2009] in this zone.

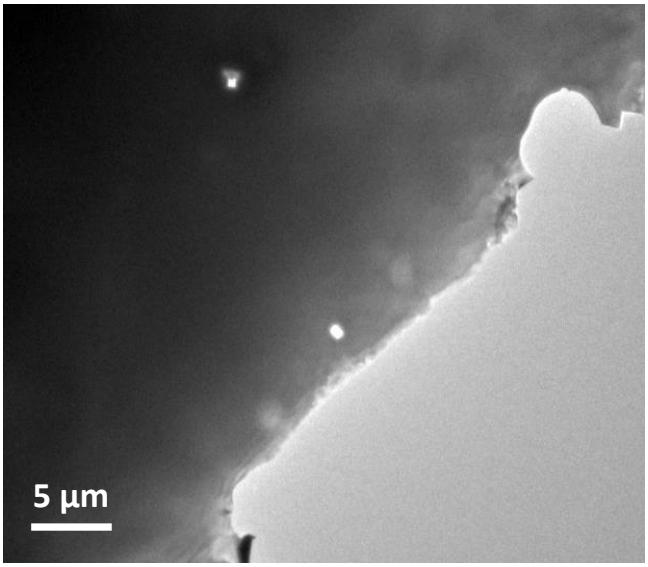

Figure 4-1: Bright-field TEM image recorded on a UO_2 thin foil before irradiation. Almost no defect can be seen (last step of thin foil prepared by chemical etching see the chapter 2).

When increasing the fluence of La ions, the following steps are seen:

(i) The thin foil was heated up to 773 K in 15 minutes under vacuum (~$1x10^{-3}$ Pa), and then was implanted with $5x10^{13}$ cm^{-2} La ions with a mean flux of $4x10^{11}$ $cm^{-2}.s^{-1}$. The bright field images show the creation of black dots defects as shown in figure 4-2, having a mean diameter of 6 nm and a density of approximately $8x10^{23}m^{-3}$.

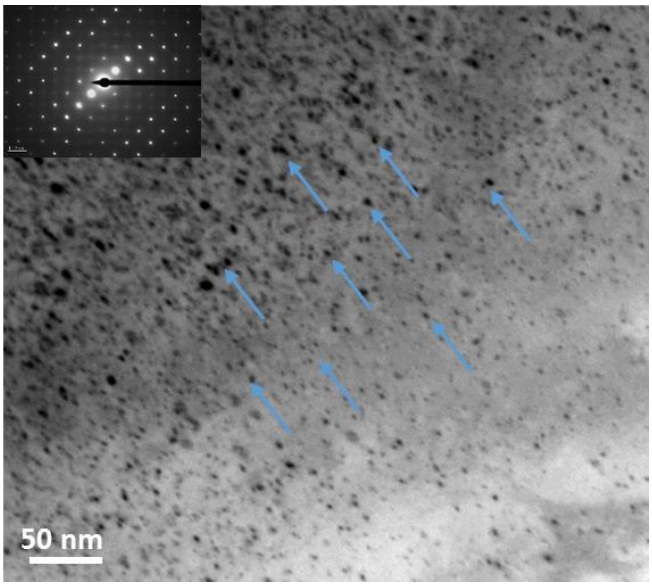

Figure 4-2: Bright field TEM image recorded on a UO_2 thin foil implanted at $\Phi = 5x10^{13}$ cm^{-2} with La ions at 773 K. The inset shows the corresponding diffraction pattern. Black dot defects are indicated by arrows.

(ii) The thin foil was further implanted at $1x10^{14}$ cm^{-2}. Black dots defects (mean diameter is 8 nm) are observed and dislocation loops, with a mean diameter is 13 nm, start to appear, as shown in figure 4-3.

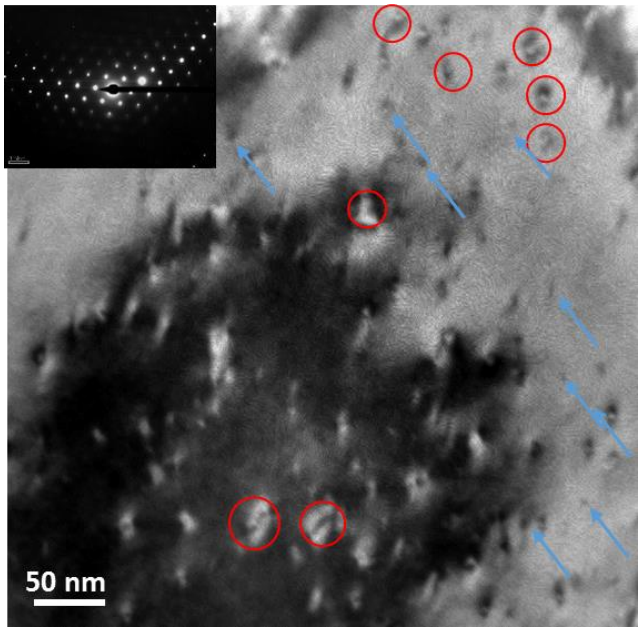

Figure 4-3: Bright field TEM image recorded on a UO_2 thin foil implanted at $\Phi = 1x10^{14}$ cm^{-2} with La ions at 773 K. Back dots defects and dislocation loops are indicated by blue arrows and red circles, respectively. The inset shows the corresponding diffraction pattern.

(iii) The thin foil was further implanted up to $2x10^{14}$ cm^{-2}, at 773 K. We still observed black dots defects with a mean diameter is 8 nm and larger dislocation loops (mean diameter is increasing to 30 nm) as it was noticeable by eyes as shown in figure 4-4.

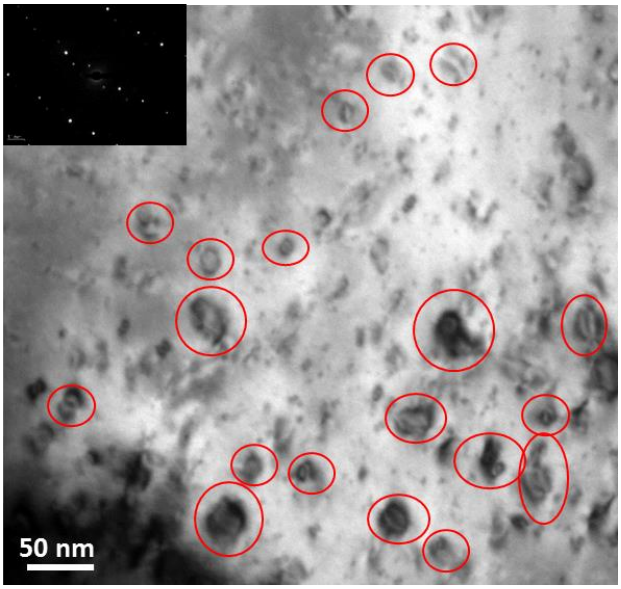

Figure 4-4: Bright field TEM image recorded on a UO_2 thin foil implanted at $\Phi = 2x10^{14}$ cm^{-2} with La ions at 773 K. Dislocation loops are indicated by red circles. The inset shows the corresponding diffraction pattern.

(iv) The thin foil was further implanted up to $3x10^{14}$ cm^{-2}. The TEM images show the presence of black dots with a mean diameter is 7 nm, more large dislocation loops with a mean diameter is 34 nm. Dislocation lines, with a mean length is 36 nm, start to be created, as shown in figure 4-5.

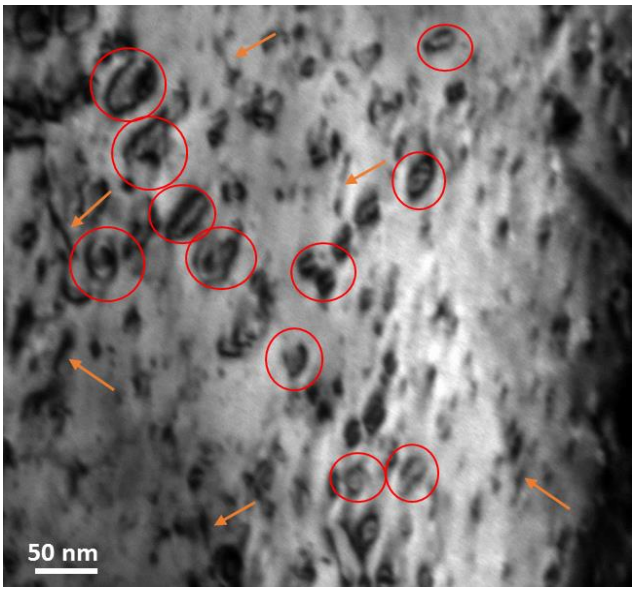

Figure 4-5: Bright field TEM image recorded on a UO_2 thin foil implanted at $\Phi = 3x10^{14}$ cm^{-2} at 773 K. Dislocation lines and loops are indicated by orange arrows and red circles, respectively.

(v) The thin foil was futher implanted at a fluence $4x10^{14}$ cm^{-2}. Some black dots with a mean diameter 8 nm, dislocation lines and loops with mean length and diameter 37 and 27 nm, respectively, were observed and they started to organize in certain directions to form a network of a tangled dislocations as shown in figure 4-6.

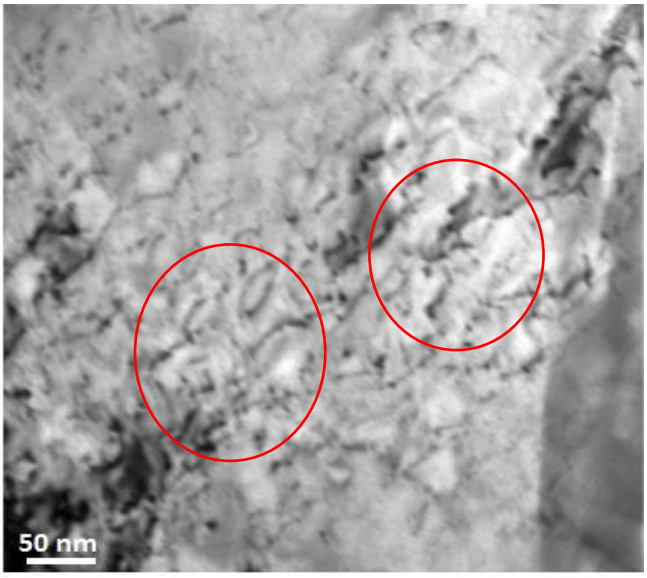

Figure 4-6: Bright field TEM image recorded on a UO_2 thin foil implanted at $\Phi = 4x10^{14}$ cm^{-2} with La ions at 773 K. Dislocation networks are indicated by red circles.

(vi) The thin foil was implanted with $5x10^{14}cm^{-2}$, and then up to $7x10^{14}cm^{-2}$, at 773 K. The TEM images show clearly a network of tangled dislocations (see figure 4-7).

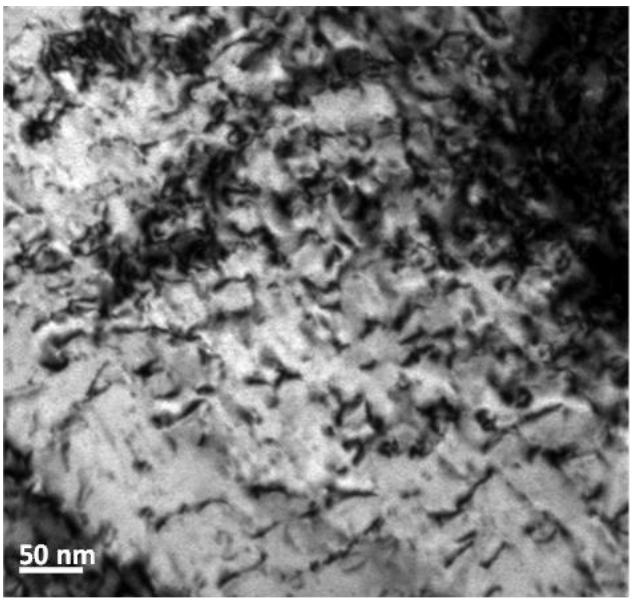

Figure 4-7: Bright field TEM image recorded on a UO_2 thin foil implanted at $\Phi = 7x10^{14}$ cm^{-2} with La ions at 773 K. A tangled dislocation network is evidenced.

The damage evolution of 265 KeV La implanted UO_2 single crystal at 773 K can be summarized as shown in figure 4-8. The results obtained can be summarized into three regions:

(i) The first fluence range ($\Phi < 5x10^{13}$ cm^{-2}): the main defects is the black dot defects.
(ii) The second fluence range ($1x10^{14}$ $cm^{-2} < \Phi < 3x10^{14}$ cm^{-2}): the main defects are dislocation loops and lines.
(iii) The third fluence range ($\Phi > 3x10^{14}$ cm^{-2}): the main defects are tangled dislocation networks and dislocation loops.

Table 4-2 summarized the types of defects that were observed and their characteristics as a function of the fluence. Density of dislocation loops and lines are not given here as they are not distributed uniformly in the zones where the defects were created. It is also important to mention that the diffraction pattern that were provided for TEM image shows a highly oriented diffraction pattern even when the crystal heavily restructured and many defects created that means the UO_2 crystal keeps its crystalline structure under irradiation.

Table 4-2: Various types of defects were observed in a UO_2 thin foil implanted with La ions at 773 K with at different fluences: Mean size and confidence interval are given $[\bar{x} - \frac{2\sigma}{\sqrt{N}}, \bar{x} + \frac{2\sigma}{\sqrt{N}}]$.

Fluence (cm^{-2})	**Black dots**		**Dislocation loops Mean diameter (nm)**	**Dislocation lines Mean length (nm)**	**Dislocation network**
	Mean diameter (nm)	**Density ($x10^{23}$ m^{-3})**			
$5x10^{13}$	6 ± 0.1	8 ± 2	_	_	_
$1x10^{14}$	8 ± 0.3	8 ± 2.5	13 ± 1	_	_
$2x10^{14}$	8 ± 0.3	9.7 ± 3.5	30 ± 2.5	_	_
$3x10^{14}$	7 ± 0.5	5.5 ± 2.8	34 ± 3.5	36 ± 5	_
$4x10^{14}$	9 ± 1	2 ± 1	27 ± 4	37 ± 6	Starts to appear
$5x10^{14}$	_	_	_	_	Clearly observed

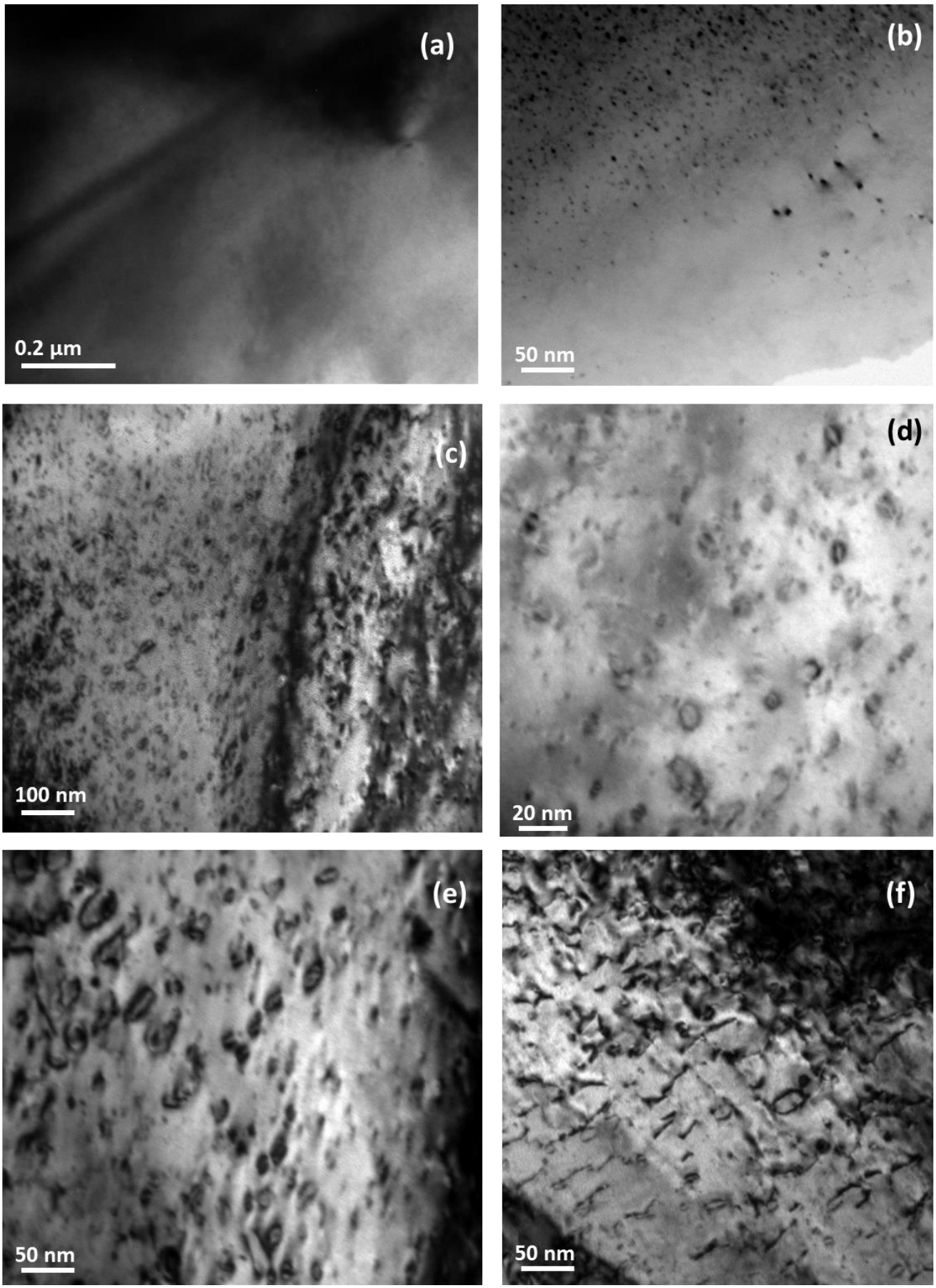

Figure 4-8: Bright-field TEM images recorded on a UO_2 thin foil during irradiation with 265 keV La ions at 773 K at different fluence steps: (a) before implantation, (b) $5x10^{13}cm^{-2}$, (c) $1x10^{14}$ cm^{-2}, (d) $2x10^{14}$ cm^{-2}, (e) $3x10^{14}$ cm^{-2}, (f) $7x10^{14}$ cm^{-2}.

4.1.3 Irradiation with noble gas xenon ions

Before irradiation the virgin crystal was examined. We observed on bright field (BF) images (see figure 4-9) the presence of some small black dots defects, which were created during the preparation of the thin foil by mechanical polishing and ion milling (see the chapter 2 describing the experimental procedure). These black dots defects were not observed in the thin foil that was prepared by chemical etching. The black dots also observed in the studies performed by previous workers: Ye *et al.* observed these defects in virgin crystal after preparation [Ye *et al*. 2013]. Their size (mean diameter) is within the range 6-7 nm, and their density is approx. 5.6×10^{23} m^{-3}. The thin foil has a thickness of 40 to 60 nm as measured by Electron Energy Loss Spectroscopy (EELS) in this zone.

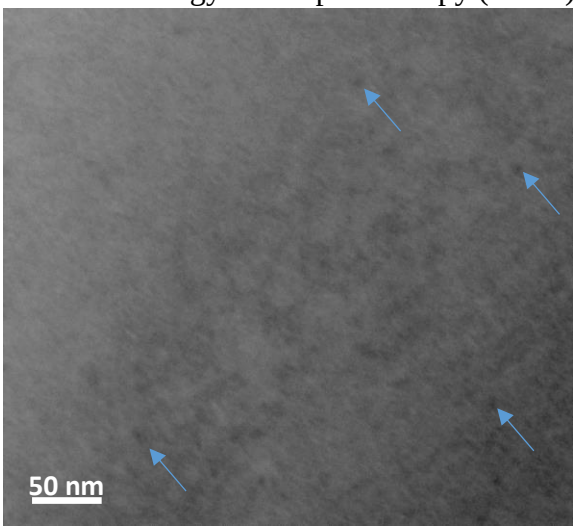

Figure 4-9: Bright field TEM image recorded on a virgin crystal (last step of thin foil prepared by ion milling). Black dot defects are seen and indicated by arrows.

The following section describes the characteristic implantation steps associated to the main evolution in the irradiation UO_2 with Xe ions.

(i) The thin foil was heated up to 773 K in 10 minutes under vacuum (~1×10^{-3} Pa), and was then implanted as a first step with 1×10^{13} cm^{-2} Xe ions, with a mean flux of 1×10^{11} $cm^{-2}.s^{-1}$. The bright field (BF) images (see figure 4-10) show a higher density of black dots defects, created by irradiation [Rosenbaum 1975], having a mean diameter of 6 nm and a density of approximately 6.64×10^{23} m^{-3}.

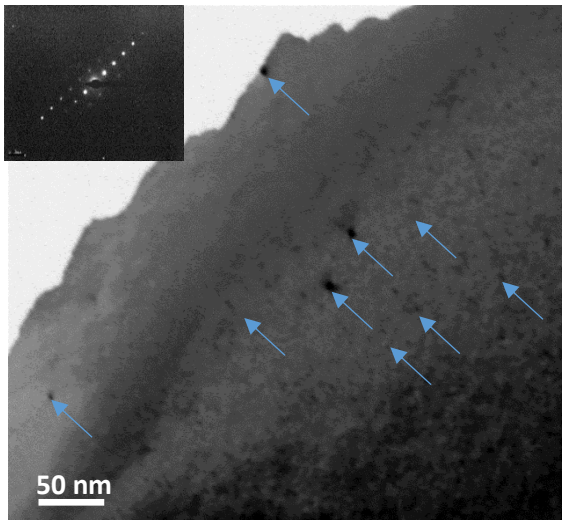

Figure 4-10: Bright field TEM image recorded on a UO_2 thin foil implanted at $\Phi = 1 \times 10^{13}$ cm^{-2} with Xe ions at 773 K. The inset shows the corresponding diffraction pattern. Black dot defects are indicated by arrows.

(ii) The thin foil was implanted up to $1x10^{14}$ cm^{-2} with the same mean flux at 773 K. A higher density of black dots defects (with a mean diameter is 6 nm) is observed and dislocation loops (with a mean diameter 11 nm) start to appear with some dislocation lines, as shown in Figure 4-11.

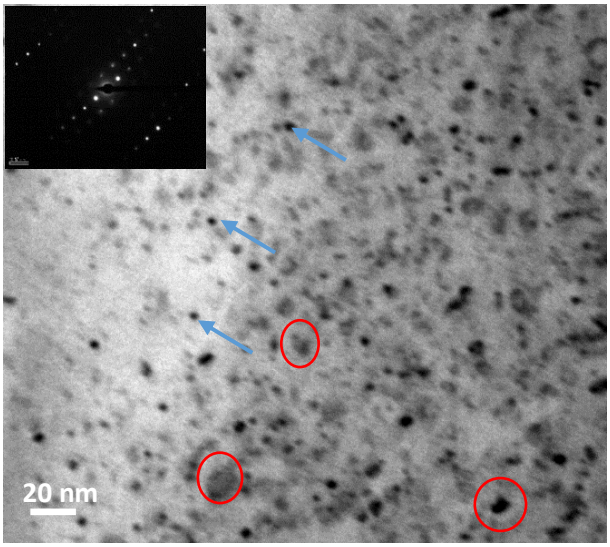

Figure 4-11: Bright field TEM image recorded on a UO_2 thin foil implanted at $\Phi = 1x10^{14}$ cm^{-2} with Xe ions at 773 K. Back dots defects and dislocation loops are indicated by blue arrows and red circles, respectively. The inset shows the corresponding diffraction pattern.

(iii) The thin foil was further implanted up to $2x10^{14}$ cm^{-2}, at 773 K, we still observe black dots defects with a mean diameter is 10 nm, longer dislocation lines with a mean length of 34 nm and larger dislocation loops with a mean diameter of 31 nm.

(iv) In the next step, thin foil was implanted up to $4x10^{14}$ cm^{-2}, we still observed black dots with a mean diameter is 7 nm, a higher density of larger dislocation lines with a mean length is 54 nm and dislocation loops with a mean diameter is 27 nm (see figure 4-12).

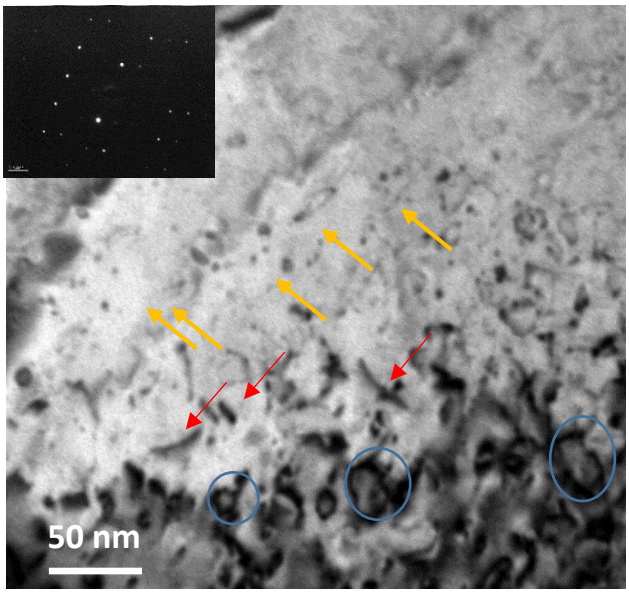

Figure 4-12: Bright field TEM image recorded on a UO_2 thin foil implanted at $\Phi = 4x10^{14}$ cm^{-2} with Xe ions at 773 K. Back dots defects, dislocation loops and lines are indicated by yellow arrows, blue circles and red arrows, respectively. The inset shows the corresponding diffraction pattern.

(v) We continue implanting up to fluence $6x10^{14}$ cm^{-2}, at 773 K. The TEM images show the presence of several types of defects: black dots defects with a mean diameter is 7 nm, dislocation lines with a mean length is 47 nm and dislocation loops with a mean diameter is 19 nm.

(vi) The thin foil was implanted at fluence $8x10^{14}$ cm^{-2}. The black dots were still observed, with a mean diameter is 4 nm, dislocation lines and loops with a mean length and diameter is 8 and 18 nm, respectively. Shorter dislocation lines are observed because they start to connect together and organize in certain directions to form a network of a tangled dislocations as shown in figure 4-13.

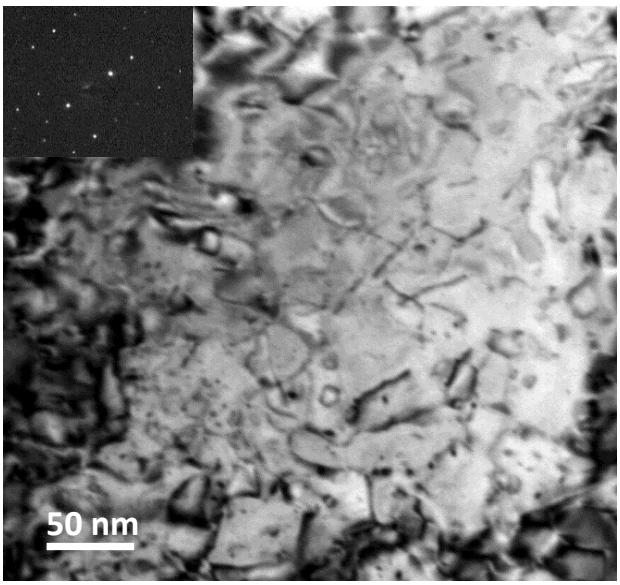

Figure 4-13: Bright field images showing apparition of tangled dislocation network in UO_2 thin foil implanted with 260 KeV Xe at 773 K at $\Phi = 8x10^{14}$ cm^{-2}. The inset shows the corresponding diffraction pattern.

(VII) The thin foil was implanted up to $1x10^{15}$ cm^{-2}. TEM images show mainly a network of tangled dislocations as shown in figure 4-14.

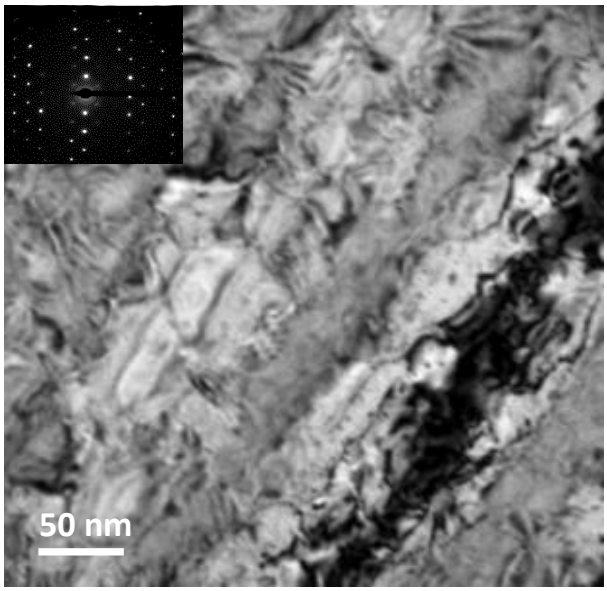

Figure 4-14: Bright field TEM images recorded on a UO_2 thin foil implanted with 260 KeV Xe at 773 K at $\Phi = 1x10^{15}$ cm^{-2} showing the formation of a tangled dislocation network. The inset shows the corresponding diffraction pattern.

(viii) The upper fluence investigated in this study was $4x10^{15}$ cm^{-2}. A network of tangled dislocations is seen in the TEM images.

The damage evolution of implanting 260 KeV Xe ions in single crystal UO_2 at 773 K can be summarized as in figure 4-15, where the defect apparition and evolution observed as a function of the fluence up to $4x10^{15}cm^{-2}$. The diffraction pattern that were provided for each TEM image shows a highly oriented diffraction pattern for Xe implanted crystal even when the crystal heavily restructured and many defects created that means the UO_2 crystal keeps its crystalline structure under irradiation. The results obtained can be summarized into three regions:

(i) The first fluence range ($\Phi < 2x10^{14}$ cm^{-2}): the main created defects is the black dot defects.
(ii) The second fluence range ($2x1014$ $cm^{-2} < \Phi < 5x10^{14}$ cm^{-2}): the main defects are dislocation loops, lines.
(iii) The third fluence range ($\Phi > 5x10^{14}$ cm^{-2}): the main defects observed is a network of tangled dislocation.

Table 4-3 summarized the types of defects that were observed and their characteristics as a function of the fluence.

Table 4-3: Various types of defects were observed in a UO_2 thin foil implanted with Xe ions at 773 K with at different fluences: Mean size and confidence interval are given $[\bar{x} - \frac{2\sigma}{\sqrt{N}}, \bar{x} + \frac{2\sigma}{\sqrt{N}}]$.

Fluence (cm^{-2})	**Black dots**		**Dislocation loops Mean diameter (nm)**	**Dislocation lines Mean length (nm)**	**Dislocation network**
	Mean diameter (nm)	**Density ($x10^{23}$ m^{-3})**			
$1x10^{13}$	6 ± 0.7	6.5 ± 2.5	_	_	_
$1x10^{14}$	6 ± 0.6	6.3 ± 2	11 ± 2.5	Starts to appear	_
$2x10^{14}$	10 ± 0.3	3.0 ± 0.9	31 ± 6	34 ± 8.5	_
$4x10^{14}$	7 ± 0.4	5.2 ± 1.7	27 ± 8	54 ± 12	_
$6x10^{14}$	7 ± 0.4	5.3 ± 1.7	18.6 ± 3	47 ± 10	_
$8x10^{14}$	4 ± 1	_	18 ± 3	28 ± 4	Starts to appear
$1x10^{15}$	_		_	_	Clearly observed
$4x10^{15}$	_		_	_	Clearly observed

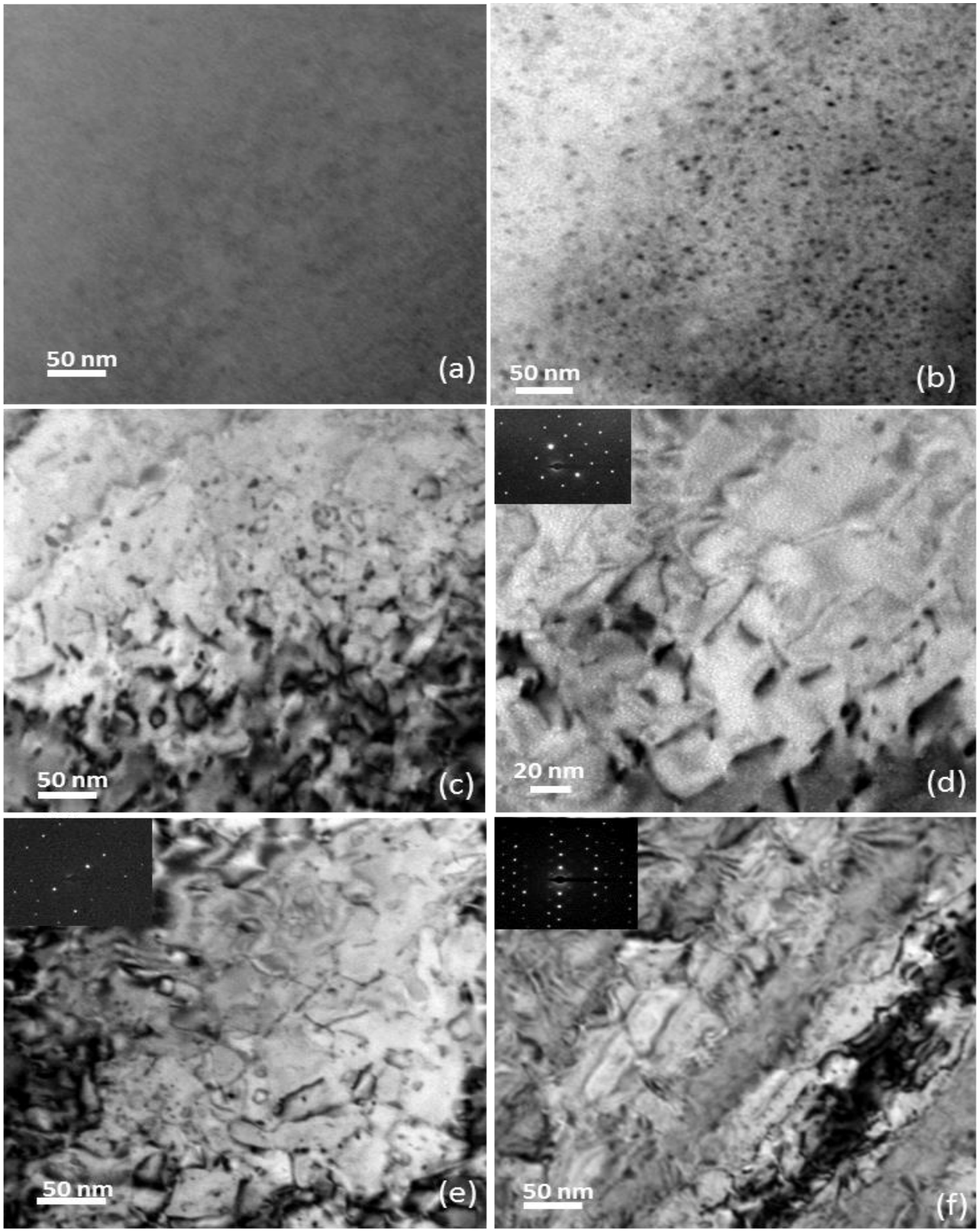

Figure 4-15: Bright-field TEM images recorded on UO_2 thin foil during irradiation with 260-keV Xe ions at 773 K at different fluences: (a) before implantation, (b) $1x10^{14}$ cm^{-2}, (c) $4x10^{14}$ cm^{-2}, (d) $6x10^{14}$ cm^{-2}, (e) $8x10^{14}$ cm^{-2}, (f) $4x10^{15}$ cm^{-2}. The inset shows the corresponding diffraction pattern.

After presenting the damage evolution of implanting 260 keV Xe ions or 265 keV La ions in single crystals UO_2 at 773 K, as summarized in figure 4-8 and figure 4-15, we can conclude that similar defects appear for both ions and the same evolution of defects as a function of the fluence is observed. The various defects evolved as the following: formation the black dot defects were observed as a first type of defects created, then dislocation lines and loops appeared and evolved as a function of the fluence until they started to be become less distinguishable and some of them merge and interact together. This process continued by forming a tangled dislocation network. The diffraction pattern that were provided for each TEM image shows that the UO_2 crystal keeps its crystalline structure under irradiation regardless the nature of the implanted ion.

4-2 Investigation of the presence of bubbles or cavities

Several attempts to see the formation of Xe bubbles were performed at low fluences. Small Xe bubbles with a mean diameter is 4.5 nm and a density of 1.3×10^{24} m^{-3} are observed at a threshold fluence of 4×10^{14} cm^{-2}. The images of bubbles were taken at 773 K using under/over focus conditions of 10 microns. It is important to mention, that we were not able to see the bubbles by eye at lower fluences than 4×10^{14} cm^{-2} and with lower values of under/over focus conditions at 773 K.

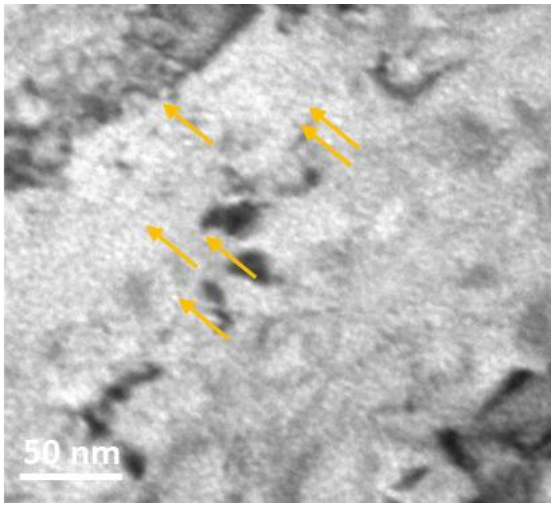

Figure 4-16: Bright field TEM images recorded in with underfocusing conditions of 10 microns showing bubbles in UO_2 thin foil implanted with 260 KeV Xe at 773 K at $\Phi = 4 \times 10^{14}$ cm^{-2}. Bubbles are indicated by yellow arrows. (The image were taken at 773 K).

When the thin foil was implanted with Xe ions at 6×10^{14} cm^{-2} at 773 K, the TEM images were taken at room temperature to record better images for the bubbles, as the images that taken at high temperature seems to be affected by the vibration of matrix atoms at high temperature that makes difficulties to adjust the focus and astigmatism of the images, especially when we were working at high magnification (see figure 4-16). Figure 4-17 shows the images recorded at room temperature at a fluence 6×10^{14} cm^{-2} with under/over focus conditions 2 microns where the bubbles are clearly seen.

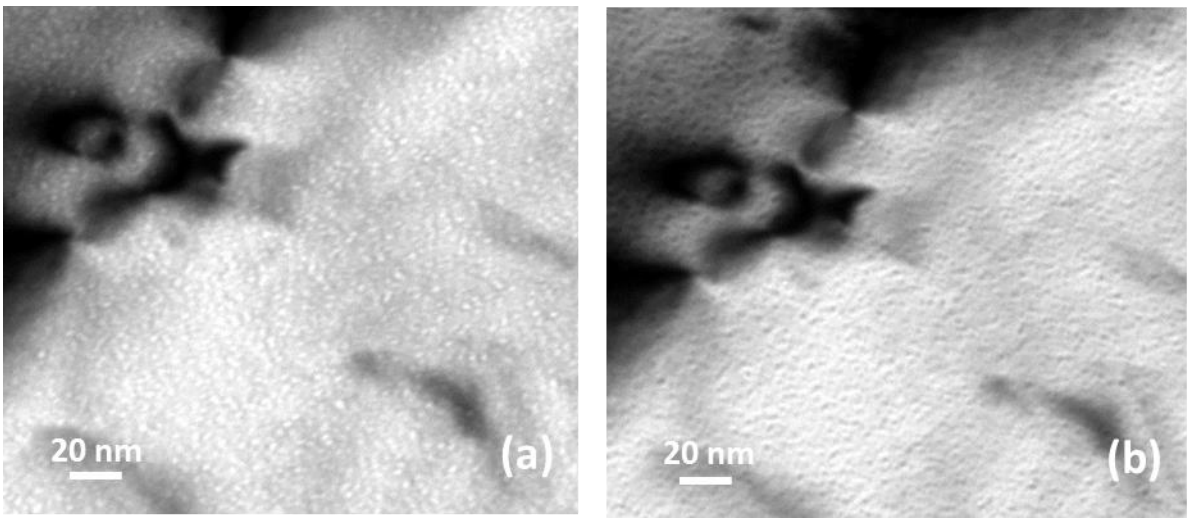

Figure 4-17: Bright field TEM images recorded on a UO_2 thin foil implanted with 260 KeV Xe at 773 K at $\Phi = 6x10^{14}$ cm^{-2}. Images were registered with (a) underfocusing and (b) overfocusing condition with 2 microns (The image was taken at room temperature).

The mean diameter of Xe bubbles measured at this fluence is about 1.9 nm, using under/over focus conditions of 2 microns. The size which was obtained at room temperature in this experiment is in a good agreement with the results of the literature: Kashibe *et al.* observed a high density of small bubbles of about 2 nm in diameter uniformly distributed in the matrix of irradiated UO_2 fuel with maximum irradiation temperature being around 1073 K [Kashibe *et al.* 1993]. Michel *et al.* observed the presence of nanometer size of Xe bubbles in irradiated thin UO_2 foil with 390 keV Xe at 870 K [Michel *et al.* 2012]. In these studies, the size of bubbles were measured on TEM images recorded at room temperature.

The thin foil was implanted further up to $1x10^{15}$ cm^{-2}. TEM images taken at 773 K show bubbles with a mean diameter is 3.9 nm as shown in figure 4-18. The size which was obtained at 773 K in this experiment is in a good agreement with the results that were obtained by Sattonnay *et al.* where they observed Xe bubbles with a diameter of 3-5 nm in 260 keV Xe irradiated UO_2 single crystal at room temperature and further annealed up to 670 K [Sattonnay *et al.* 2006].

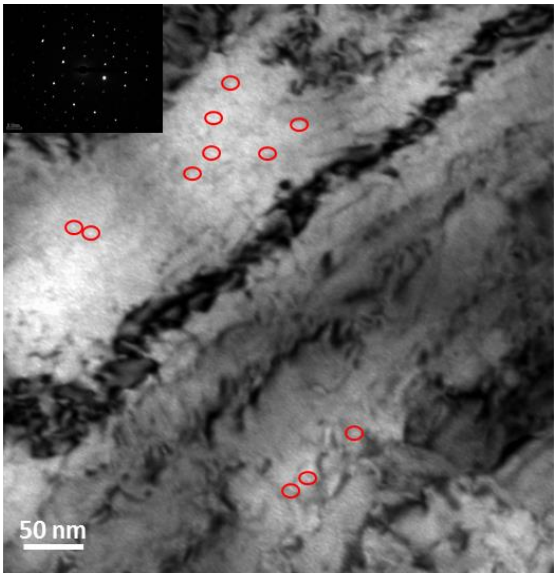

Figure 4-18: Bright field (measured at 9 microns underfocus) TEM images recorded on a UO_2 thin foil implanted with 260 KeV Xe at 773 K at $\Phi = 1x10^{15}$ cm^{-2} (Image taken at 773 K). Bubbles are indicated by red circles.

At the upper fluence exposed in this study was $4x10^{15}$ cm^{-2}, the bubbles were observed with a mean diameter is 2 nm at room temperature (measured at ±2 microns) as shown in figure 4-19.

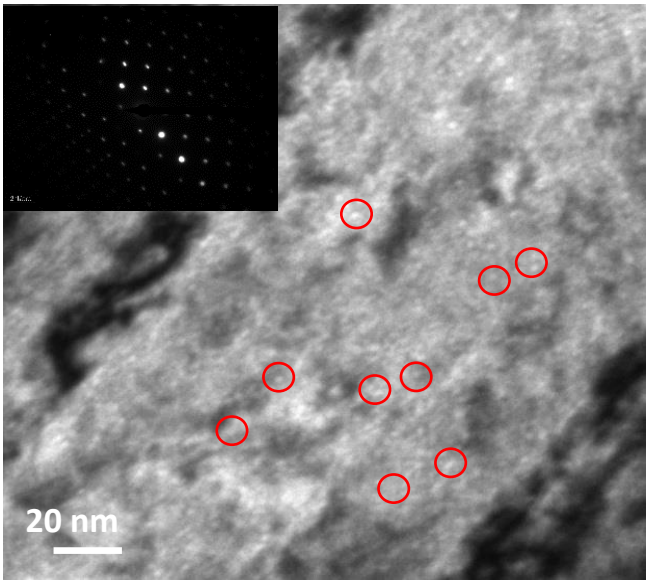

Figure 4-19: Bright field (2 microns underfocus) TEM images recorded on a UO_2 thin foil implanted with 260 KeV Xe at 773 K at $\Phi = 4x10^{15}$ cm^{-2} (Image taken at room temperature). Bubbles are indicated by red circles.

Obtaining bubbles with bigger diameter at 773 K compare to the bubbles that were observed at room temperature could be explained by the ideal gas law:

$$PV = nRT \tag{5-1}$$

Where: P: pressure of gas in the bubbles; V: volume of the gas particles, n: the number of moles of the gas, R: is the specific gas constant, T the absolute temperature. By assuming the volume of a Xe bubble:

$$V = \frac{4}{3}\pi R^3 \tag{5-2}$$

Where R: radius of the bubble.
Assuming the bubble is in equilibrium with the surrounding medium; so the overpressure can be expressed by Laplace's law:

$$P = \frac{2\gamma}{R} \tag{5-3}$$

Where: γ: is the surface tension.
By substituting equation 2 and 3 in equation 1, we can have the relationship between the temperature and the radius of the bubble:

$$\frac{R(T_2)}{R(T_1)} = \sqrt{\frac{T_2}{T_1}}$$

Taking an example the temperature at which we preformed the experiment: 773 K:

$$\frac{R(773)}{R(293)} = \sqrt{\frac{773}{293}} = 1.6$$

As the bubble diameter observed at room temperature is: 2 nm (R = 1 nm) then according to the relationship the radius of the bubble at 773 K is about 3.2 nm. Such a result is in a good agreement with diameter that was experimentally observed for the bubbles at 773 K.

Figure 4-20 and table 4-4 present the bubble evolution: (a) the mean diameter and in (b) the density as a function of fluence based on TEM images recorded at room temperature. The bubble density was calculated at each of fluence by assuming that the thin foil thickness is ~ 45 nm. The statistical uncertainties were calculated using the confidence interval of 95%.

The following expression was used to calculate the upper and lower 95% confidence limits:

Upper 95% limit = $\overline{x} + (1.96 * \frac{\sigma}{\sqrt{N}})$ and Lower 95% limit = $\overline{x} - (1.96 * \frac{\sigma}{\sqrt{N}})$

Where: $\overline{x}$: Mean diameter
σ: standard deviation of the bubble distribution.
N: total number of observed bubbles
1.96: quantile of the normal distribution.

The uncertainty in measuring the density of Xe bubbles was calculated by taking into account the error in the total number of the observed bubbles ($\frac{\Delta N}{N}$) and the error in measuring the thickness of the thin foil ($\frac{\Delta e}{e}$). The following expression used to calculate the uncertainty in the bubbles density:

$$\Delta D = D * \left(\frac{\Delta N}{N} + \frac{\Delta e}{e}\right)$$

Where $\frac{\Delta N}{N} = \frac{1}{\sqrt{N}}$ and $\frac{\Delta e}{e}$ is fixed with 20% that is the uncertainty in the model that was used to measure the thickness of the thin foil.

Table 4-4: Mean diameter and density of the bubble population as a function of fluence. Mean value and the uncertainty of the distribution of observed bubbles are provided.

Fluence (cm^{-2})	**Density ($x10^{24}\ m^{-3}$)**		**Diameter (nm)**	
	Mean Value	**Uncertainty**	**Mean value**	**Uncertainty**
$4x10^{14}$	7.91	2.6	1.9	0.3
$6x10^{14}$	5.92	1.6	2.1	0.3
$8x10^{14}$	7.49	3.5	1.9	0.9
$1x10^{15}$	10.30	3.2	1.7	0.2
$2x10^{15}$	10.63	3.6	1.7	0.3
$4x10^{15}$	6.16	1.6	2.1	0.4

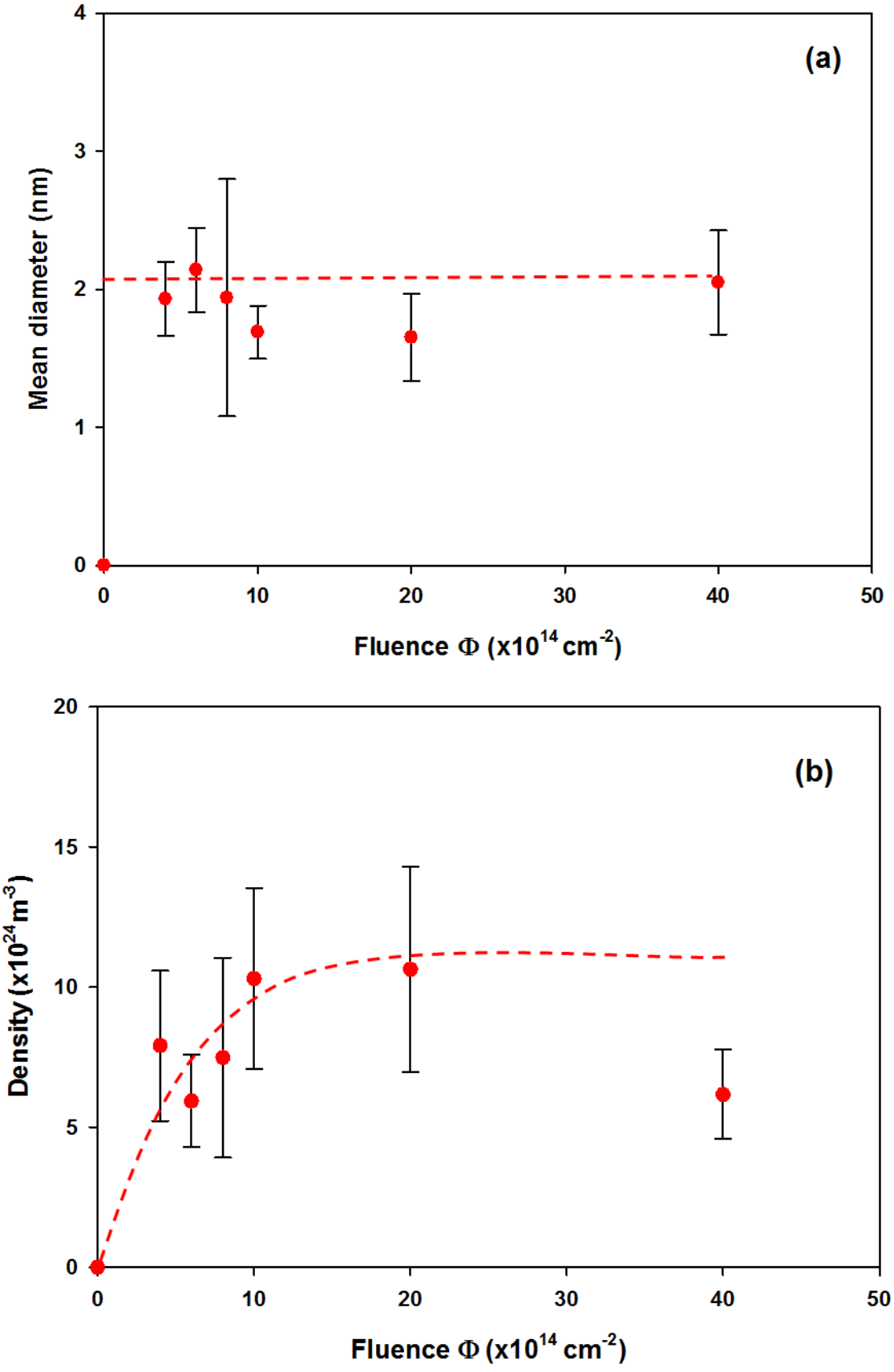

Figure 4-20: Evolution of the characteristics of bubbles: (a) the mean diameter and (b) the density as a function of the Xe fluence Φ for a thin foil implanted with 260 keV ions. The measurements were performed a room temperature.

The mean diameter of Xe bubbles almost saturates at about 2 nm as measured at room temperature up to the fluence $\Phi = 4x10^{15}$ cm^{-2}. Conversely, the bubbles density increases sharply between $4x10^{14}$ cm^{-2} and $1x10^{15}$ cm^{-2}, a stage at which the saturation bubble density is reached. Such a phenomenon was not expected since more Xe is implanted but the mean diameter of bubbles stays almost constant. A similar evolution of bubble density was also obtained by [Michel *et al*. 2012]. This is could be due to several reasons: (i) projection-limitation in the TEM technique where the image of TEM has no depth sensitivity. In other words, a single TEM image with 2D for the bubbles created in real thin foil with 3D may overlaps some bubbles and as a consequence we count less bubbles, or/and (ii) as some images taken at 773 K (see page 115 the explanation), some small bubbles were hardly seen by eyes, or/and (iii) it can be also due to not all the implanted Xe is located in bubbles. It is important to mentioned, that the small bubbles with a diameter less than 1 nm were not seen or counted due to the limitation in the TEM technique.

In summary the bubbles formation, a high density of small bubbles of about 2 nm in diameter were observed in the matrix implanted with Xe ions starting at the threshold fluence $\Phi = 4x10^{14}$ cm^{-2}. The density of these bubbles lies within a range of $1x10^{24}$ to $1x10^{25}$ m^{-3} (see figure 4-20). It was previously observed by Michel *et al*. [Michel *et al*. 2012] that nanometer-sized bubbles were observed above the fluence of $6x10^{12}$cm^{-2} at 870. Sattonnay *et al*. [Sattonnay *et al*. 2006] were also able to observe bubbles at $1x10^{16}$cm^{-2} after post annealing treatments at a threshold temperature of 670 K. According to the literature and what we observed in the experiment, there is a threshold fluence to observe bubbles at a given temperature. Regarding the formation of La cavities, several attempts to examine the formation of La precipitates or cavities were performed. No cavity was observed up to the fluence $7x10^{14}$ cm^{-2} (see figure 4-21), as demonstrated by the images taken in under/over focus conditions with 2 micron.

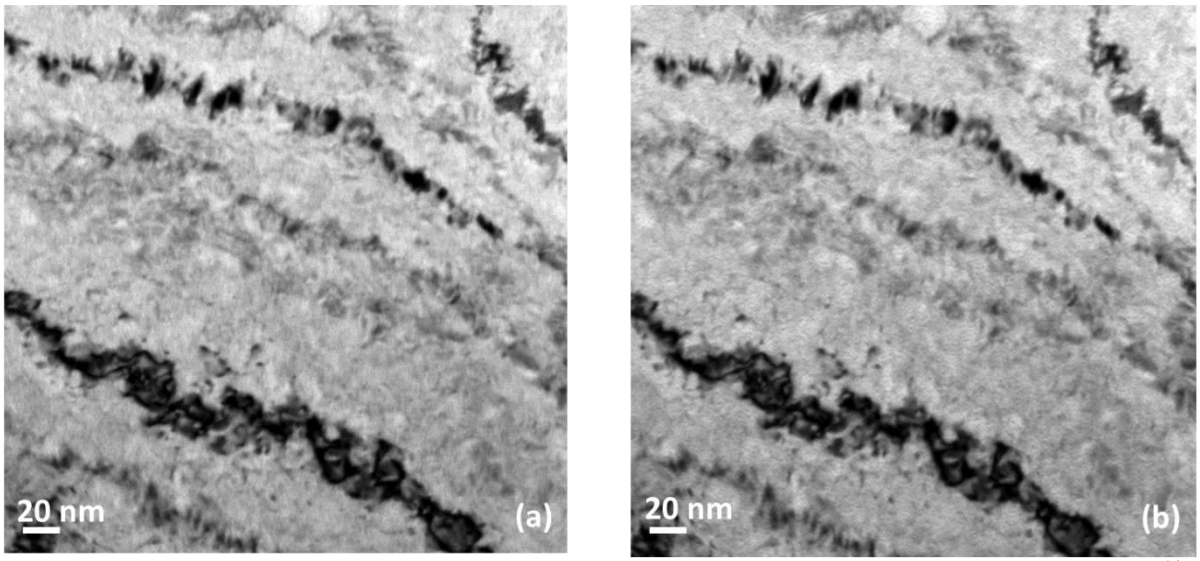

Figure 4-21: Bright field TEM image recorded on a UO_2 thin foil implanted with 265 KeV La ions at $\Phi = 7x10^{14}$ cm^{-2}. The images are registered in (a) underfocusing and (b) overfocusing condition with 2 micron.

To conclude the *in situ* TEM results, we observed that the evolution of damage in UO_2 single crystals implanted with Xe and La ions at 773 K was almost the same: the same types of defects are observed and the evolution of damage is similar for both ions, starting by the apparition of the black dots defects, creation of defects clusters and dislocation lines and loops that are then connected to form a dislocation network. The main difference that was observed between the two ions is the observation of high density of Xe bubbles, with mean diameter of 2 nm at room temperature, in the crystal implanted with Xe ions with a threshold fluence $\Phi = 4x10^{14}$ cm^{-2}, a feature that was not seen for La. Such a feature is due to the difference in the solubility between the ions since La is soluble and Xe insoluble in UO_2 lattice, this difference in behavior may likely affect the damage evolution, as it is discussed in the next chapter that discusses the evolution as measured by channeling and TEM.

References

[Brillant *et al*. 2011]
G. Brillant, F. Gupta, A. Pasturel. Fission products stability in uranium dioxide. Journal of Nuclear Material 412:170–176, 2011.

[Egerton 2009]
R F Egerton, Electron energy-loss spectroscopy in the TEM. Rep. Prog. Phys. 72:016502, 2009. (25pp).

[IMOTO 1986]
S. IMOTO. Chemical state of fission products in irradiated UO_2. Journal of Nuclear Materials, 140:19-27, 1986.

[Kashibe *et al.* 1993]
S. Kashibe, K. Une, K. Nogita. Formation and growth of intragranular fission gas bubbles in UO_2 fuels with burnup of 6-83 GWd/t. Journal of Nuclear Materials 206:22-34, 1993.

[Michel *et al*. 2012]
A. Michel, C. Sabathier, G. Carlot, O. Kaïtasov, S. Bouffard, P. Garcia, C. Valot. An in situ TEM study of the evolution of Xe bubble populations in UO2 Nucl. Instrum. Methods B 272:218-221, 2012.

[Rosenbaum 1975]
H. S. Rosenbaum, Microstructures of Irradiated Materials: Treatise on Materials, Volume 7, 1975.

[Sattonnay *et al*. 2006]
G. Sattonnay L. Vincent, F. Garrido and L. Thome´ a *et al*., Journal of Nuclear Materials 355:131-135, 2006.

[Ye *et al.* 2013]
B. Ye, A. Oaks, M. Oaks, D. Yun, W. Chen, B. Holtzman, J. Stubbins. Irradiation effects in UO_2 and CeO_2. Journal of Nuclear Materials 441:525–529, 2013.

Chapter 5

Damage evolution in urania under irradiation: role played by the foreign elements and by the temperature

The first section of this chapter discusses the role played by implanting foreign elements on the damage evolution in irradiated UO_2. The two chosen elements are La and Xe ions. We discuss in this section the damage evolution that was determined by both RBS/C and TEM and we examine the coupling between the results obtained by the two techniques in a complementary way.
The second section discusses the effect of temperature on the damage evolution in irradiated UO_2, as the temperature is one of the relevant parameters involved in the damaging process of the fuel and more specifically in the formation of High Burnup Structure. The results of this thesis are compared to similar experiments performed at room temperature on urania single crystal irradiated with the same ions and in the same irradiation conditions.

5.1 Effect of foreign elements on the damage evolution

In order to study the effect of foreign elements on damage evolution, let us start the discussion with the analysis of the channelling data that were recorded for low-energy ions implanted in UO_2 single crystals at 773 K by using the Monte Carlo simulation code and assuming the two-class model of defects: (i) the randomly displaced atoms and (ii) the bent channels. This model allowed us to take into account many types of defects such as point defects (interstitials and vacancies) and extended defects (dislocations, dislocation network), or even polygonization or amorphization.

As it was shown in the section 3.2, the two-defect model containing RDA and BC allowed us to analyze the channelling data and extract from the simulations the damage profile of RDA (providing the distribution of RDA versus depth) and the fraction of BC that represents the modification of the material structure. The two-defect model showed excellent fits and good agreement with the experimental data over a large depth (see from figure 3-14 to figure 3-17) and it succeed in fitting essentially all the characteristic features of the channelling spectra. The kinetics of damage evolution corresponding to the maximum fraction measured from the distribution versus fluence were extracted. In parallel, *in situ* TEM experiments were performed to investigate the formation of the radiation-induced defects and the presence of bubbles as a function of the ion fluence.

5.1.1 Kinetics of damage accumulation

After performing *in situ* RBS/C and TEM experiments, both techniques coupled to ion irradiation, and in order to compare and summarize the results of both techniques, the evolution of maximum fraction of RDA and BC created at each implanted fluence and the distributions of RDA and BC versus depth are plotted in figures 5-1 to figure 5-4 , as a function of the two relevant parameters for a low-energy ion implanted solid: (i) the number of displacements per atom (*dpa*) that is one of the most important scaling parameter in the field of the radiation damage, that is used to compare the radiation effects induced by elastic collisions; this parameter calculates the average number of times that a given atoms of the solid is displaced from its regular lattice site as a result of ion bombardment for a given ion fluence; (ii) the concentration of incorporated impurities in the material, which may have a significant role in creating an extra reorganization of the solid at large fluence. The *dpa* scale was calculated by using the SRIM code assuming values of displacement threshold $E_d(U) = 40$ eV and $E_d(O) = 20$ eV [Soullard et al. 1985].

According to the SRIM code, the following mathematical expression were applied for converting the fluence to *dpa* and concentration scales:

$$dpa = D_{TRIM} * 10^8 * \frac{\phi}{\left(\frac{N}{V}\right)_{UO2}}$$

$$C_{impurities} = \frac{(N/V)_{ion}}{(N/S)_{ion}} * \phi$$

$$f_{impurities} = \frac{C_{impurities}}{(N/V)_{UO2}} * 100\%$$

Where: D_{TRIM}: is the maximum of the collision events plot calculated by the SRIM code expressed in number of vacancies per ion and per angstrom, ϕ: is the ion fluence expressed in cm^{-2}, 10^8 is the conversion factor between centimeter and Angstrom, $C_{impurities}$: is the concentration of incorporated impurities, $f_{impurities}$: is the fraction of incorporated impurities, $(N/V)_{UO2}$ is the theoretical density of UO_2 (7.339 x 10^{22} atoms.cm^{-3}) and $(N/V)_{ion}/(N/S)_{ion}$: is expressed in atoms.cm^{-1} that is calculated by SRIM. Both the values of *dpa* and the fraction of incorporated impurities were calculated at the maximum of their respective distributions.

The evolution of RDA and BC are presented in figure 5-1 versus *dpa* and fraction of impurities for both ions Xe and La to compare the effects between the two ions similar in mass and different in nature: one is soluble (La) and the other is insoluble (Xe).

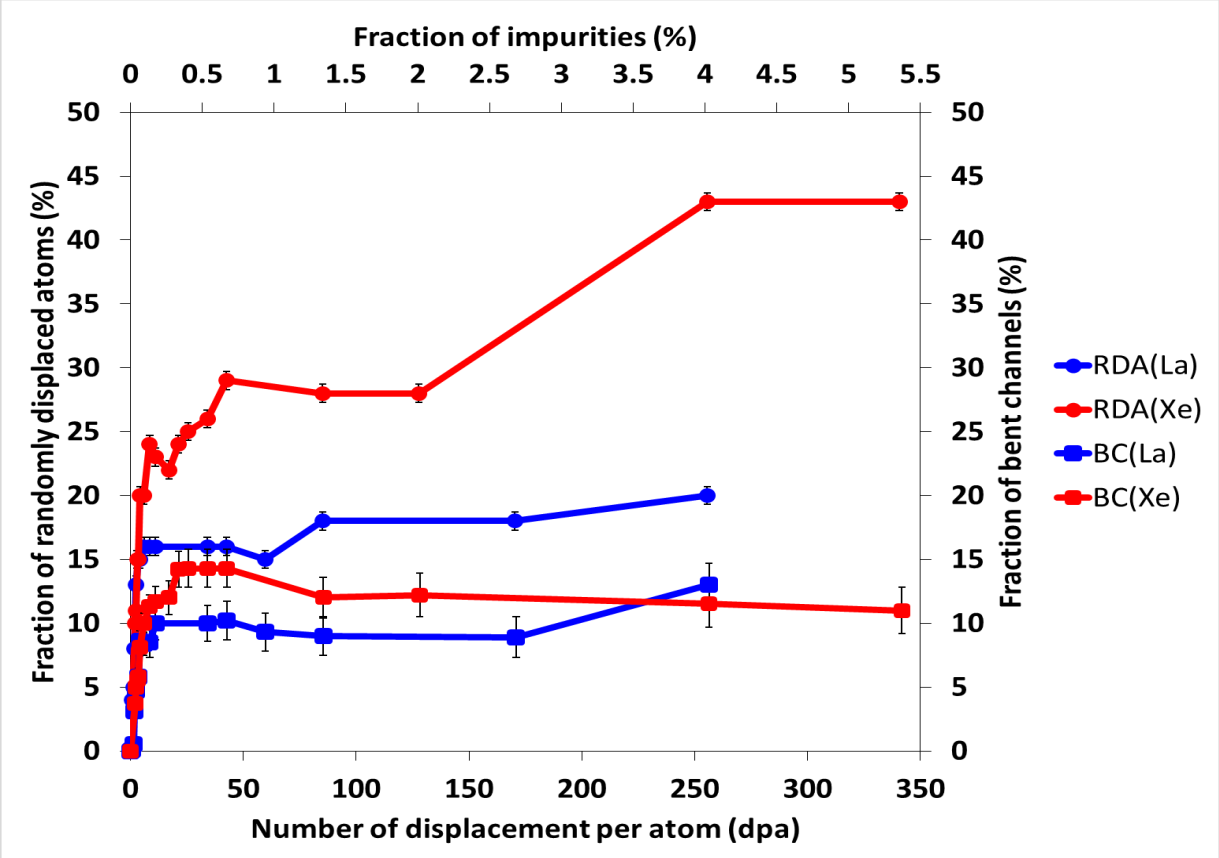

Figure 5-1: Evolution of RDA and BC versus *dpa* and versus the fraction of implanted impurities for a UO_2 crystal bombarded with 500 keV La ions or with 470 keV Xe ions.

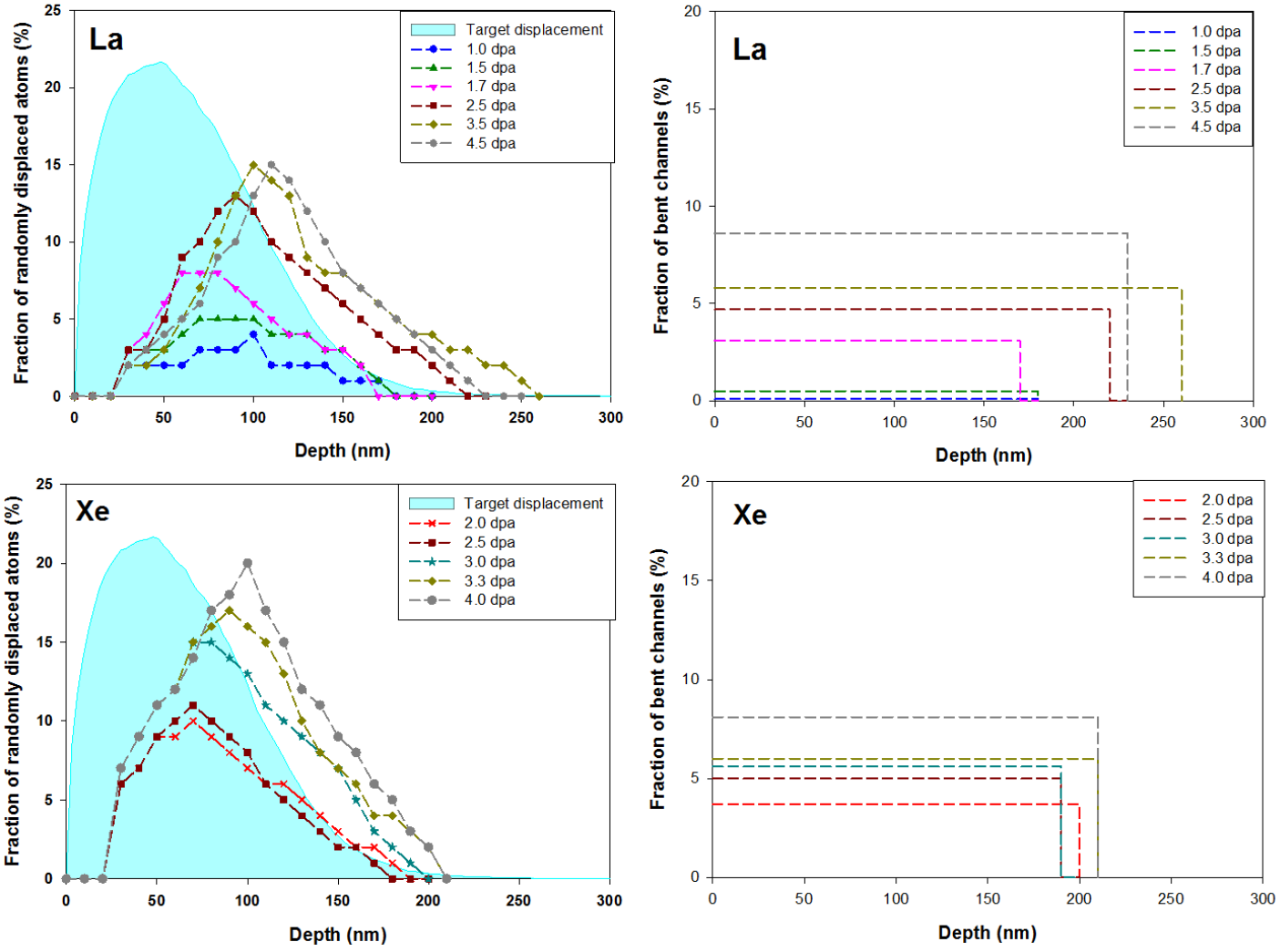

(a) (b)

Figure 5-2: Fraction of RDA (a) and BC (b) versus depth in UO_2 crystals implanted with La or Xe at low *dpa* range (*dpa* ≤ ~5 *dpa*) extracted from MC simulations. The parameters for BC are L = 50 nm and η = 25°. Depth distribution of displaced matrix atoms according to SRIM (Cyan filled area) are plotted in an arbitrary unit.

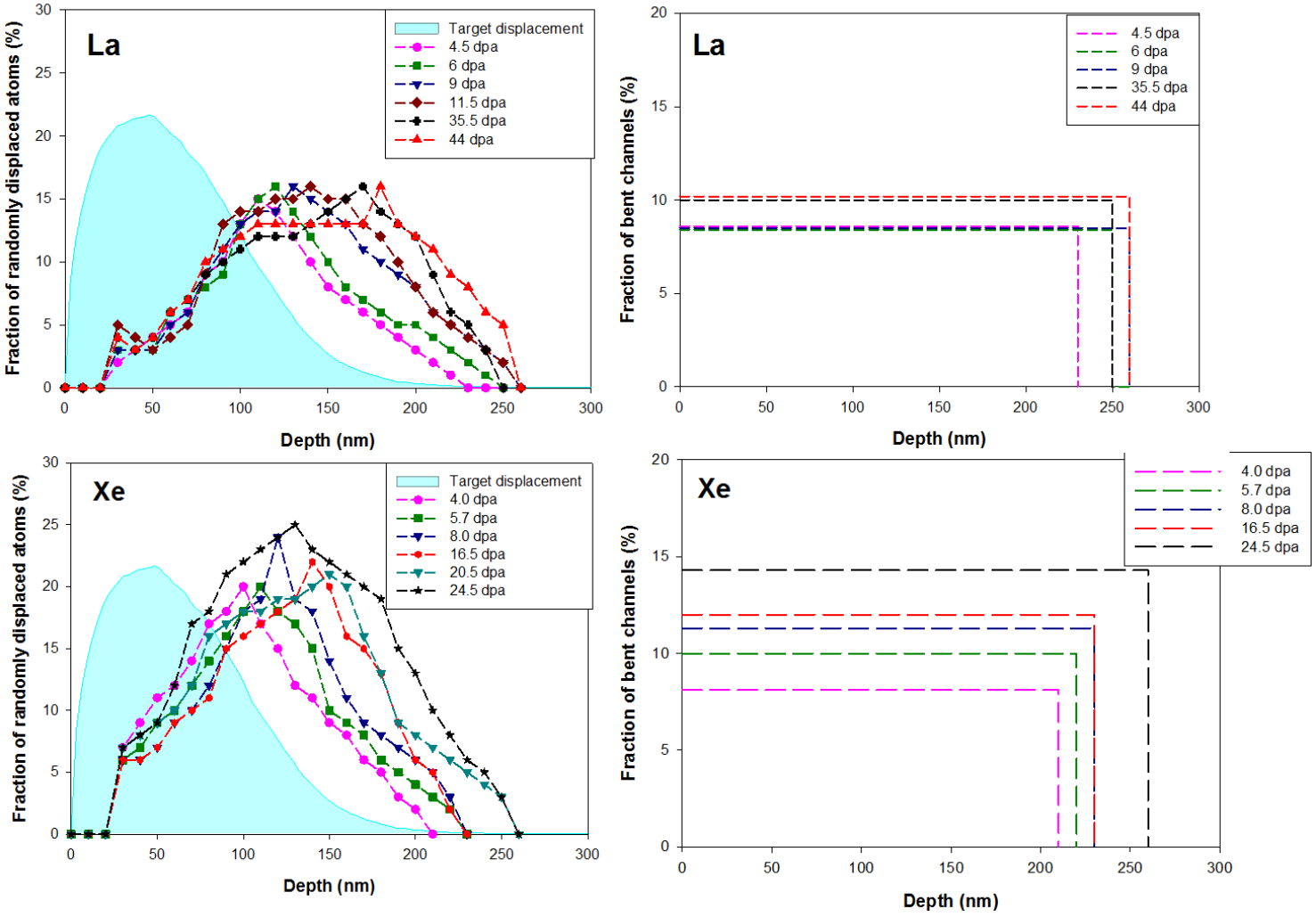

Figure 5-3: Fraction of RDA (a) and BC (b) versus depth in UO_2 crystals implanted with La or Xe at medium *dpa* range ($\sim 5 \leq dpa \leq \sim 45$) extracted from MC simulations. The parameters for BC are L = 50 nm and $\eta = 25°$. Depth distribution of displaced matrix atoms according to SRIM (Cyan filled area) are plotted in an arbitrary unit.

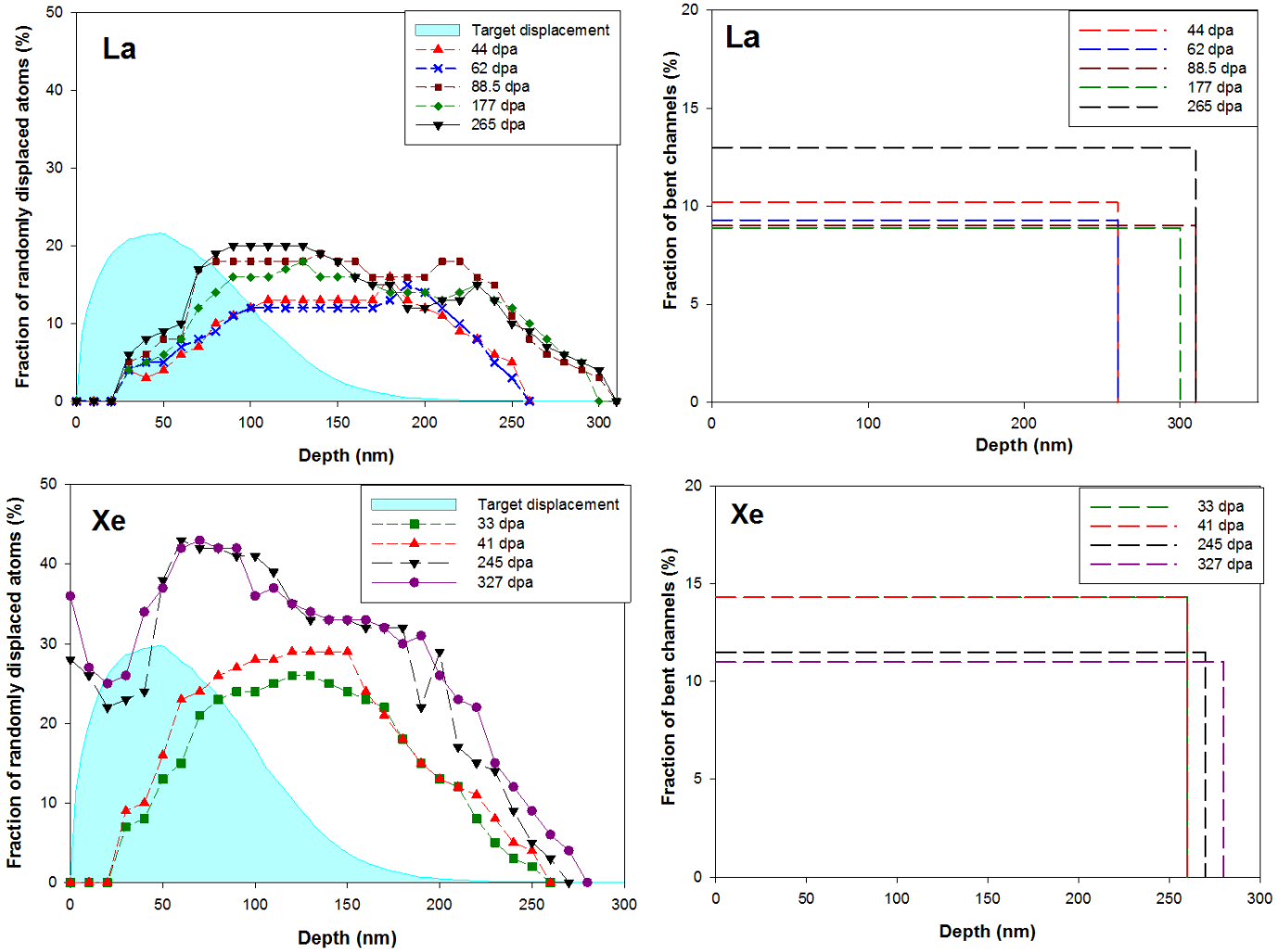

Figure 5-4: Fraction of RDA (a) and BC (b) versus depth in UO_2 crystal implanted with La or Xe at high *dpa* range (*dpa* $\geq \sim 45$) extracted from MC simulations. The parameters for BC are L = 50 nm and $\eta = 25°$. Depth distribution of displaced matrix atoms according to SRIM (Cyan filled area) are plotted in an arbitrary unit.

Table 5-1 and 5-2 summarize the types of defects that were observed by TEM for both ions and their characteristics as a function of the *dpa* (see the chapter 4). Similar type of defects appear for both ions and the same evolution of defects as a function of *dpa* is observed. The various defects evolved as the following sequence: black dot defects that were first observed, then dislocation lines and loops appeared and evolved as a function of *dpa* until they started to be become less distinguishable: some of them merge and interact together and this process continued by forming a tangled dislocation network.

Table 5-1: Various types of defects observed in a UO_2 thin foil implanted with La ions at 773 K with at different *dpa* during *in situ* TEM experiment. Mean size and confidence interval are given $[\bar{x} - \frac{2\sigma}{\sqrt{N}}, \bar{x} + \frac{2\sigma}{\sqrt{N}}]$.

dpa	**Black dots**		**Dislocation loops Mean diameter (nm)**	**Dislocation lines Mean length (nm)**	**Dislocation network**
	Mean diameter (nm)	**Number density ($x10^{23}$ m^{-3})**			
0.55	6 ± 0.1	8 ± 2	_	_	_
1.0	8 ± 0.3	8 ± 2.5	13 ± 1	_	_
2.2	8 ± 0.3	9.7 ± 3.5	30 ± 2.5	_	_
3.3	7 ± 0.5	5.5 ± 2.8	34 ± 3.5	36 ± 5	_
4.4	9 ± 1	2 ± 1	27 ± 4	37 ± 6	Starts to appear
5.5	_	_	_	_	Clearly observed

Table 5-2: Various types of defects observed in a UO_2 thin foil implanted with Xe ions at 773 K with at different *dpa* during *in situ* TEM experiment. Mean size and confidence interval are given $[\bar{x} - \frac{2\sigma}{\sqrt{N}}, \bar{x} + \frac{2\sigma}{\sqrt{N}}]$.

dpa	**Black dots**		**Dislocation loops Mean diameter (nm)**	**Dislocation lines Mean length (nm)**	**Dislocation network**
	Mean diameter (nm)	**Number density ($x10^{23}$ m^{-3})**			
0.11	6 ± 0.7	6.5 ± 2.5	_	_	_
1.0	6 ± 0.6	6.3 ± 2	11 ± 2.5	Starts to appear	_
2.2	10 ± 0.3	3.0 ± 0.9	31 ± 6	34 ± 8.5	_
4.4	7 ± 0.4	5.2 ± 1.7	27 ± 8	54 ± 12	_
6.5	7 ± 0.4	5.3 ± 1.7	18.6 ± 3	47 ± 10	_
8.7	4 ± 1	_	18 ± 3	28 ± 4	Starts to appear
11	_		_	_	Clearly observed
44	_		_	_	Clearly observed

5.1.2 Evolution of damage in the low fluence range

Figure 5-5 shows in parallel the evolution of defects that were observed by two different characterization techniques, RBS/C and TEM. The figure shows the evolution of both RDA and BC at low fluence range, where both the *dpa* and the concentration of incorporated impurities are low (*dpa* less than 5 and the maximum concentration is less than 0.1%). The evolutions of RDA and BC show a progressive increase of the damage from 0.4 to 4 *dpa* (corresponding to the concentration of implanted ions of less than 0.06%). This increase is observed for both ions (La and Xe) regardless their nature and for both RDA and BC that behave in the same way. The TEM analysis shows that the kinetics of the radiation damage are eventually identical for both Xe and La implanted crystals. They follow the sequence formation of black dots, dislocation loops transforming into dislocation lines, as it can be compared for both ions in the figure 5-5. It is worth to stress that no bubbles or cavities were detected in this fluence range. The influence of a given defect on channeling can always be decomposed into an obstruction type contribution and a distortion type one. In the two-defect model that we applied to fit the channeling data, pure obstruction-type defects leads eventually to a RDA contribution alone with only a very small contribution to distortion, while pure distortion-type defect give rise only to BC. From a theoretical point of view, dislocation lines and loops are responsible for the distortion of the crystal excluding the dislocation core, leading to dechannelling, with little contribution to direct scattering. Conversely, interstitial type, stacking fault, bubbles, or cavities have mostly a direct scattering contribution. In the present case, the increase of the fraction of bent channels as seen by RBS/C can be ascribed to the formation of dislocation loops and dislocation lines as it is demonstrated by TEM.

The progressive increase of RDA that reaches almost 20% ~ 4 *dpa* appears to have a much less obvious origin. In principle it might be related to the formation of black dots defects whose detailed internal structure is unknown to our knowledge. It can be also related to a given fraction of U and O atoms displaced off their regular positions (interstitials and vacancies), unseen by TEM. The contribution coming from a presence of hidden bubbles in TEM can be excluded, since no significant difference can be made between Xe- and La- irradiated crystals.
In conclusion, the progressive increase in both RDA and BC is a consequence of the radiation effect (defects created due to ballistic collision) which is independent of the nature of ions. The defects were created by elastic collisions (nuclear interaction) since the concentration of the implanted ions is very small and their incorporation in the crystal has a negligible effect on the channeling spectra. Irradiation at low fluence range is responsible for defect creation: several defects including: black dots defects, dislocation loops, and lines.

5.1.3 Evolution of damage in the medium fluence range

As we discussed in the section 3.3.2, the medium fluence range is characterized by the formation of a far wider damaged zone, compared to the case of the low-fluence range: as it can be seen from figure 5-3, the damage zone as measured by the RDA contribution broadens up to a depth of 250 nm and largely exceeds the profile of defects predicted by the SRIM calculation code. Moreover, a clear difference between the saturation levels of RDA is evidenced for both ions. The corresponding evolution of the BC shows a similar difference between an almost saturated value for the La-implanted crystal but a clear increase for the Xe-implanted one. Such features are summarized in the Figure 5-6 that shows the evolution of both fractions as function of *dpa*: in this fluence range, both RDA and BC are essentially saturated and a marked distinction between the behaviors of Xe- and La-implanted crystals is evidenced. The saturation plateau of RDA recorded for the Xe-irradiated solid

exceeds the La-implanted by typically 8%. The difference between BC at saturation is less but it is still significant 4%.

The corresponding *in situ* TEM experiments performed in this fluence range (see Figure 5-6) shows the progressive transformation of the radiation-induced defects while increasing the ion dose: dislocation loops and dislocation lines reorganize to form a network of tangled dislocations. Moreover, as we discussed in the chapter 4, for the specific case of the Xe-irradiated crystals, the presence of nanometer-sized has bubbles is evidenced, with a size and density that appear essentially constant over the whole *dpa* range. It is worth mentioning that the presence of bubbles were not detected in the low fluence range (below 4 dpa) and that they appear at a threshold corresponding to the lower values of the medium fluence range.

Let us discuss the two main characteristics as seen by the channeling analysis:

(i) The transformation of the dislocation lines into a dislocation network leads to a progressive formation of a damage zone located at large depth according to the channeling analysis. In fact very few experiments tackle the effect of the presence of a forming dislocation network on the channeling behavior: the presence of very nicely organized dislocation network at a given depth in silicon crystals give rise to a clear step in the aligned spectra [Feldman *et al.* 1982]. There is thus a strong likelihood that the formation of the dislocation network at an increasing depth, while the *dpa* increases, is responsible for the progressive broadening of the damaged zone. It is worth stressing that the sole information given by the kinetics gives the apparent erroneous information that the crystal reached as steady-state, but it is in fact not the case;
(ii) The main difference between La- and Xe-implanted crystals as seen by TEM in this *dpa* range is the presence of Xe bubbles, whilst neither cavities nor bubbles were detected for the La-implanted crystal as shown in figure 5-7. The presence of bubbles in equilibrium in the solid on the channeling properties is well established [Ronikier *et al.* 1975]. The main expected contribution is an increase of the direct backscattering yield due to the obstruction of channeled ions, as measured by the RDA contribution. In fact after crossing a bubble the channelled probing ion may lose its spatial relationship relative to the atoms rows, giving rise to an increase of the obstruction-type channelling. A little contribution coming from the distortion of the lattice around the bubble should be responsible for an extra distortion-type channelling. Conversely – except for the very high fluence that are not discussed in this section - the scattering of the probing ions by the gas atoms, leading to an extra dechannelling that makes channeling impossible in the re-entry in the crystal can be neglected. As it appears from the comparison between the two different ions – insoluble Xe versus the soluble La – the difference in height between the RDA plateaus can be directly ascribed to the presence of the bubbles, whilst the similar increase of the BC fraction for Xe-restricted to the implanted crystals, supports also this demonstration, since the sole formation of a dislocation network does not increase significantly the fraction of BC, as seen for the La-implanted crystal. It is worth stressing here that in the present version of the McChasy code, the influence of the gas bubbles can be modeled only indirectly (i.e. by the RDA and BC parameters) since no genuine bubble is included in the solid;

Overall, Xe and La-implanted crystals show strong similarities in the crystal restructuration in the medium dose range. The most striking effect is the progressive formation of a dislocation network and the increase of the radiation damage towards the greater depths in the crystal. Conversely, the main difference between Xe and La is of course related to the solubility of implanted species. As it is well established, La can form solid solution with UO_2 up to very high concentration (up to 80%) [Kleykamp 1984], [Imoto 1986], [Fujino 1988], [Grimes & Catlow 1991], [Brillant *et al.* 2011] while keeping the cubic fluorite-type structure; it stays most probably in substitutional positions or at empty octahedral locations. Such locations are responsible for only a low stress field in the irradiated crystal. As it was stated before, all Monte Carlo simulations were performed assuming that La atoms are sited in octahedral locations. The presence of Xe in the lattice modifies the radiation damage in two

different ways. First, as it was measured by TEM, part of the Xe is not located in bubbles since both the size and the density of bubbles are constant while the ion fluence increases (see Figure of the chapter 4). Recent works on X-ray spectroscopic methods performed on polycrystalline UO_2 implanted with Xe have shown that a large fraction of foreign atoms are stabilized in Schottky-type defects [Bès *et al.* 2015]. Such defects are well modeled by the two-defect model applied to our channeling data. Although the radius of Xe atom is far larger r_{Xe} = 218 pm than the radius of the U^{4+} cation r_U = 97 pm, the steering power of the Xe ions is low because the fraction of incorporated impurities is still small in this fluence range (less than 0.5%). Second, Xe forms nanometer-sized bubbles: this contribution has a direct and measurable influence on the channeling spectra, as measured by an increase of the RDA fraction, and BC fraction to a smaller extent.

5.1.4 Evolution of damage in the high fluence range

In this fluence range, no TEM experiments were performed. We have thus to rely on the information provided by the channeling technique alone. Figure 5-4 shows both the RDA and BC profiles and the Figure 5-1 displays the kinetics recorded at the maximum of the profile. Let us stress here that, both the dpa (larger than 50 and that reaches several hundreds of *dpa*) and concentration of incorporated impurities – that reaches a few atomic percent – are high: the material is submitted to extreme conditions in terms of irradiation.

The La-implanted crystal presents a clear increase of the RDA recorded at the maximum of the distribution when the fluence reaches 177 *dpa*, corresponding to a fraction of 2.7%. Moreover, the thickness that reaches the highest fraction of RDA is located at depth ranging from 70 to 150 nm (see figure 5-4), while the deepest zone of the crystal is less affected by irradiation and stays at an almost constant level as it was in the medium fluence range. This zone corresponds in fact to the part of the crystal having the highest concentration of La ($R_P + \Delta R_P$ = 122 nm, but ΔR_P is well known to be underestimated in the SRIM calculation code). A concomitant increase of the fraction of BC is also recorded. The increase of the disorder is still limited but it indicates that the influence of impurities is likely no more negligible. In fact, the incorporation of La in interstitial-type positions at increasing dose may lead to the significant displacements of adjacent atoms. Increasing the ion fluence to higher values is therefore needed to conclude on such evolution and to test whether the presence of the fully soluble La might play a role. Nevertheless, let us emphasize here that at the highest investigated fluence performed in the framework of this thesis, the maximum fraction of La already reaches 4%, i.e. a value far larger than any concentration of impurities in the spent fuel (the typical concentration of La is spent fuel is ~ 0.2%). At such much lower values, the influence of La must be therefore limited to radiation damage. The fate of the Xe-implanted crystal is more dramatic. A huge increase of the RDA fraction (up to 43 %) is observed from 70 to 150 nm – in the zone where the Xe concentration is the highest. Such a feature was already seen for Xe-implanted crystals implanted at room temperature (see the section 5.2 that compares both temperatures) and it was ascribed to the progressive microstructural transformation from the single crystal to the polycrystal. Although it was not possible to extend the fluence range during this PhD because experiments are really time-consuming, we are most confident that we do observe here the first step of a similar process. Provided our speculation is correct, it is worth stressing that this strong restructuring of the crystal occurs at essentially the same Xe concentration at both temperatures such a transformation occurs for a typical Xe concentration of 4%. This value is larger than the concentration of Xe in the spent fuel (the typical concentration of Xe is spent fuel is ~ 1%).

In conclusion to the role played by implanting foreign elements on the damage evolution in irradiated UO_2, it is observed a distinct behavior of incorporated elements (La and Xe) in UO_2. As a matter of fact, the main reasons why more damage is observed in the Xe-implanted crystal compare to La-implanted crystal are: (i) The solubility of La compared to Xe ions leading to the formation of nanometer-sized gas bubbles, (ii) the size of implanted species in UO_2 matrix where the insoluble Xe

atoms have an atomic radius (r_{Xe} = 218 pm) much larger than the cationic radius of U^{4+} atoms (r_U = 97 pm), (La^{3+} atoms have a similar atomic radius as U^{4+} atoms) responsible for more stress in UO_2 crystal leading to a larger displacement of adjacent atoms.

(a)

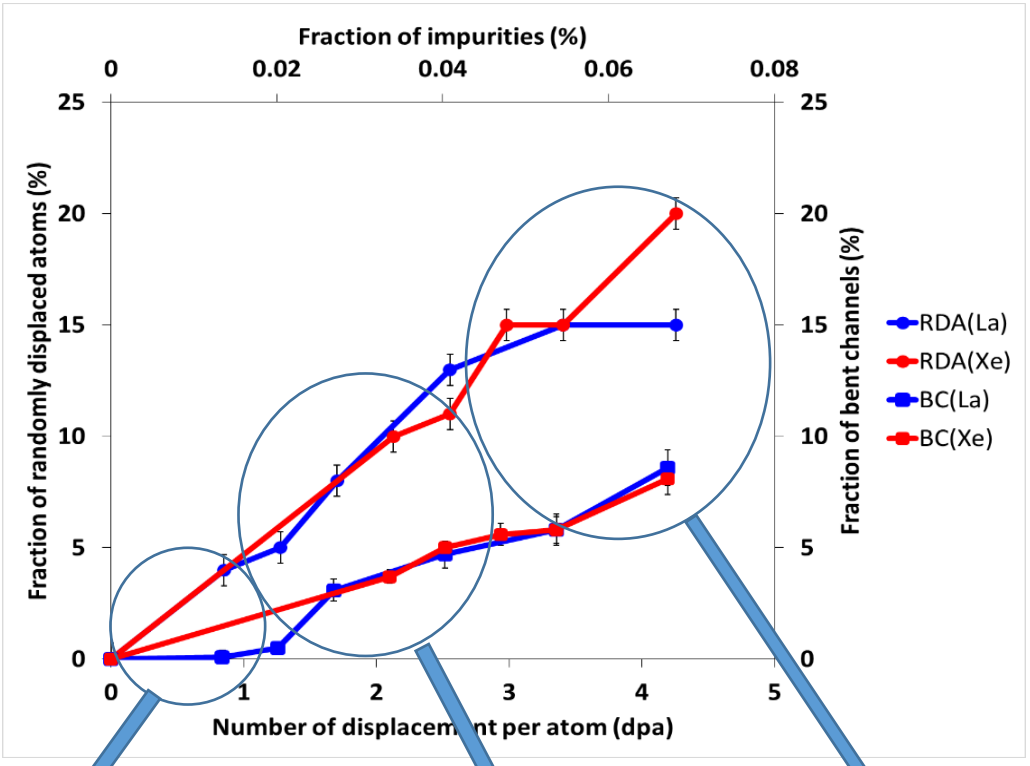

(b)

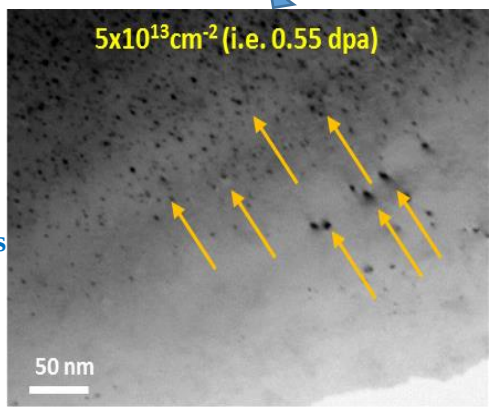

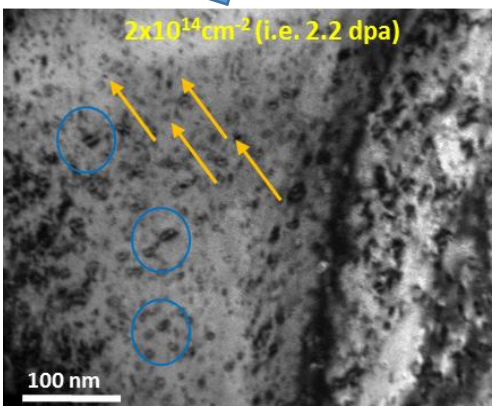

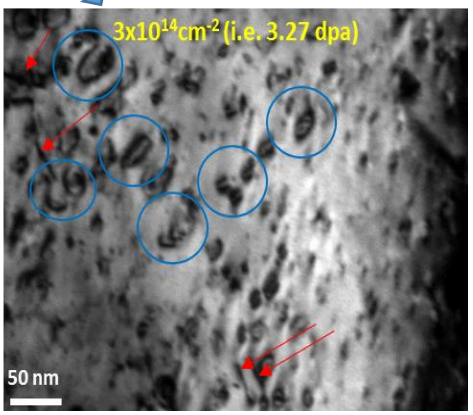

La ions

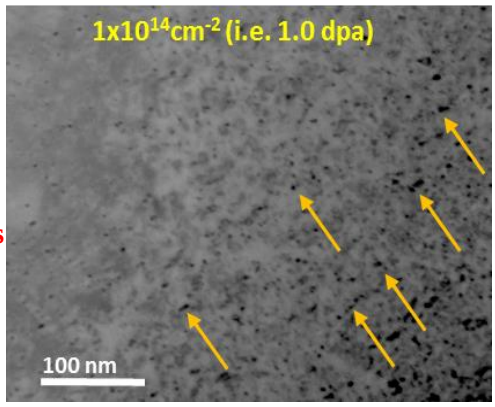

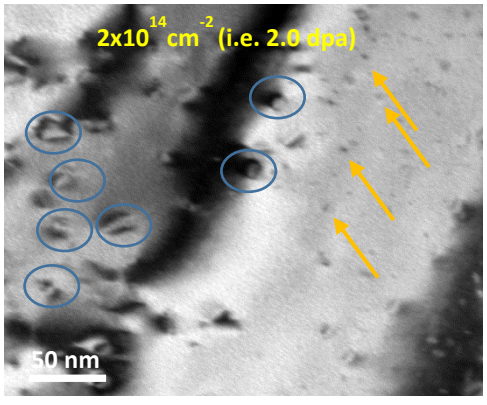

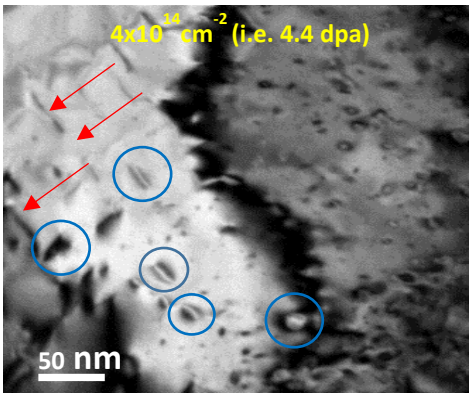

Xe ions

Black dot defects

Black dot defects and small dislocation loops

Black dot defects and dislocation lines and loops

Figure 5-5: Evolution of defects at low fluence range: (a) Kinetics of damage evolution obtained by RBS/C; (b) Evolution of the radiation damage as seen by TEM.

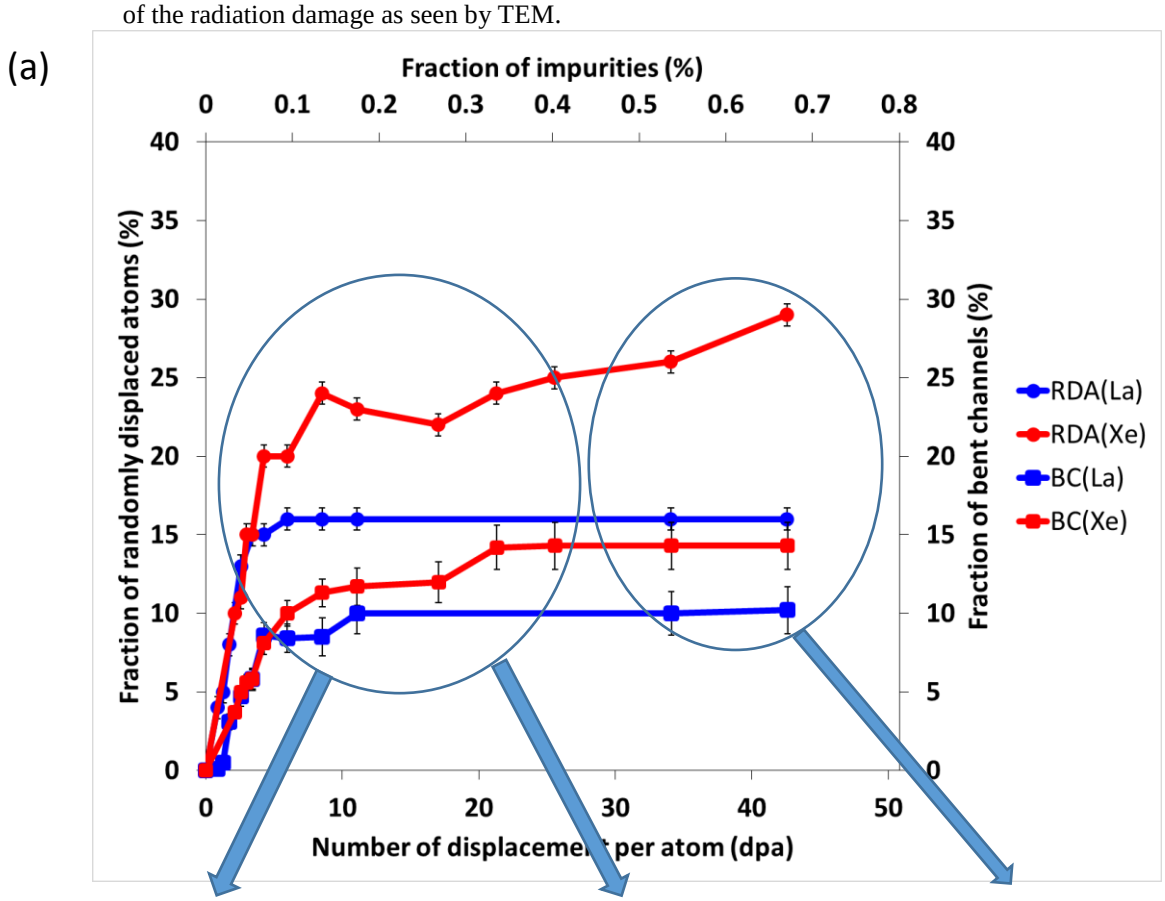

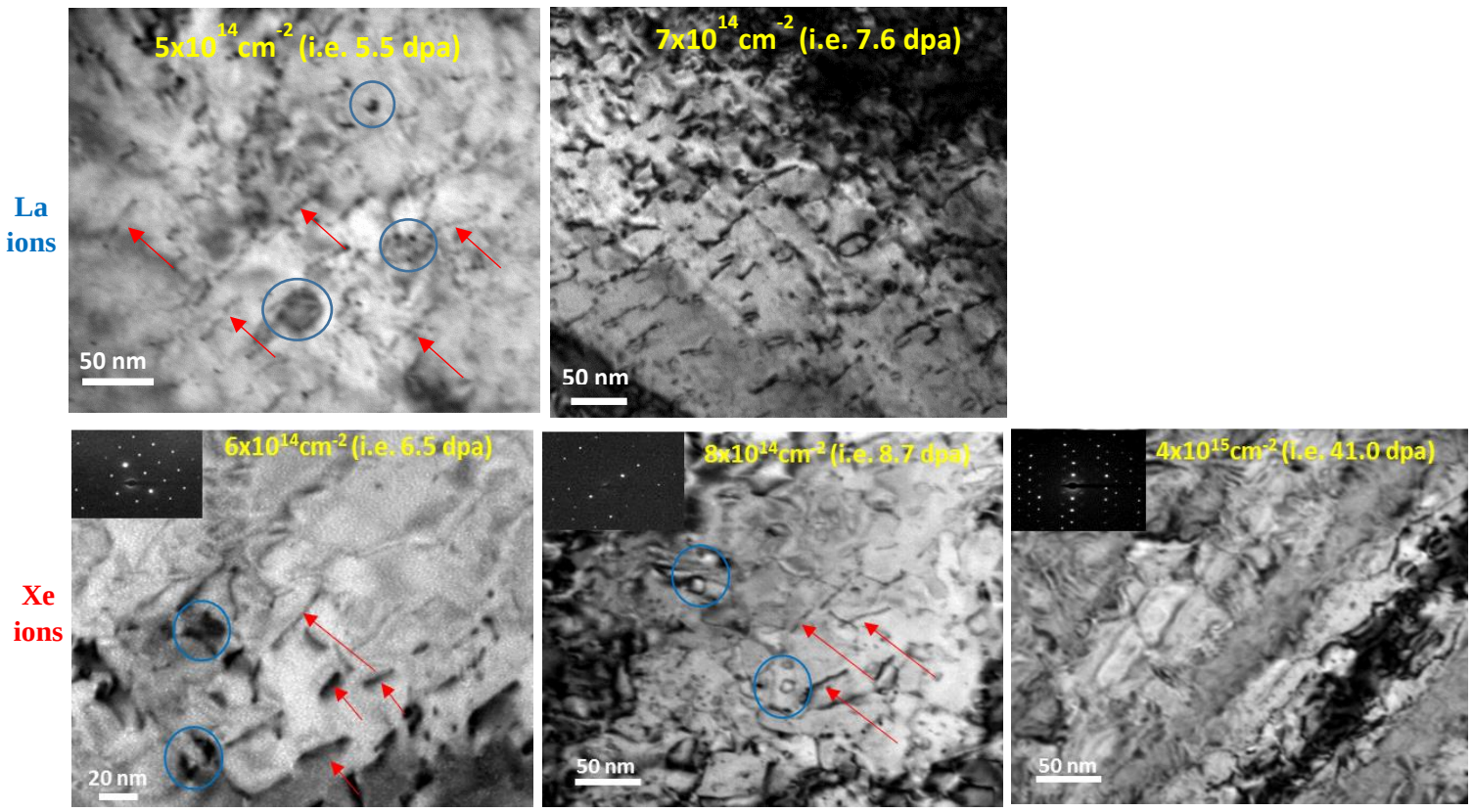

Figure 5-6: Evolution of defects at medium fluence range: (a) Kinetics of damage evolution obtained by RBS/C; (b) Evolution of the radiation damage as seen by TEM.

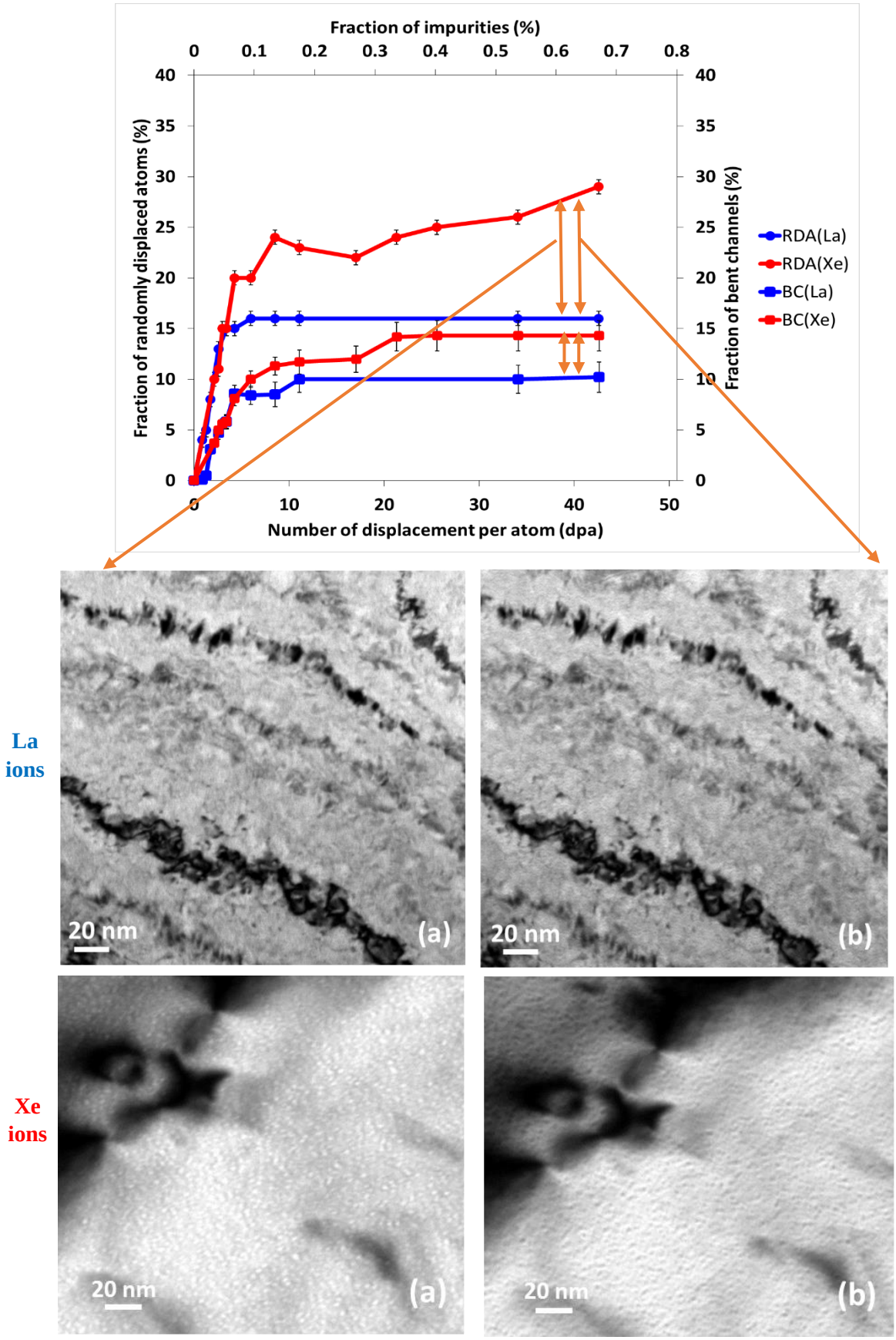

Figure 5-7: Bright filed (±2 microns under/over focus) TEM images (showing there are no cavities in UO_2 thin foil implanted at $7x10^{14}$ cm^{-2} with 265 KeV La ions at 773K and showing bubbles in UO_2 thin foil implanted at $6x10^{14}$ cm^{-2} with 260 KeV Xe at 773 K.

5.2 Effect of temperature on damage evolution

This section presents the analysis of the Channelling spectra of *in situ* RBS/C experiments recorded on a UO_2 single crystals implanted at 773 K with either the noble gas xenon (Xe) or with lanthanum (La) ions by using the two-defect model but assuming different values of BC parameters compared to that used in previous analysis (see the chapter 3). Such an approach is motivated by the will to directly compare the evolution of both RDA and BC for crystals irradiated at different temperatures. As a matter of fact, similar experiments at room temperature were conducted in the framework of the PhD thesis of T. H. Nguyen [Nguyen thesis 2013]. In this section, the damage evolution that we obtained at 773 K is compared with the one that was obtained at room temperature. The analysis of the spectra was done by T. H. Nguyen is summarized in the Appendix E.

5.2.1 Analysis of channelling spectra recorded at 773 K

Channeling data of implanting 500-keV La ions or 470-KeV Xe ions implanted in UO_2 single crystals at 773 K were analyzed assuming different values for the BC parameters from the values were used in all the analysis before. The following simulations will focus on the use of the two-defect model (RDA + BC) to analyze the channeling spectrum in which the values of angle and the length of BC are fixed to be L = 5 nm and $\eta = 1.5°$. Let us remind the reader that in the chapter 3, the BC parameters L and η were fixed to L = 50 nm and $\eta = 25°$, in accordance with the values derived by TEM. The values L = 5 nm and $\eta = 1.5°$ correspond to the ones used by T. H. Nguyen.

5.2.1.1 Monte Carlo simulations for RBS/C spectra assuming new values for the BC parameters

Figure 5-8 to Figure 5-11 display the MC simulations performed with the two-defect model for the Channeling spectra recorded on implanted UO_2 single crystals with either La ions or Xe ions, as it can be seen from the figures. Regarding the axial channeling spectra, a good agreement between MC simulation spectra and the experimental data in the energy window from 2000 keV to 2887 keV is evidenced when assuming the new values for L and η. It is also observed that the damage peak is well fitted by using the two-defect model with these values over the whole fluence range of our simulations.

Some discrepancy at some fluences can be observed just after the damage peak (i.e. corresponding to energy range from 2500 keV to 2725 keV) and at depths that largely exceed the damage zone (z > 1 μm), as they were obtained by analysis the RBS/C spectra performed by assuming L = 50 nm and $\eta = 25°$, for the same reasons as mentioned before (see section 3.3.1). It is important to mention that we observed more discrepancy between experimental values and simulations in the simulations that were done by assuming the new values for the BC parameters. The fits with L = 50 nm and $\eta = 25°$ is better compared to the new values. Such a conclusion is in fact not surprising since the values L = 5 nm strongly differs from the real dislocation length observed by TEM.

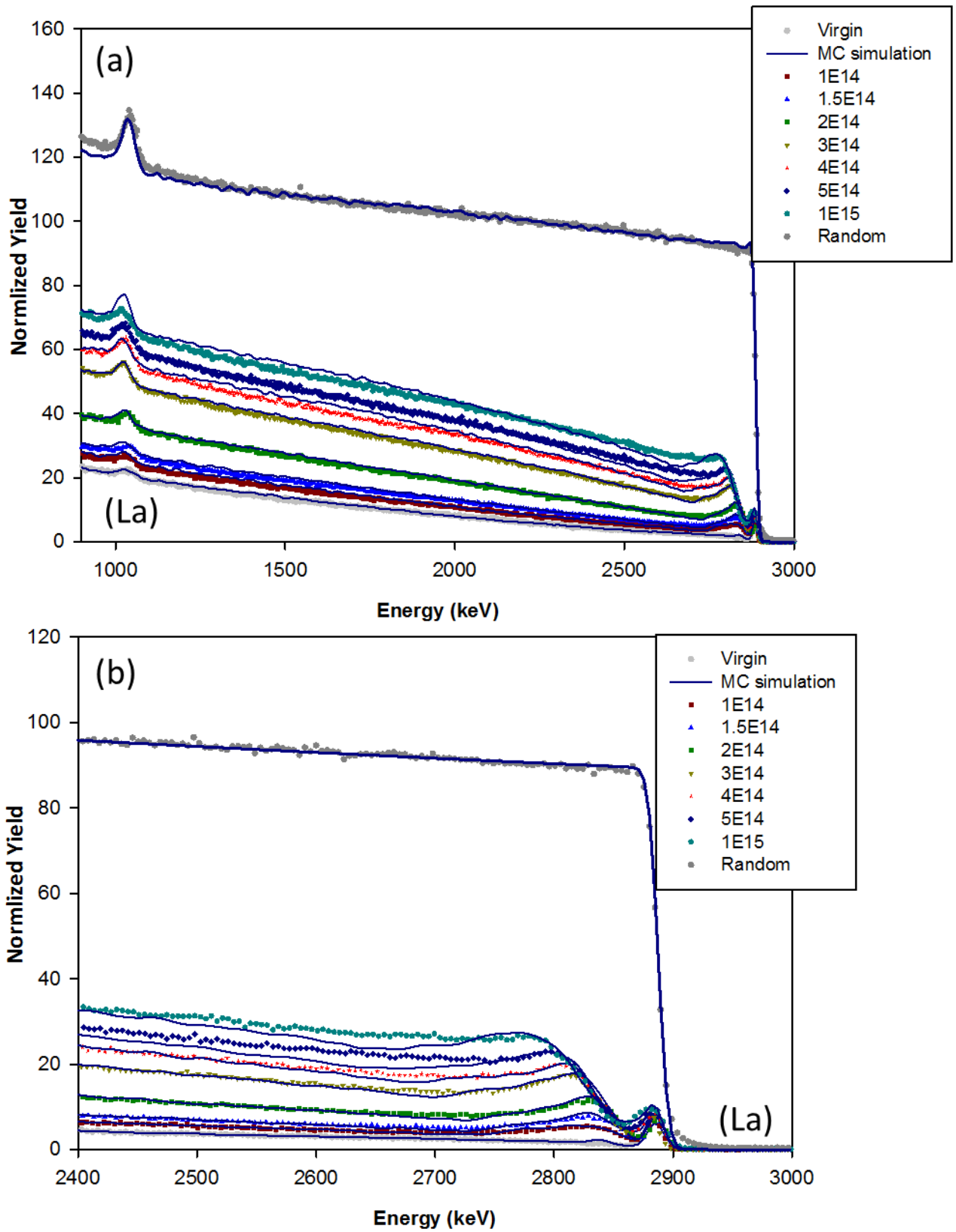

Figure 5-8: Random and aligned MC simulation to RBS channelling spectra (a) and high energy part of channelling spectra (b) recorded on a UO_2 crystal implanted sequentially with La ions at low fluence**.** Fluences are measured in unit of cm^{-2}. Implantation temperature is 773 K. The random spectrum was recorded at a fluence $\Phi = 3x10^{14}$ cm^{-2} (grey circles). Experimental channelling spectra are plotted in symbols for fluences of $\Phi = 1x10^{14}$ cm^{-2} (dark red squares), $1.5x10^{14}$ cm^{-2} (blue triangles up), $2x10^{14}$ cm^{-2} (green squares), $3x10^{14}$ cm^{-2} (dark yellow triangles down), $4x10^{14}$ cm^{-2} (red stars), $5x10^{14}$ cm^{-2} (dark blue diamonds), $1x10^{15}$ cm^{-2} (dark cyan circles). Fits were performed assuming L = 5 nm and $\eta = 1.5°$ (see text).

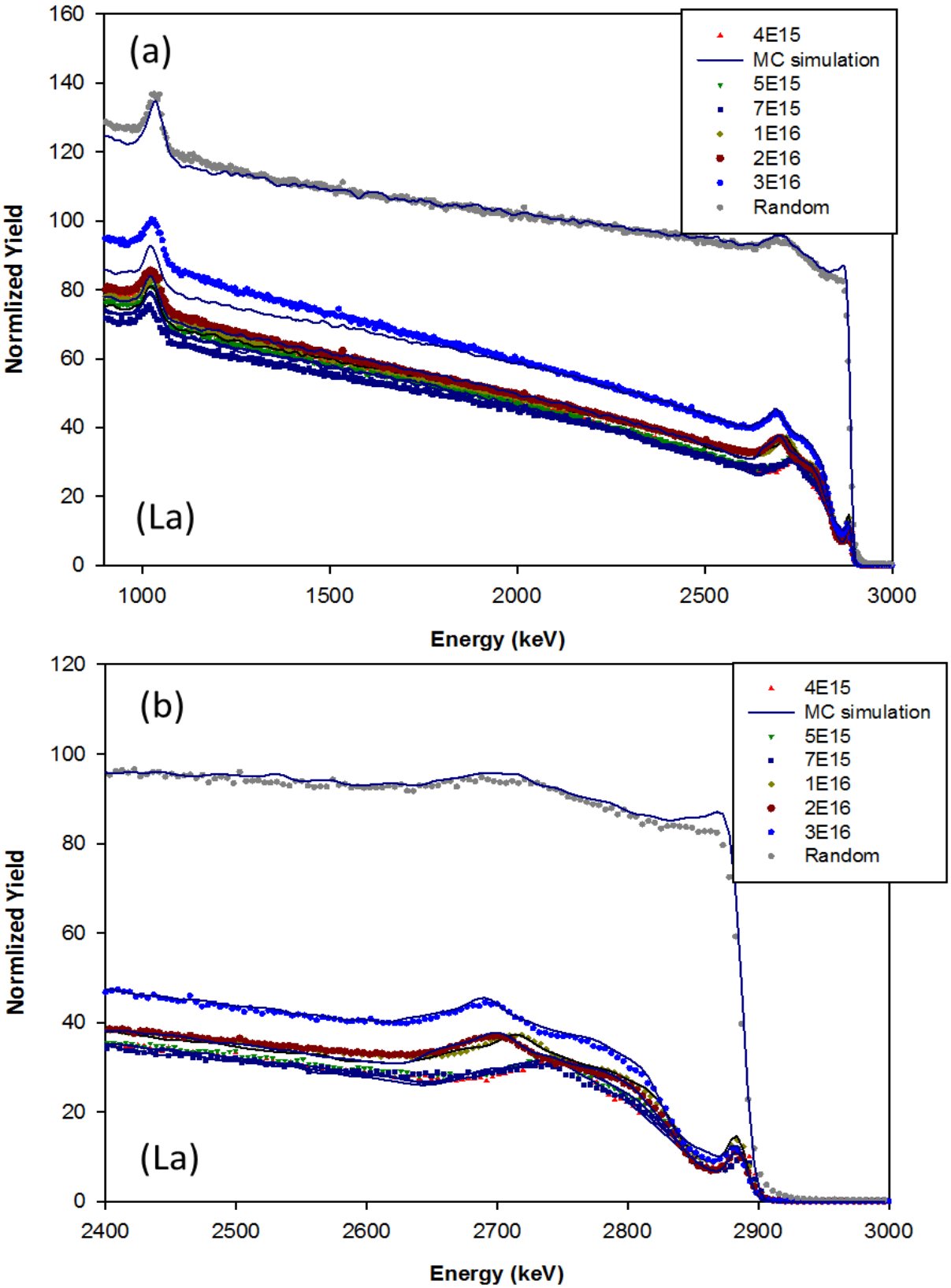

Figure 5-9: Random and aligned MC simulation to RBS channelling spectra (a) and high energy part of channelling spectra (b) recorded on a UO_2 crystal implanted sequentially with La ions at high fluence. Fluences are measured in unit of cm^{-2}. Implantation temperature is 773 K. The random spectrum was recorded at a fluence $\Phi = 2x10^{16}$ cm^{-2} (black circles). Experimental channelling spectra are plotted in symbols for fluences of $\Phi = 4x10^{15}$ cm^{-2} (red triangles up), $5x10^{15}$ cm^{-2} (green triangles down), $7x10^{15}$ cm^{-2} (dark blue squares), $1x10^{16}$ cm^{-2} (dark yellow diamonds), $2x10^{16}$ cm^{-2} (dark red circles), $3x10^{16}$ cm^{-2} (blue circles).Fits were performed assuming L = 5 nm and η =1.5° (see text).

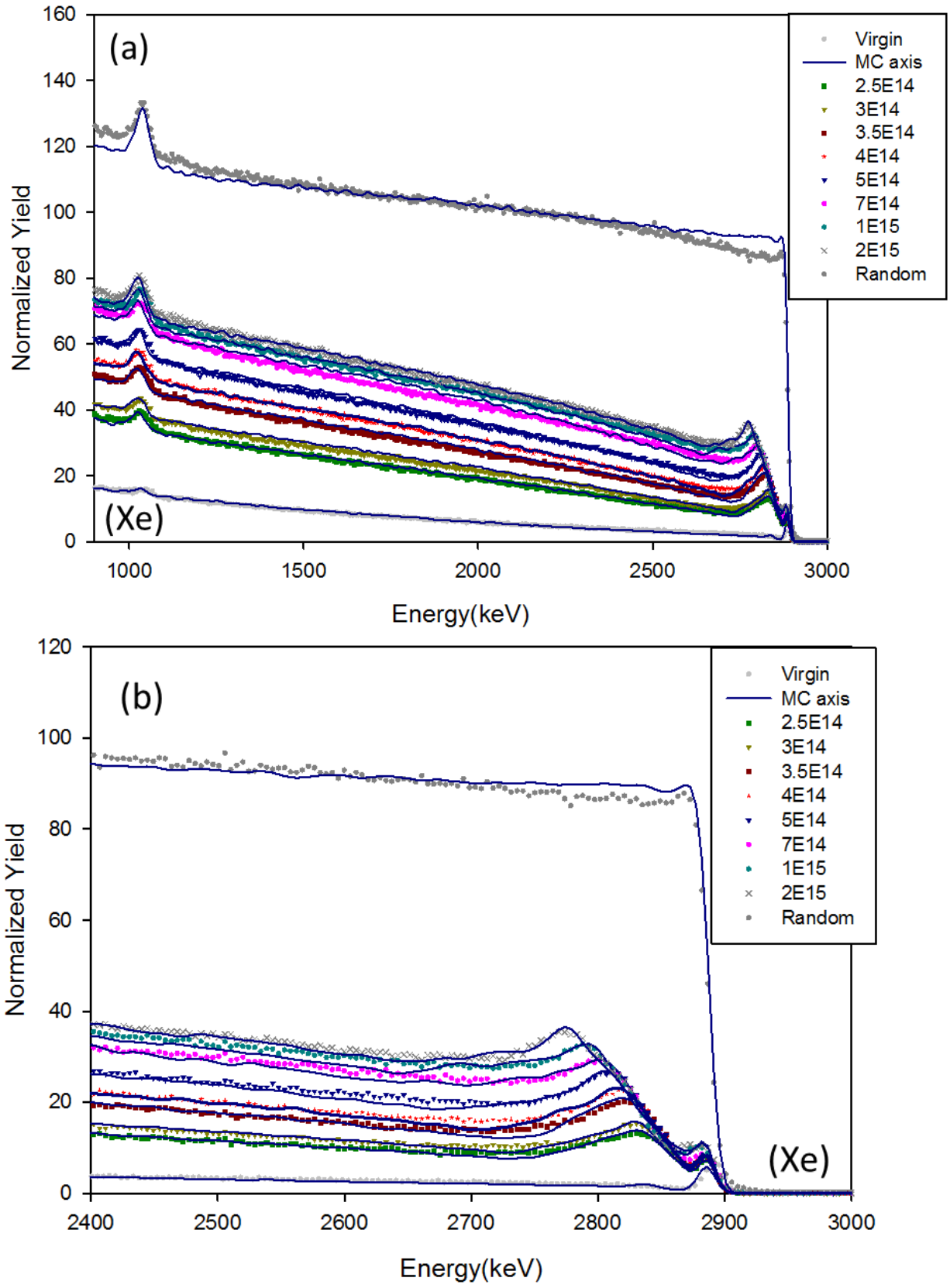

Figure 5-10: Random and aligned MC simulation to RBS channelling spectra (a) and high energy part of channelling spectra (b) recorded on a UO_2 crystal implanted sequentially with Xe ions at low fluence**.** Fluences are measured in unit of cm^{-2}. Implantation temperature is 773 K. The random spectrum was recorded at a fluence $\Phi = 2.5x10^{14} cm^{-2}$ (black circles). Experimental channelling spectra are plotted in symbols for fluences of $\Phi = 2.5x10^{14}$ cm^{-2} (green squares), $3x10^{14}$ cm^{-2} (dark yellow triangles down), $3.5x10^{14}$ cm^{-2} (dark red squares), $4x10^{14}$ cm^{-2} (red stars), $5x10^{14}$ cm^{-2} (dark blue triangles down), $7x10^{14}$ cm^{-2} (pink circles), $1x10^{15}$ cm^{-2} (dark cyan circles), $2x10^{15}$ cm^{-2} (dark grey crosses). Fits were performed assuming L = 5 nm and $\eta = 1.5°$ (see text).

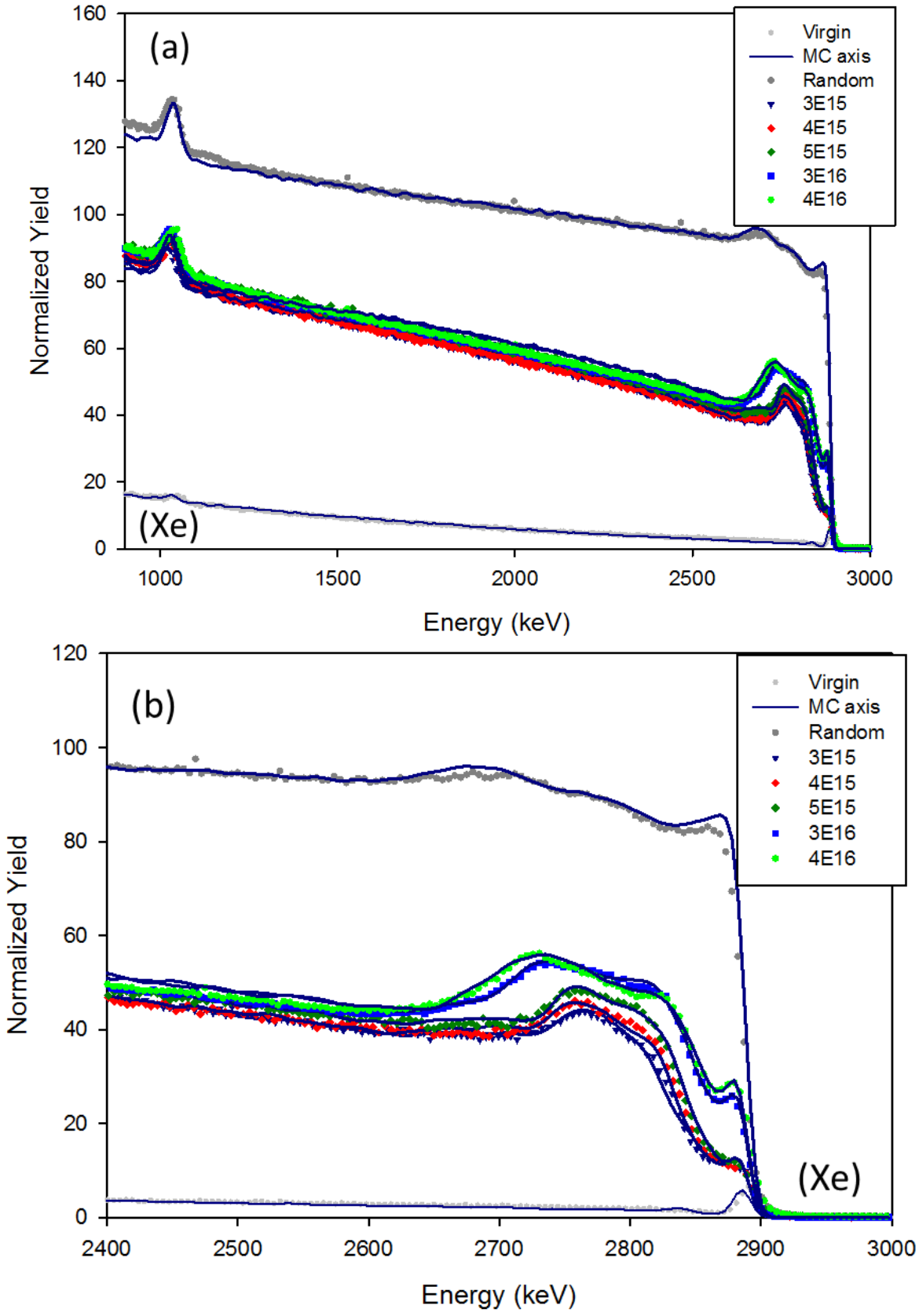

Figure 5-11: Random and aligned MC simulation to RBS channelling spectra (a) and high energy part of channelling spectra (b) recorded on a UO_2 crystal implanted sequentially with Xe ions at high fluence**.** Fluences are measured in unit of cm^{-2}. Implantation temperature is 773 K. The random spectrum was recorded at a fluence $\Phi = 3x10^{16} cm^{-2}$ (black circles). Experimental channelling spectra are plotted in symbols for fluences of $\Phi = 3x10^{15}$ cm^{-2} (dark blue triangles down), $4x10^{15}$ cm^{-2} (red squares), $5x10^{15}$ cm^{-2} (green diamonds), $3x10^{16}$ cm^{-2} (blue circles), $4x10^{16}$ cm^{-2} (green circles). Fits were performed assuming L = 5 nm and $\eta = 1.5°$ (see text).

5.2.1.2 Evolution of the depth distribution of RDA-type and BC-type defects versus ion fluence (RDA & BC)

In this section the evolution of RDA and BC fraction are discussed. For sake of simplicity and to allow an easy comparison with previous results obtained with L = 50 nm and η = 25°, the results are divided into the same three range that were used in section 3.3.2.1: (i) low implanted fluence range (0 to $\Phi \leq 5x10^{14}$ cm^{-2}), (ii) medium implanted fluence range ($5x10^{14}$ $cm^{-2} \leq \Phi \leq \sim 5x10^{15}$ cm^{-2}) and (iii) high implanted fluence range ($\Phi \geq \sim 5x10^{15}$ cm^{-2}).

The evolution of the distribution of both RDA and BC are very similar to the ones derived with the previous values of (L, η) used in the chapter 3. Regarding the evolution of RDA fraction:

(i) *In the low fluence range*: figure 5-12.a represents the distribution of RDA versus depth for low La and Xe implanted fluences. The distribution of RDA for both ions shows a similar behavior: the maximum RDA defects for each fluence are mainly located between 85 to100 nm which is around the range of the implanted ions. The fraction of RDA increases and the profile broadens with increasing the fluence of implanted ions. The distribution of RDA appears to be very similar to the one obtained on figure 3-18 assuming L = 50 nm and η = 25°. The distribution for La and Xe ions shows that for both ions, the features are similar regardless the nature of ions and their different chemical contributions.

(ii) *Medium fluence range:* Figure 5-13.a represents the distribution of RDA at medium fluence range. A similar behavior of the RDA evolution is seen for this range of fluence, where the width of the distribution of RDA is progressively increased toward larger depths as the fluence increases. It is observed that within this medium ion fluence range, the maximum fraction of RDA is almost constant and it is saturated for crystals implanted with La ions and Xe ions. Moreover, there is a clear difference in this fraction recorded at the maximum of the distribution between the two ions: the damage in crystal implanted with 470 keV Xe ions saturates at a much higher level (the average maximum fraction of RDA is 23%) in comparison to the crystal implanted with 500 keV La ions (the average maximum fraction of RDA is only 16%). It is observed that the defects saturate at almost same level of maximum fraction of RDA for both ions compared to the previous analysis that obtained assuming L = 50 nm and η = 25°.

(iii) *High fluence range:* Regarding the La-implanted crystal, as shown in figure 5-14.a, the maximum fraction of RDA does not increase with increasing the fluence even for the highest fluences, the maximum value is 20%. An increase in the width of the damage zone is clearly seen especially near the surface compared to the medium fluence range. With respect to the Xe- implanted crystal, a different distribution of RDA is obtained specially in case of high fluence of implantation $\Phi \geq 3 \times 10^{16}$ cm^{-2} (corresponding to concentration over 3 at. %), where a huge damage is recorded close to the surface as shown in figure 5-14.a. To conclude, the distribution of the maximum RDA for all the fluence ranges for both ions shows a very similar evolution as the distribution obtained before for L = 50 nm and η = 25°.

Regarding the evolution of BC fraction:

(i) *Low fluence ranges:* in this fluence range both La and Xe ions show a slow and regular evolution for the BC fraction that increases with increasing the ion fluence. The fraction of BC is always very small.

(ii) *Medium fluence range:* in this fluence range La and Xe implanted crystals strongly differ: a dramatic increase of BC fraction was observed for Xe-implanted crystal, the maximum fraction of BC increased from 8% to 20%, while for La-implanted crystal the fraction stays around 4%.

(iii) *High fluence range:* The fraction of BC almost saturates and the value stay almost constant 20% for Xe and 5% for La, even if the crystal is implanted with high concentration of impurities. A sudden increase with 15% is clearly seen in the fraction of the BC regarding La-implanted crystal at high concentration of implanted La about (3 at. %).

In conclusion, the comparison of the results that were obtained from the analysis of the evolution of BC fraction by assuming L = 5 nm and η = 1.5° with the results that obtained by assuming L = 50 nm and η = 25°, shows that the fraction of BC increases progressively for both ions up to the range of high fluences where suddenly the fraction increasing a lot. In summary, the evolution of BC is very similar for both sets of (L, η) values. Although the fraction of BC differs from a quantitative point of view, the evolution is the same.

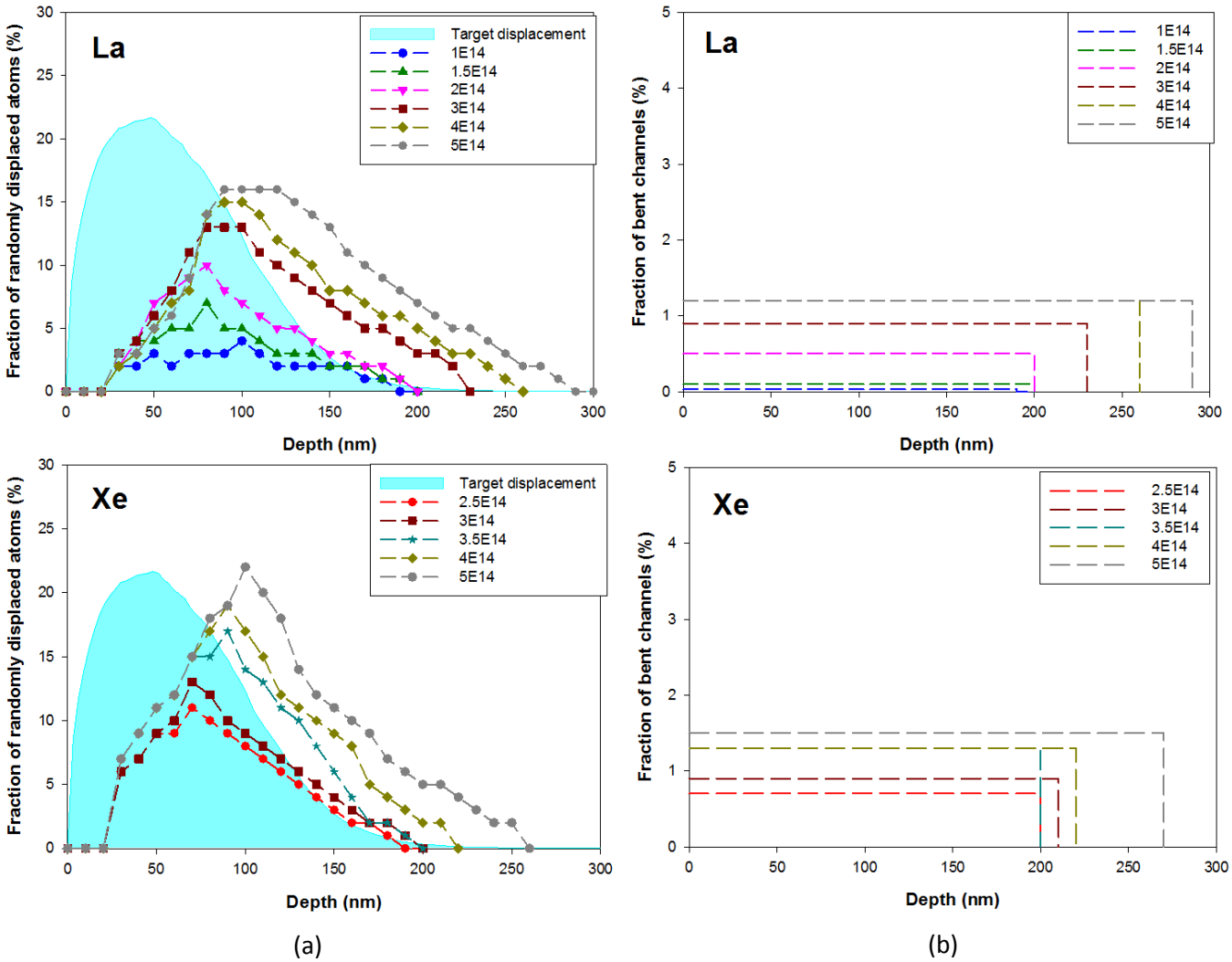

Figure 5-12: fraction of RDA (a) and BC (b) versus depth in UO_2 crystal implanted with La and Xe at low fluence ($\Phi \leq 5x10^{14}$ cm^{-2}) extracted from MC simulations. The parameters for BC are L = 5 nm and η = 1.5°. La and Xe distribution profile in UO_2 calculated by SRIM (Cyan filled area) are plotted in arbitrary unit. This figure can be compared to figure 3-21 for comparison (L = 50 nm; η = 25°).

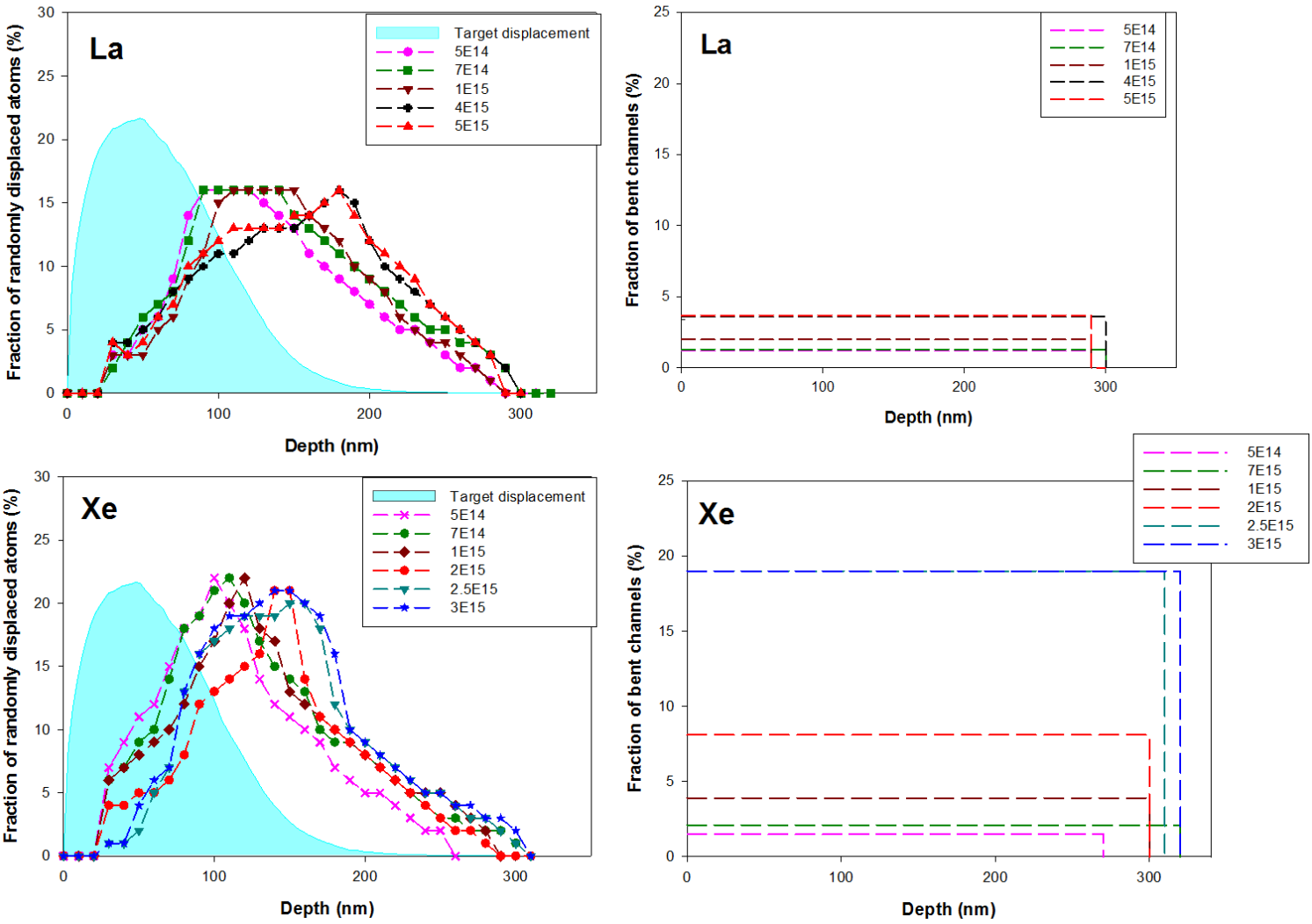

Figure 5-13: fraction of RDA (a) and BC (b) versus depth in UO_2 crystal implanted with La and Xe at medium fluence range ($5x10^{14}$ $cm^{-2} \leq \Phi \leq \sim 5x10^{15}$ cm^{-2}) extracted from MC simulations. The parameters for BC are L = 5 nm and η = 1.5°. La and Xe distribution profile in UO_2 calculated by SRIM (Cyan filled area) are plotted in arbitrary unit. This figure can be compared to figure 3-22 for comparison (L = 50 nm; η = 25°).

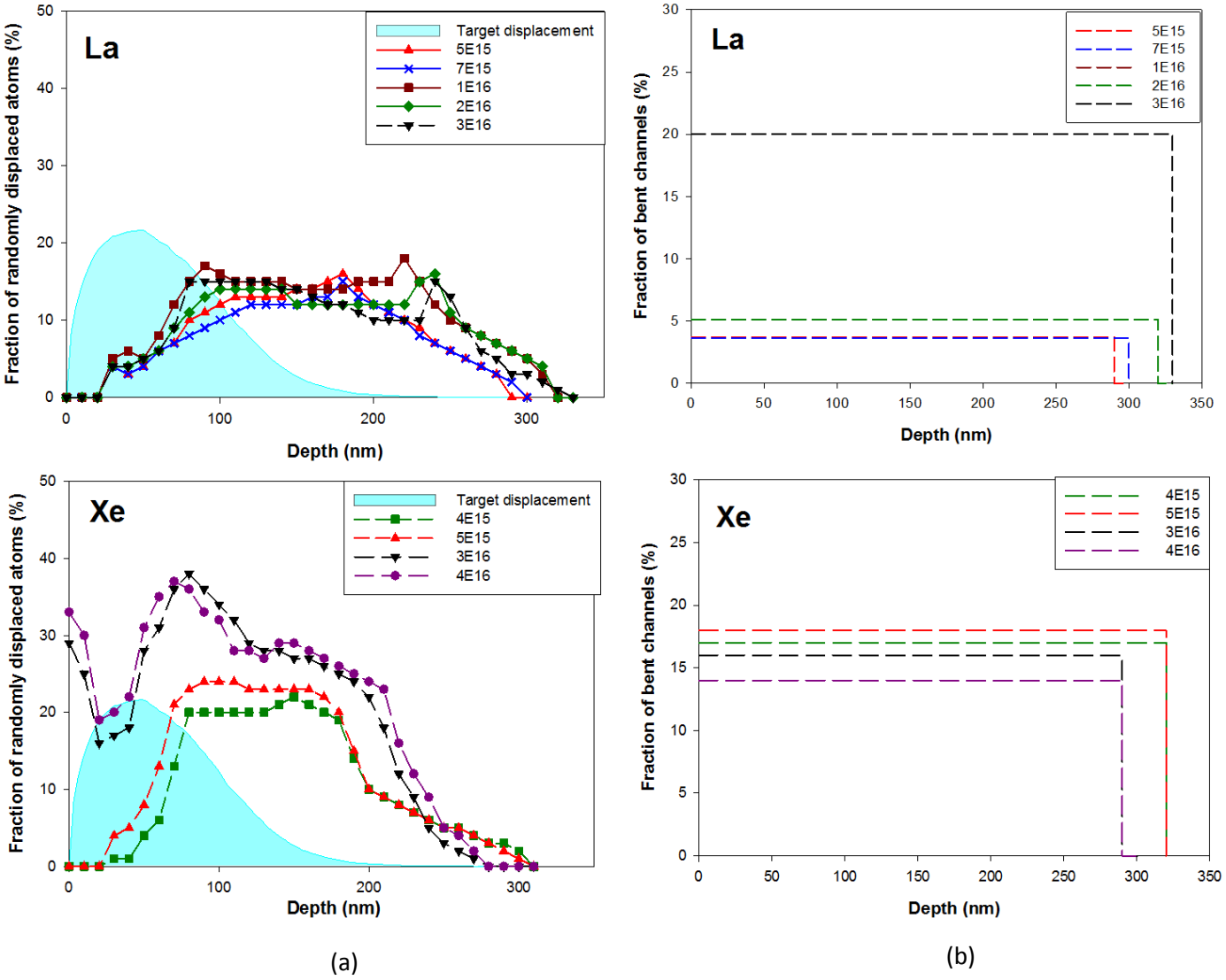

Figure 5-14: fraction of RDA (a) and BC (b) versus depth in UO_2 crystal implanted with La and Xe at high fluence range ($\Phi \geq \sim 5x10^{15}$ cm^{-2}) extracted from MC simulations. The parameters for BC are L = 5 nm and η = 1.5°. La and Xe distribution profile in UO_2 calculated by SRIM (Cyan filled area) are plotted in arbitrary unit. This figure can be compared to figure 3-23 for comparison (L = 50 nm; η = 25°).

5.2.2 The effect of temperature on the kinetic of damage accumulation

The Figures 5-15 and 5-16 shows the comparison between the evolution of RDA and BC at the two temperatures: 293K and 773K. Let us stress while making this comparison that all the experimental parameters are identical at the two temperatures (ions, energies, fluence range, flux) and that the Monte Carlo simulations were performed assuming the same type of defect with the same parameters for the BC-type defects. For the sake of simplicity the comparison is divided between the low and medium dose range, from one hand, and the high dose range, on the other hand.

- *Low- and medium dose range.*

(i) In the low dose regime (less than 10 dpa), a similar evolution is seen for RDA for both Xe and La ions at a given temperature (see figure 5-15). However, the high temperatures experiments show that the increase of RDA appears at a much lower dpa (the front at mid height is reached at 1.4 and 5 dpa for 773 K and 293 K experiments, respectively). Moreover the increase of the RDA fraction is smoother at high temperature, while at room temperature the front is better defined. Such features were also observed on cubic zirconia (that exhibits also a fluorite-type structure) irradiated with 4-MeV Au ions in the same temperature range [Debelle *et al.* 2014].

(ii) The comparison on the RDA levels on the saturation plateaus (dpa larger than 10) shows that a higher value for the Xe-implanted crystal with respect to the La-implanted one at both temperatures. As we discuss before this difference can be ascribed to the formation of nanometer-sized Xe bubbles. As a matter of fact the presence of Xe bubbles in the same dpa and concentration range in urania single crystals at room temperature was demonstrated by He *et al.* [He *et al.* 2014]. The comparison of both temperatures (see figure 5-15) shows that the saturation plateaus have a large fraction at room temperature (25% for Xe, 20% for La) compared to 773 K (23% for Xe, 16% for La). Increasing the temperature leads to a reduction of the RDA fraction, most likely in relation with an enhanced recombination efficiency. The higher difference in the saturation values between the Xe and La at high temperature is likely related to the characteristics of the bubbles, although no significant difference was recorded between the sizes of bubbles measured by us at 773 K and at 293 K in similar conditions by He et al. (approximately 2 nm in both cases).

(iii) The evolution of the BC fraction shows a very distinct behavior between the two irradiation temperatures (see figure 5-16). In both cases the fraction is very low up to 7 dpa. Then for room temperature implanted crystals the fraction increases almost linearly with the same large slope for La and Xe and reaches almost 60% at 100 dpa (it is saturating at a slightly higher dpa); conversely at 773 K the increase is much less for both ions (5% for La and 20% for Xe) and reaches a saturation plateau at about 20 dpa. The shift of the damage evolution towards the low dose while increasing the irradiation temperature – as seen in the RDA fraction evolution – is not recorded here and the increase in BC appears at a slightly larger dpa value at larger temperature.

Let us remind the reader that in this dpa range, *in situ* TEM performed at 773 K showed the following evolution of defects: black dots defects, dislocation loops transforming progressively in dislocation lines, and finally the formation of a network of tangled dislocations. This evolution is essentially identical for both La and Xe-implanted crystals. Xe implantation experiments performed at room temperature by He *et al.* [He *et al.* 2014] demonstrated the same evolution sequence for the crystal restructuring. In this context, the channeling analysis provides us with a different picture of the progressive damaging of the crystal. In overall the fractions of both RDA and BC are lower while increasing the temperature. The role played by the temperature on the RDA is only little, with

essentially a shift towards low dpa values. A larger difference is observed for the BC evolution: the saturation plateau is strongly reduced (from 60% to 20%) and the saturation plateau occurs at a much lower dpa (20 dpa versus 100 dpa) when the temperature increases. These results support the idea that the restructuring process at higher temperature leading to the formation of the network of tangled dislocation is accompanied by a much lower distortion of atomic rows induced by the enhanced atomic mobility.

- *High dose range.*

In the high fluence range, both the high number of displacements suffered by matrix atoms during irradiation and the high concentration of impurities are likely to play a role in the restructuring process of the crystal. Contrarily to the case of the room temperature irradiations, the very large irradiation fluence was not explored at 773 K due to a lack of time. Few illustrative information are nevertheless accessible.

(i) At room temperature a marked difference is observed between the Xe-implanted crystal that suffers a huge increase of the RDA fraction (up to 80%) associated to a single crystal-polycrystal microstructural transformation, and the almost unaffected La-implanted crystal that keeps its monocrystallinity and keeps a saturation fraction of RDA at 21%. It is clear at this temperature that the solubility of the atom in the lattice has a direct influence on the radiation tolerance of urania, in relation with the formation of the HBS structure. At 773 K the partial available data shows a similar difference between Xe-implanted crystal, whose RDA fraction increases dramatically at almost the same fluence as for room temperature, and the La-implanted crystal that remains stable.

(ii) The BC evolutions show a parallel evolution at both temperatures – the fraction of BC is saturating in both cases – both the saturation level is far larger at room temperature.

In summary, based on the uncompleted data at 773 K (that will be completed within a few months), we speculate that a similar single crystal to polycrystal microstructural transformation occurs for the Xe-implanted crystal due to the presence of the nanometer-sized Xe bubbles. Conversely the La-implanted crystal, that was demonstrated to be stable at room temperature up to 20% La incorporation at room temperature, is most likely stable as well as 773 K.

To concluded the role played by the temperature on the damage evolution in irradiated UO_2, the results show that at high temperature, the increase of RDA appears at a much lower dpa and lower fractions of RDA and BC for both ions are observed compared to room temperature. The lower fraction of defects observed due to the enhancement of the recombination efficiency at high temperature. A higher value of saturation level for the Xe-implanted crystal with respect to the La-implanted one at both temperatures is also observed. This difference can be ascribed to the formation of nanometer-sized Xe bubbles.

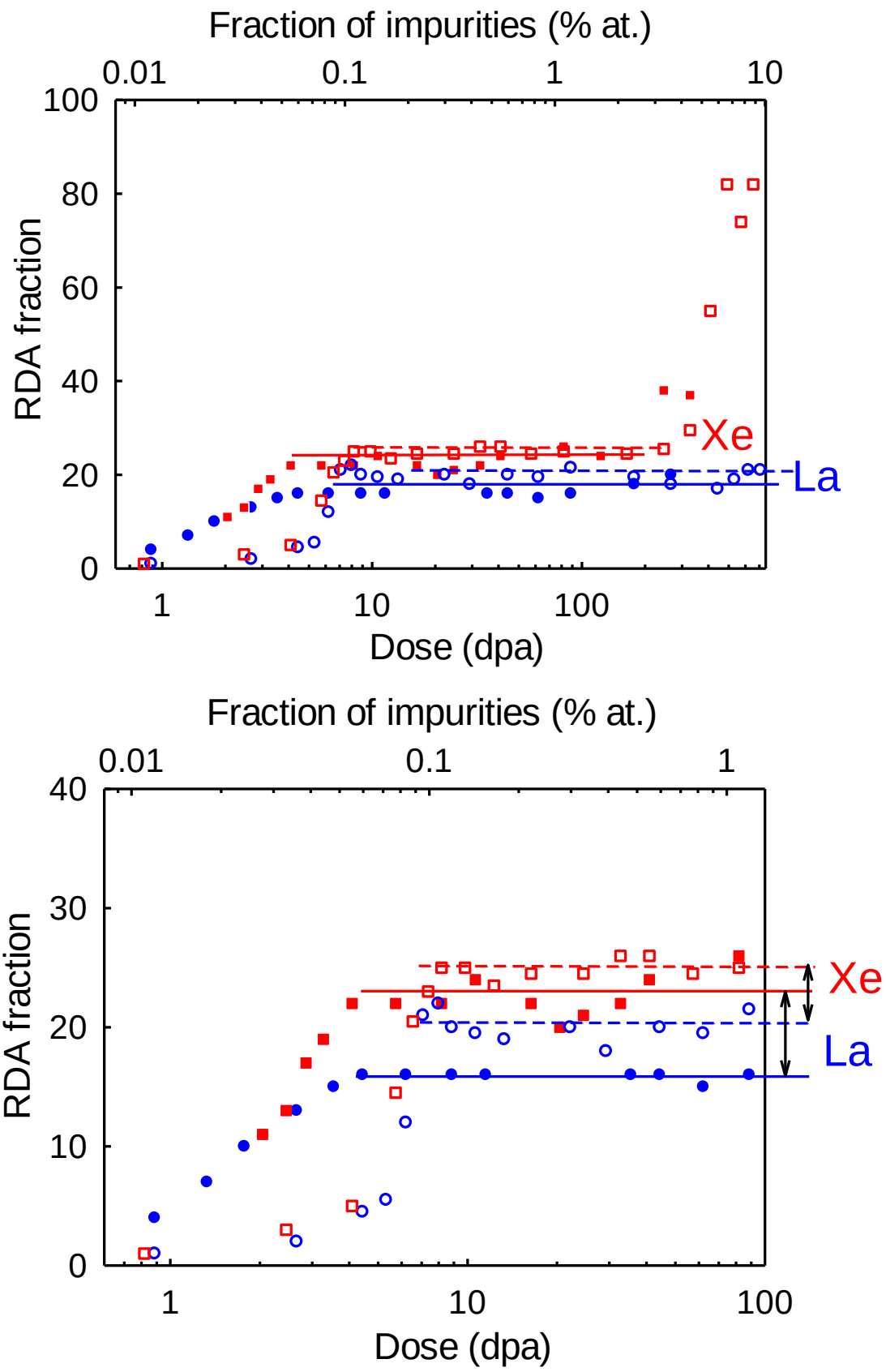

Figure 5-15: Evolution of Randomly Displaced Atoms (RDA) in UO_2 crystals (a) and the low dose part in (b), as measured by RBS-C, implanted at 773K (full symbols and solid lines) and at 293 K (opened symbols and dashed lines) with Xe (red squares) or La (blue circles) versus *dpa* and concentration of implanted elements in the solid recorded at the maximum of the distributions.

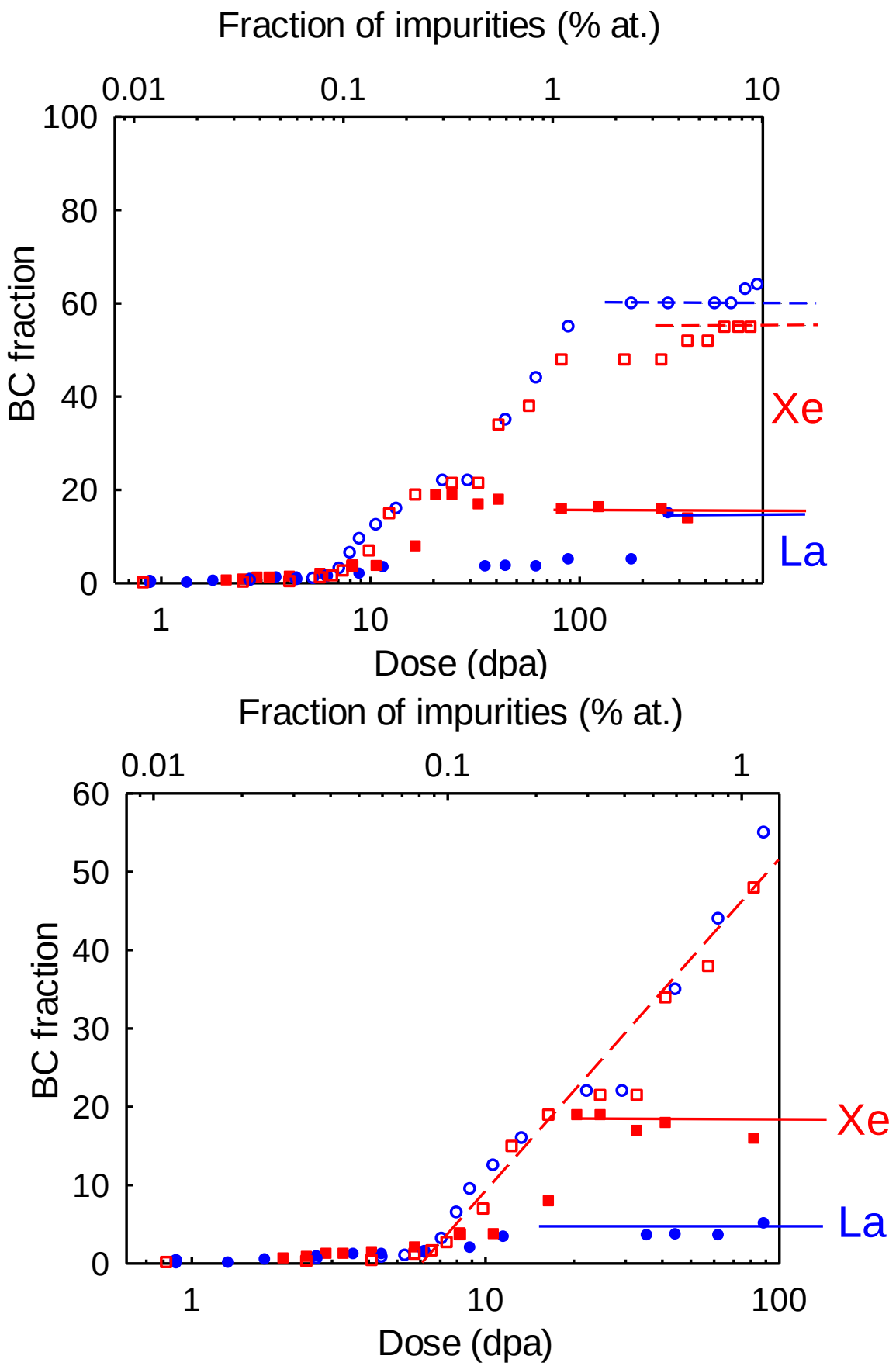

Figure 5-16: Evolution of Bent Channels (BC) in UO_2 crystals (a) and the low dose part in (b), as measured by RBS-C, implanted at 773K (full symbols and solid lines) and at 293 K(opened symbols and dashed lines) with Xe (red squares) or La (blue circles) versus *dpa* and concentration of implanted elements in the solid recorded at the maximum of the distributions.

References

[Bès *et al.* 2015]
René Bès, Philippe Martin, Emerson Vathonne, Rémy Delorme, Catherine Sabathier, Michel Freyss, Marjorie Bertolus, and Pieter Glatzel. Experimental evidence of Xe incorporation in Schottky defects in UO_2. Applied Physics Letters 106: 114102, 2015.

[Brillant *et al*. 2011]
G. Brillant, F. Gupta, A. Pasturel. Fission products stability in uranium dioxide. Journal of Nuclear Material 412:170–176, 2011.

[Debelle *et al.* 2014]
A. Debelle, J. Channagiri, L. Thomé, B. Décamps, A. Boulle, S. Moll, F. Garrido, M. Behar and J. Jagielsk, Comprehensive study of the effect of the irradiation temperature on the behavior of cubic zirconia. Journal of Applied Physics 115,183504, 2014.

[Feldman *et al.* 1982]
L. C. Feldman, J. W. Mayer, and S. T. Picraux. Materials Analysis by Ion Channeling: Submicron Crystallography. New York: Academic Press, 1982.

[Fujino 1988]

Takeo Fujino. Thermodynamics of fluorite type solid solutions containing plutonium, lanthanide elements or alkaline earth metals in uranium dioxide host lattices. Journal of Nuclear Materials, 154(1):14 – 24, 1988.

[Grimes & Catlow 1991]

R. W. Grimes, C. R. A. Catlow. The Stability of Fission Products in Uranium Dioxide. Physical Sciences and Engineering, 335(1639):609– 634, 1991.

[He *et al.* 2014]
L.F. He, J. Pakarinen, M.A. Kirk, J. Gan, A.T. Nelson, X.-M. Bai, A. El-Azab, T.R. Allen, Microstructure evolution in Xe-irradiated UO_2 at room temperature. Nuclear Instruments and Methods in Physics Research B 330:55–60, 2014.

[Imoto 1986]
S. IMOTO. Chemical state of fission products in irradiated UO_2. Journal of Nuclear Materials, 140:19-27, 1986.

[Kleykamp 1984]

H. Kleykamp. The chemical state of the fission products in oxide fuels. Journal of Nuclear Materials 131: 221-246, 1985.

[Nguyen thesis 2013]
Tien Nguyen, Channelling investigation of the behavior of urania under low-energy ion irradiation, in: PhD thesis, université Paris-Sud, 2013.

[Ronikier *et al.* 1975]
D. Ronikier-Polonsky, G. Désarmot, N. Housseau, Y. Quéré, Dechanneling by gas bubbles in a solid. Radiation Effects 27, 81 (1975)

[Soullard *et al.* 1985]
J. Soullard. High voltage electron microscope observations of UO_2. Journal of Nuclear Materials, 135(2 - 3):190 – 196, 1985.

Conclusions and perspectives

This thesis has been focused on reproducing the specific microstructure of the high burnup structure of the irradiated nuclear fuel and on the exploration of the various relevant parameters involved in the formation of such a structure, in evaluating their importance, and in clarifying the synergies between them. Although several studies of the specific microstructure HBS were performed to understand the polygonization process that appears in the HBS and to identify the mechanisms and the conditions of the formation of this structure (burnup, temperature, the high concentration of fission product and fission gases, pressure, grain size, etc.) in the nuclear fuel, the exact mechanisms are still not fully understood. For this reason, the specific microstructure of the nuclear spent fuel was experimentally simulated by using a very simplified model system - namely uranium dioxide single crystals - and the use of energetic ion beams for generating both the radiation damage and doping of the solid. This thesis is the first step forward a better understanding of the relevant parameters. The main idea aims to understand the role played by the chemical nature of bombarding ions on the matrix destabilization by using both soluble atoms in the urania matrix (lanthanum) and insoluble ones (xenon). A series of *in situ* experiments - *in situ* Transmission electron Microscopy (TEM) and *in situ* Rutherford Backscattering Spectrometry in the channeling mode (RBS/C), both techniques coupled to ion irradiation, were performed at 773 K to investigate the effects of the main parameters including: (i) radiation defects induced by collision cascades at low energy corresponding to the main mechanisms of stopping for fission fragments at the end of their range; (ii) soluble and insoluble impurities located in the crystal structure (iii) temperature of the fuel. The impurities that were chosen in this work are Xe and La due to their importance in the nuclear fuel as abundant fission products, they are similar in masses and atomic numbers, but they strongly differs with respect to the chemical properties.

The creation of defects was monitored with the ion channeling and TEM techniques. Channelling data were analyzed by Monte-Carlo simulation with the McChasy code. Simulations were performed assuming a two-defect model including randomly displaced atoms (RDA) and bent channels (BC). This simplified model includes many classes of genuine defects, such as point defects, extended defects, defects clusters or dislocations, polygonization of the solid or even a full amorphization. The results obtained to investigate the role of the first two parameters that were mentioned before can be summarized as the following:

(i) In the low implanted fluence range: a progressive increase in both RDA and BC are observed around 0.4 to 4 *dpa* (corresponding to the concentration of implanted ions of less than 0.06%) as a consequence of the radiation effects (defects created due to ballistic collision), which is independent of the nature of ions. The TEM analysis shows that the kinetics of the radiation damage are eventually identical for both Xe and La implanted crystals. They follow the sequence formation of black dots, dislocation loops transforming into dislocation lines. As the concentration of implanted impurities is very small within this fluence range, the chemical contribution of implanted species is too small to play a role in the defect creation.

(ii) In the medium fluence range: a wider damage zone observed compared to the case of the low-fluence range with a progressive formation of a dislocation network. The fractions of RDA and BC saturate for both ions and the RDA saturation plateau recorded for the Xe-irradiated solid exceeds the La-implanted by typically 8%, while the difference between BC at saturation is less but it is still significant 4%.

Different saturation levels were observed for the two ions within this fluence range due to the difference in solubilities of the two ions in UO_2. Lanthanum atoms are a soluble species and forms a solid solution in UO_2 (La most probably locates at substitutional positions or at empty octahedral sites). Such locations are responsible for only a low displacement of matrix atoms. In comparison, Xe atoms are insoluble in UO_2 and forms Xe nano-sized bubbles, leading to strong constraints in the matrix. As a consequence more displacement of matrix atoms are evidenced in Xe-implanted UO_2 crystal.

Regarding the BC evolution, a larger difference between the two ions (Xe and La) is evidenced in this fluence range compare to the low fluence range, where the fraction of BC for La-implanted crystal shows only a small evolution (increase of about 3%), while in Xe-implanted crystal, the BC fraction increases with increasing the fluence from 8% up to 14%.

In conclusion, irradiation in the medium fluence range creates a progressive formation of a dislocation network and the increase of the radiation damage towards greater depths in the crystal. The main difference between Xe and La is related to the solubility of implanted species.

(iii) In the high fluence range: When the crystals are implanted at a very high fluence (corresponding to the concentration of implanted ions of over 2.5 at. %), a clear increase of the RDA is recorded at the maximum of the distribution for both ions in the zone corresponding to the highest concentration of implanted impurities. Different behaviors were observed for both crystals implanted with soluble and insoluble elements. The fraction of RDA induced by soluble La ions is smaller than the fraction induced by implanting Xe ions, where a dramatic increase of RDA is observed. The fraction of RDA observed at the highest fluence reaches 43%, far larger compared to the saturation plateau of La. More damage is observed in the Xe-implanted crystal due to several reasons: (i) the solubility of La compared to Xe ions leading to the formation of nanometer-sized gas bubbles, (ii) the size of implanted species in UO_2 matrix where the insoluble Xe atoms have an atomic radius (r_{Xe} = 218 pm) much larger than the cationic radius of U^{4+} atoms (r_U = 97 pm), (La^{3+} atoms have a similar atomic radius as U^{4+} atoms) that eventually lead to polycrystalline the structure.

Regarding the BC evolution, the fraction for both ions in this fluence range almost saturate even if the crystal is implanted with a high concentration of impurities. Some increase with 3% regarding La ions at high concentration of implanted La about (4 at. %) is seen.

In this work, the effect of temperature on the kinetic of damage evolution in irradiated UO_2 was also investigated by comparing our results obtained at 773 K with room temperature experiments. The results show that at high temperature, the increase of RDA appears at a much lower dpa and a lower fractions of RDA and BC on the saturation plateaus for both ions are observed compared to room temperature experiments. The lower fraction of defects is due to the enhancement of the recombination efficiency at high temperature. A higher saturation level for the Xe-implanted crystal with respect to the La-implanted one is observed at both temperatures. This difference can be ascribed to the formation of nanometer-sized Xe bubbles.

After investigating the effects of the main parameters including: (i) radiation defects induced by collision cascades at low energy; (ii) the role played by soluble and insoluble impurities located in the crystal structure (iii) role of the temperature of the fuel on the damage evolution and the creation of HBS, we can conclude that the microstructural modifications occurring during the HBS formation is mainly due to the presence of the nanometer-sized bubbles that plays the most deleterious effect.

This work also opens several important questions to be answered:

First, a characterization of defects created in UO_2 single crystal by RBS/C and TEM technique at higher fluences should be performed. Angular scans by channeling ion technique will be useful for more details regarding the radiation damage. Such an angular scans are time consuming. Therefore, extra *ex-situ* crystals have to be prepared at selected fluence corresponding to characteristic steps in the damage accumulation. Crystals have to be then mostly analyzed along the major planes and cross major axes.

Second, an improved model of radiation-induced defects created by ion irradiation should be performed including the incorporation of true dislocations (involving dislocation core and distorted rows), clusters defects and precipitates or gas bubbles embedded into a crystalline structure. The description of a realistic model for dislocation is currently being developed at the NCBJ Warsaw.

Last but not least, in the situation of a real nuclear fuel, the UO_2 is irradiated by different particles including neutrons, alpha and gamma particles, and fission products. Uranium dioxide (UO_2) is subjected to significant restructuring processes during its operating life in the reactor core due to the slowing-down and interaction of the fission fragments with the UO_2 matrix, which affect the material structure and its mechanical and chemical properties. Those fission fragments induce the damage not only by nuclear damages, mainly at low energies inducing atomic displacements, but also by electronic damages, for high energy leading to excitations. Therefore, it is important to investigate the stability of uranium dioxide and their behavior under irradiation taking into account the combined effect of nuclear and electronic damage in UO_2. This can be carried out by using ion beam irradiation on JANNuS-Saclay platform. It may be used in single or dual beam conditions on poly- and monocrystalline sample. Different *in situ* characterization techniques may be used to perform this study, such as Raman analysis (JANNuS-Saclay), TEM observation (JANNuS-Orsay) and RBS/C.

Appendices

Appendix A

Résumé

Le dioxyde d'uranium (UO_2) est essentiellement utilisé comme combustible dans les réacteurs nucléaires depuis le début des années 1950, et peut être également utilisé sous la forme d'un mélange de dioxyde d'uranium UO_2 et de dioxyde de Plutonium (PuO_2). En effet, $(U,Pu)O_2$ appelé mélange d'oxydes (MOX) est également utilisé comme combustible nucléaire [1]. Au cours de sa durée dans le cœur du réacteur, il est sujet à des processus de restructuration significatifs et des changements importants; ceux-ci sont dus aux défauts induits par l'irradiation dans le matériau [2] [3].

Depuis que les combustibles nucléaires usés de type REP ont commencé à être testés, une microstructure poreuse à grains fins a été observée à taux de combustion élevé. Cette microstructure dite *High Burnup Structure* (HBS) se produit dans la région périphérique de la pastille de combustible sur une épaisseur typique comprise entre 100 à 200 μm. Cette structure est caractérisée par la formation des grains sous-micrométriques d'une taille environ 0.2 μm et par le développement de pores de gaz de fission [4-8]. La formation de cette nouvelle structure durant l'irradiation est un sujet d'importance et le processus de polygonisation présente à la fois un intérêt scientifique majeur et une importance technologique considérable. Il est ainsi nécessaire de comprendre et de modéliser les propriétés de cette structure à fort taux de combustion pour évaluer son influence sur les performances du combustible irradié, et capital de comprendre scientifiquement les mécanismes régissant la formation du HBS.

L'objectif de cette Thèse de doctorat est d'étudier les mécanismes de formation de la structure à taux de combustion élevé. Cet objectif est réalisé par la reproduction de cette microstructure spécifique du combustible irradié en utilisant un système de modèle ultra simplifié – à savoir des monocristaux d'UO_2 – et par l'utilisation de faisceaux d'ions énergétiques. Ces derniers ont pour double but de générer à la fois les dégâts d'irradiation et d'assurer le dopage du solide, afin d'examiner le rôle joué par les différents paramètres mis en jeu, en évaluant leur importance et en clarifiant leurs synergies.

Des monocristaux de dioxyde d'uranium ont été implantés et caractérisés *in situ* – sur la plate-forme SCALP/JANNuS-Orsay située au CSNSM – par les techniques de la Spectrométrie de Rétrodiffusion Rutherford en canalisation (RBS/C) et de Microscopie Électronique en Transmission (TEM). Des cristaux ont été implantés avec des ions xénon (Xe) et du lanthane (La) de basse énergie à la température de 773 K et à différentes fluences dans le but d'explorer le rôle joué par les éléments solubles et insolubles les plus abondants dans le combustible usé lors de la création de la structure HBS. Les énergies et les masses des projectiles ont été choisies dans ce travail de thèse afin d'étudier les dégâts d'irradiation pouvant résulter principalement: (i) des collisions nucléaires élastiques en fin de parcours des ions dans le solide et (ii) de la contribution chimique de l'implantation d'impuretés à forte concentration.

[1] Getting to the Core of the nuclear fuel cycle - From the mining of uranium to the disposal of nuclear waste, International Atomic Energy Agency, Department of Nuclear Energy.
[2] G. Knoll, Radiation Detection and Measurement, third ed., John Wiley & Sons, Inc., USA, 2000.
[3] F. Garrido, L. Vincent, L. Nowicki, G. Sattonnay, L. Thomé, Nucl. Instrum. Meth. B 266 (2008) 2842–2847.
[4] V. Rondinella, T. Wiss, Mater. Today, 13 (2010)12.
[5] Hj.Matzke, J. Nucl. Mater. 189 (1992) 141-148.
[6] K. Lassmann, C.T. Walker, J. van de Laar, F. Lindstrom, J. Nucl. Mater. 226 (1995) 1-8.
[7] K. Une, K. Nogita, S. Kashibe and M. Imamura, J. Nucl. Mater. 188 (1992) 65-72.
[8] K. Nogita, K. Une, M. Hirai, K. Ito, y. Shirai, J. Nucl. Mater. 248 (1997) 196-203.

Les expériences de RBS/C conduites *in situ* ont été conduites sur les cristaux implantés avec des ions Xe^{3+} de 470 *keV* (correspondant à un parcours projeté Rp ~ 83 nm et à un écart type ΔRp ~ 39 nm) ou La^{3+} de 500 *keV* (correspondant à un parcours projeté Rp ~ 86 nm et à un écart type ΔRp ~ 41 nm) à la température de 773 K. Les fluences variaient de 5×10^{13} à quelques 10^{16} cm^{-2}. Les échantillons implantés ont été caractérisés avec un faisceau d'ions ^{4}He de 3.085 *MeV*. Le code SRIM [9] a été utilisé dans le but d'évaluer le nombre de déplacements par atome (dpa) créé à un niveau d'un maximum de distribution et la fraction d'impuretés incorporées.

Le code de simulation Monte-Carlo McChasy a été utilisé pour analyser les données expérimentales de canalisation et pour extraire la fraction de défauts présente dans la structure cristalline. Ces calculs ont été réalisés en admettant la présence de deux catégories de défauts: (i) des atomes aléatoirement déplacés (RDA) et (ii) des distorsions des rangés atomiques (BC). Les atomes aléatoirement déplacés, qui supposent qu'une fraction donnée des deux atomes U et O est déplacée de manière aléatoire dans le réseau à une profondeur donnée, sont utilisés pour modéliser des défauts de type obstruction (tels que les défauts de type interstitiel ou des fautes d'empilement). Les défauts de distorsion des rangés atomiques, supposent l'existence de rangées atomiques déformées sous irradiation (similaire à l'effet de dislocations), et contribuent à la décanalisation des particules d'analyse. Par souci de simplification, la fraction de distorsions des rangés atomiques est supposée constante sur toute la profondeur endommagée du solide, alors que la fraction des atomes aléatoirement déplacés possède une distribution donnée en fonction de la profondeur. Les paramètres de distorsions des rangés atomiques ont été paramétrés par leur longueur L=50 nm et l'angle de désorientation η=25°, en accord avec les mesures de microscopie électronique. Ce modèle permet d'analyser les données de canalisation et d'extraire les distribution en profondeur des défauts de type RDA et BC. Le modèle à deux défauts présente un très bon accord avec les données expérimentales même à grande profondeur, et reproduit essentiellement les caractéristiques du spectre de canalisation à toute fluence d'irradiation. La cinétique de l'évolution du défaut correspondant à la fraction maximale mesurée en fonction des dpa a été extraite (voir figure A-1). L'évolution de la fraction de défauts de type RDA montre une forte augmentation entre 0.4 à 4.0 dpa (correspondant à une très faible concentration des ions implantés), indépendamment de la nature des ions. Elle est suivie par une saturation de cette fraction pour les deux ions sur une large gamme d'irradiation et s'étend au-delà de 100 dpa. Une forte élévation de cette fraction est observée en particulier pour les cristaux implantés avec des ions Xe pour une concentration élevée dépassant les 4% (pourcentage correspondant à la dose de plus de 250 dpa). L'évolution des défauts de type BC montre une augmentation jusque 4 dpa puis une saturation pour ces deux ions considérés.

[9] J. F. Ziegler, M.D. Ziegler, J.P. Biersack, the Stopping and Range of Ions in Solids, Pergamon, New York, 1985.

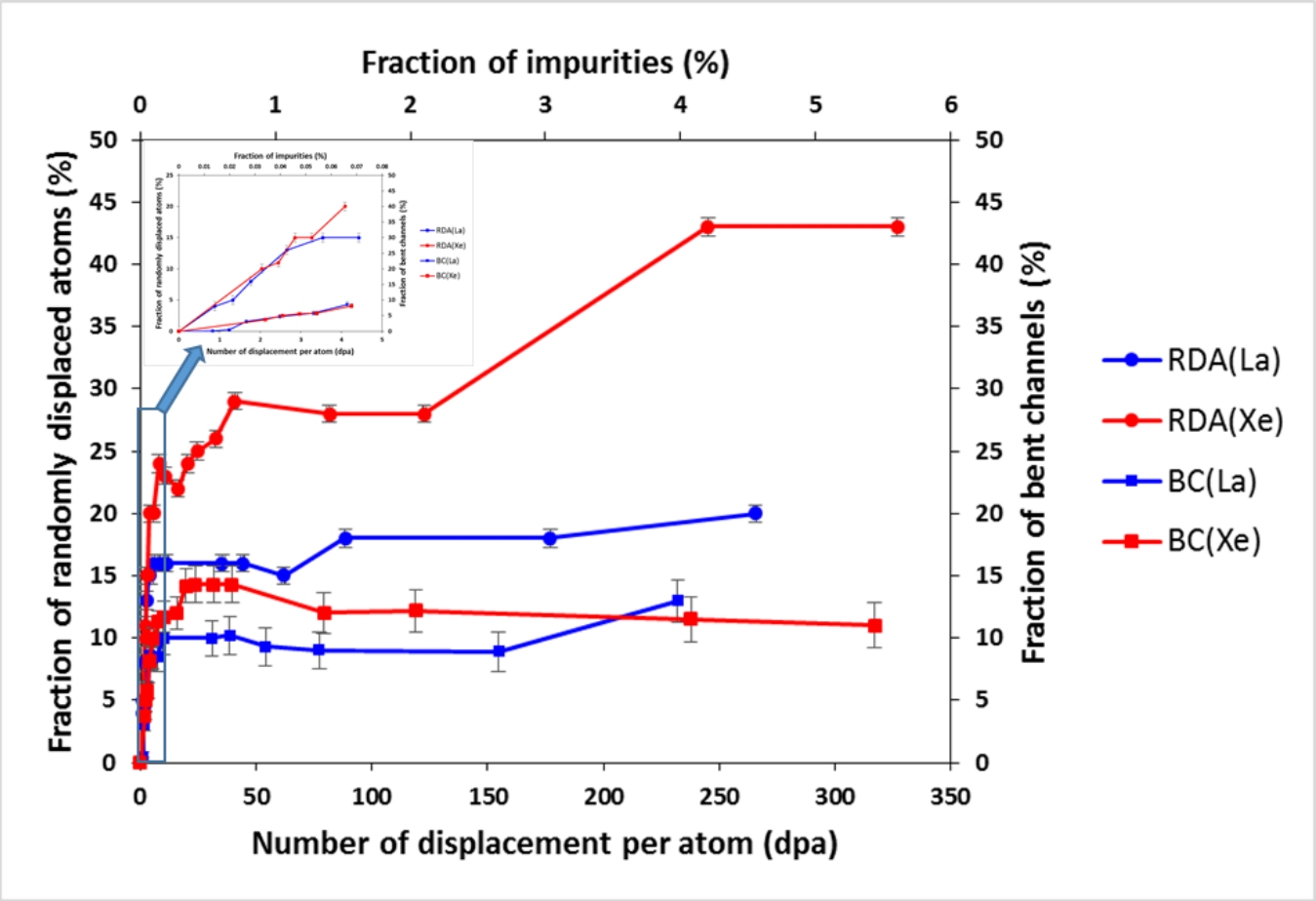

Figure A-1: Évolution de la fraction de RDA et de BC en fonction de dpa et de la fraction d'impuretés implantées dans un cristal UO_2 bombardé avec des ions La de 500 keV ou avec des ions Xe de 470 keV.

En parallèle des expériences précédentes, les expériences de microscopie électronique à transmission *in situ* ont été effectuées sue la plateforme JANNuS-Orsay pour étudier l'évolution microstructurale et la formation des défauts induits par irradiation dans les monocristaux de UO_2. Les monocristaux minces ont été implantés avec des ions La de 265 KeV (Rp ~ 39 nm) ou avec des ions Xe de 260 KeV (Rp ~ 39 nm) à 773 K. L'angle d'incidence entre le faisceau d'ions et la normale à la surface de l'échantillon est égal à 42°. Les images TEM en champ clair ont été enregistrées aux différentes étapes jusqu'à la fluence $4\times10^{15}cm^{-2}$, à 773 K ou à la température ambiante. Les résultats de microscopie électronique *in situ* montrent que des défauts identiques sont produits pour les deux ions (voir figures A-2 et A-3) et présentent la même évolution en fonction de la fluence. Différents défauts apparaissent en fonction de la fluence : la première étape correspond à la formation de 'black dots' ; la deuxième étape est caractérisée par la formation de boucles puis de lignes de dislocations, qui évoluent finalement jusqu'à commencer à devenir moins différenciables; certaines d'entre elles fusionnent alors, interagissent, et le processus de restructuration se poursuit par la formation d'un réseau de dislocations enchevêtrées. Une forte densité de bulles de gaz, de taille nanométrique et avec un diamètre moyen de 2 nm est observée pour le cristal Xe implanté à une dose seuil de 4 dpa.

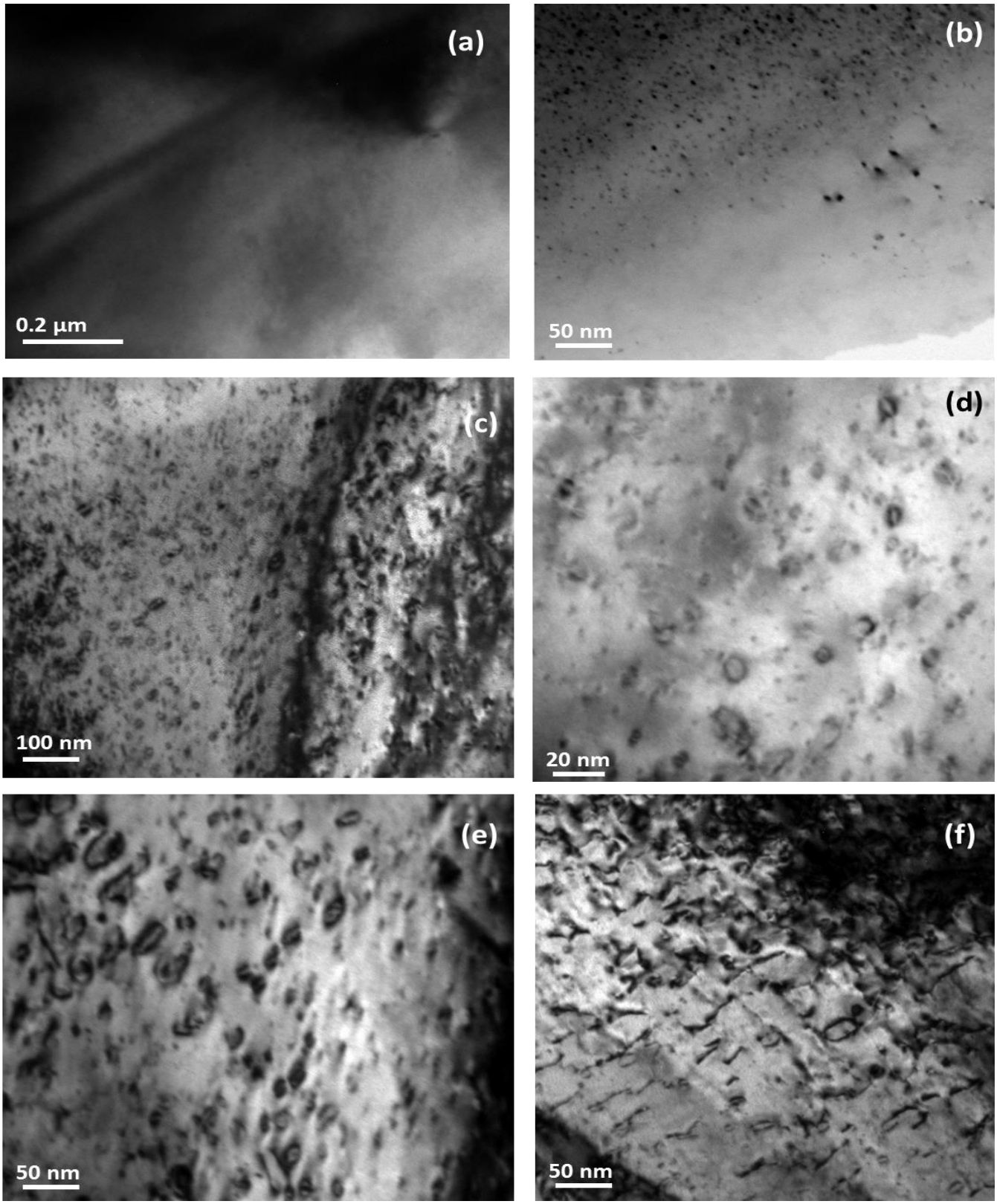

Figure A-2: Les images TEM en champ clair enregistrées sur une lame mince de UO_2 pendant l'irradiation avec des ions La de 265 keV à la température 773 K et à différentes fluences: (a) avant l'implantation, (b) 0.55 dpa, (c) 1.1 dpa, (d) 2.2 dpa, (e) 3.3 dpa et (f) 7.6 dpa.

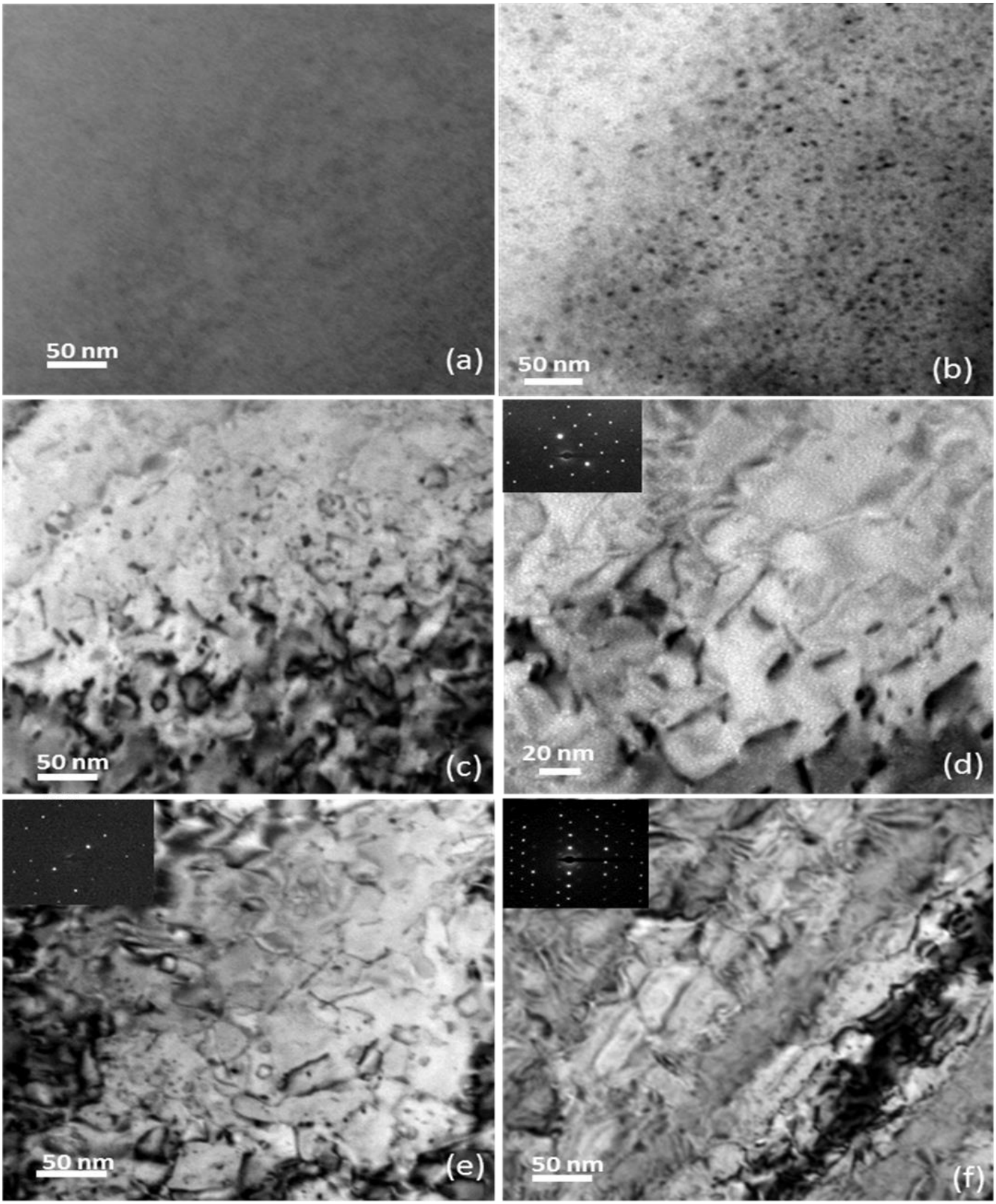

Figure A-3: Les images TEM en champ clair enregistrées sur une feuille mince de UO_2 pendant l'irradiation avec des ions Xe de 260 keV à la température 773 K et à différentes fluences: (a) avant l'implantation, (b) 1.1 dpa, (c) 4.4 dpa, (d) 6.5 dpa, (e) 8.8 dpa et (f) 43.6 dpa.

Le couplage entre les deux techniques RBS/C et TEM conduites *in situ* montre que la différence entre les plateaux à saturation pour les deux ions, d'une part, et l'augmentation drastique de la fraction de défauts de type RDA sous une forte concentration d'ions Xe implantés, d'autre part, peuvent être attribuées à: (i) la solubilité des ions La par rapport aux Xe conduisant à la formation des bulles de gaz de taille nanométrique et (ii) la taille des espèces implantées dans la matrice UO_2 où les atomes Xe insolubles ont un rayon atomique beaucoup plus grand que le rayon cationique des atomes U^{4+} (les atomes La^{3+} ont un rayon atomique similaire à celui des atomes U^{4+}), responsables de plus fortes contraintes dans le cristal de UO_2.

Cette thèse est organisée en cinq chapitres comme suit:

1. Le premier chapitre introduit le dioxyde d'uranium comme un matériau nucléaire en décrivant ses propriétés et les processus et les changements qui se produisent pendant sa durée de vie dans le noyau du réacteur. L'effet de l'irradiation dans le combustible nucléaire, la théorie de l'interaction entre des particules chargées et le matériau et l'apparition d'effets spécifiques se produisant dans une structure soumise à un taux de combustion très élevé, sont abordés dans ce chapitre.
2. Le deuxième chapitre présente en détail l'expérience de simulation qui a été effectuée pour reproduire et étudier la structure à fort taux de combustion et les différentes techniques de caractérisation qui ont été appliquées pour étudier une telle structure, i.e. cla Microscopie Électronique en Transmission et la Spectrométrie de Rétrodiffusion Rutherford en canalisation. Une introduction générale sur le code de simulation Monte-Carlo qui a été utilisé pour quantifier ces défauts est discutée.
3. Dans le troisième chapitre, les détails des expériences de Spectrométrie de Rétrodiffusion Rutherford en canalisation réalisées au cours de cette thèse sont présentés, ainsi que leur analyse, pour les cristaux implantés avec les deux ions, en utilisant le modèle de deux défauts de Monte-Carlo. L'évolution des défauts extraite des simulations numériques est également discutée.
4. Le quatrième chapitre présente les résultats expérimentaux de la Microscopie Électronique en Transmission. L'évolution des défauts de l'implantation des différents ions (La ou Xe) est détaillée.
5. Le cinquième chapitre traite du rôle joué par les éléments étrangers sur la stabilité des cristaux de dioxyde d'uranium et de l'effet de la température sur l'évolution des défauts produits. Dans ce chapitre, l'évolution des défauts est obtenue par le couplage des deux techniques RBS/C et TEM.
6. Ce travail de Thèse se termine par une conclusion et des perspectives de futurs travaux.

Appendix B

Example of an input/output file from SRIM

The following figure show the input parameters used to obtain the stopping power of xenon ion in UO_2 as a function of its energy calculated by SRIM code using Stopping/Range Tables, and the corresponding output text file. In this example the stopping powers and the ion range have been calculated for Xe ions between 300 and 800 keV in UO_2.

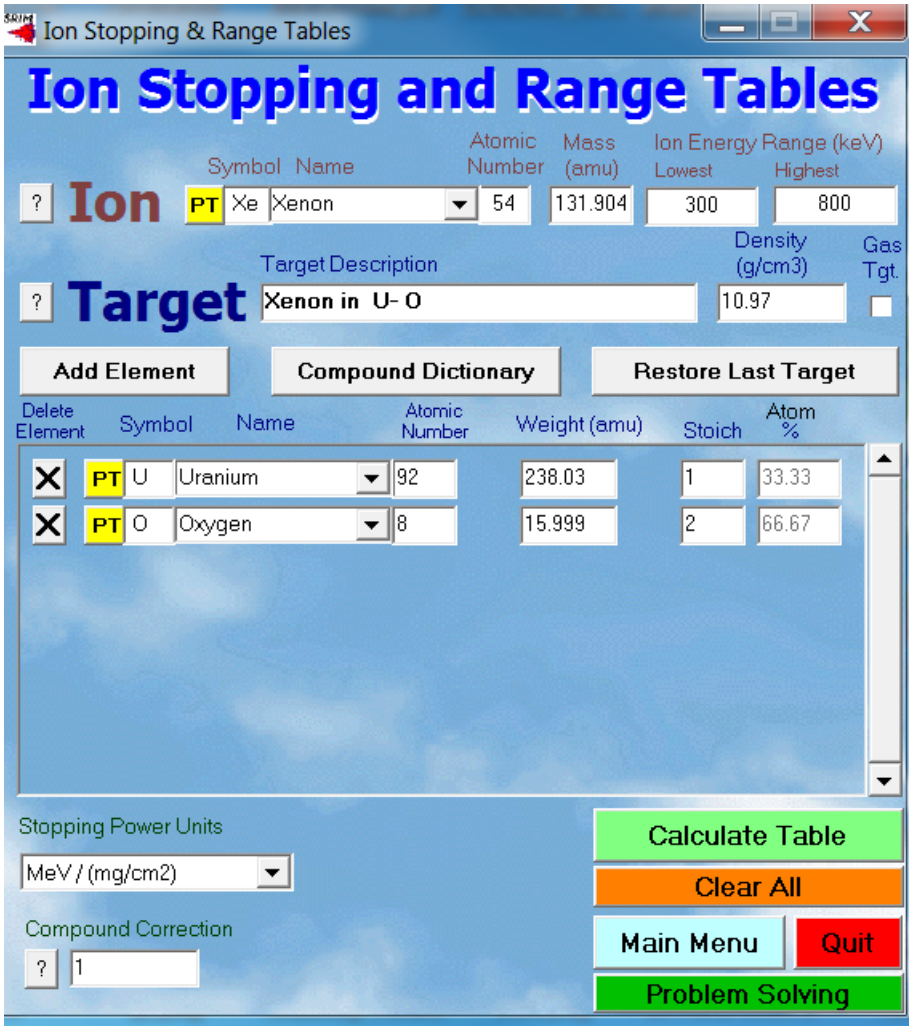

```
==========================================================================
              Calculation using SRIM-2006
              SRIM version ---> SRIM-2013.00
              Calc. date   ---> October 03, 2017
==========================================================================

Disk File Name = SRIM Outputs\Xenon in  U- O

Ion = Xenon [54] , Mass = 131.904 amu

Target Density =  1.0970E+01 g/cm3 = 7.3400E+22 atoms/cm3
======= Target  Composition ========
   Atom   Atom   Atomic    Mass
   Name   Numb   Percent   Percent
   ----   ----   -------   -------
     U     92    033.33    088.15
     O      8    066.67    011.85
====================================
Bragg Correction = 0.00%
Stopping Units =  MeV / (mg/cm2)
See bottom of Table for other Stopping units

  Ion          dE/dx       dE/dx      Projected  Longitudinal   Lateral
 Energy        Elec.       Nuclear      Range     Straggling   Straggling
----------   ----------  ----------  ----------  ----------  ----------
300.00 keV   4.964E-01   3.401E+00      525 A       286 A       205 A
325.00 keV   5.131E-01   3.398E+00      563 A       305 A       218 A
350.00 keV   5.296E-01   3.392E+00      601 A       324 A       231 A
375.00 keV   5.459E-01   3.383E+00      639 A       342 A       244 A
400.00 keV   5.617E-01   3.373E+00      678 A       361 A       257 A
450.00 keV   5.918E-01   3.348E+00      755 A       398 A       283 A
500.00 keV   6.202E-01   3.320E+00      832 A       435 A       308 A
550.00 keV   6.471E-01   3.288E+00      910 A       472 A       333 A
600.00 keV   6.730E-01   3.255E+00      989 A       509 A       359 A
650.00 keV   6.981E-01   3.221E+00     1068 A       545 A       384 A
700.00 keV   7.227E-01   3.187E+00     1148 A       582 A       409 A
800.00 keV   7.710E-01   3.117E+00     1309 A       655 A       460 A
--------------------------------------------------------------------
Multiply Stopping by        for Stopping Units
--------------------        ------------------
 1.0970E+02                  eV / Angstrom
 1.0970E+03                 keV / micron
 1.0970E+03                 MeV / mm
 1.0000E+00                 keV / (ug/cm2)
 1.0000E+00                 MeV / (mg/cm2)
 1.0000E+03                 keV / (mg/cm2)
 1.4945E+02                  eV / (1E15 atoms/cm2)
 7.6719E-02                 L.S.S. reduced units
==========================================================================
(C) 1984,1989,1992,1998,2008 by J.P. Biersack and J.F. Ziegler
```

Appendix C

Practical use of the code- typical example of McChasy file

A typical example of McChasy file that used to analyze the RBS/C channelling spectra. This specific file corresponds to the analysis of a single crystal UO_2 irradiated with 470-KeV Xe ions at 773 K at fluence $3x10^{14}$ cm^{-2}.

```
*** Along (001) plane across [110] axis
OMC 4.1 12.5
ESP off                  (Elemental spectra)
BSP on                   (Backscattering spectra)
PRO helium               (Projectile)
RES 15                   (RBS energy resolution in keV)
BEC 4.704 101.891        (Width of RBS energy channel in keV)
THI 3000                 (Range of simulation)
IBD 0.12                 (Ion-beam dispersion)
MIR on
ENE 3085                 (Projectile energy in keV)
SCA 165                  (Scattering angle in deg)
ANG 0 15
TGT UO2                  (Target material)
PAR 200000               ( Number of particles)
KLM 001                  (Channelling axis)
ESC on
LEL 2                    (local energy loss)
*** Depth (nm) value       obligatory comment
  1   0         0.5        subsequent layers start at 0, at 100 nm, at 250 nm, etc...
  2   2999      0.5
***
FOR rump                 ( program used to calculate dE/dx)
CRS O O165.CRS           (Cross section file)
VIB U    8.1             (Atomic vibration for U)
VIB O    8.5             (Atomic vibration for O)
GON scan 10
TET 1
1    0.0
*** include Bent Channels
*** DIS eta   L   Q
DIS     25  50  1
DID     3
***     depth     factor
1       0         5.0
2       180       0.0
3       3000      0.0
DEF   all 21 step depth (nm) UNI GAU DIC RIN
1                      0   6      0    0    0
2                     10   0      0    0    0
```

3	20	5	0	0	0
4	30	6	0	0	0
5	40	7	0	0	0
6	50	9	0	0	0
7	60	10	0	0	0
8	70	11	0	0	0
9	80	10	0	0	0
10	90	9	0	0	0
11	100	8	0	0	0
12	110	6	0	0	0
13	120	5	0	0	0
14	130	4	0	0	0
15	140	3	0	0	0
16	150	2	0	0	0
17	160	2	0	0	0
18	170	1	0	0	0
19	180	0	0	0	0
20	190	0	0	0	0
21	200	0	0	0	0

GON rotate 4
EXE Random
GON static 0 0 (Goniometer control)
EXE Aligned (Execute file)

Appendix D

The uncertainties in the fraction of RDA and BC

The certainty of the channelling spectrum for virgin crystal depends strongly on the quality of the crystal. The existence of any imperfection has an effect on the axial channelling spectrum by increasing the level of the dechannelling signal that is recorded. Regarding the implanted crystal that contains defects, the channelling spectrum is affected by two additional things: (i) obstruction-type defects (defects locate in the channels that are directly backscattered the ions) and/or (ii) small angle scattering of the channelling ions i.e. distortion-type defects. In both cases the channelling spectrum is affected depending on the nature and on the concentration of defects.

As mentioned before, RDA represent the obstruction-type of defects have a main effect on the direct backscattering of ions, while the BC represent the distortion-type of defects that effect the backscattering event in different way. Any modification or small change in RDA will affect immediately the backscattering of ions and it modifies the channelling spectrum directly. The modification of BC have a more pronounced influence on the channelling spectrum when the fraction is small; in comparison when the crystal is heavily damaged, a small increase of BC has a negligible influence on the axial spectrum. The channelling spectra are more sensitive to the presence of BC at low concentration rather than at high concentration of BC.

The uncertainties in the fraction of RDA and BC are defined after fitting the channelling spectra with the best agreement as mentioned in section 3.4 by the following procedure:

Uncertainties in RDA: To determine the uncertainty in the RDA fraction, the fraction of BC is kept constant as it was defined for the best fit of the channelling spectrum, then the fraction of RDA is modified in small steps to define the uncertainty. It has been observed that modifying the fraction of RDA up to 1% still gives an acceptable agreement between the simulation and the experimental spectrum. Conversely, modifying the fraction of RDA by more than 1% breaks the agreement. Figure D-1 shows one example of modifying the RDA fraction in order to define the uncertainty. The figure presents the MC simulation for channelling spectrum obtained by implanting UO_2 with La at fluence 2 $x10^{14}$ cm^{-2} . As it can be seen from the figure, the uncertainty with 1% of RDA is acceptable compared to 2%.

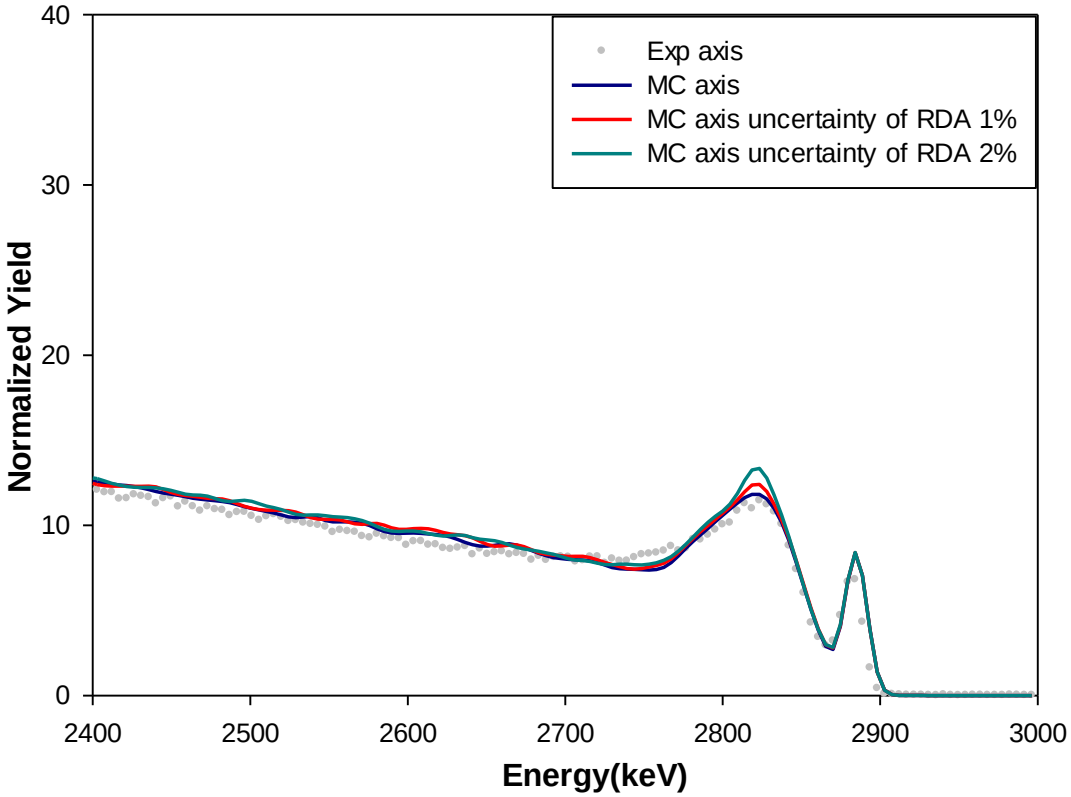

Figure D-1: The uncertainty in RDA and its effects on MC simulation

- Uncertainties in the BC fraction: To determine the uncertainty in the BC fraction, the fraction of RDA is kept constant as the values obtained the best fit of channelling spectrum and the fraction of BC is then modified in a small steps to define the uncertainty. The variation in the BC fraction should be in a small steps at low concentration of BC (corresponding to low fluence) as the channelling is more sensitive to the variation of BC fraction at low fluence than at higher concentration (corresponding to high fluence). After trying to define the uncertainty in BC fraction, it has been defined at 0.1% for low fluence (as shown in figure D-2.a) up to 2% to high fluence (as shown in figure D-2.b).

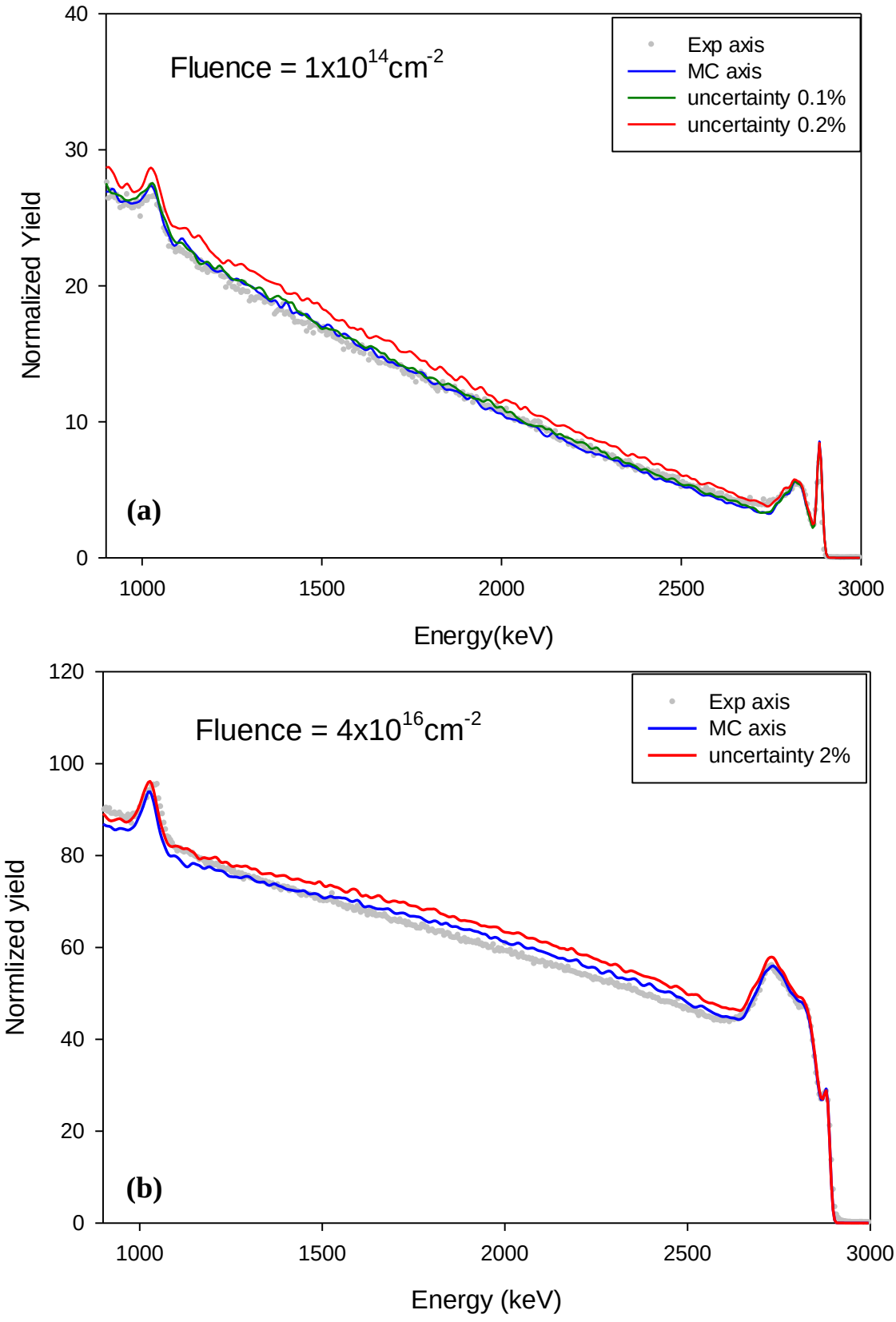

Figure D-2: The uncertainty in RDA and its effects on MC simulation for low fluence (a) and high fluence (b) examples.

Appendix E

Analysis of channeling spectra obtained at room temperature

This section presents the analysis of RBS/C spectra were obtained under the same experimental conditions but at room temperature by Tien Nguyen during his thesis by using two-defect model assuming L = 5 nm and η = 1.5° for the BC parameters. The damage evolution and the kinetic of damage accumulation that were extracted from MC also discussed. Results were used in the chapter 5 to investigate the effect of temperature.

E.1 Monte Carlo simulations for RBS/C spectra obtained at room temperature.

Channeling data of implanting 500-keV La ions and 470-keV Xe ions implanted in UO_2 single crystal at room temperature are analyzed by Tien Nguyen during his thesis [Nguyen thesis 2014] by using Monte-Carlo simulation code assuming a two-defect model. Figures E-1 and E-2 display the MC simulation with two-defect model (combination of RDA and BC) spectrum that show the best fit and good agreement with the experimental data. Some discrepancy also appear at depths that largely exceeding the damage zone as what observed in previous analysis.

Figures E-1 and E-2 show clearly the good agreement between MC simulation spectra and the experimental data. Even increase of this damage peak and the broaden by increasing the fluence is nicely fitted. At high fluence (higher than $1x10^{16}$ cm^{-2}) where a big change in the shape and depth of damage peak is observed, the fit also successfully reproduces the data. Therefore, we can conclude that the two-defect model (RDA and BC) is able to fit and reproduce successfully all channeling spectra that were recorded in single crystals implanted with low energy ions at room temperature and at 773 K.

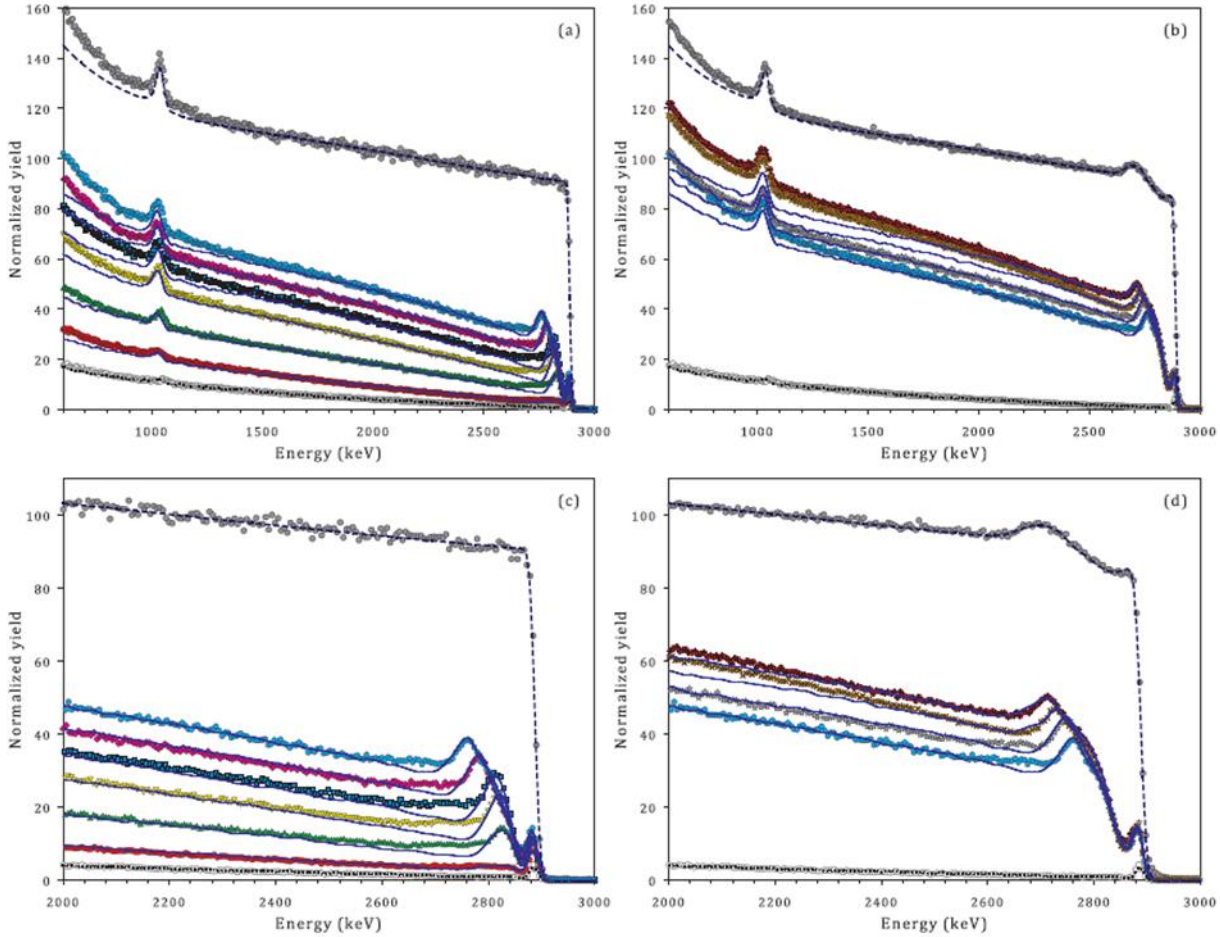

Figure E-1: Best MC simulations to RBS/C spectra recorded for La implanted crystal at room temperature in random condition (dashed line) and in axial aligned condition for virgin (dotted) and UO_2 implanted crystal (solid line). Experimental channelling spectra are plotted in symbols for fluences of $\Phi = 3x10^{14}$ cm^{-2} (red circles), $7x10^{14}$ cm^{-2} (green triangles up), $8x10^{14}$ cm^{-2} (yellow triangles down), $1x10^{15}$ cm^{-2} (violet squares), $2.5x10^{15}$ cm^{-2} (pink diamonds), $5x10^{15}$ cm^{-2} (cyan hexagons), $1x10^{16}$ cm^{-2} (gray stars), $2x10^{16}$ cm^{-2} (orange crosses) and $3x10^{16}$ cm^{-2} (red crossed-circles). (c) and (d) are zooms in the surface region of figure (a) and (b). Fits were performed assuming L = 5 nm and $\eta = 1.5°$.

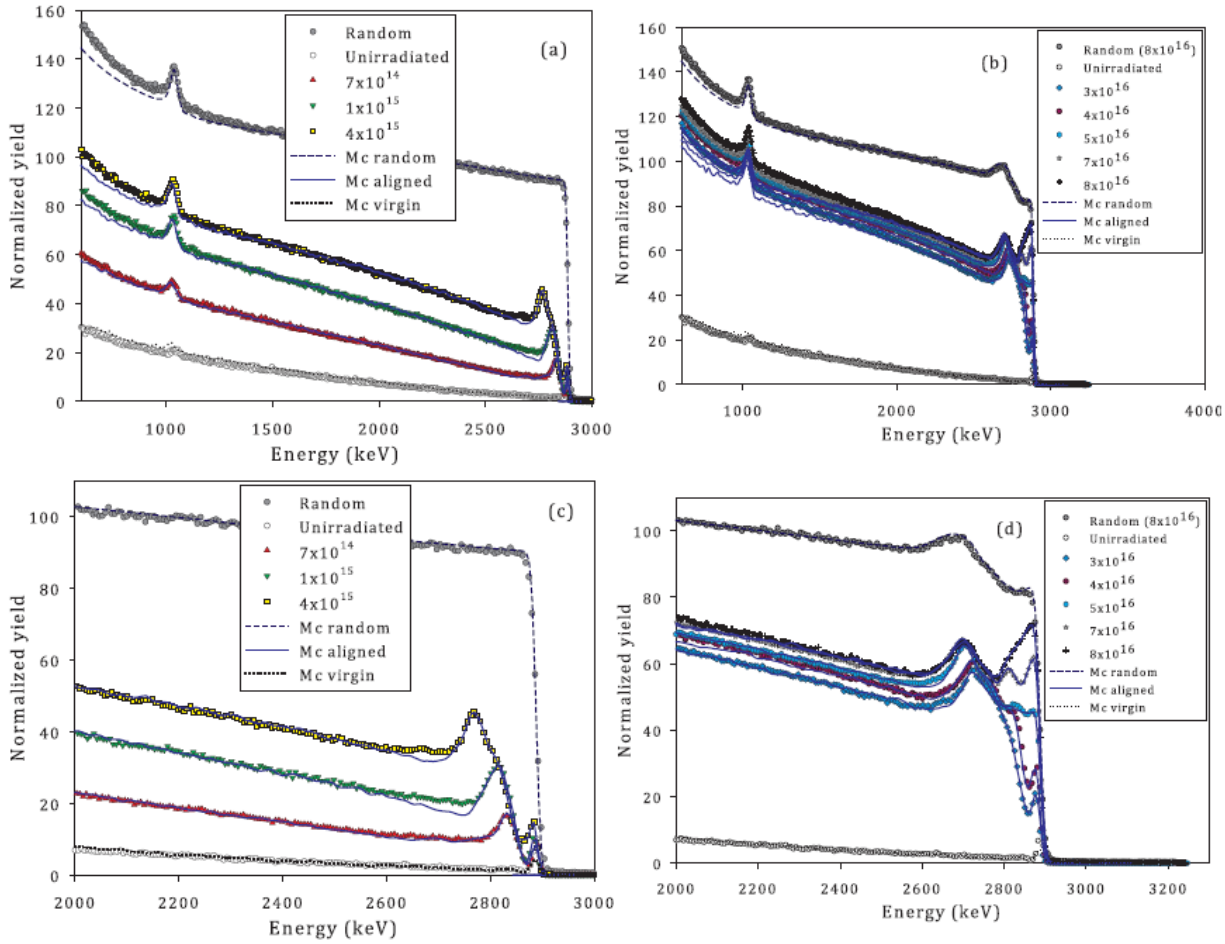

Figure E-2: Best MC simulations to RBS/C spectra recorded for Xe implanted crystal at room temperature in random condition (dashed line) and in axial aligned condition for virgin (dotted) and UO_2 implanted crystal (solid line). Experimental channelling spectra plotted in symbols for fluences of $\Phi = 2x10^{14}$ cm^{-2} (red circles), $7x10^{14}$ cm^{-2} (green triangles up), $8x10^{14}$ cm^{-2} (yellow triangles down), $1x10^{15}$ cm^{-2} (violet squares), $2.5x10^{15}$ cm^{-2} (pink diamonds), $5x10^{15}$ cm^{-2} (cyan hexagons), $1x10^{16}$ cm^{-2} (gray stars), $3x10^{16}$ cm^{-2} (red crossed-circles) and $4x10^{16}$ cm^{-2} (green crossed-squares). (c) and (d) are zooms in the surface region of figure (a) and (b). Fits were performed assuming L = 5 nm and $\eta = 1.5°$.

E.2 Evolution of defects (RDA & BC)

In this section the evolution of RDA and BC fraction are be shown. The results divided into three range according to the irradiated fluence: (i) low implanted fluence range (0 to $\Phi \leq 1x10^{15}$ cm^{-2}), (ii) medium implanted fluence range ($1x10^{15}$ $cm^{-2} \leq \Phi \leq 1x10^{16}$ cm^{-2}) and (iii) high implanted fluence range ($\Phi \geq 1x10^{16}$ cm^{-2}).

(i) Low fluence range: figure E-3.a represents the destitution of RDA versus depth for low La and Xe implanted fluences. The distribution of RDA for both ions shows a similar behavior: the maximum RDA defects for each fluence is centered mainly around 80 nm, which is close to the range of the implanted ions and the fraction of RDA increases with increasing the fluence of implanted ions. The distribution of RDA for La and Xe ions shows that for both ions the features are similar regardless the nature of ions and their different chemical contribution.

(ii) Medium fluence range: Figure E-4.a represents the distribution of RDA at medium fluence range. The radiation damage follows a completely different behavior compared to the low ion fluence range. Nevertheless, a similar behavior is obtained for this range of fluence for both ions: the width of the distribution of RDA is progressively increased as the fluence increases, and the damage zone extends

to greater depth with increasing the fluence for both ions, i.e. larger than the (Rp+ΔRp) = 127 nm given by the SRIM calculations. It is observed that within this medium ion fluence range, the maximum fraction of RDA is almost not varying and it saturates for crystals implanted with La ions and Xe ions. A difference in this fraction is observed between the two ions: the damage in crystal implanted with 470 keV Xe ions saturates at higher level (the average maximum fraction of RDA is 25%), while for the crystal implanted with 500 keV La ions shows a lower fraction (the average maximum fraction of RDA is 20%).

(ii) High fluence range: the distribution of RDA presents both similarities and differences for irradiation with noble gas Xe ion compared to La. Figure E-5.a shows that in both cases, the creation of radiation damage seems to reach a depth limit that does not exceed 300 nm. Beyond this depth, no radiation damage is created. The maximum fraction of RDA for crystal irradiated with La saturates and does not increase dramatically with increasing the fluence even for high fluences.

Regarding implanting Xe ions, different distribution of RDA is obtained specially in case of high fluence of implantation (corresponding to concentration over 5 at. %) where a huge damage obtained close to the surface as shown in figure E-5.a. The evolution of BC fraction shows the following features: (i) at low fluences: both ions show the same increase of BC fraction with increasing the fluence .

(ii) Medium fluence range: the fraction of BC is observed to dramatically increase and extend into the larger depth within this fluence range, while the maximum fraction of RDA does not vary with ion fluence. As it can be seen on figure E-4.b, a similar evolution of BC is observed for both implanted ions regardless to the nature of ions. The fraction of BC is observed to increase regularly from around 5 to ~ 50 %, while the corresponding depth extends from 160 to 250 nm. It is more likely that the saturation of the RDA previously observed (see figure E-4.a) is reached by the consequential transformation between two classes of defects. When the saturation of RDA takes place, further irradiation lead to the creation of RDA that immediately transform into BC.

(ii) High fluence range: The fraction of BC for both ions in this fluence range almost saturates and the value stay almost constant around 80%. For both ions the fraction of BC does not exceed the thickness of 300 nm.

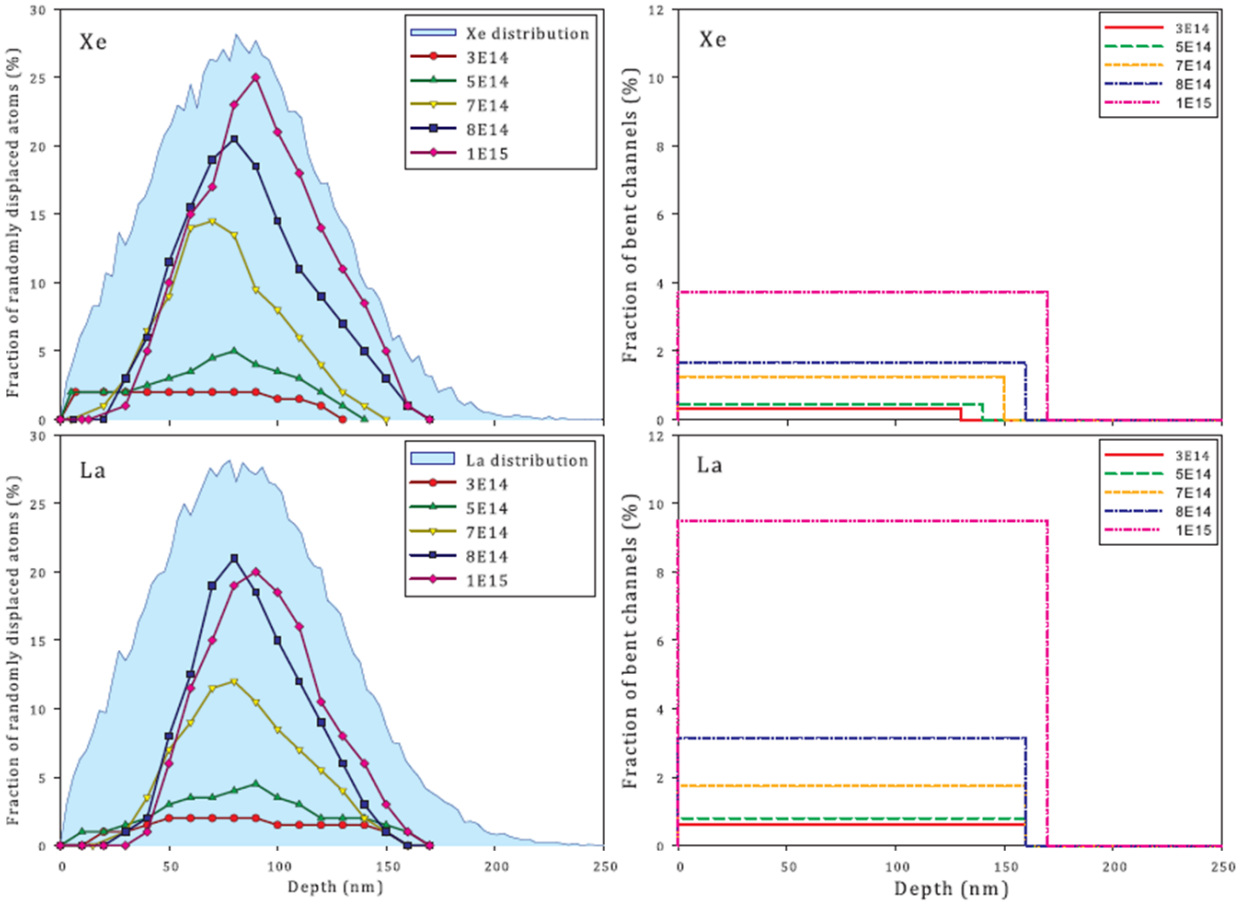

Figure E-3: fraction of RDA (a) and BC (b) versus depth in UO_2 crystal implanted with La and Xe at low fluence ($\Phi \leq 1x10^{15}$ cm^{-2}) extracted from MC simulations. The parameters for BC are L = 5 nm and $\eta = 1.5°$. La and Xe distribution profile in UO_2 calculated by SRIM (Cyan filled area) are plotted in arbitrary unit.

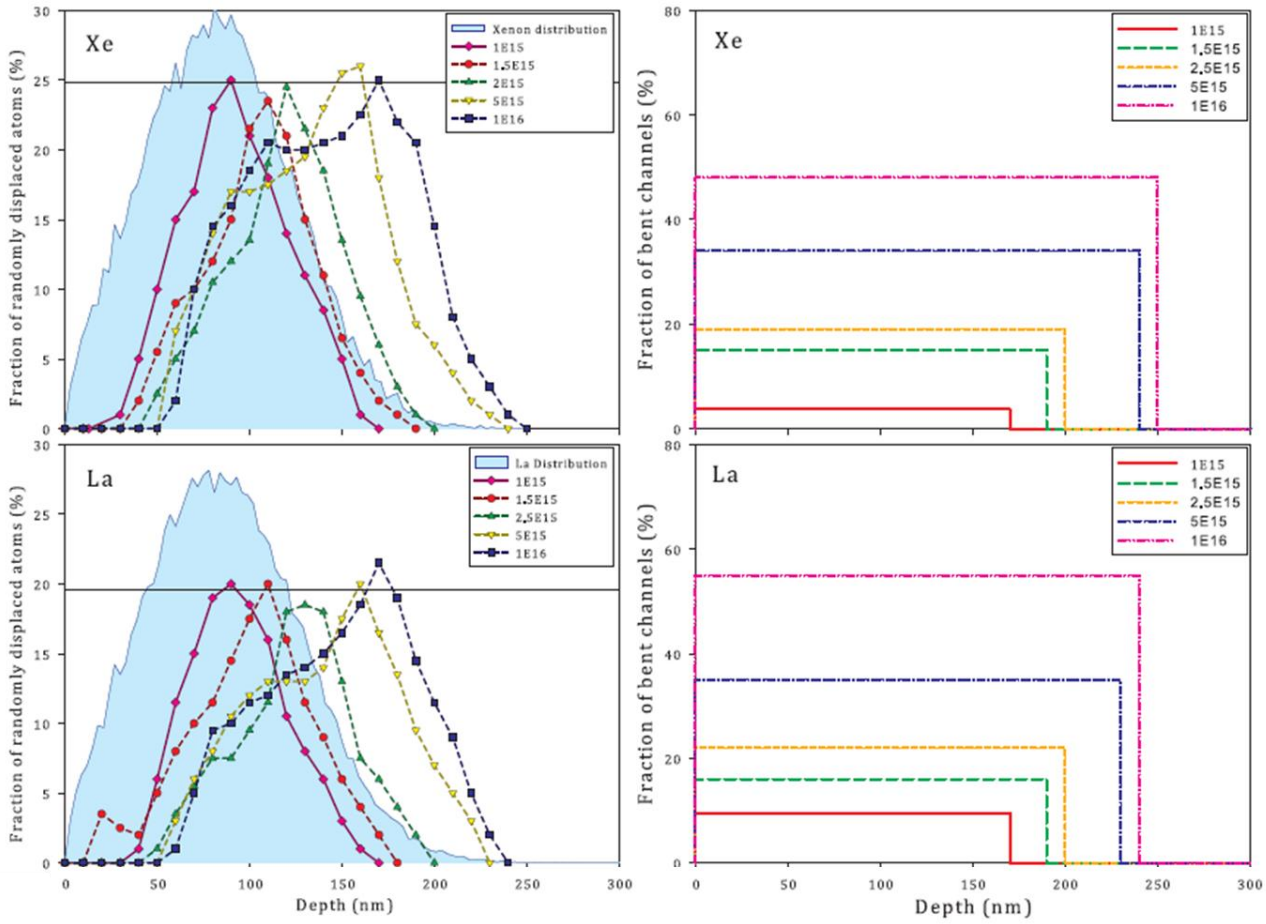

(a) (b)

Figure E-4: fraction of RDA (a) and BC (b) versus depth in UO_2 crystal implanted with La and Xe at medium fluence range ($1x10^{15}$ $cm^{-2} \leq \Phi \leq 1x10^{16}$ cm^{-2}) extracted from MC simulations. The parameters for BC are L = 5 nm and η = 1.5°. La and Xe distribution profile in UO_2 calculated by SRIM (Cyan filled area) are plotted in arbitrary unit.

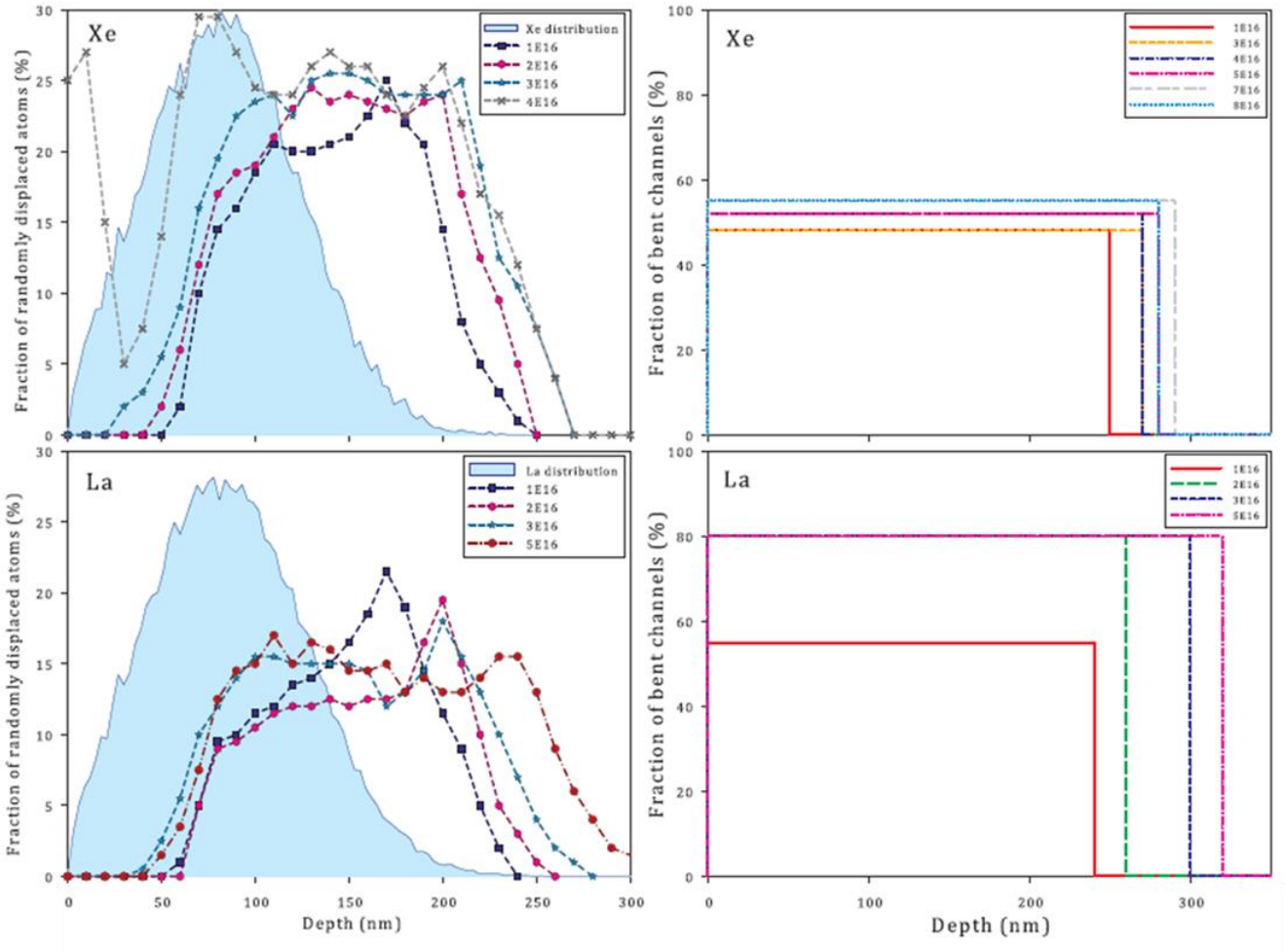

(a) (b)

Figure E-5: fraction of RDA (a) and BC (b) versus depth in UO_2 crystal implanted with La and Xe at high fluence range ($\Phi \geq 1x10^{16}$ cm^{-2}) extracted from MC simulations. The parameters for BC are L = 5 nm and η = 1.5°. La and Xe distribution profile in UO_2 calculated by SRIM (Cyan filled area) are plotted in arbitrary unit.

List of Figures

List of Tables

List of Abbreviations

CNRS	Centre National de la Recherche Scientifique
CSNSM	Centre de Sciences Nucléaires et de Sciences de la Matière
JANNuS	Joint Accelerators for Nano-science and Nuclear Simulation
LWR	Light water reactor
PWR	Pressurized Water Reactor
MOX	Mixed OXide fuel, specially a mixture of UO_2 and PuO_2
HBS	High Burnup Structure
RBS/C	Rutherford Backscattering Spectrometry in Channelling mode
TEM	Transmission Electron Microscopy
HRTEM	High Resolution Transmission Electron Microscopy
ED	Electron Diffraction
XRD	X-Ray diffraction analysis
SRIM	The Stopping and Range of Ions in Matter
TRIM	The Transport of Ions in Matter
MC	Monte-Carlo
RDA	Randomly displaced atoms
BC	Bent Channels
dpa	displacements per atom
DF	Dark field
BF	Bright field
DP	Diffraction pattern
RT	Room temperature

Titre : Élucidation des mécanismes de formation de la structure HBS (High Burnup Structure) dans le combustible nucléaire – Simulation expérimentale par faisceaux d'ions

Mots clés : Oxyde d'uranium, Structure HBS, Irradiation, Techniques de caractérisation, Simulation de Monte-Carlo.

Résumé : L'objectif de cette thèse est d'étudier et de reproduire les caractéristiques spécifiques de la microstructure du combustible nucléaire irradié à fort taux de combustion, appelée structure HBS (High Burnup Structure). Il s'agit d'étudier les différents paramètres pertinents impliqués dans la formation d'une telle structure, en évaluant leur importance, et en clarifiant leurs éventuelles synergies. Cet objectif a été réalisé en utilisant un système de modèle ultra simplifié, à savoir des monocristaux de dioxyde d'uranium (UO_2) irradiés par des ions de basse énergie (quelques centaines de keV) de Lanthane (La) ou de xénon (Xe) à une température de 773 K, correspondant à celle de la périphérie des véritables pastilles de combustible en réacteur. Les énergies et les masses des ions ont été choisies pour étudier la déstabilisation du solide en fonction de deux paramètres-clefs: (i) les collisions nucléaires élastiques et (ii) la contribution chimique de l'incorporation d'impuretés à forte concentration. Les deux espèces ont été choisies délibérément pour leurs solubilités très différentes dans le dioxyde d'uranium: les ions La sont solubles dans l'UO_2 jusqu'à de très fortes concentrations, tandis que les ions Xe sont insolubles. Les techniques de la Microscopie Électronique en Transmission (TEM) et de Spectrométrie de Rétrodiffusion Rutherford en canalisation RBS/C ont été conduites *in situ* couplée avec l'irradiation. Ces deux techniques utilisées pour visualiser, quantifier et fournir des informations concernant la fraction des défauts induits par l'irradiation et la formation des bulles, de cavités ou de précipités dans le solide. Les données de canalisation ont été analysées par simulation Monte-Carlo en supposant l'existence de deux catégories de défauts : (i) des atomes aléatoirement déplacés (RDA) et (ii) des distorsions des rangés atomiques (BC). L'évolution de la fraction de défaut de type RDA montre une forte augmentation entre 0.4 à 4.0 dpa (correspondant à une très faible concentration des ions implantés), indépendamment de la nature des ions. Elle est suivie par une saturation de la fraction de RDA pour les deux ions sur une large gamme d'irradiation qui s'étend jusque 100 dpa. Une forte élévation de la fraction de RDA est observée en particulier pour les cristaux implantés avec des ions Xe pour une concentration élevée dépassant les 4% (pourcentage correspondant à la dose de plus de 250 dpa). En ce qui concerne l'évolution de BC, pour les deux ions, elle augmente fortement jusqu'à 4 dpa et sature ensuite. Les résultats de microscopie électronique *in situ* montrent que des défauts identiques pour apparaissent les deux ions induits par l'irradiation, et présentent la même évolution en fonction de la fluence. Les différents défauts évoluent en fonction de la fluence : la première étape correspond à la formation de 'black dots'; la deuxième étape est caractérisée par la formation de boucles puis de lignes de dislocations, qui évoluent finalement jusqu'à commencer à devenir moins différenciables; le processus de restructuration se poursuit et forme un réseau de dislocations enchevêtrées. Une forte densité de bulles de gaz, de taille nanométrique et avec un diamètre moyen de 2 nm est observée pour le cristal Xe implanté à une dose seuil de 4 dpa. Le couplage des deux techniques (RBS/C et TEM) conduites *in situ* montre que la différence entre les valeurs à saturation des fractions RDA des deux ions, d'une part, et l'augmentation drastique de RDA à très forte concentration d'ions Xe implantés, d'autre part, peuvent être attribuées à: (i) la solubilité des ions La vis-à-vis des ions Xe, conduisant à la formation des bulles de gaz de taille nanométrique et (ii) la taille des espèces implantées dans la matrice UO_2, pour laquelle les atomes Xe insolubles ont un rayon atomique beaucoup plus grand que le rayon cationique des atomes U^{4+} (les atomes La^{3+} ont un rayon atomique similaire à celui des atomes U^{4+}), responsable de contraintes supplémentaires dans la structure cristalline. Ces expériences soulignent le rôle décisif des gaz de fission insolubles dans les mécanismes de déstabilisation du cristal irradié.

Title: Investigation of the formation mechanisms of the HBS (High Burnup Structure) in the spent nuclear fuel – Experimental simulation with ions beams.

Keywords : Uranium oxide, High burnup structure (HBS), Irradiation, Characterization techniques, Monte-Carlo simulation

Abstract: The aim of this thesis is to investigate and reproduce the specific features of the microstructure of the high burnup structure of the irradiated nuclear fuel and to explore the various relevant parameters involved in the formation of such a structure, in evaluating their importance, and in clarifying the synergies between them. This have been performed by using a very simplified model system – namely uranium dioxide single crystals- irradiated with low energy La and Xe ions at 773 K, corresponding to the temperature at the periphery of the genuine fuel. The energies and masses of bombarding ions were chosen to investigate the destabilization of the solid due to: (i) the elastic nuclear collisions and by (ii) the chemical contribution of implanting impurities at high concentrations by implanting different ions in UO_2, namely Xe and La, having a very different solubility: La species are soluble in UO_2 while Xe ions are insoluble. *In situ* Transmission electron Microscopy (TEM) and *in situ* Rutherford Backscattering Spectrometry in the channeling mode (RBS/C), both techniques coupled to ion irradiation, were performed to visualize, quantify, and provide information with respect to the fraction of radiation-induced defects and the formation of bubbles, cavities, or precipitates. The channeling data were analyzed afterwards by Monte Carlo simulations assuming two class of defects comprising (i) randomly displaced atoms (RDA) and (ii) bent channels (BC) defects. Regarding the RDA evolution, a sharp increase step appears from 0.4 to 4.0 *dpa* (corresponding to a low concentration of implanted ions) regardless of nature of ions followed by a saturation of the fraction of RDA for both ions over a wide range of irradiation. A sharp increase of RDA fraction is observed specifically for crystals implanted with Xe ions at a high concentration exceeding 1.5% (corresponding to the dose of more than 125 *dpa*). Regarding the BC evolution, for both ions, the evolution shows an increase in the fraction of BC up to 4.0 *dpa* then the fraction of BC almost saturates for Xe and La ions. *In situ* TEM results show that a similar radiation-induced defects appear for both ions and the same evolution of defects as a function of the fluence is observed. The various defects evolved as a function of the fluence: black dot defects were observed as a first type of defects created, then dislocation lines and loops appeared and evolved until they started to be become less distinguishable, the restructuring process continued by forming a tangled dislocation network. A high density of nanometer-sized gas bubbles with a mean diameter 2 nm was observed at room temperature for the Xe-implanted crystal at a threshold dose of 4 *dpa*. The coupling between both techniques demonstrates that the difference between the two plateaus of saturation between the two ions and the dramatic increase of RDA at high concentration of implanted Xe ions can be ascribed to: (i) the solubility of La compared to Xe ions leading to the formation of nanometer-sized gas bubbles and (ii) the size of implanted species in UO_2 matrix where insoluble Xe atoms have an atomic radius much larger than the cationic radius of U^{4+} atoms, (La^{3+} atoms have a similar atomic radius as U^{4+} atoms) responsible for more stress in UO_2 crystal. These experiments emphasize the decisive role of insoluble fission gases in the destabilization mechanisms of the irradiated crystal.

Université Paris-Saclay
Espace Technologique / Immeuble Discovery
Route de l'Orme aux Merisiers RD 128 / 91190 Saint-Aubin, France